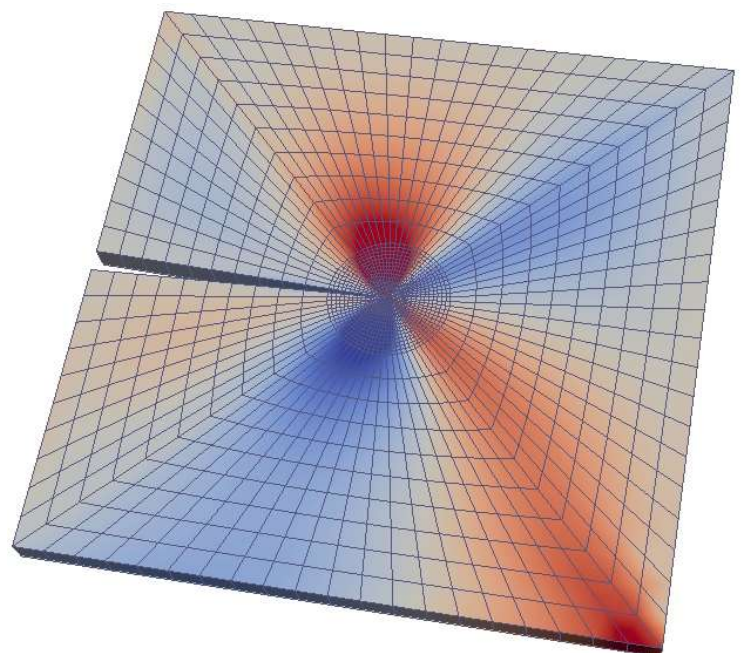
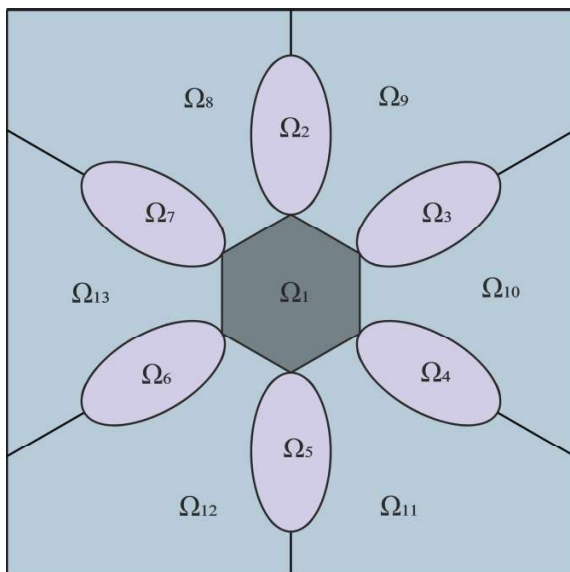


Relaxation Based Modeling of Inelastic Materials — Effective Models and Evolution of Microstructures

Ghina Jezdan



Dissertation

Relaxation Based Modeling of Inelastic Materials
-
Effective Models and Evolution of Microstructures

Zur Erlangung des akademischen Grades

Dr.-Ing.

vorgelegt der

Fakultät für Bau- und Umweltingenieurwissenschaften

an der Ruhr-Universität Bochum

von

Ghina Nabil Jezdan,

Bochum 2024

Mitteilungen aus dem Institut für Mechanik Nr. 192

Herausgeber:
Institut für Mechanik
— Schriftenreihe —
Ruhr-Universität Bochum
D-44780 Bochum

ISBN 978-3-935892-70-4

Dieses Werk ist urheberrechtlich geschützt. Die dadurch begründeten Rechte, insbesondere die der Übersetzung, des Nachdrucks, des Vortrags, der Entnahme von Abbildungen und Tabellen, der Funksendung, der Mikroverfilmung oder der Vervielfältigung auf anderen Wegen und der Speicherung in Datenverarbeitungsanlagen, bleiben, auch bei nur auszugsweiser Verwertung, vorbehalten. Eine Vervielfältigung dieses Werkes oder von Teilen dieses Werkes ist zulässig. Sie ist grundsätzlich vergütungspflichtig. Zuwiderhandlungen unterliegen den Strafbestimmungen des Urheberrechtsgesetzes.

©2024 Institut für Mechanik der Ruhr-Universität Bochum

Printed in Germany

Einreichung der Dissertation (thesis submission): 20.11.2023

Mündliche Prüfung (thesis defence): 29.04.2024

1. Gutachter (first referee): Prof. Dr. rer. nat. Klaus Hackl
 2. Gutachter (second referee): Prof. Dr.-Ing. habil. Daniel Balzani
 3. Gutachter (third referee): Prof. Dr.-Ing. habil. Philipp Junker
- Vorsitzender (committee chair): Prof. Dr.-Ing. habil. Torsten Wichtmann

To my beloved husband and children: Jan, Philep and Thomas
To my supportive parents and siblings

Summary

In this dissertation the findings from an open research topic in the field of variational methods are presented. They are used to model inelastic materials comprising microstructure. The derivation is based on the laws of thermodynamics implemented within the variational principles. A time-incremental approach is introduced to yield a set of equations applicable to numerical computations. This thesis consists of two major topics, one dealing with effective models in the field of homogenization, and a second one with relaxation.

The first part covers reduced models designed by means of multi-scale modeling with effective properties. The coarse-scale model in terms of the free energy and dissipation potential is based on the free energy and dissipation potentials defined at the fine-scale, employing a coarse-scale model that comprises the same structure of the fine-scale model. A main feature for this scheme is the careful selection of the essential variables prescribing the inelastic behavior. Applying the variational formulation results in a set of incremental evolution solution for the internal variables, which allows the application to numerical examples. The proposed approach is applicable to structural elements in addition to computations in homogenization problems.

The second part of this thesis prescribes materials with parameter-dependency defining inelastic behavior. The parameter covered in this investigation is pressure. Such pressure-dependent plastic materials are characterized by non-associative flow rules and a concave yield surface for the critical transition between ductile and brittle behavior. Concavity results in a non quasiconvex variational problem having no regular solutions. Moreover, experimental results from granular media have revealed the existence of shear band microstructures. Non quasiconvex numerical problems are accompanied with numerical instabilities. Solution techniques are given by means of relaxation, i.e., minimization with respect to small scale structures. However, computing a quasiconvex envelope is in most cases too complex, therefore, in the beginning, a one-dimensional toy model is investigated for which an analytical solution is defined. Lastly, a generalization to higher dimensions is done by approximating a convex envelope of the free energy instead of a quasiconvex envelope. Various numerical calculations are provided.

Acknowledgments

Thinking back of 2017, when I started at the Institute of Mechanics of Materials at Ruhr University Bochum, first as a master student and then getting the opportunity to proceed as a Doctor Associate, I'd like to acknowledge my sincere appreciation to everyone who supported me to accomplish the work presented in this thesis. Without their continuous support, it would have never been possible to do it.

Especially, I'd like to express the highest gratitude to my supervisor Prof. Klaus Hackl, who gave me the chance to join his team at the Institute since my Master studies. Thanks for his continuous scientific support and his patience with me till I got my current level of knowledge. He introduced me to the field of homogenization and relaxation, and provided fruitful ideas and approaches, which led to the results reported in this thesis. I would like further to admire his social assistance and understanding especially within my pregnancy period and when coming back from the maternity leave, he behaved as a caring father. Moreover, I'm grateful for his style in leading the Institute in which he allows the employees a huge amount of flexibility and focuses on the achievements.

I would like also to give my appreciation to Prof. Philipp Junker from the Leibniz University of Hannover who supervised my Master thesis during his time at the Ruhr-University Bochum, and proceeded to offer continuous scientific support upon demands in my research.

As well, I'd like to thank Prof. Sanjay Govindjee from Berkeley University of California, for the joint work in the field of multi-scale and homogenization. He provided scientific insights and generous support for the numerical implementation through the finite element analysis program (FEAP). Equally, I'd like to express my deep appreciation to Prof. Georg Dolzmann from the University of Regensburg for the joint work in the field of relaxation within the Priority Program SPP 2256. His scientific curiosity motivated the work and enabled an open space of interaction.

I gratefully thank the funding by the German Research Foundation (DFG) within the Priority Program 2256 "Variational Methods for Predicting Complex Phenomena in Engineering Structures and Materials". Not only the financial support is greatly acknowledged, but rather more the fruitful conferences and schools as a great environment for gaining knowledge.

Finally, I'd like to thank all those who have been around till this work is accomplished. First thanks to all my colleagues at the Institute of Mechanics of Materials, the former and the current ones, for the friendly working atmosphere and the precious scientific inspiration. I especially thank Dr.-Ing Golnaz Hoormazdi for the pure friendship starting at the Institute and proceeding apart from the work. I sincerely thank as well Dr.-Ing Ulrich Hoppe, who is always there to assist and encourage the team whether scientifically or technically. At most I thank my family for believing in me, for their continuous support and patience when I worked late or spent weeks abroad on conferences or schools. Special thank as well to my parents, my siblings with families and all my friends for their motivation and assistance.

Nomenclature

Latin Notations

\mathbf{a}	General tensor of first order
$\mathbf{a}_i, \mathbf{a}_j$	Amplitude vectors at the sides of the polyhedral subdomains
\mathbb{A}_i	Stiffness in subdomain Ω_i
\mathbb{A}_{eff}	Effective stiffness for the representative volume element
\mathbf{A}, \mathbf{B}	General tensor of second order
b	Nondimensional hardening modulus
\mathbf{b}	Body force and normal vector
\mathbb{B}	Strain concentration tensor
c	Cohesion
\mathbb{C}	Tensor of elastic moduli
\mathbb{C}_R	Reuss stiffness
D	Dissipation distance
\mathbf{e}_i	Strain tensor in subdomain Ω_i
\mathbf{e}_M	Macroscopic strain
\mathbf{e}_{pi}	Plastic strain tensor in subdomain Ω_i
\mathbf{e}_{pM}	Macroscopic plastic strain tensor
$\mathbf{e}_{p,1}$	Plastic strain tensor for laminates in the 1 st direction, Sec. 4.7
$\mathbf{e}_{p,2}$	Plastic strain tensor for laminates in the 2 nd direction, Sec. 4.7
E	Young's modulus
f_{ext}	Potential of external forces, Sec. 3.1
f_{ess}	Potential of external forces in terms of the essential parameters, Sec. 3.1
F	Force
\mathbf{F}	Deformation gradient
I	Identity matrix
J	Jacobian
\mathbf{J}	Jacobian matrix
K	Bulk modulus
L	Length of the cylinder in Sec. 3.1.2
\mathbf{n}	Normal vector
N_e	Number of elements
N_{GP}	Number of Gauß points
N_{sd}	Number of subdomains
p	Plastic parameter in Sec. 4
q	Hardening parameter in Sec. 3.1
\mathbf{q}	Driving force in Sec. 3.2
Q, Q_p	Positive definite quadratic potentials
r	Radial coordinate
\mathbf{r}	Position vector
R	radius of the cylindrical body
t	Time
\mathbf{t}	Traction forces
T	Torque
u	Displacement
\mathbf{u}	Displacement field
\mathbf{u}_{per}	Displacement field satisfying the periodic boundary conditions
v	Velocity
\mathbf{x}	Vector of external state variables

x	Space coordinates in current configuration
\mathbf{X}	Space coordinates in reference configuration
z	Axial coordinate of the cylinder in Sec. 3.1.2
\mathbf{z}	Vector of internal state variables.

Greek notations

α	Hardening modulus in Sec. 3.1
β	Hardening modulus in Sec. 4
γ	Viscous parameter in Sec. 4.7
Δ	Dissipation potential
Δ_{macro}	Macroscopic dissipation potential
ε	Strain
$\boldsymbol{\varepsilon}$	Strain tensor
$\boldsymbol{\varepsilon}_e$	Elastic strain tensor
$\boldsymbol{\varepsilon}_p$	Plastic strain tensor
θ	Rotation angle
θ'	Twist rate in Sec. 3.1.2
κ	Consistency parameter in Sec. 4
λ	Consistency parameter in Sec. 3.2
λ_i	Volume fraction in Sec. 3.2
λ_1	Volume fraction for laminates in the 1 st direction, Sec. 4.7
λ_2	Volume fraction for laminates in the 2 nd direction, Sec. 4.7
μ	Shear modulus
ν	Poisson's ratio
ξ_{\min}, ξ_{\max}	Lower and upper sides of the interval for the pressure-dependent function, Sec 4
ρ	Lagrange multiplier in Sec. 3.2
τ	Shear stress field
σ_y	Yield stress
$\boldsymbol{\sigma}$	Stress tensor
ϕ	Friction angle
Φ	Yield function
ψ, Ψ	Free energy
Ψ_{macro}	Macroscopic energy
Ω	Volume of a body
Ω_i	Volume of a subdomain
$\partial\Omega$	Surface of a body

Abbreviations

macro	Macroscopic
vol	Volumetric
dev	Deviatoric
eff	Effective
ess	Essential
RVE	Representative volume element
per	Periodic
cond	Condensed
rel	Relaxed
ext	External
GP	Gauß point

Mathematical operators

$\delta(\cdot)$	Variation
$\partial(\cdot)$	Partial derivative
$\Delta(\cdot)$	Increment
$\nabla(\cdot)$	Nabla operator
$\arg \min(\cdot)$	Argument of the minimum
$\arg \max(\cdot)$	Argument of the maximum
$\text{div}(\cdot)$	Divergence
$\det(\cdot)$	Determinant
$\text{grad}(\cdot)$	Gradient
$\text{inf}(\cdot)$	Infimum
$\text{lim}(\cdot)$	Limit of a function
$\min(\cdot)$	Minimum
$\max(\cdot)$	Maximum
$\text{sign}(\cdot)$	Signum function
$\text{sup}(\cdot)$	Supremum
$\text{sym}(\cdot)$	Symmetric part of a matrix
$\text{tr}(\cdot)$	Trace
$\text{dev}(\cdot)$	Deviator
$d(\cdot)/dt = \dot{(\cdot)}$	Time derivative/ rate
$d(\cdot)/dx$	Total derivative with respect to x
$\partial(\cdot)/\partial x$	Partial derivative with respect to x
$\langle \cdot \rangle$	Averaged quantity
$[\cdot]_+$	Permits only positive values
$(\cdot)^k$	Reference to last iteration step
$(\cdot)^{k+1}$	Reference to current iteration step
$(\cdot)'$	First derivative
$(\cdot)''$	Second derivative
$(\cdot)^{-1}$	Inverted
$(\cdot)^T$	Transposed

Contents

1	Introduction	1
1.1	Motivation	1
1.2	Outline	2
2	Fundamentals	3
2.1	Mathematical notations	3
2.1.1	Tensor products	4
2.1.2	Tensor analysis	5
2.1.3	Voigt notation	5
2.2	Continuum mechanics and thermodynamics	6
2.2.1	Kinematics	6
2.2.2	Balance laws	8
2.2.3	Conservation of mass	9
2.2.4	Balance of linear and angular momentum	9
2.2.5	First law of thermodynamics: Balance of energy	10
2.2.6	Second law of thermodynamics: Entropy inequality	11
2.2.7	Constitutive equations	11
2.3	Variational principle	12
2.3.1	General form of Hamilton's principle	13
2.3.2	The principle of the minimum dissipation potential - PMDP	14
2.4	Two-scale homogenization scheme	15
2.4.1	Basic concepts in micro-macro mechanics	16
2.4.2	Effective properties	17
2.5	Variational modeling of microstructure	17
2.5.1	Condensed energy	18
2.5.2	Essential microstructure	18
2.5.3	Relaxation via lamination	19
2.6	Convex analysis	21
2.6.1	Definitions	21
2.6.2	Notions of convexity	23
3	Effective models for inelastic materials	25
3.1	First effective model - RM_1	25
3.1.1	Elastoplasticity with isotropic hardening	27
3.1.2	Cylindrical body under torsion	28
3.1.3	Pressurized spherical body	35
3.1.4	Homogenization of elastoplastic materials with periodic microstructure	39
3.1.5	Polyhedral sub-domains	42
3.1.6	Basic example	43
3.1.7	Non-symmetric RVE	45
3.1.8	RVE with octagon center inclusion	50

3.1.9	Two-scale homogenization scheme including the reduced model RM_1	53
3.1.10	Conclusion - RM_1	54
3.2	Second effective model - RM_2	55
3.2.1	Derivation of the model	55
3.2.2	Numerical preparation	62
3.2.3	RVE with square center inclusion	63
3.2.4	RVE with octagon center inclusion	65
3.2.5	RVE with ellipse center inclusion	66
3.2.6	RVE with random inclusions	69
3.2.7	Conclusion - RM_2	69
4	Pressure dependent plasticity	75
4.1	Classical models in pressure-dependent plasticity	75
4.2	Variational settings	78
4.3	A one-dimensional model problem	81
4.4	Extension to three-dimensional model problem	86
4.5	Numerical results 1D	87
4.6	Numerical results 2D	90
4.6.1	A plate with a hole	95
4.6.2	Double notch	97
4.6.3	Crack problem	98
4.7	Evolution of the microstructure	100
4.7.1	Initiation	107
4.7.2	Numerical treatment	109
4.7.3	Material subject to uniaxial compression and simple shear	110
4.7.4	Material under shearing and constant pressure	110
4.7.5	Finite element comparison for the plate with a hole	112
4.7.6	Finite element comparison for the double notch	114
4.7.7	Finite element comparison for the crack problem	116
4.8	Conclusion - pressure-dependent plasticity	117
5	Outlook	127
	Bibliography	129
	Reference to pre-publications	135
	Curriculum Vitae	137

1 Introduction

1.1 Motivation

Engineering technological change and the arising industrial demand for modern materials with special characteristics, increases the level of difficulty to model such materials. Complex materials are assigned with heterogeneous properties at the micro level. Therefore, models with multi-scale character can be the best choice to prescribe them. Nevertheless, modeling such systems to the full extent requires high computation times and data storage. It is desirable now to investigate effective models to capture the essential behavior of the system as close as possible, but rely only on a small set of effective variables. Common used methods in the literature to model complex materials are based on phenomenological models. These try to mimic the material behavior directly at the macro-scale, reducing the computation costs extremely. However, such models observe elaborate behavior and require a large number of parameters. Many parameters have often no physical meaning and are difficult to identify. The other possibility to model complex materials is the direct numerical simulation. It captures the behavior at the micro-scale efficiently with a few number of parameters. Yet, generating information at the macro-scale from the micro-scale can be done through only computationally expensive procedures. So, the target is to apply a variational approach to the homogenization of inelastic materials with microstructure in which only few number of physically well-defined parameters are involved. Then, it is possible to capture the essential material behavior at the macro-scale as well at the micro-scale without increasing the computational costs. Implementations of variational methods in the field of homogenization for inelastic systems is not new. Similar models have been derived for examples in shape memory alloys, see (Govindjee, Hackl, and Heinen 2007), (Junker and Hackl 2011), (Junker and Hackl 2014), (Waimann, Junker, and Hackl 2016), and in the prediction of dislocation patterns in single crystal metals, see (Aubry, Fago, and Ortiz 2003), (Conti and Ortiz 2005), (Conti, Dolzmann, and Klust 2009), (Frankenreiter, Rosato, and Miehe 2010), (Günther, Junker, and Hackl 2015), (Gürses and Miehe 2011).

In this thesis, two reduced models are investigated: the first reduced model RM_1 and the second reduced model RM_2 , where the second one is developed to overcome some examined drawbacks resulting from the first model.

An additional objective of this thesis is to investigate elastoplastic materials with pressure-dependency (like soils and granular media). The interest in such materials is regarded to the experimental results, which show shear band microstructures under deformation.

Starting from investigations of elastoplastic materials characterized with microstructure as shown in (Ball and James 1987), (Chipot and Kinderlehrer 1988) and (Ball

and James 1992) led to the realization that such experiments (comprising the evolution of microstructure) can be well explained by energy minimization. This emphasized the usage of the variational methods to understand the behavior of complex materials. Therefore, we apply the variational approach to prescribe the evolving microstructure in pressure-dependent plastic materials, namely, granular media.

A minimization with respect to these small scale microstructures leads to non-convex potentials, resulting in numerical and stability issues. Therefore, the aim is to introduce a paradigm that solves the problems of non-quasiconvexity by means of model reduction via relaxation. We employ the variational approach to describe the essential model features with as few parameters as possible for materials in soil mechanics. This goal is implemented first by applying the relaxation approach to a one-dimensional toy model in which analytical and numerical results are provided. Then the evolution of the microstructure approximated by a convex envelope is covering the problem. Well-posedness of the introduced relaxation schemes is checked by fulfillment of mesh-independency.

1.2 Outline

This thesis is structured as follows: we start with Chapter 1 under which this introduction and outline follows, then in Chapter 2 the mathematical and mechanical background for this work is provided. Some introductory sections to the variational approach, the homogenization concept and the recipes to the relaxation scheme are given as well. Two novel effective models are derived in Chapter 3 in a variational manner prescribing systems with inelastic materials. Their applications are shown in structural elements and in microstructural homogenization problems under periodic boundary conditions. The first effective model returns very promising results and is open to a large field of applications, but is restricted in microstructural problems to polyhedral subdomains. The second effective model, with additional quadratic constraints, was able to overcome this problem. This chapter is concluded with the main findings from both models. In Chapter 4 models of pressure-dependent plastic materials are investigated. We discuss first the classical models in soil mechanics, motivating the critical issues leading to the problem of lack of quasiconvexity. Two models are introduced in this chapter: the first one provides an analytical relaxed solution for a one-dimensional problem and is then extended in a heuristic manner to three-dimensions. The second model studies an evolution of the observed microstructure by applying a convexification technique. Detailed discussion of the results concludes this chapter. Lastly, a short outlook giving insights to possible future work is presented in Chapter 5.

2 Fundamentals

In this chapter, some mathematical and mechanical fundamentals are given to clarify the methodology applied to the models presented in this thesis. First, in Sec. 2.1, some mathematical notations and conventions from tensor analysis are given. Second, in Sec. 2.2, the main continuum mechanical basics and laws of thermodynamics are introduced. An introduction to the variational formulation, which applies all over this thesis, is given in Sec 2.3, then a short review of multi-scale modeling is presented to enhance the derivation of the models presented in Sec. 3. Some introductory definitions prescribing inelastic materials with microstructure are given later in Sec. 2.5. Lastly, a brief introduction to convex analysis is given in Sec. 2.6, which is applied to the models outlined in Sec. 4.

2.1 Mathematical notations

The mathematical conventions presented here are based on the works of (Holzapfel 2002) and (Chou and Pagano 1992). In a Cartesian coordinate system, with basis $\{e_i\}; i = 1, 2, 3$ and using the indicial notation, a tensor of zeroth order corresponds to a scalar, denoted as $a, b, c..$, whereas a tensor of first order corresponds to a vector denoted as $\mathbf{a}, \mathbf{b}, \mathbf{c}..$, and a tensor of second order corresponds to a matrix denoted as $\mathbf{A}, \mathbf{B}, \mathbf{C}, \dots$ with

$$\mathbf{a} = (a_i) = \begin{pmatrix} a_1 \\ a_2 \\ a_3 \end{pmatrix}, \quad \mathbf{A} = (A_{ij}) = \begin{pmatrix} A_{11} & A_{12} & A_{13} \\ A_{21} & A_{22} & A_{23} \\ A_{31} & A_{32} & A_{33} \end{pmatrix}. \quad (2.1.1)$$

We will use all over this thesis boldface symbols for vector-valued or matrix-valued objects.

There are also higher order tensors as for example the fourth order tensor expressing the material stiffness, denoted as $\mathbb{A}, \mathbb{B}, \mathbb{C}, \dots$.

Applying Einstein summation convention to a vector \mathbf{a} is given as

$$\mathbf{a} = a_i e_i := \sum_i a_i e_i = a_1 e_1 + a_2 e_2 + a_3 e_3. \quad (2.1.2)$$

2.1.1 Tensor products

Dyadic or tensor product: any second order tensor \mathbf{A} can be expressed as a dyadic product of two vectors \mathbf{a} and \mathbf{b} , given with Cartesian basis $\{e_i\}$ as

$$\mathbf{A} = \mathbf{a} \otimes \mathbf{b} = a_i b_j e_i \otimes e_j = A_{ij} e_i \otimes e_j . \quad (2.1.3)$$

The same can be generalized to a tensor of fourth order

$$\mathbb{A} = A_{ijkl} e_i \otimes e_j \otimes e_k \otimes e_l . \quad (2.1.4)$$

The dot product (also known as scalar product) of two vectors gives a scalar c

$$\mathbf{a} \cdot \mathbf{b} = a_i b_j \delta_{ij} = c , \quad (2.1.5)$$

where δ_{ij} is the Kronecker delta written as

$$\mathbf{e}_i \cdot \mathbf{e}_j = \delta_{ij} = \begin{cases} 1, & \text{if } i = j, \\ 0, & \text{if } i \neq j. \end{cases} \quad (2.1.6)$$

The dot product of a vector and a second order tensor gives a vector

$$\mathbf{a} \cdot \mathbf{B} = a_i B_{ij} e_j = \mathbf{c} . \quad (2.1.7)$$

The dot product of two second order tensors is again a second order tensor

$$\mathbf{A} \cdot \mathbf{B} = A_{ij} B_{jk} e_i \otimes e_k = \mathbf{C} . \quad (2.1.8)$$

The double contraction of two second order tensors is a scalar

$$\mathbf{A} : \mathbf{B} = \mathbf{B} : \mathbf{A} = A_{ij} B_{ij} . \quad (2.1.9)$$

The double contraction of a fourth order tensor and a second order tensor gives a second order tensor

$$\mathbb{A} : \mathbf{B} = A_{ijkl} B_{kl} e_i \otimes e_j = \mathbf{C} . \quad (2.1.10)$$

The cross-product known also as vector product of two vectors \mathbf{a} and \mathbf{b} gives a new vector \mathbf{c}

$$\mathbf{c} = \mathbf{a} \times \mathbf{b} = a_i \mathbf{e}_i \times b_j \mathbf{e}_j = \epsilon_{ijk} a_i b_j \mathbf{e}_k = c_k \mathbf{e}_k , \quad (2.1.11)$$

where ϵ_{ijk} is the altering- or Levi-Civita symbol defined as

$$\epsilon_{ijk} = \begin{cases} 1, & \text{for even permutations of } (i, j, k) \quad (i.e. 123, 231, 312), \\ -1, & \text{for odd permutations of } (i, j, k) \quad (i.e. 132, 213, 321), \\ 0, & \text{if there is a repeated index.} \end{cases} \quad (2.1.12)$$

2.1.2 Tensor analysis

Scalar- $\phi(\mathbf{x})$, vector- $\mathbf{u}(\mathbf{x})$ and tensor-valued $\mathbf{A}(\mathbf{x})$ functions do assign a scalar, vector and tensor to each material point \mathbf{x} varying in space at a fixed time. Nabla (also gradient) is a vector operator giving the partial derivatives of a function field $f(\mathbf{x})$ with respect to the coordinates x_i

$$\nabla(\cdot) = \frac{\partial(\cdot)}{\partial x_i} \mathbf{e}_i = \frac{\partial(\cdot)}{\partial x_1} \mathbf{e}_1 + \frac{\partial(\cdot)}{\partial x_2} \mathbf{e}_2 + \frac{\partial(\cdot)}{\partial x_3} \mathbf{e}_3 , \quad (2.1.13)$$

$$\text{grad} f = \nabla(f) = \frac{\partial f}{\partial x_i} \mathbf{e}_i . \quad (2.1.14)$$

The divergence of a vector field results from the dot-product of the nabla operator with any vector field

$$\text{div} \mathbf{u} = \nabla \cdot \mathbf{u} = \frac{\partial u_i}{\partial x_i} . \quad (2.1.15)$$

The trace of a second order tensor \mathbf{A} is a scalar that sums up the diagonal terms of the matrix

$$\text{tr}(\mathbf{A}) = A_{ii} , \quad (2.1.16)$$

whereas the deviatoric part of a tensor is computed as

$$\text{dev}(\cdot) = (\cdot)_{ij} - \frac{1}{3}(\cdot)_{kk} \delta_{ij} . \quad (2.1.17)$$

2.1.3 Voigt notation

The equations relating stress and strain are called constitutive equations. In the case of elastic solids, the constitutive equations take the form of generalized Hooke's law

$$\boldsymbol{\sigma} = \mathbb{C} : \boldsymbol{\varepsilon} , \quad (2.1.18)$$

where \mathbb{C} is the fourth order tensor (elastic moduli) and the stress and strain tensors are given respectively as

$$\boldsymbol{\sigma} = \begin{pmatrix} \sigma_{11} & \sigma_{12} & \sigma_{13} \\ \sigma_{21} & \sigma_{22} & \sigma_{23} \\ \sigma_{31} & \sigma_{32} & \sigma_{33} \end{pmatrix} , \quad \boldsymbol{\varepsilon} = \begin{pmatrix} \varepsilon_{11} & \varepsilon_{12} & \varepsilon_{13} \\ \varepsilon_{21} & \varepsilon_{22} & \varepsilon_{23} \\ \varepsilon_{31} & \varepsilon_{32} & \varepsilon_{33} \end{pmatrix} . \quad (2.1.19)$$

In order to simplify the notation and numerical implementation, the Voigt notation introduced by (Voigt 1910) is used. It makes use of the symmetry, transforming the second order stress and strain tensors into vectors with six components. Then the

resulting tensor of elastic moduli, prescribing the material properties, is reduced into a tensor of second order with only 6×6 components. The stresses can be expressed as a linear combination of the strain components as

$$\begin{pmatrix} \sigma_{11} \\ \sigma_{22} \\ \sigma_{33} \\ \sigma_{23} \\ \sigma_{13} \\ \sigma_{12} \end{pmatrix} = \begin{pmatrix} \mathbb{C}_{1111} & \mathbb{C}_{1122} & \mathbb{C}_{1133} & \mathbb{C}_{1123} & \mathbb{C}_{1113} & \mathbb{C}_{1112} \\ \mathbb{C}_{2211} & \mathbb{C}_{2222} & \mathbb{C}_{2233} & \mathbb{C}_{2223} & \mathbb{C}_{2213} & \mathbb{C}_{2212} \\ \mathbb{C}_{3311} & \mathbb{C}_{3322} & \mathbb{C}_{3333} & \mathbb{C}_{3323} & \mathbb{C}_{3313} & \mathbb{C}_{3312} \\ \mathbb{C}_{2311} & \mathbb{C}_{2322} & \mathbb{C}_{2333} & \mathbb{C}_{2323} & \mathbb{C}_{2313} & \mathbb{C}_{2312} \\ \mathbb{C}_{1311} & \mathbb{C}_{1322} & \mathbb{C}_{1333} & \mathbb{C}_{1323} & \mathbb{C}_{1313} & \mathbb{C}_{1312} \\ \mathbb{C}_{1211} & \mathbb{C}_{1222} & \mathbb{C}_{1233} & \mathbb{C}_{1223} & \mathbb{C}_{1213} & \mathbb{C}_{1212} \end{pmatrix} \cdot \begin{pmatrix} \varepsilon_{11} \\ \varepsilon_{22} \\ \varepsilon_{33} \\ 2\varepsilon_{23} \\ 2\varepsilon_{13} \\ 2\varepsilon_{12} \end{pmatrix}. \quad (2.1.20)$$

2.2 Continuum mechanics and thermodynamics

The continuum mechanics is a powerful and effective tool to explain various physical problems successfully without detailed knowledge about their microstructure. This section reviews some basic mechanical concepts of continuous media, where macroscopic systems can be prescribed. Therefore, a study of motion and deformation is clarified. Then the classical balance principles in thermodynamics with their consequences are discussed. For a detailed review of the aforementioned topics, please refer to (Holzapfel 2002), (de Souza Neto, Peric, and Owen 2011) (Truesdell, Noll, Truesdell, and Noll 2004), (Silhavy 1997), (Gurtin, Fried, and Anand 2010) and (Wolfgang Demtroder 2017).

2.2.1 Kinematics

Kinematics is the study of motion and deformation. Let \mathcal{B} be a body with continuous distribution of matter in space and time. As a continuum body moves in space from one instant into another, it occupies a continuous sequence of geometrical regions denoted by Ω_0, \dots, Ω . Thus, every particle, or material point, $p \in \mathcal{B}$ has a position in the mentioned regions. These regions that are occupied by the continuum body at a given time t are called the configurations. We refer to the region Ω_0 at initial time $t = 0$ and the position vector \mathbf{X} by the reference (undeformed configuration). When body is in motion, the region Ω_0 moves in space into a new region Ω occupied by the continuum body \mathcal{B} at time $t > 0$. This is called the current (deformed configuration) prescribed by the spatial position vector \mathbf{x} , see Fig. 2.1. The displacement field of a material point relates its position vector in the reference configuration to its position on the current configuration at time t .

$$\mathbf{u}(\mathbf{X}, t) = \mathbf{x}(\mathbf{X}, t) - \mathbf{X}. \quad (2.2.1)$$

The motion and deformation of a continuum body in solid mechanics are described in terms of the displacement field. However, the primary field quantities in fluid mechanics describing the fundamental kinematic properties are the velocity field (first time derivative of the motion) and the acceleration field (second time derivative of

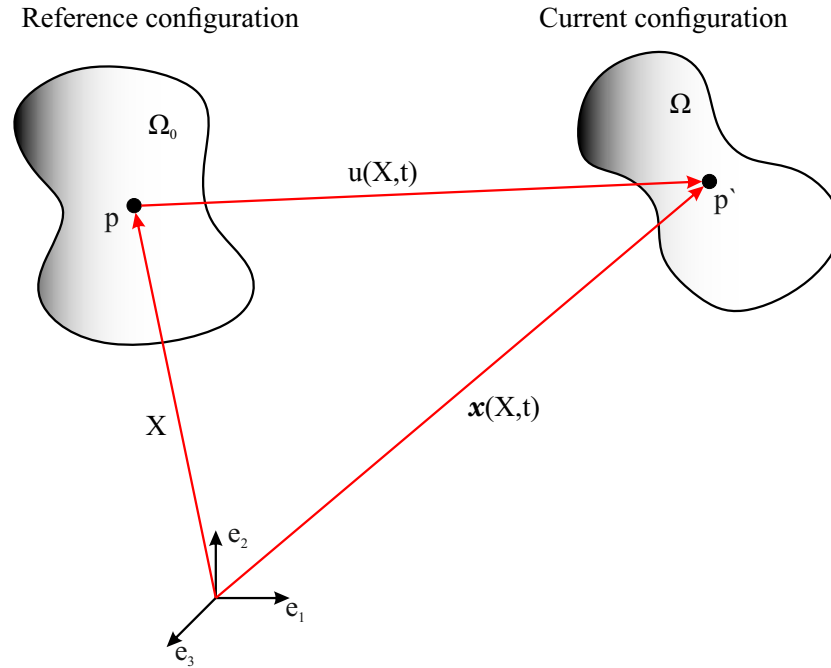


Figure 2.1: Deformation of a body \mathcal{B} . Representation of configurations.

the motion).

$$\mathbf{v}(\mathbf{X}, t) = \frac{d\mathbf{x}}{dt} = \frac{\partial \mathbf{x}(\mathbf{X}, t)}{\partial t}, \quad (2.2.2)$$

$$\mathbf{a}(\mathbf{X}, t) = \frac{d^2\mathbf{x}}{dt^2} = \frac{d\mathbf{v}}{dt} = \frac{\partial \mathbf{v}(\mathbf{X}, t)}{\partial t}. \quad (2.2.3)$$

The deformation gradient tensor \mathbf{F} maps a line element $d\mathbf{X}$ from the reference configuration to a corresponding line element in the current configuration $d\mathbf{x}$.

$$d\mathbf{x} = \mathbf{F} \cdot d\mathbf{X}, \quad (2.2.4)$$

hence, we get the relation for the displacement gradient tensor,

$$\mathbf{F} = \frac{\partial \mathbf{x}}{\partial \mathbf{X}} = \frac{\partial (\mathbf{u} + \mathbf{X})}{\partial \mathbf{X}} = \text{Grad} \mathbf{u} + \mathbf{I}. \quad (2.2.5)$$

The deformation gradient is said to be a two point tensor, as it involves points in two distinct configurations. One index describes the spatial coordinates, x_a , and the other material coordinates, X_A .

Analogously, mapping a volume element from the reference to the current configurations at time t is defined according to the relation

$$dv = J(\mathbf{X}, t)dV, \quad J(\mathbf{X}, t) = \det \mathbf{F}(\mathbf{X}, t) > 0, \quad (2.2.6)$$

where $J > 0$ is the volume ratio (Jacobian determinant) insuring the impenetrability of matter. We have seen, that points, lines or curves map onto points, lines

and curves via the deformation gradient \mathbf{F} . However, a unit vector \mathbf{N} normal to infinitesimal material surface element dS does not map to a unit vector \mathbf{n} normal to the associated infinitesimal spatial surface element ds via \mathbf{F} . The relation for this surface map is called Nanson's Formula

$$ds = J\mathbf{F}^{-T}dS. \quad (2.2.7)$$

In non-linear continuum mechanics, the strain tensor is subject to the different configurations. Therefore, we define the material strain tensors dependent solely on the material point, which are the Green-Lagrange strain tensor,

$$\mathbf{E} = \frac{1}{2}(\mathbf{F}^T \cdot \mathbf{F} - \mathbf{I}), \quad \text{with} \quad \mathbf{E} = \mathbf{E}^T, \quad (2.2.8)$$

and the right Cauchy-Green tensor $\mathbf{C} = \mathbf{F}^T \cdot \mathbf{F}$, which is symmetric and positive definite at each $\mathbf{X} \in \Omega_0$. On the other hand, the spatial strain tensors associated with the current configuration are, Euler-Almansi strain tensor,

$$\mathbf{e} = \frac{1}{2}(\mathbf{I} - (\mathbf{F} \cdot \mathbf{F}^T)^{-1}), \quad \text{with} \quad \mathbf{e} = \mathbf{e}^T, \quad (2.2.9)$$

and the left Cauchy-Green tensor $\mathbf{B} = \mathbf{F} \cdot \mathbf{F}^T$, which is as well symmetric and positive definite. Rewriting the aforementioned strain tensors in terms of the displacement gradient tensors in the reference and current configurations respectively is given as follows

$$\mathbf{E} = \frac{1}{2}(\text{Grad}^T \mathbf{u} + \text{Grad} \mathbf{u}) + \frac{1}{2} \text{Grad}^T \mathbf{u} \cdot \text{Grad} \mathbf{u}, \quad (2.2.10)$$

$$\mathbf{e} = \frac{1}{2}(\text{grad}^T \mathbf{u} + \text{grad} \mathbf{u}) + \frac{1}{2} \text{grad}^T \mathbf{u} \cdot \text{grad} \mathbf{u}, \quad (2.2.11)$$

where

$$\text{Grad} \mathbf{u} = \frac{\partial \mathbf{u}}{\partial \mathbf{X}}, \quad \text{and} \quad \text{grad} \mathbf{u} = \frac{\partial \mathbf{u}}{\partial \mathbf{x}}. \quad (2.2.12)$$

Considering the case of small strains with $x \approx X$, which applies all over this thesis, allows us to neglect the quadratic terms in the Green-Lagrange strain tensor as well in the Euler-Almansi strain tensor. Hence, both strains coincide in the linearized strain tensor.

$$\boldsymbol{\varepsilon} = \frac{1}{2}(\text{grad}^T \mathbf{u} + \text{grad} \mathbf{u}). \quad (2.2.13)$$

2.2.2 Balance laws

In this section the fundamental balance principles, i.e. the conservation of mass, balance of linear and angular momentum and the first and second laws of thermodynamics are given. Conservation laws are valid in all branches of continuum mechanics and must be satisfied for all times.

2.2.3 Conservation of mass

In non-relativistic physics mass cannot be produced or destroyed. It is assumed that during a motion there are neither mass sources nor mass sinks, so that the mass m of a body Ω is a conserved quantity.

$$m = \int_{\Omega} \rho dV, \quad (2.2.14)$$

where $\rho(x, t)$ is the mass density, a continuous scalar field depending on the position $x \in \Omega$ and time t throughout the body.

2.2.4 Balance of linear and angular momentum

Consider a continuum body \mathcal{B} occupying a region Ω with a boundary surface $\partial\Omega$. A body force \mathbf{b} is acting per the volume of the body and the surface of the body is subject to Cauchy traction vector $\mathbf{t} = \boldsymbol{\sigma} \cdot \mathbf{n}$, where \mathbf{n} is the outward normal vector to the surface. Hence, the global form of the balance of linear momentum is given as

$$\frac{d}{dt} \int_{\Omega} \rho \mathbf{v} dV = \int_{\partial\Omega} \mathbf{t} dA + \int_{\Omega} \mathbf{b} dV, \quad (2.2.15)$$

applying the divergence theorem to Cauchy's formula gives

$$\int_{\partial\Omega} \mathbf{t} dA = \int_{\partial\Omega} \boldsymbol{\sigma} \cdot \mathbf{n} dA = \int_{\Omega} \nabla \cdot \boldsymbol{\sigma} dV. \quad (2.2.16)$$

Substitute into Eq. 2.2.16 and utilize the conservation of mass, the resulting equation should hold for any volume. Hence, we get the equilibrium equation in the local form

$$\nabla \cdot \boldsymbol{\sigma} + \mathbf{b} = \rho \mathbf{a}. \quad (2.2.17)$$

The balance of angular momentum in terms of the resultant moment \mathbf{M} (the moment of the resultant force \mathbf{F} about a point x_0 on the body), with the position vector \mathbf{r} , has the form

$$\frac{d}{dt} \int_{\Omega} \mathbf{r} \times \rho \mathbf{v} dV = \int_{\partial\Omega} \mathbf{r} \times \mathbf{t} dA + \int_{\Omega} \mathbf{r} \times \mathbf{b} dV. \quad (2.2.18)$$

Making use of the balance of linear momentum and the divergence theorem we obtain the symmetry of the Cauchy stress tensor.

$$\boldsymbol{\sigma} = \boldsymbol{\sigma}^T. \quad (2.2.19)$$

2.2.5 First law of thermodynamics: Balance of energy

The first law of thermodynamics governs the transformation from one type of energy involved in a thermodynamic process into another, but it never governs the direction of that energy transfer. It states that the rate of change of the total energy (kinetic \mathcal{K} and internal energy \mathcal{E}) of a thermodynamic system equals the change of the external mechanical work \mathcal{P}_{ext} done by surface tractions and body forces plus the thermal power (heat power) \mathcal{Q} done by heat fluxes and heat sources.

$$\dot{\mathcal{K}} + \dot{\mathcal{E}} = \mathcal{P}_{\text{ext}} + \mathcal{Q} . \quad (2.2.20)$$

The kinetic energy is given by

$$\mathcal{K} = \int_{\Omega} \frac{1}{2} \rho \mathbf{v} \cdot \mathbf{v} dV, \quad (2.2.21)$$

and the internal energy is defined as follows

$$\mathcal{E} = \int_{\Omega} \Psi dV + \int_{\Omega} \theta s dV. \quad (2.2.22)$$

Ψ is the Helmholtz free energy, θ is the absolute temperature and s is the entropy. The external mechanical work is given as

$$\mathcal{P}_{\text{ext}} = \int_{\Omega} \mathbf{b} \cdot \mathbf{v} dV + \int_{\partial\Omega} \mathbf{t} \cdot \mathbf{v} dA , \quad (2.2.23)$$

and finally the heat power in terms of the heat source h and the heat flux q_n has the form

$$\mathcal{Q} = \int_{\Omega} h dV + \int_{\partial\Omega} q_n dA. \quad (2.2.24)$$

The heat flux measures the rate at which heat enters the body across the boundary surface $\partial\Omega$ and is defined per Stoke's heat flux theorem shown below

$$q_n = -\mathbf{q} \cdot \mathbf{n} . \quad (2.2.25)$$

In Eq. 2.2.25, the heat flux has a negative sign due to the opposite direction to the normal vector \mathbf{n} (outward normal to the surface element). Substituting into Eq. 2.2.20, gives

$$\frac{d}{dt} \int_{\Omega} \left(\frac{1}{2} \rho \mathbf{v} \cdot \mathbf{v} + \Psi + \theta s \right) dV = \int_{\partial\Omega} (\mathbf{t} \cdot \mathbf{v} + q_n) dA + \int_{\Omega} (\mathbf{b} \cdot \mathbf{v} + h) dV. \quad (2.2.26)$$

The surface integrals can be changed into volume ones by applying the divergence theorem and making use of the prior laws and identical integrals. Hereafter, we get the local form of the balance of energy (first law of thermodynamics).

$$\dot{\Psi} + \dot{\theta} s + \theta \dot{s} = \boldsymbol{\sigma} : \dot{\boldsymbol{\epsilon}} - \nabla \cdot \mathbf{q} + h. \quad (2.2.27)$$

2.2.6 Second law of thermodynamics: Entropy inequality

The second law of thermodynamics is responsible for the direction of an energy transfer process, as physical observations show that the heat always flows from the warmer to the colder region of a body (from the source of heat). A mechanical energy can be transformed into heat by friction and this can not be converted back into mechanical energy. Therefore the entropy is an important thermodynamic property, which is viewed as a quantitative measure of microscopic randomness or disorder. The second law of thermodynamics is known by the total production of entropy, which is supposed to be a positive quantity.

$$\Gamma = \frac{d}{dt} \int_{\Omega} s dV + \int_{\Omega} (\nabla \cdot \frac{\mathbf{q}}{\theta} - \frac{\dot{h}}{\theta}) dV \geq 0. \quad (2.2.28)$$

Finally the local form of the entropy production inequality (known as Clausius-Duhem inequality) is

$$\boldsymbol{\sigma} : \dot{\boldsymbol{\varepsilon}} - s\dot{\theta} - \dot{\Psi} - \frac{1}{\theta} \mathbf{q} \cdot \nabla(\theta) \geq 0. \quad (2.2.29)$$

2.2.7 Constitutive equations

To characterize a continuous media within the context of thermodynamics we need to define thermodynamic potentials, which prescribe all thermodynamic properties of a system. A thermodynamic potential is a function (scalar-valued) from which we may derive the state variables of a system. One example is the Helmholtz free energy as a function of the strain tensor $\boldsymbol{\varepsilon}$, the temperature θ , the temperature gradient $\nabla\theta$ and the vector of internal state variables (for a system with irreversible processes) \mathbf{z} .

$$\Psi = \Psi(\boldsymbol{\varepsilon}, \theta, \nabla\theta, \mathbf{z}). \quad (2.2.30)$$

To make use of the second law of thermodynamics, we need to compute the rate of the free energy applying the chain rule.

$$\dot{\Psi} = \frac{\partial \Psi}{\partial \boldsymbol{\varepsilon}} : \dot{\boldsymbol{\varepsilon}} + \frac{\partial \Psi}{\partial \theta} \dot{\theta} + \frac{\partial \Psi}{\partial (\nabla\theta)} \cdot (\nabla\dot{\theta}) + \frac{\partial \Psi}{\partial \mathbf{z}} \cdot \dot{\mathbf{z}}. \quad (2.2.31)$$

Plugging into Eq. 2.2.29, we get

$$\left(\boldsymbol{\sigma} - \frac{\partial \Psi}{\partial \boldsymbol{\varepsilon}} \right) : \dot{\boldsymbol{\varepsilon}} - \left(s + \frac{\partial \Psi}{\partial \theta} \right) \dot{\theta} - \frac{\partial \Psi}{\partial (\nabla\theta)} \cdot (\nabla\dot{\theta}) - \frac{\partial \Psi}{\partial \mathbf{z}} \cdot \dot{\mathbf{z}} - \frac{1}{\theta} \mathbf{q} \cdot \nabla(\theta) \geq 0. \quad (2.2.32)$$

Eq. 2.2.32 holds at every point of the continuum body and for all times. The terms in brackets given by Coleman-Noll procedure, refer to (Noll, Coleman, and Noll 1974) and (Coleman and Gurtin 1967), are the general forms of the constitutive

equations for the Cauchy stress tensor and the entropy describing thermal processes defined respectively as

$$\boldsymbol{\sigma} = \frac{\partial \Psi}{\partial \boldsymbol{\varepsilon}}, \quad \text{and} \quad s = -\frac{\partial \Psi}{\partial \theta}. \quad (2.2.33)$$

Moreover, we get from Eq. 2.2.32 an additional vanishing term due to the case that the free energy of simple materials is independent of the temperature gradient

$$\frac{\partial \Psi}{\partial (\nabla \theta)} = 0. \quad (2.2.34)$$

We still have to define the part dependent on \mathbf{z} (the vector of internal variables). This is done by considering a new quantity \mathbf{q} , which is known as the thermodynamically driving force prescribing the evolution of internal variables.

$$-\frac{\partial \Psi}{\partial \mathbf{z}} \cdot \dot{\mathbf{z}} \geq 0, \quad \text{with} \quad \mathbf{q} = -\frac{\partial \Psi}{\partial \mathbf{z}}, \quad \text{giving} \quad \mathbf{q} \cdot \dot{\mathbf{z}} \geq 0. \quad (2.2.35)$$

The last term in Eq. 2.2.35 is known as the internal dissipation (for ex. in the form of heat), which is a non-negative quantity (irreversible).

2.3 Variational principle

In this section, the variational formulation in terms of the total energy for a non-conservative continuous material is given. We start with a general form of the Gibbs energy (including the gradient of the internal variables), then come to a special case known as the principle of the minimum dissipation potential (PMDP), as implemented afterwards in this dissertation. The relations for Hamilton's principle are inspired from the works of (Hamilton 1834), (Hamilton 1835) and (Bedford and Bedford 1985). PMDP representation is based on the work of (Onsager 1931), (Hackl 1997), (Ortiz and Stainier 1999) and (Ortiz and Repetto 1999), (Carstensen, Hackl, and Mielke 2002) and (Hackl and Fischer 2008) and for non-isothermal processes from the works of (Hackl, Fischer, and Svoboda 2011) and (Junker, Makowski, and Hackl 2014).

To prescribe Hamilton's principle, we introduce the Gibbs energy \mathcal{G} for a continuous material as follows

$$\mathcal{G} = \Pi_{\text{int}} + \Pi_{\text{ext}}, \quad (2.3.1)$$

where Π_{int} represents the internal potential dependent on the Helmholtz free energy as a function of the strain tensor and the vector of internal variables.

$$\Pi_{\text{int}} = \int_{\Omega} \Psi(\boldsymbol{\varepsilon}, \mathbf{z}) dV. \quad (2.3.2)$$

Whereas Π_{ext} is the external potential dependent on the body forces \mathbf{b} and the traction forces \mathbf{t} .

$$\Pi_{\text{ext}} = - \int_{\Omega} \mathbf{b} \cdot \mathbf{u} dV - \int_{\partial\Omega} \mathbf{t} \cdot \mathbf{n} dA, \quad (2.3.3)$$

implying the Gibbs energy to be

$$\mathcal{G} = \int_{\Omega} \Psi(\boldsymbol{\varepsilon}, \mathbf{z}) dV - \int_{\Omega} \mathbf{b} \cdot \mathbf{u} dV - \int_{\partial\Omega} \mathbf{t} \cdot \mathbf{n} dA. \quad (2.3.4)$$

Then Hamilton's principle for non-conservative and continuous materials is given as

$$\int_{t_0}^{t_1} (\delta\mathcal{K} - \delta\mathcal{G} + \delta\mathcal{V}) dt = 0. \quad (2.3.5)$$

$\delta\mathcal{K}$ representing the virtual work of the kinetic energy and $\delta\mathcal{V}$ is the virtual work of the dissipative forces. To describe the behavior of non-conservative processes, a demand arises for additional scalar potential, called the dissipation function \mathcal{D} , which prescribes the irreversible transformation of the elastic energy into dissipation energy. A new force, called the dissipation force $\hat{\mathbf{q}}$, can be derived from the dissipation potential as follows

$$\hat{\mathbf{q}} = - \frac{\partial \mathcal{D}}{\partial \dot{\mathbf{z}}}. \quad (2.3.6)$$

Then the virtual work of the dissipative forces can be given as

$$\delta\mathcal{V} = \int_{\Omega} \hat{\mathbf{q}} \cdot \delta\mathbf{z} dV. \quad (2.3.7)$$

Let us restrict ourselves to the static case neglecting the velocity terms, i.e. the kinetic energy, then we get a simplified form of Eq. 2.3.5

$$\delta\mathcal{G} - \int_{\Omega} \hat{\mathbf{q}} \cdot \delta\mathbf{z} dV = \delta\mathcal{G} + \int_{\Omega} \frac{\partial \mathcal{D}}{\partial \dot{\mathbf{z}}} \cdot \delta\mathbf{z} dV. \quad (2.3.8)$$

It is worth mentioning that for conservative materials, Hamilton's principle is reduced only to the variation of the Gibbs energy (first term in Eq. 2.3.8) as no dissipation function exists. In the following, we distinguish between different cases for the Gibbs energy.

2.3.1 General form of Hamilton's principle

The most general case for Hamilton's principle considers the Gibbs energy to be dependent on the strain tensor (displacement field), internal variables and the gradient of the internal variables, hence

$$\mathcal{G} = \mathcal{G}(\mathbf{u}, \mathbf{z}, \nabla\mathbf{z}). \quad (2.3.9)$$

Applying the first variation and substituting into Eq. 2.3.8 gives

$$\delta_{\mathbf{u}} \mathcal{G} + \delta_{\mathbf{z}} \mathcal{G} + \int_{\Omega} \frac{\partial \mathcal{D}}{\partial \dot{\mathbf{z}}} \cdot \delta \mathbf{z} dV = 0, \quad \forall \delta \mathbf{u}, \delta \mathbf{z}. \quad (2.3.10)$$

The variations $\delta \mathbf{u}, \delta \mathbf{z}$ can be selected separately, then stationarity with respect to the displacement field gives

$$\int_{\Omega} \frac{\partial \Psi}{\partial \boldsymbol{\varepsilon}} : \delta \boldsymbol{\varepsilon} dV - \int_{\Omega} \mathbf{b} \cdot \delta \mathbf{u} dV - \int_{\partial \Omega} \mathbf{t} \cdot \delta \mathbf{u} dA = 0, \quad \forall \delta \mathbf{u}. \quad (2.3.11)$$

This gives back the equilibrium equation and Cauchy's theorem

$$\nabla \cdot \boldsymbol{\sigma} + \mathbf{b} = \mathbf{0}, \quad \forall \mathbf{x} \in \Omega, \quad (2.3.12)$$

$$\boldsymbol{\sigma} \cdot \mathbf{n} = \mathbf{t}, \quad \forall \mathbf{x} \in \partial \Omega. \quad (2.3.13)$$

Similarly, stationarity with respect to the internal variables gives

$$\int_{\Omega} \frac{\partial \Psi}{\partial \mathbf{z}} \cdot \delta \mathbf{z} dV + \int_{\Omega} \frac{\partial \Psi}{\partial \nabla \mathbf{z}} : \delta \nabla \mathbf{z} dV + \int_{\Omega} \frac{\partial \mathcal{D}}{\partial \dot{\mathbf{z}}} \cdot \delta \mathbf{z} dV = 0, \quad \forall \delta \mathbf{z}. \quad (2.3.14)$$

Integration by parts returns

$$\frac{\partial \Psi}{\partial \mathbf{z}} - \nabla \cdot \left(\frac{\partial \Psi}{\partial \nabla \mathbf{z}} \right) + \frac{\partial \mathcal{D}}{\partial \dot{\mathbf{z}}} = 0, \quad \forall \mathbf{x} \in \Omega, \quad (2.3.15)$$

$$\left(\frac{\partial \Psi}{\partial \nabla \mathbf{z}} \right) \cdot \mathbf{n} = 0, \quad \forall \mathbf{x} \in \partial \Omega. \quad (2.3.16)$$

Eq. 2.3.15 is called Helmholtz equation and Eq. 2.3.16 gives again the Neumann boundary condition. An example for the implementation of this general case of Hamilton's principle can be seen in damage modeling in the work of (Junker, Schwarz, Jantos, and Hackl 2019), another application is presented in the field of topology optimization by (Junker and Hackl 2016).

2.3.2 The principle of the minimum dissipation potential - PMDP

A special case of Hamilton's principle can be derived considering no more dependency of the Gibbs energy on the gradient of the internal variables. The resulting principle is called the principle of the minimum dissipation potential (PMDP), which applies to the models to be introduced throughout this thesis. Stationarity with respect to the internal variable $\delta \mathbf{z}$ and in comparison to Eq. 2.3.14 gives

$$\int_{\Omega} \frac{\partial \Psi}{\partial \mathbf{z}} \cdot \delta \mathbf{z} dV + \int_{\Omega} \frac{\partial \mathcal{D}}{\partial \dot{\mathbf{z}}} \cdot \delta \mathbf{z} dV = 0, \quad \forall \delta \mathbf{z}. \quad (2.3.17)$$

The previous relation can be simplified to the expression

$$\frac{\partial \Psi}{\partial \mathbf{z}} + \frac{\partial \mathcal{D}}{\partial \dot{\mathbf{z}}} = 0, \quad (2.3.18)$$

known as Biot's equation, see (Biot 1962). Integration with respect to $\dot{\mathbf{z}}$ gives the minimization problem

$$\frac{\partial \Psi}{\partial \mathbf{z}} \cdot \dot{\mathbf{z}} + \mathcal{D} + \mathcal{A} \rightarrow \min_{\dot{\mathbf{z}}}, \quad (2.3.19)$$

with \mathcal{A} , an integration constant to be defined as follows

$$\mathcal{A} = \frac{\partial \Psi}{\partial \boldsymbol{\varepsilon}} : \dot{\boldsymbol{\varepsilon}}. \quad (2.3.20)$$

Now we can rewrite the minimization problem in terms of a Lagrangian \mathcal{L} as

$$\mathcal{L} = \dot{\Psi} + \mathcal{D} \rightarrow \min_{\dot{\mathbf{z}}}. \quad (2.3.21)$$

But according to Eqs. 2.2.35, differentiating the Helmholtz free energy with respect to the internal variable returns the thermodynamically driving force, then the minimization problem shown above delivers the equations prescribing the set of internal variables known as the evolution equations, see (Carstensen, Hackl, and Mielke 2002).

Applications of the PMDP in the literature are manifold, like for example in the field of damage models by (Dimitrijevic and Hackl 2008) and (Schwarz 2019) or in damage-plasticity models by (Hoormazdi 2021). Further implementations are as well in models of shape memory alloy by (Waimann 2018).

A similar approach is the principle of the maximum dissipation, presented in the works of (Hackl and Fischer 2008) and (Hackl, Fischer, and Svoboda 2011).

2.4 Two-scale homogenization scheme

Constitutive models are available for classical materials, nevertheless, for many modern materials needed in several fields of technical applications no phenomenological law can be meaningfully found to prescribe the effective macroscopic behavior. As these effective properties are dependent on the complex description of the microstructure. Therefore, it is favorable to attach an appropriate representative volume element (RVE) prescribing the fine-scale, micro-scale, at each point of the macro-structure. Implying two boundary value problems to be solved on both scales, which is known as FE^2 homogenization scheme. The transition between the scales should fulfill the macro-homogeneity condition or known as Hill-Mandel condition, see (Hill 1965) and (Mandel 1973). Further details and applications of the multi-scale homogenization scheme can be inferred from the works of (Zienkiewicz and Taylor 2005), (Kouznetsova, Brekelmans, and Baaijens 2001), (Zohdi and Wriggers 2001), (Bakhvalov and Panasenko 2012) and (Balzani, Schröder, and Brands 2010).

2.4.1 Basic concepts in micro-macro mechanics

It is assumed that the macro-scale is homogeneous and the micro-scale is heterogeneous (including e.g. inclusions, cavities or other components). The main target of two-scale homogenization is to define the effective response and properties at the macrostructure in terms of suitable averaging (surface or volume integrals over the RVE) for constituents from the micro-scale. Which means, for a given macroscopic strain field $\langle \boldsymbol{\varepsilon} \rangle$, find the macroscopic stress tensor $\langle \boldsymbol{\sigma} \rangle$ and the effective stiffness \mathbb{C}_{eff} . This is to be performed at each integration point of the elements of the macrostructure. Therefore, this macroscopic strain field is passed into the microstructure, RVE, and can be used to formulate the boundary conditions on the RVE. The solution of the boundary value problem of the RVE is then used to obtain the macroscopic counterparts by averaging. Averaging relation to compute the effective components at the macro-structure starting from an RVE with the volume Ω is given as

$$\langle f \rangle = \frac{1}{|\Omega|} \int_{\Omega} f dV, \quad (2.4.1)$$

The effective response is defined by the relation

$$\langle \boldsymbol{\sigma} \rangle = \mathbb{C}_{\text{eff}} : \langle \boldsymbol{\varepsilon} \rangle, \quad (2.4.2)$$

where \mathbb{C}_{eff} does not prescribe material properties but rather averaging relations. Furthermore, the RVE should be selected to satisfy the aforementioned homogeneity condition (Hill's condition or Hill-Mandel condition). Requiring the virtual macroscopic work to be equal to the averaged virtual work from the microstructure (the RVE).

$$\langle \boldsymbol{\sigma} : \boldsymbol{\varepsilon} \rangle = \langle \boldsymbol{\sigma} \rangle : \langle \boldsymbol{\varepsilon} \rangle. \quad (2.4.3)$$

Meaning that the RVE should be large enough to prescribe the microstructure without introducing nonexisting properties, at the same time, it should be small enough relative to the size of the macrostructure. According to (Hill 1963), the RVE can be defined as:

This phrase (the RVE) will be used when referring to a sample that (a) is structurally entirely typical of the whole structure on average, and (b) contains sufficient number of inclusions for the apparent overall moduli to be effectively independent of the surface value of traction and displacement, so long as these values are "macroscopically uniform".

One additional requirement in the field of homogenization, is the periodic boundary conditions that should apply to the microstructure, i.e. $\mathbf{u}_{\text{per}}(\mathbf{r}-) = \mathbf{u}_{\text{per}}(\mathbf{r}+)$ on the boundary points $\mathbf{r}-, \mathbf{r}+$ on opposite sides of the RVE. Hence, the macroscopic strain $\mathbf{e}_m = \langle \boldsymbol{\varepsilon} \rangle$ is related to the displacement field in terms of the following decomposition

$$\mathbf{u} = \mathbf{e}_m \cdot \mathbf{r} + \mathbf{u}_{\text{per}}. \quad (2.4.4)$$

where \mathbf{u}_{per} is a fluctuation field.

2.4.2 Effective properties

Voigt, see (Voigt 1889), is the first to analyze the effective mechanical properties of micro-heterogeneous solids. He assumed the strain field within a sample of heterogeneous material is uniform. Leading to Voigt effective stiffness to be $\mathbb{C}_{\text{eff}} = \langle \mathbb{C} \rangle$. On the other hand, Reuss (see (Reuß 1929)) approximated the stress field within polycrystalline materials to be uniform. Thus, if the Reuss field is assumed to be within the RVE, then Reuss effective stiffness would be $\mathbb{C}_{\text{eff}} = \langle \mathbb{C}^{-1} \rangle^{-1}$. These two bounds provide only rough qualitative information about the effective property, as given in the following fundamental inequality, see (Hill 1952).

$$\langle \mathbb{C}^{-1} \rangle^{-1} \leq \mathbb{C}_{\text{eff}} \leq \langle \mathbb{C} \rangle. \quad (2.4.5)$$

For the comparison of the effective properties from the reduced models to be introduced in 3.1 and 3.2, Reuss lower bound and Voigt upper bound suffices. Although a significant more progress in estimating the effective properties of composites has been achieved, the interested reader is referred to the works of (Hashin and Shtrikman 1963), (Hashin 1983), (Suquet 1997) and (Willis 1981).

2.5 Variational modeling of microstructure

We have examined so far materials consisting of sophisticated micro-scale, requiring the application of multi-scale homogenization scheme. However, some experimental results of inelastic materials are characterized with the formation of a fine structure, i.e. a microstructure. This is an outcome due to the often resulting non-convex variational problem under minimization. In which the gradient of displacement field is no more continuous but exhibits small-scale oscillations, which are related to mesh dependency. Energy models with similar properties are calculated via energy relaxation, which is a general theory to study the effective macroscopic behavior of materials which develop microstructure. A detailed mathematical insight to the concepts of convexity and relaxation can be found in Sec. 2.6.

Variational homogenization of inelastic materials has been extensively investigated in the literature, there are examples for models of shape memory alloy, see (Govindjee, Hackl, and Heinen 2007) and (Junker and Hackl 2011). Other examples are from the prediction of dislocation patterns in metal single crystals given by (Conti and Ortiz 2005), (Miehe, Lambrecht, and Gürses 2004) and (Kochmann and Hackl 2011).

The definitions and concepts presented in this chapter are based on the works of (Bartels, Carstensen, Hackl, and Hoppe 2004), (Carstensen, Conti, and Orlando 2008) and (Schröder and Hackl 2013). In the following sections 2.5.1, 2.5.2 and 2.5.3, we give a brief introduction to the terms and schemes common in the field of variational modeling of inelastic materials with microstructure, which we investigate later on through out this dissertation.

2.5.1 Condensed energy

Approaches to model inelastic materials with microstructure must provide information about (a) the initiation of microstructure and (b) the evolution of microstructure (formation of new microstructural patterns). Where the initiation of microstructure usually follows from loss of material stability (local instability) and results in energy reduction by breaking up the homogeneous deformation state into finer structures. Initiation of microstructure can be investigated by writing the potentials in time incremental settings using the so called condensed energy functional, which has been often mentioned in the literature as in the works of (Bartels, Carstensen, Hackl, and Hoppe 2004), (Carstensen, Conti, and Orlando 2008), (Mielke 2004) and (Ortiz and Repetto 1999).

For a given free energy $\Psi(\nabla\phi, \mathbf{z})$, a dissipation potential $\Delta(\mathbf{z}, \dot{\mathbf{z}})$ and a finite time increment $[t_n, t_{n+1}]$ one can write the dissipation distance $D(z_0, z_1)$, (Mielke 2002) and (Carstensen, Hackl, and Mielke 2002), as follows.

$$D(\mathbf{z}_0, \mathbf{z}_1) = \inf \left\{ \int_0^1 \Delta(\mathbf{z}(s), \dot{\mathbf{z}}(s)) ds \mid \mathbf{z}(0) = \mathbf{z}_0, \mathbf{z}(1) = \mathbf{z}_1 \right\}. \quad (2.5.1)$$

Then the values ϕ_{n+1} and \mathbf{z}_{n+1} can be approximated from the formulation

$$\{\phi_{n+1}, \mathbf{z}_{n+1}\} = \arg \min \left\{ \int_{\Omega} [\Psi(\nabla\phi, \mathbf{z}) + D(\mathbf{z}_n, \mathbf{z})] dV - l(t_{n+1}, \phi) \mid \phi, \mathbf{z} \right\}, \quad (2.5.2)$$

where $l(t_{n+1}, \phi)$ is the potential of external forces. Then the minimization with respect to the vector of internal variables \mathbf{z} gives the condensed energy.

$$\Psi_{\text{cond}}(\nabla\phi) = \inf \left\{ \Psi(\nabla\phi, \mathbf{z}) + D(\mathbf{z}_n, \mathbf{z}) \mid \mathbf{z} \right\}, \quad (2.5.3)$$

used to calculate the initiation of microstructure. Assuming that no microstructure exists at the beginning of the time step, turns the problem of inelastic evolution to be solely elastic problem with the relation

$$\phi_{n+1} = \arg \min \left\{ \int_{\Omega} \Psi_{\text{cond}}(\nabla\phi) dV - l(t_{n+1}, \phi) \mid \phi \right\}, \quad (2.5.4)$$

and the update of internal variables can be computed from the following equation

$$\mathbf{z}_{n+1} = \arg \min \left\{ \Psi_{\text{cond}}(\nabla\phi_{n+1}) + D(\mathbf{z}_n, \mathbf{z}) \mid \mathbf{z} \right\}. \quad (2.5.5)$$

2.5.2 Essential microstructure

The condensed energy gives information only about the onset of the microstructure due to the assumption that no microstructure exists at the beginning of the time step.

But if we want to model a time continuous evolution, then we need to take into account the incremental update of the internal variables including the dependence on their values from the preceding time step. Therefore, the condensed energy has no more physical meaning. This problem can be overcome by considering the material behavior to evolve within a closed class of microstructure, for example by refinement. This class is called essential microstructure, given as a spatial distribution of the deformation field ϕ and the internal variables \mathbf{z} are parametrized in the form

$$\phi = \hat{\phi}(\mathbf{x}, \mathbf{z}_{\text{ess}}, \mathbf{z}_{\text{mar}}), \quad \mathbf{z} = \hat{\mathbf{z}}(\mathbf{x}, \mathbf{z}_{\text{ess}}, \mathbf{z}_{\text{mar}}). \quad (2.5.6)$$

The essential parameters \mathbf{z}_{ess} can be altered only by inelastic deformation, examples for these parameters would be the volume fractions, normal directions or values of the internal variables. On the other hand, the marginal parameters \mathbf{z}_{mar} can be relaxed elastically, as for example the amplitudes of fluctuation fields. With this parametrization and considering an appropriate representative volume element Ω_{rep} , for example by considering periodicity of the microstructure, then we are able to compute the effective relaxed quantities by volume averaging. The relaxed energy is then given as

$$\Psi_{\text{rel}}(\nabla\phi, \mathbf{z}_{\text{ess}}) = \inf \left\{ \frac{1}{|\Omega_{\text{rep}}|} \int_{\Omega_{\text{rep}}} \Psi(\nabla\phi + \nabla\hat{\phi}(\mathbf{x}, \mathbf{z}_{\text{ess}}, \mathbf{z}_{\text{mar}}), \hat{\mathbf{z}}(\mathbf{x}, \mathbf{z}_{\text{ess}}, \mathbf{z}_{\text{mar}})) dV \mid \mathbf{z}_{\text{mar}} \right\}, \quad (2.5.7)$$

and the relaxed dissipation potential

$$\Delta_{\text{rel}}(\mathbf{z}_{\text{ess}}, \dot{\mathbf{z}}_{\text{ess}}) = \inf \left\{ \frac{1}{|\Omega_{\text{rep}}|} \int_{\Omega_{\text{rep}}} \Delta\left(\frac{d}{dt}\hat{\mathbf{z}}(\mathbf{x}, \mathbf{z}_{\text{ess}}, \mathbf{z}_{\text{mar}})\right) dV \mid \mathbf{z}_{\text{mar}}, \dot{\mathbf{z}}_{\text{mar}} \right\}. \quad (2.5.8)$$

Implying the variational structure of the problem to be the same, but with a reduction from an infinite variable \mathbf{z} to a finite set of parameters \mathbf{z}_{ess} . The new minimization problem then has the form

$$\mathbf{0} \in \frac{\partial\Psi_{\text{rel}}}{\partial\mathbf{z}_{\text{ess}}} + \frac{\partial\Delta_{\text{rel}}}{\partial\dot{\mathbf{z}}_{\text{ess}}}. \quad (2.5.9)$$

These relations will be further elaborated and supported with numerical examples in Sec. 3 of this thesis.

2.5.3 Relaxation via lamination

For a general microstructure, computing the relaxed potentials in Eq. 2.5.7 and Eq. 2.5.8 will be hard to achieve. Therefore, one possibility would be to compute an approximation via lamination. This is done by computing a rank-one relaxation for the condensed energy. Implementations of this procedure to time-incremental problems can be found in the works of (Bartels, Carstensen, Hackl, and Hoppe 2004), (Kochmann and Hackl 2011) and (Hackl and Kochmann 2008).

We will present in the following first-order laminates, but an extension to general laminates can be done in a straightforward manner. Let the laminates of first-order be characterized by N volume fractions λ_i assigned to parallel planes. Each plane has a normal vector \mathbf{b} and every volume fraction is provided by a value z_i of the corresponding internal variable. Each plane has its deformation gradient according to the relation

$$\mathbf{F}_i = \mathbf{F}(\mathbf{I} + a_i \otimes \mathbf{b}), \quad (2.5.10)$$

with the amplitudes a_i . Eq. 2.5.10 means that the deformation gradients are rank-one connected to enforce the compatibility of laminate interfaces and ensure the existence of a corresponding deformation field ϕ . By volume averaging we get

$$\sum_{i=1}^N \lambda_i \mathbf{F}_i = \mathbf{F}, \quad (2.5.11)$$

implying

$$\sum_{i=1}^N \lambda_i a_i = 0. \quad (2.5.12)$$

This means, that any change in the direction of the normal vector \mathbf{b} would lead to a change in the internal variables and cause dissipation, therefore we consider the normal vector \mathbf{b} to be related to the material. Oppositely, we consider the amplitudes a_i can be changed purely elastically. Then a semi-relaxed energy can be computed by enforcing the following minimization

$$\Psi_{\text{rel}}(\mathbf{F}, \lambda, \mathbf{z}, \mathbf{b}) = \inf \left\{ \sum_{i=1}^N \lambda_i \Psi(\mathbf{F}_i, z_i) \mid a_i, \sum_{i=1}^N \lambda_i a_i = 0 \right\}. \quad (2.5.13)$$

Notice that the given energy is only partially relaxed, since a full relaxation requires further minimization with respect to all internal variables and normal vectors. Considering the numbering $\{1, \dots, N\}$, the former quantities are defined as $\lambda = \{\lambda_1, \dots, \lambda_N\}$ and $\mathbf{z} = \{z_1, \dots, z_N\}$. Let the lamination follows the same ordering and the normal vector \mathbf{b} remains fixed, then we can write a relaxation for the dissipation potential as

$$\Delta_{\text{rel}}(\lambda, \mathbf{z}, \dot{\lambda}, \dot{\mathbf{z}}) = \sum_{i=1}^N \lambda_i \Delta(z_i, \dot{z}_i) + \inf \left\{ \sum_{i,j=1}^N \Delta \lambda_{ij} D(z_i, z_j) \mid \Delta \lambda_{ij}, \right. \\ \left. \sum_{i=1}^N \Delta \lambda_{ij} = \dot{\lambda}_j, \sum_{j=1}^N \Delta \lambda_{ij} = \dot{\lambda}_i, \Delta \lambda_{ij} = 0 \text{ for } |(i-j) \bmod N| \neq 1 \right\}. \quad (2.5.14)$$

A convexification technique will be implemented later on in Sec. 4.7 of this thesis. There, the relaxed potentials are computed with $N = \{0, 1, 2\}$. However, the implementation of the semi-relaxed energy requires a check whether the formation of a microstructure is becoming favorable or not. Meaning that solving Eq. 2.5.13 (numerical minimization) is enhanced by considering an initiation scheme, which gives properly selected values at the beginning of each time-step.

2.6 Convex analysis

In this section some basic concepts from the field of convex analysis are given, in order to clarify the mathematical background of the schemes and derivations implemented within this thesis. The following definitions are inferred from the works of (Rockafellar 1997) and (Dacorogna 2007).

2.6.1 Definitions

Convex set: a subset C of \mathbb{R}^n is said to be convex if $(1 - \lambda)x + \lambda y \in C$ whenever $x \in C, y \in C$ and $0 < \lambda < 1$.

The intersection of an arbitrary collection of convex sets is convex.

Convex combination: is a vector sum $\lambda_1 x_1 + \lambda_2 x_2 + \dots + \lambda_m x_m$ of x_1, x_2, \dots, x_m if the coefficients λ_i are all non-negative and $\lambda_1 + \dots + \lambda_m = 1$. Then a subset of \mathbb{R}^n is convex if and only if it contains all the convex combinations of its elements.

Convex hull: of a given subset S is the intersection of all the convex sets containing S of \mathbb{R}^n .

Convex cone: a subset K of \mathbb{R}^n is called a cone if and only if it contains all linear combinations of its elements. $\lambda_1 x_1 + \dots + \lambda_m x_m$ where all the coefficients are positive.

The orthogonal projection of a convex set C on a subspace L is another convex set. As the orthogonal projection mapping onto L is a linear transformation assigning to each point x a unique point $y \in L$.

Epigraph of a function: if f is a function with real values or $\pm\infty$ and whose domain is a subset S of \mathbb{R}^n , then the set $\{(x, \mu) | x \in S, \mu \in \mathbb{R}, \mu \geq f(x)\}$ is called the epigraph of f and is denoted by $epif$. f is a convex function on S if its $epif$ is convex as a subset of \mathbb{R}^{n+1} . The negative of a concave function on S is convex.

Convex function: let f be a function from a convex subset C to $(-\infty, +\infty]$. Then f is convex on C if and only if

$$f((1 - \lambda)x + \lambda y) \leq (1 - \lambda)f(x) + \lambda f(y), \quad 0 < \lambda < 1. \quad (2.6.1)$$

If $C = \mathbb{R}^n$ then Jensen's inequality reads as

$$f(\lambda_1 x_1 + \dots + \lambda_m x_m) \leq \lambda_1 f(x_1) + \dots + \lambda_m f(x_m), \quad (2.6.2)$$

$$\text{whenever } \lambda_i \geq 0, \quad \lambda_1 + \dots + \lambda_m = 1. \quad (2.6.3)$$

Let f be a twice continuously differentiable real-valued function on an open convex set $C \in \mathbb{R}^n$. Then f is convex on C if and only if its Hessian matrix is positive semi-definite for every $x \in C$.

A function f on \mathbb{R}^n is 1st degree positively homogeneous if for every x the following relation applies

$$f(\lambda x) \leq \lambda f(x), \quad 0 < \lambda < \infty. \quad (2.6.4)$$

Lower semicontinuity (l.s.c.): an extended-real-valued function f on an set $S \subset \mathbb{R}^n$ is lower-semi-continuous at a point x of S if

$$f(x) \leq \lim_{i \rightarrow \infty} \lambda f(x_i), \quad (2.6.5)$$

or for a sequence x_1, x_2, \dots , in S , where x_i converges to x and the limit of $f(x_i)$ exists in $[-\infty, +\infty]$. Then lower semicontinuity is expressed as

$$f(x) = \lim_{y \rightarrow x} \inf f(y) = \lim_{\varepsilon \downarrow 0} \left(\inf \{ f(y) \mid |y - x| \leq \varepsilon \} \right). \quad (2.6.6)$$

Lipschitz condition: A function f on a set S is called Lipschitzian and satisfies a uniform Lipschitz continuity with a coefficient ϵ , if and only if

$$|f(y) - f(x)| \leq \epsilon |y - x|, \quad \forall y \in S, \quad \forall x \in S. \quad (2.6.7)$$

This implies, that for f to be a convex function on any closed bounded subset S of the domain of f , then f is Lipschitzian relative to S .

Legendre transformation: let f be a differentiable real-valued function on an open subset C of \mathbb{R}^n . The Legendre conjugate of the pair (C, f) is defined to be the pair (D, g) , where D is the image of C under gradient mapping ∇f , and g is the function on D given by the formula

$$g(x^*) = \langle (\nabla f)^{-1}(x^*), x^* \rangle - f((\nabla f)^{-1}(x^*)). \quad (2.6.8)$$

It is not actually necessary to have ∇f one to one on C in order that g be well-defined. It suffices if

$$\langle x_1, x^* \rangle - f(x_1) = \langle x_2, x^* \rangle - f(x_2), \quad \nabla f(x_1) = \nabla f(x_2) = x^*. \quad (2.6.9)$$

Then the value of $g(x^*)$ can be obtained from Eq. 2.6.8 by replacing $(\nabla f)^{-1}(x^*)$ by any of the vectors it contains. Therefore, passing from (C, f) to the Legendre conjugate (D, g) , if the latter is well-defined, is called the Legendre transformation.

Let f be a (finite) differentiable convex function on \mathbb{R}^n . In order that ∇f be a one to one mapping from \mathbb{R}^n onto itself, it is necessary and sufficient that f be strictly convex and co-finite. When these conditions hold, f^ is likewise a differentiable convex function on \mathbb{R}^n which is strictly convex and co-finite, and f^* is the same as the Legendre conjugate of f , the Legendre conjugate of f^* is then in turn f .*

Weak lower semicontinuity:

Let the matrix $\eta \in \mathbb{R}^{m \times n}$ be defined with $T(\eta) = (\eta, \text{adj}_2 \eta, \dots, \text{adj}_{n \wedge m} \eta) \in \mathbb{R}^{\tau}$, where $\text{adj}_s \eta$ stands for the vector formed by all the $s \times s$ minors of the matrix η . For the special case $m = n = 2$, then $T(\eta) = (\eta, \det \eta)$.

In the minimization problem 2.3.21, η would be the gradient of the displacement field $\nabla \mathbf{u}$. The target is to make sure about the existence of minimizers. This depends on the choice of admissible functions. But if we tend to solve the differential equations arising from the minimization problem, the strategy will be too hard in most problems. Therefore, the essence of the direct methods of calculus of variations is to split the problem into two parts. First to enlarge the space of admissible functions, for example by considering spaces like Sobolev space $W^{1,p}$, where a general existence theorem is guaranteed, then we prove some regularity results in order to satisfy any minimizer of the aforementioned problem. The existence of minimizers in the above space relies on the fundamental property of weak lower semicontinuity defined as

$$u_v \rightharpoonup \bar{u} \text{ in } W^{1,p} \Rightarrow \liminf_{v \rightarrow \infty} I(u_v) \geq I(\bar{u}), \quad (2.6.10)$$

with \rightharpoonup to define a weak convergence. This property is necessary for the existence of minimizer. In the scalar case, it is strongly satisfied if and only if $\eta \rightarrow f(x, u, \eta)$ is affine, then we get

$$u_v \rightharpoonup \bar{u} \text{ in } W^{1,p} \Rightarrow \lim_{v \rightarrow \infty} I(u_v) = I(\bar{u}). \quad (2.6.11)$$

But this is not the case for the vectorial case, therefore we need to consider the notions from quasiconvex analysis introduced first by (Morrey 1966).

2.6.2 Notions of convexity

Let $f : \mathbb{R}^{m \times n} \rightarrow \mathbb{R}$,

- The function f is said to be rank one convex if

$$f(\lambda \eta_1 + (1 - \lambda) \eta_2) \leq \lambda f(\eta_1) + (1 - \lambda) f(\eta_2), \quad (2.6.12)$$

for every $\eta_1, \eta_2 \in \mathbb{R}^{m \times n}$ with $\text{rank}\{\eta_1 - \eta_2\} \leq 1$ and every $\lambda \in [0, 1]$.

- If f is Borel measurable and locally integrable, then it is said to be quasiconvex if

$$f(\eta) \leq \frac{1}{\text{meas } D} \int_D f(\eta + \nabla \phi(x)), \quad (2.6.13)$$

for every bounded open set $D \subset \mathbb{R}^n$, $\eta \in \mathbb{R}^{m \times n}$ and $\phi \in W_0^{1,\infty}(D; \mathbb{R}^m)$.

- A function f is said to be polyconvex if there exists $F : \mathbb{R}^{\tau(n,m)} \rightarrow \mathbb{R}$ convex, such that

$$f(\eta) = F(T(\eta)), \quad (2.6.14)$$

where

$$T(\eta) = (\eta, \text{adj}_2 \eta, \dots, \text{adj}_{n \wedge m} \eta). \quad (2.6.15)$$

- The different envelopes of a given function f are defined as

$$\begin{aligned}
 Cf &= \sup \{g \leq f : g \text{ convex}\}, \\
 Pf &= \sup \{g \leq f : g \text{ polyconvex}\}, \\
 Qf &= \sup \{g \leq f : g \text{ quasiconvex}\}, \\
 Rf &= \sup \{g \leq f : g \text{ rank one convex}\}.
 \end{aligned}
 \tag{2.6.16}$$

implying

$$f \text{ convex} \Rightarrow f \text{ polyconvex} \Rightarrow f \text{ quasiconvex} \Rightarrow f \text{ rank one convex.}$$

Hence

$$Cf \leq Pf \leq Qf \leq Rf \leq f,$$

in the scalar case all these envelopes do coincide.

- For rank one convexity and polyconvexity the sets could be extended in a straightforward manner to $f : \mathbb{R}^{m \times n} \rightarrow \mathbb{R} \cup \{+\infty\}$. But this is not the case for quasiconvexity. Therefore, the strategy to compute a quasiconvex envelope is in general by defining the polyconvex one then verifying that it is rank one convex, which means that they are identical and this would be the quasiconvex envelope. The theory covering the techniques to compute a quasiconvex envelope within a mechanical problem is called the relaxation theory. An analytical relaxed solution for a nonconvex energy of a 1D boundary value problem is included in Sec. 4 and an approximation of a convex envelope in higher dimensions is presented in Sec. 4.7 of this thesis.

3 Effective models for inelastic materials

In this section we want to introduce effective models that are capable of prescribing the behavior of complex materials. This applies to materials that are characterized by heterogeneous micro-scale, refer to Sec. 2.4, or to inelastic materials that show under deformation, an evolving complex pattern at the microstructure, see Sec. 2.5. Such complex materials are usually treated in the literature by multi-scale homogenization. Nevertheless, the implementation of a multi-scale scheme is a very time and memory consuming procedure. The fine scale boundary value problem (RVE at the microstructure) is to be computed for each integration point at every element of the macroscale. Hence, we get the (full) effective coarse scale response by averaging. This problem becomes rather more complicated for systems in three dimensions. Therefore, we present in the following reduced models based on the variational method to produce a system of equations in incremental settings. For this purpose, we start with the free energy and the dissipation potential and assume the infinite dimensional spaces can be reduced into finite ones. This would be achieved by considering that the potentials are insensitive to any small changes taking place in the marginal spaces, formerly defined in Sec. 2.5.

An introduction of the first reduced model is given in Sec. 3.1, then a view of an elastoplastic material model is presented in Sec. 3.1.1. Later on, two computational examples of structural elements are given in Secs. 3.1.2 and 3.1.3. In the next, the theory is extended to problems with periodic microstructure, i.e. in homogenization settings, as clarified in Sec. 3.1.4. Then, a sufficient number of numerical examples are given in Secs. 3.1.5, 3.1.6, 3.1.7 and 3.1.8 to prove the introduced theory. These examples prescribe composite inclusions assigned to polyhedral sub-domains (RVEs). A Comparison of a two-scale homogenization implementation is explained in Sec. 3.1.9 and lastly the final results of the first effective model are concluded in Sec. 3.1.10.

3.1 First effective model - RM_1

We want to describe inelastic processes based on extremum principles. Therefore, we consider a physical system defined by a set of external state variables \mathbf{x} and internal state variables \mathbf{z} with a parametrization in a suitable parameter space $\xi \in \Omega$,

$$\mathbf{x} = \mathbf{x}(\xi), \quad \mathbf{z} = \mathbf{z}(\xi). \quad (3.1.1)$$

The system's behavior is assumed to be defined considering two scalar potentials, the free energy $\Psi(\nabla \mathbf{x}, \mathbf{x}, \mathbf{z})$ and the dissipation potential $\Delta(\mathbf{z}, \dot{\mathbf{z}})$. Minimizing the systems's potential energy gives the evolution equations, where the gradient ∇ is

with respect to ξ .

$$\inf_{\mathbf{x}} \left\{ \int_{\Omega} \Psi(\nabla \mathbf{x}, \mathbf{x}, \mathbf{z}) d\xi + f_{\text{ext}}(\mathbf{x}) \mid \mathbf{x} = \mathbf{x}_0 \text{ on } \partial\Omega \right\}, \quad (3.1.2)$$

and $f_{\text{ext}}(\mathbf{x})$ is the potential of external forces. Stationarity of the minimization problem in Eq. 2.3.21 gives the evolution of the internal variables, known as Biot-equation,

$$\frac{\partial \Psi}{\partial \mathbf{z}} + \frac{\partial \Delta}{\partial \dot{\mathbf{z}}} = \mathbf{0}. \quad (3.1.3)$$

However, as mentioned in Sec. 2.5, we want to capture the behavior of the system with only a finite number of variables instead of infinite ones. So we define suitable function spaces $\mathbf{x} \in X$, $\mathbf{z} \in Z$ and linear projection operators onto the finite dimensional spaces

$$P : X \longrightarrow \mathbb{R}^M, \quad Q : Z \longrightarrow \mathbb{R}^N. \quad (3.1.4)$$

Then the essential parameters and the marginal remainders are given by the projection operators as shown below

$$\mathbf{x}_{\text{ess}} = P\mathbf{x}, \quad \mathbf{z}_{\text{ess}} = Q\mathbf{z}, \quad (3.1.5)$$

$$X_{\text{mar}} = \{\mathbf{x} \in X \mid P\mathbf{x} = \mathbf{0}\}, \quad Z_{\text{mar}} = \{\mathbf{z} \in Z \mid Q\mathbf{z} = \mathbf{0}\}. \quad (3.1.6)$$

Our goal now is to sufficiently describe the system using only essential parameters. Meaning that our potentials, the free energy and dissipation potential, are invariant under variation within the marginal spaces, which results as a stationarity of specific minimization problems

$$\begin{aligned} \frac{\partial \Psi}{\partial \mathbf{x}} : \delta \mathbf{x} = 0 & \quad \text{for } \delta \mathbf{x} \in X_{\text{mar}}, \\ \frac{\partial \Psi}{\partial \mathbf{z}} : \delta \mathbf{z} = 0 & \quad \text{for } \delta \mathbf{z} \in Z_{\text{mar}}, \\ \frac{\partial \Delta}{\partial \mathbf{z}} : \delta \mathbf{z} = 0 & \quad \text{for } \delta \mathbf{z} \in Z_{\text{mar}}, \\ \frac{\partial \Delta}{\partial \dot{\mathbf{z}}} : \delta \dot{\mathbf{z}} = 0 & \quad \text{for } \delta \dot{\mathbf{z}} \in Z_{\text{mar}}. \end{aligned} \quad (3.1.7)$$

Now we are capable of writing the macroscopic potentials in terms of the essential parameters,

$$\Psi_{\text{macro}}(\mathbf{x}_{\text{ess}}, \mathbf{z}_{\text{ess}}) = \inf_{\mathbf{x} \in X, \mathbf{z} \in Z} \left\{ \frac{1}{|\Omega|} \int_{\Omega} \Psi(\nabla \mathbf{x}, \mathbf{x}, \mathbf{z}) d\xi \mid \mathbf{x}_{\text{ess}} = P\mathbf{x}, \mathbf{z}_{\text{ess}} = Q\mathbf{z} \right\}, \quad (3.1.8)$$

$$\Delta_{\text{macro}}(\mathbf{z}_{\text{ess}}, \dot{\mathbf{z}}_{\text{ess}}) = \inf_{\mathbf{z} \in Z, \dot{\mathbf{z}} \in \dot{Z}} \left\{ \frac{1}{|\Omega|} \int_{\Omega} \Delta(\mathbf{z}, \dot{\mathbf{z}}) d\xi \mid \mathbf{z}_{\text{ess}} = Q\mathbf{z}, \dot{\mathbf{z}}_{\text{ess}} = Q\dot{\mathbf{z}} \right\}. \quad (3.1.9)$$

Assume that the minimization problem of the infinite dimensional problem can be replaced by the following minimization problem

$$\inf_{\mathbf{z}_{\text{ess}} \in \mathbb{R}^N} \left\{ \dot{\Psi}_{\text{macro}} + \Delta_{\text{macro}} \right\}. \quad (3.1.10)$$

Now consider the potential of external forces and the boundary condition to be expressed in terms of the essential parameters, with $f_{\text{ess}}(\mathbf{x}) = f_{\text{ess}}(\mathbf{x}_{\text{ess}})$ and the projection for the boundary conditions is given by $\mathbf{B}\mathbf{x}_{\text{ess}} = \mathbf{x}_{\text{ess}0}$ on $\partial\Omega$. Then Eq. 3.1.2 can be rewritten as follows

$$\inf_{\mathbf{x}_{\text{ess}} \in \mathbb{R}^M} \left\{ \int_{\Omega} \Psi_{\text{macro}}(\mathbf{x}_{\text{ess}}, \mathbf{z}_{\text{ess}}) d\xi + f_{\text{ess}}(\mathbf{x}_{\text{ess}}) \mid \mathbf{B}\mathbf{x}_{\text{ess}} = \mathbf{x}_{\text{ess}0} \text{ on } \partial\Omega \right\}. \quad (3.1.11)$$

Thus the reduced model is approximating the original system, and for a given f_{ess} and $\mathbf{x}_{\text{ess}0}$ as functions of time, one can compute \mathbf{x}_{ess} and \mathbf{z}_{ess} as functions of time as well.

3.1.1 Elastoplasticity with isotropic hardening

We apply the introduced theory to bodies with standard rate-independent elastoplastic material with $\Omega \subset \mathbb{R}^n$ as a domain in Euclidean space representing the material body. The external space variable $\mathbf{u} = \mathbf{u}(\mathbf{r}, t)$ is given by the displacement field as a function of the position vector $\mathbf{r} \in \Omega$ and the time parameter t . The internal space variable $\mathbf{z} = \{\boldsymbol{\varepsilon}_p, q\}$ represents the trace free plastic strain tensor, $\text{tr}\boldsymbol{\varepsilon}_p = 0$, and the hardening parameter q (scalar). The free energy for standard elastoplastic material with linear isotropic hardening is given as

$$\Psi(\boldsymbol{\varepsilon}, \boldsymbol{\varepsilon}_p) = \frac{1}{2}(\boldsymbol{\varepsilon} - \boldsymbol{\varepsilon}_p) : \mathbb{C} : (\boldsymbol{\varepsilon} - \boldsymbol{\varepsilon}_p) + \frac{1}{2}\alpha q^2, \quad (3.1.12)$$

with $\boldsymbol{\varepsilon} = \frac{1}{2}(\nabla\mathbf{u} + \nabla\mathbf{u}^T)$, the total strain tensor, $\mathbb{C} = \mathbb{C}(\mathbf{r})$ is the tensor of elastic moduli and $\alpha(\mathbf{r})$ is the hardening modulus. The dissipation potential for rate-independent plastic materials has the form

$$\Delta(\dot{\boldsymbol{\varepsilon}}_p) = \sqrt{\frac{2}{3}} \sigma_y \|\dot{\boldsymbol{\varepsilon}}_p\|, \quad (3.1.13)$$

with $\sigma_y = \sigma_y(\mathbf{r})$ is the initial yield stress. The evolution of the hardening parameter q is related to the plastic strain with the relation

$$\dot{q}(\mathbf{r}, t) = \|\dot{\boldsymbol{\varepsilon}}_p\|. \quad (3.1.14)$$

To construct the Lagrangian, we insert the constraint given in Eq. 3.1.14 with the Lagrange-parameter γ into the extremum problem.

$$L = \dot{\Psi} + \Delta + \gamma(\dot{q} - \|\dot{\boldsymbol{\varepsilon}}_p\|) = \boldsymbol{\sigma} : (\dot{\boldsymbol{\varepsilon}} - \dot{\boldsymbol{\varepsilon}}_p) + \alpha q \dot{q} + \sqrt{\frac{2}{3}} \sigma_y \|\dot{\boldsymbol{\varepsilon}}_p\| + \gamma(\dot{q} - \|\dot{\boldsymbol{\varepsilon}}_p\|), \quad (3.1.15)$$

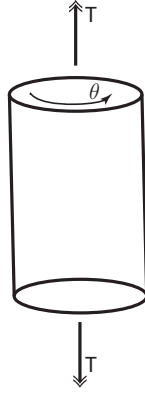


Figure 3.1: Cylindrical body problem: A circular bar with a radius R subject to twist θ or torque T .

where $\boldsymbol{\sigma} = \mathbb{C} : (\boldsymbol{\varepsilon} - \boldsymbol{\varepsilon}_p)$ is the stress tensor. Variations with respect to γ , \dot{q} , and $\dot{\boldsymbol{\varepsilon}}_p$ yield the Biot-equation

$$\dot{q}(\mathbf{r}, t) = \|\dot{\boldsymbol{\varepsilon}}_p\|, \quad (3.1.16)$$

$$\alpha q + \gamma = 0, \quad (3.1.17)$$

$$\text{dev} \boldsymbol{\sigma} \in \left(\sqrt{\frac{2}{3}} \sigma_y + \alpha q \right) \frac{\dot{\boldsymbol{\varepsilon}}_p}{\|\dot{\boldsymbol{\varepsilon}}_p\|}. \quad (3.1.18)$$

We observe a subdifferential due to the non-differentiability of the norm, which can be expressed in terms of the yield function

$$\|\text{dev} \boldsymbol{\sigma}\| \leq \sqrt{\frac{2}{3}} \sigma_y + \alpha q. \quad (3.1.19)$$

The flow rule with the consistency parameter $\lambda \geq 0$ reads as

$$\dot{\boldsymbol{\varepsilon}}_p = \lambda \text{dev} \boldsymbol{\sigma}. \quad (3.1.20)$$

3.1.2 Cylindrical body under torsion

Let us consider a circular bar, a cylindrical body, Ω with a radius R , subject at both ends to rotation θ or torques T , see Fig. 3.1. This is a well understood problem in the field of mechanics. The given loading implies a strict rotational motion with the following displacement field

$$u = u_\phi(r, z, t) = r z \theta'(t), \quad (3.1.21)$$

where z is the axial coordinate, r is the radial coordinate, and $\theta' = \frac{\theta(t)}{L}$ is the twist, i.e. the rotation per unit length of the cylinder with the length L . To come up with the relations for the low dimensional model (reduced model) prescribing the torsion bar, we give first in a similar outline to Sec. 3.1.1 the kinematics and response

defining this problem. Under symmetry and using the cylindrical coordinates, the only remaining strain components for this pure shear deformation state are the ones in $z - \theta$ plane, i.e.

$$\gamma_{z\theta} = 2\varepsilon_{z\phi} = 2\varepsilon_{\phi z} = \theta' r. \quad (3.1.22)$$

Analogously, we can define the plastic strain component $p = p(r, t)$ as

$$p = 2\varepsilon_{pz\phi} = 2\varepsilon_{p\phi z}, \quad (3.1.23)$$

and the shear stresses in the cylinder with the shear modulus μ are given by

$$\tau(r) = \sigma_{z\phi} = \sigma_{\phi z} = \mu(\gamma - p). \quad (3.1.24)$$

Substituting into Eqs. 3.1.12 and 3.1.13 and plugging τ_y as the yield stress in shear, we get

$$\Psi = \frac{1}{2}\mu(\gamma - p)^2 + \frac{1}{2}\alpha q^2, \quad \Delta(\dot{p}) = \tau_y |\dot{p}|. \quad (3.1.25)$$

The yield function and the flow rule can be given similar to the previous section by

$$|\tau| \leq \tau_y + \alpha q, \quad \dot{p} = \lambda \tau, \quad \lambda \geq 0. \quad (3.1.26)$$

As well the evolution of hardening

$$\dot{q}(r, t) = |\dot{p}(r, t)|. \quad (3.1.27)$$

Note that the original problem in Sec. 3.1.1 is now reduced to a one dimensional case (scalar setting). To cover the full set of equations, we additionally give the relation connecting the shear stresses with the internal forces, i.e the relation for the imposed end torque

$$T = \int_A \tau r \, dA = \int_0^R 2\pi r^2 \tau \, dr, \quad (3.1.28)$$

Observe that the internal variables $p(r, t), q(r, t)$ are functions implying an infinite dimensional space. In order to construct a lower dimensional setting, we need to apply refinement, meaning we subdivide the given domain Ω into a number of sub-domains N_{sd} over the radius of the cylinder, refer to Sec. 2.5.2. Note that the split is along the radius and not the length of the cylinder as the symmetry turns a dependency only on the radius of the cylinder. So we split the cylinder into a number of concentric rings

$$\Omega = \bigcup_{i=1}^{N_{sd}} \Omega_i, \quad \text{with } r_0 = 0 < r_1 < \dots < r_{N_{sd}-1} < r_{N_{sd}} = R. \quad (3.1.29)$$

We define for convenience the following terms

$$m_i^{(1)} = \int_{r_{i-1}}^{r_i} r \, dr = \frac{(r_i^2 - r_{i-1}^2)}{2}, \quad m_i^{(2)} = \int_{r_{i-1}}^{r_i} r^2 \, dr = \frac{(r_i^3 - r_{i-1}^3)}{3}. \quad (3.1.30)$$

Then the averages for each sub-domain from Eq. 2.4.1 can be written as

$$\langle f \rangle_i = \frac{1}{m_i^{(1)}} \int_{r_{i-1}}^{r_i} f r \, dr, \quad (3.1.31)$$

The essential external parameter is simply the twist rate

$$\mathbf{x}_{\text{ess}} = \{\theta'\}. \quad (3.1.32)$$

and the essential internal parameters are assumed to be arranged by

$$\mathbf{z}_{\text{ess}} = \{p_i, q_i\}, \quad i \in \{1, 2, \dots, N_{\text{sd}}\}. \quad (3.1.33)$$

The mean values for the plastic parameter and hardening parameter per each sub-domain are given respectively

$$p_i = \langle p \rangle_i = \frac{1}{m_i^{(1)}} \int_{r_{i-1}}^{r_i} p r \, dr, \quad (3.1.34)$$

$$q_i = \langle q \rangle_i = \frac{1}{m_i^{(1)}} \int_{r_{i-1}}^{r_i} q r \, dr. \quad (3.1.35)$$

Due to the simplicity of the problem (assumption made in Eq. 3.1.21), then Eq. 3.1.34 provides an exact representation of the displacement field. The macroscopic (also called effective) free energy given in terms of the essential parameters has the form

$$\begin{aligned} & \Psi_{\text{macro}}(\theta', p_1, \dots, p_{N_{\text{sd}}}, q_1, \dots, q_{N_{\text{sd}}}) \\ &= \inf_{p, q} \left\{ \int_0^R 2\pi \left[\frac{1}{2} \mu (r\theta' - p)^2 + \frac{1}{2} \alpha q^2 \right] r \, dr \mid p_i = \langle p \rangle_i, q_i = \langle q \rangle_i \right\}. \end{aligned} \quad (3.1.36)$$

We can now construct the Lagrangian considering the aforementioned constraints with the Lagrange-parameters λ_i, ξ_i

$$\begin{aligned} L = \sum_{j=1}^{N_{\text{sd}}} \left[\int_{r_{j-1}}^{r_j} 2\pi \left(\frac{1}{2} \mu (r\theta' - p)^2 + \frac{1}{2} \alpha q^2 \right) r \, dr + \lambda_j \left(p_j - \frac{1}{m_j^{(1)}} \int_{r_{j-1}}^{r_j} p r \, dr \right) \right. \\ \left. + \xi_j \left(q_j - \frac{1}{m_j^{(1)}} \int_{r_{j-1}}^{r_j} q r \, dr \right) \right]. \end{aligned} \quad (3.1.37)$$

Stationarity conditions give

$$p = r\theta' + \frac{1}{2\pi\mu} \frac{\lambda_j}{m_j^{(1)}}, \quad q = \frac{1}{2\pi\alpha} \frac{\xi_j}{m_j^{(1)}} \quad \text{in } \Omega_j. \quad (3.1.38)$$

implying the essential internal variables per sub-domain Ω_j to be

$$p_j = \frac{m_j^{(2)}}{m_j^{(1)}} \theta' + \frac{1}{2\pi\mu} \frac{\lambda_j}{m_j^{(1)}}, \quad q_j = \frac{1}{2\pi\alpha} \frac{\xi_j}{m_j^{(1)}}. \quad (3.1.39)$$

Substituting the previous equations into Eq. 3.1.36 gives

$$\begin{aligned} \Psi_{\text{macro}}(\theta', p_1, \dots, p_{N_{\text{sd}}}, q_1, \dots, q_{N_{\text{sd}}}) \\ = \sum_{j=1}^{N_{\text{sd}}} \left[2\pi m_j^{(1)} \left(\frac{1}{2} \mu \left(\frac{m_j^{(2)}}{m_j^{(1)}} \theta' - p_j \right)^2 + \frac{1}{2} \alpha q_j^2 \right) \right]. \end{aligned} \quad (3.1.40)$$

We apply the same steps to the dissipation potential

$$\Delta_{\text{macro}}(\dot{p}_1, \dots, \dot{p}_{N_{\text{sd}}}) = \inf_{\dot{p}} \left\{ \int_0^R 2\pi \tau_y |\dot{p}| r dr \mid \dot{p}_i = \langle \dot{p} \rangle_i \right\}. \quad (3.1.41)$$

employing the Lagrange-multipliers η_i to enforce the constraints, stationarity conditions yield

$$\text{sign}(\dot{p}) = \frac{\eta_j}{m_j^{(1)} 2\pi \tau_y} \quad \text{in } \Omega_j, \quad (3.1.42)$$

which means that $\text{sign}(\dot{p}_j)$ is constant in each Ω_j implying $|\dot{p}_j| = \langle |\dot{p}| \rangle_j$, then the macroscopic dissipation potential is given as

$$\Delta_{\text{macro}}(\dot{p}_1, \dots, \dot{p}_{N_{\text{sd}}}) = \sum_{j=1}^{N_{\text{sd}}} 2\pi m_j^{(1)} \tau_y |\dot{p}_j|. \quad (3.1.43)$$

Taking into account that the minimizers for $q(r, t)$ in Eq. 3.1.36 and for $\dot{p}(r, t)$ in Eq. 3.1.41, are constant in each sub-domains, then Eq. 3.1.27 turns to be

$$\dot{q}_i = |\dot{p}_i|, \quad \text{for } i = 1, \dots, N_{\text{sd}}. \quad (3.1.44)$$

Balance laws give the relation for the torque as follows

$$T = \frac{\partial \Psi_{\text{macro}}}{\partial \theta'} = 2\pi\mu \sum_{j=1}^{N_{\text{sd}}} \left(\frac{(m_j^{(2)})^2}{m_j^{(1)}} \theta' - m_j^{(2)} p_j \right). \quad (3.1.45)$$

and the effective Biot-equations are

$$0 \in \frac{\partial \Psi_{\text{macro}}}{\partial p_i} + \frac{\partial \Delta_{\text{macro}}}{\partial \dot{p}_i}. \quad (3.1.46)$$

This results in the following yield conditions and evolution equations per each sub-domain Ω_i

$$\mu \left(\frac{m_i^{(2)}}{m_i^{(1)}} \theta' - p_i \right) \in (\tau_y + \alpha q_i) \text{sign } \dot{p}_i, \quad \text{for } i = 1, \dots, N_{\text{sd}}. \quad (3.1.47)$$

$$\mu \left| \frac{m_i^{(2)}}{m_i^{(1)}} \theta' - p_i \right| \leq \tau_y + \alpha q_i, \quad \dot{p}_i = \lambda_i \left(\frac{m_i^{(2)}}{m_i^{(1)}} \theta' - p_i \right), \\ \lambda_i \geq 0, \quad \text{for } i = 1, \dots, N_{\text{sd}}. \quad (3.1.48)$$

In the next section we give the values for the material parameters and the loading used in the numerical example. For the considered material, the values are Young's modulus $E = 1000 \text{ N/mm}^2$, Poison's ratio $\nu = 0.25$, the yield stress in shear $\tau_y = 0.5 \sqrt{\frac{2}{3}} \text{ N/mm}^2$ and the hardening modulus for perfect elastoplasticity is $a = 0$ but for elastoplasticity with isotropic hardening is $a = \frac{\mu}{50} \text{ N/mm}^2$. We consider a cylinder with the radius $R = 10 \text{ mm}$, split into $N_{\text{sd}} = 5$ equal sub-domains. A cyclic load is applied in time prescribing the twist along the length of the cylinder. The load is defined by the relation $\theta' = A_1 g(t)$, where $A_1 = 1.0 \text{ rad/mm}$ describes the distribution over the length of the cylinder, and the function $g(t)$ applies the twist to the cylinder in time, see Fig. 3.2,

$$g(t) = 2 * 10^{-3} \left(1 - \cos \left(\frac{\pi t}{5 t_0} \right) \right) \cos \left(\frac{30\pi t}{5 t_0} \right), \quad \text{with } t_0 = \frac{0.1 * 5}{600} \text{ sec}. \quad (3.1.49)$$

This minimization problem is compared to a full scale boundary value problem implemented using the finite element method, which is considered to be a converged reference solution. The torque computed according to Eq. 3.1.45 is shown in Fig. 3.3 in which the behavior is calculated once for a pure elastoplastic material and once considering isotropic hardening. Very well matching behavior from the reduced model and the exact solution is obtained.

The internal variables per each sub-domain $\{p_i, q_i\}$, $i = 1, \dots, N_{\text{sd}}$ are updated using the backward-Euler scheme. The evolution of the plastic strains along the radius R at a specific time step $t = 7.5 \text{ sec}$ is given in Fig. 3.4. The lower plot shows that the minimizer, refer to Eq. 3.1.39(1), is linearly dependent on the radial position with jumps at the interfaces of the different sub-domains. But the behavior of the macro plastic strains from the effective model is constant over each sub-domain, which can be directly observed in Eq. 3.1.48. Intersection points for the FEM solution with the solution from RM_1 is captured exactly by the minimizer (same intersection points).

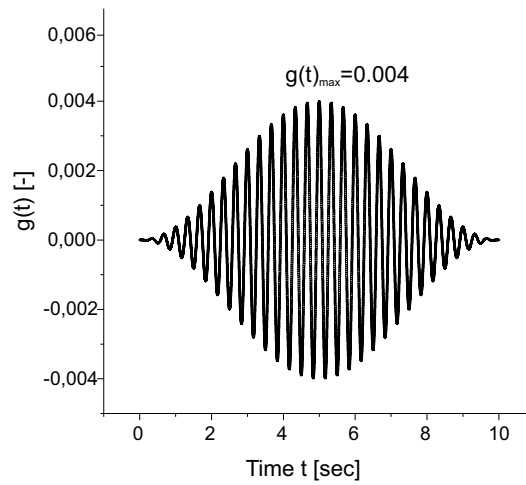


Figure 3.2: Loading applied to the torsion problem $\theta' = A_1 g(t)$ in the form of twist rate over time.

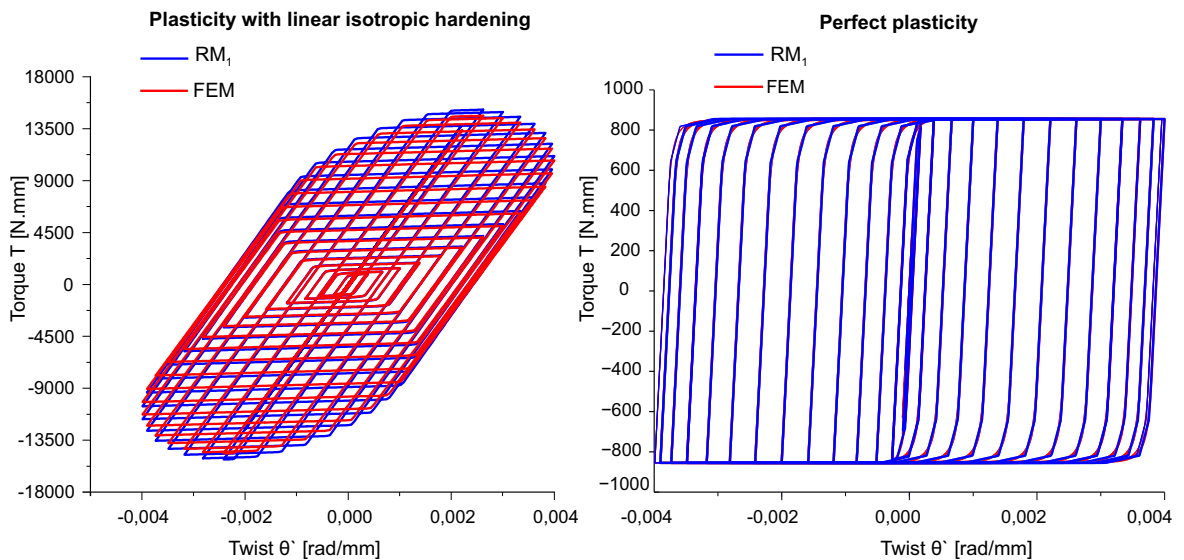


Figure 3.3: Torsion bar: torque versus twist in the form of cyclic loading for a plastic material with isotropic hardening (left) and with perfect plasticity (right).

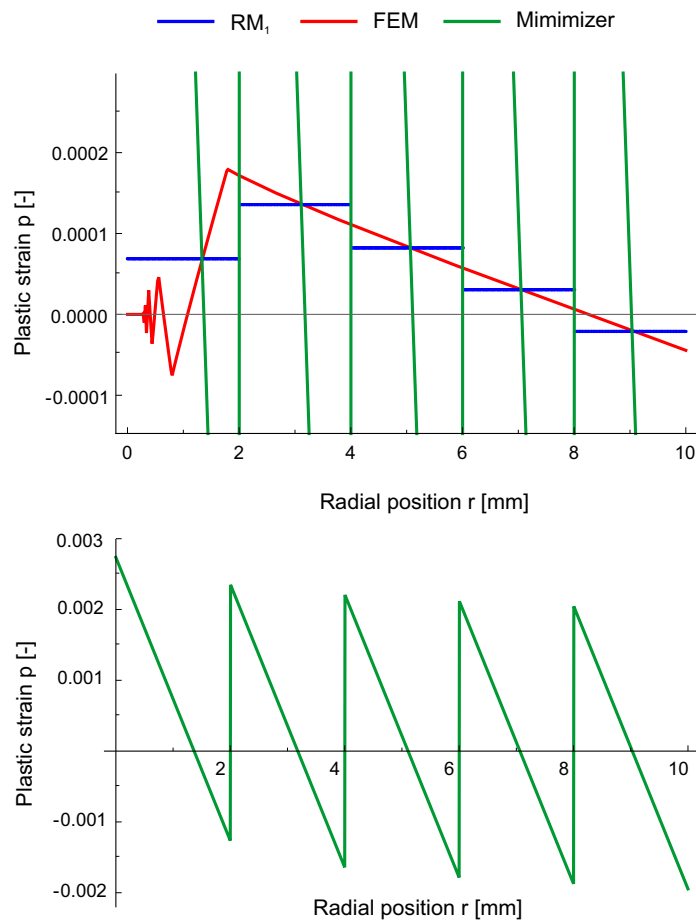


Figure 3.4: Torsion bar: the resulting plastic strains in the effective model versus radius r at time step $T = 7.5 \text{ sec}$ compared to the finite element results and the minimizer (top), the minimizer's curve in a full view (bottom).

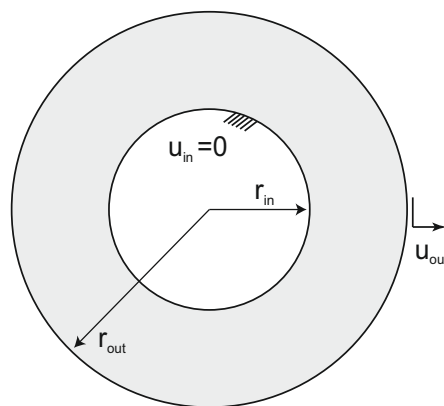


Figure 3.5: Spherical body fixed at inner radius r_{in} and displaced at outer radius r_{out} .

3.1.3 Pressurized spherical body

In this example $\Omega = \{\mathbf{r} \in \mathbb{R}^3 \mid r_{\text{in}} \leq |\mathbf{r}| \leq r_{\text{out}}\}$ is a spherical body with internal radius r_{in} and external radius r_{out} , see Fig. 3.5. The sphere is subject to a given displacement in the radial direction externally, implying the displacement field to be dependent only on the radial position \mathbf{r} , $\mathbf{u} = u_r(r, t)$. Considering spherical coordinates, we get due to axial symmetry only the following strain components which are non-trivial.

$$\varepsilon_{rr} = u', \quad \varepsilon_{\theta\theta} = \varepsilon_{\varphi\varphi} = \frac{u}{r}. \quad (3.1.50)$$

This implies the same components for the plastic strain to be non-trivial. Therefore, we introduce a function $p = p(r, t)$ in which we can express the components of the plastic strain tensor

$$\varepsilon_{prr} = p, \quad \varepsilon_{p\theta\theta} = \varepsilon_{p\varphi\varphi} = -\frac{1}{2}p. \quad (3.1.51)$$

Considering a perfectly elastoplastic material, we can write the free energy and dissipation potential in terms of the components of the strain and plastic strain tensors given above as

$$\Psi(u, p) = \frac{K}{2} \left(u' + \frac{2}{r}u \right)^2 + \frac{2}{3}\mu \left(u' - \frac{1}{r}u - \frac{3}{2}p \right)^2, \quad \Delta(\dot{p}) = \tau_y \|\dot{p}\|, \quad (3.1.52)$$

where the volumetric components are not vanishing as in the circular bar example, therefore, we notice the appearance of bulk modulus K . The full scale problem aims to find $u(r, t)$ and $p(r, t)$ for a given $u_{\text{in}}(t) = u(r_{\text{in}}, t)$ and $u_{\text{out}}(t) = u(r_{\text{out}}, t)$, which is an infinite-dimensional problem. As we need to define the internal and external variables for each radial position \mathbf{r} . Therefore, we apply the same procedure from the previous example to produce a reduced scale model. The body Ω is divided radially into N_{sd} sub-domains, so that each sub-domain is defined as

$$\Omega_i = \{\mathbf{r} \in \mathbb{R}^3 \mid r_{i-1} \leq |\mathbf{r}| \leq r_i\}, \quad (3.1.53)$$

with

$$r_{\text{in}} = r_0 < r_1 < \dots < r_{N_{\text{sd}}-1} < r_{N_{\text{sd}}} = r_{\text{out}}. \quad (3.1.54)$$

Volume averaging for the spherical sub-divisions has the form

$$\langle f \rangle_i = \frac{1}{|\Omega_i|} \int_{\Omega_i} f \, d\mathbf{r} = \frac{3}{(r_i^3 - r_{i-1}^3)} \int_{r_{i-1}}^{r_i} f \, r^2 \, dr. \quad (3.1.55)$$

We are interested only in the mean values of the plastic strains, therefore we introduce

$$p_i = \langle p \rangle_i, \quad (3.1.56)$$

giving the essential internal parameters to be

$$\mathbf{z}_{\text{ess}} = \{p_i\}. \quad (3.1.57)$$

And the essential external parameters are the boundary displacements

$$\mathbf{x}_{\text{ess}} = \{u_{\text{in}}, u_{\text{out}}\}. \quad (3.1.58)$$

Unlike the circular bar, the displacement field is now dependent on $p(r, t)$ and the boundary conditions and is not completely determined by the essential external parameter, (the twist rate) in the previous example. Therefore, we need to compute these relations (the mean value for p and the boundary displacements at each sub-domain). This implies, the macroscopic free energy can not be directly defined, but we need to define first intermediate energies for each sub-domain.

$$\Psi_{\text{int}}^i(u_{i-1}, u_i, p_i) = \inf_{u, p} \left\{ \int_{r_{i-1}}^{r_i} 4\pi \Psi(u, p) r^2 dr \mid u(r_{i-1}) = u_{i-1}, u(r_i) = u_i, \langle p \rangle_i = p_i \right\}. \quad (3.1.59)$$

resulting in the macroscopic free energy to be

$$\Psi_{\text{macro}}(u_{\text{in}}, u_{\text{out}}, p_1, \dots, p_{N_{\text{sd}}}) = \inf_{u_i} \left\{ \sum_{j=1}^{N_{\text{sd}}} \Psi_{\text{int}}^j(u_{j-1}, u_j, p_j) \mid u_0 = u_{\text{in}}, u_{N_{\text{sd}}} = u_{\text{out}} \right\}. \quad (3.1.60)$$

In order to take the constraints in Eq. 3.1.56 into account, we consider Lagrange-multipliers λ_i . Variation with respect to u in Eq. 3.1.59 gives

$$\begin{aligned} -K \left(r^2 \left(u' + \frac{2}{r} u \right) \right)' + K \left(2r \left(u' + \frac{2}{r} u \right) \right) - \frac{4}{3} \mu \left(r^2 \left(u' - \frac{1}{r} u - \frac{3}{2} p \right) \right)' \\ - \frac{4}{3} \mu \left(r \left(u' - \frac{1}{r} u - \frac{3}{2} p \right) \right) = 0, \end{aligned} \quad (3.1.61)$$

and variation with respect to p gives

$$-8\pi\mu \left(u' - \frac{1}{r} u - \frac{3}{2} p \right) = \frac{\lambda_i}{m_i^{(1)}}. \quad (3.1.62)$$

Then equations 3.1.61 and 3.1.62 have the solutions

$$u = c_1 r + c_2 \frac{1}{r^2} - \frac{1}{6K} \frac{\lambda_i}{m_i^{(1)}} r \ln r, \quad (3.1.63)$$

$$p = -2c_1 \frac{1}{r^3} - \frac{1}{\pi} \left(\frac{1}{9K} + \frac{1}{12\mu} \right) \frac{\lambda_i}{m_i^{(1)}}, \quad (3.1.64)$$

with the integration constants c_1, c_2 . In order to define the integration constants, we have to evaluate Eq. 3.1.63 for the displacements at the sides of each sub-domain, $u(r_{i-1}) = u_{i-1}$, and $u(r_i) = u_i$, this can be achieved by plugging into Eq. 3.1.59. Then Lagrange-parameters λ_i are expressed in terms of the side displacements and the means values of the plastic strains. With these steps, we obtain an explicit relation for $\Psi_{\text{int}}^i(u_{i-1}, u_i, p_i)$. As a results, the arising $\Psi_{\text{macro}}(u_{\text{in}}, u_{\text{out}}, p_1, \dots, p_{N_{\text{sd}}})$ requires solving a linear system of equations in $u_1, \dots, u_{N_{\text{sd}}}$.

Analogously, the effective dissipation potential can be given by

$$\Delta_{\text{macro}}(\dot{p}_1, \dots, \dot{p}_{N_{\text{sd}}}) = \sum_{j=1}^{N_{\text{sd}}} 2\pi m_j^{(2)} \tau_y |\dot{p}_j|. \quad (3.1.65)$$

For the evolution of the plastic strains, we introduce the thermodynamically driving forces

$$f_i = -\frac{\partial \Psi_{\text{macro}}}{\partial p_i}, \quad (3.1.66)$$

Minimizing the effective Lagrange-function results in the effective Biot-equations

$$f_i \in 2\pi m_i^{(2)} \tau_y \text{sign } \dot{p}_i, \quad \text{for } i = 1, \dots, N_{\text{sd}}. \quad (3.1.67)$$

This gives the yield condition and flow rule to be

$$|f_i| \leq 2\pi m_i^{(2)} \tau_y, \quad \dot{p}_i = \lambda_i f_i, \quad \lambda_i \geq 0, \quad \text{for } i = 1, \dots, N_{\text{sd}}. \quad (3.1.68)$$

The dependency of the driving forces on the external and internal essential parameters produces a coupled problem, known as multi-surface plasticity, which will be solved in a staggered scheme considering small time-steps to ensure the accuracy. So the yield surface is evaluated at each sub-domain for a specific plastic strain p_i and all other variables are kept fixed.

The same material parameters are considered in the numerical computation as in the torsion problem. The sphere has the internal and external radii as follows $r_{\text{in}} = 5 \text{ mm}$ and $r_{\text{out}} = 10 \text{ mm}$. For this displacement driven problem, the inner radius is restricted to move with $u_{\text{in}} = 0$, and the outer radius is exposed to $u_{\text{out}} = A_2 g(t)$, (see Fig. 3.1, where the function $g(t)$ is defined in Eq. 3.1.48), and $A_2 = 3 \text{ mm}$. Here $t_0 = \frac{0.5 \cdot 5}{600} \text{ sec}$. A finite element calculation for the prescribed model provides an exact converged solution for comparison.

Considering $N_{\text{sd}} = 2$ sub-domains, the displacements and plastic strains along the radial position for specific times $t = 2, 3, 4, 5 \text{ sec}$ are shown in Fig. 3.6. Notice the jump in the curves of the plastic strains at sub-domain interfaces. Moreover, the behavior is not constant in each sub-domain as it was in the torsion problem.

A second refinement for the sphere is computed, this time with $N_{\text{sd}} = 5$ sub-domains. A comparison from the two computations (2 sub-domains and 5 sub-domains) for

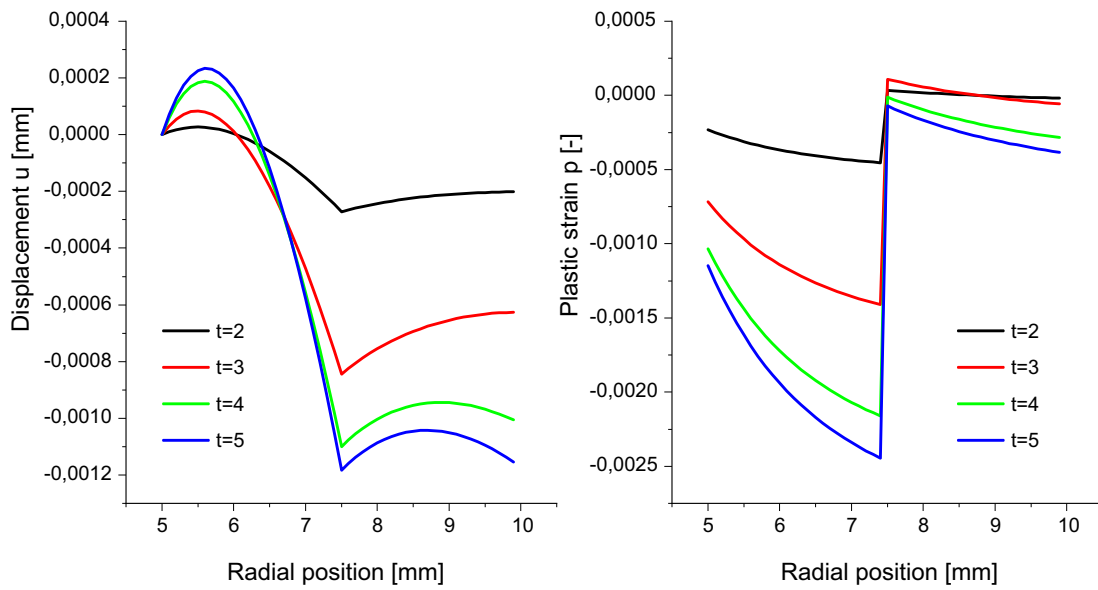


Figure 3.6: Illustration of the displacement field (left) and plastic strains (right) versus radial position between the inner and outer radius for times $t = 2, 3, 4, 5$ sec and 2 sub-domains.

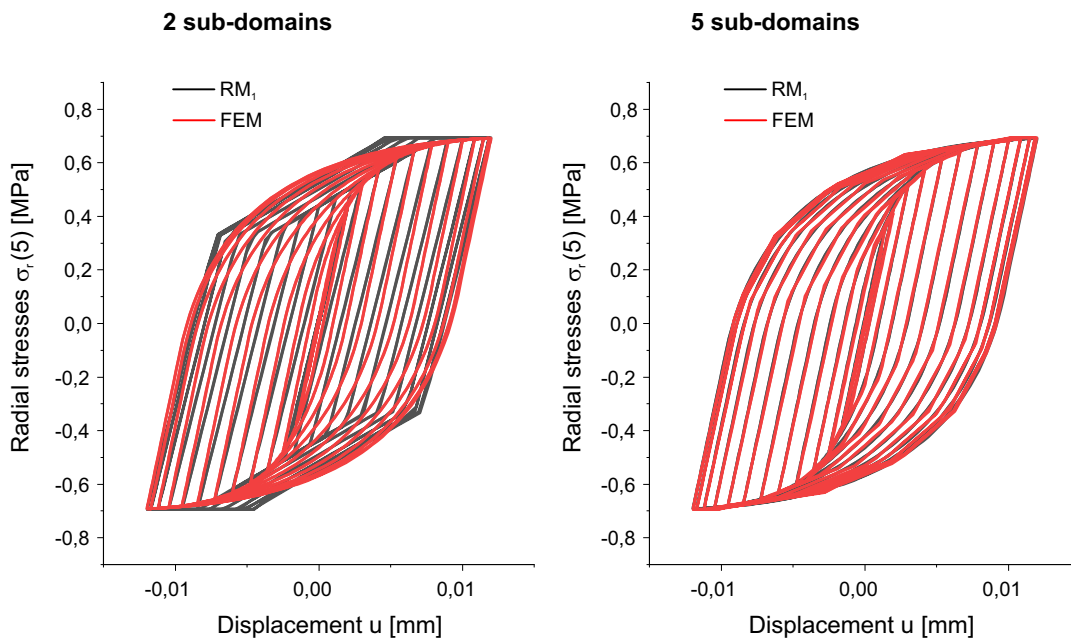


Figure 3.7: Comparison between the radial stresses against the displacement field at the position of the inner radius of the sphere from the reduced model and the finite element calculations, once for 2 sub-domains (left) and once for 5 sub-domains(right).

the normal stresses in the radial direction at the inner radius is shown in Fig. 3.7. A very good matching behavior is observed. It should be expected, that applying a higher refinement, i.e. increasing the number of sub-domains, enhances the compliance between the the reduced model and the exact solution.

3.1.4 Homogenization of elastoplastic materials with periodic microstructure

After applying the aforementioned theory to inelastic structures, we come now to the implementation to materials consisting of periodic microstructure. Assume our material is provided with a rectangular representative volume element at the microstructure, which has a varying $\mathbb{C}(\mathbf{r})$ and $\sigma_y(\mathbf{r})$ over the RVE with a volume Ω .

As defined in Sec. 2.4.1, passing a macroscopic strain (imposed at each integration point of the macrostructure) $\mathbf{e}_M = \mathbf{e}_M(t) = \langle \boldsymbol{\varepsilon} \rangle$ to the microstructure, allows us to capture the behavior of the macrostructure, for example the macroscopic stress is computed as $\boldsymbol{\sigma}_M = \boldsymbol{\sigma}_M(t) = \langle \boldsymbol{\sigma} \rangle$. The periodic boundary conditions assigned to the microstructure are defined in Eq. 2.4.4.

For the general macro-scale model, we need to define the plastic strains $\boldsymbol{\varepsilon}_p(\mathbf{r}, t)$ at each point of the domain Ω and for all times, which is an infinite-dimensional problem. In order to introduce a lower scale model, we split the representative volume element into N_{sd} distinct sub-domains Ω_i as

$$\Omega = \bigcup_{i=1}^{N_{sd}} \Omega_i, \quad (3.1.69)$$

where volume averaging is given as

$$\langle f \rangle_i = \frac{1}{|\Omega_i|} \int_{\Omega_i} f \, d\mathbf{r}. \quad (3.1.70)$$

The mean value of the plastic strains per each sub-domain can be defined by the following

$$\mathbf{e}_{pi} = \langle \boldsymbol{\varepsilon}_p \rangle_i, \quad (3.1.71)$$

resulting in the essential internal parameters

$$\mathbf{z}_{ess} = \mathbf{e}_p = (\mathbf{e}_{pi}). \quad (3.1.72)$$

On the other hand the essential external parameters are chosen as

$$\mathbf{x}_{ess} = \mathbf{e}_M. \quad (3.1.73)$$

We can now express the macroscopic free energy in terms of macroscopic strains and macroscopic plastic strains by the relation

$$\Psi_{\text{macro}}(\mathbf{e}_M, \mathbf{e}_p) = \inf_{\mathbf{u}_{\text{per}}, \boldsymbol{\varepsilon}_p} \left\{ \left\langle \frac{1}{2} (\boldsymbol{\varepsilon} - \boldsymbol{\varepsilon}_p) : \mathbb{C} : (\boldsymbol{\varepsilon} - \boldsymbol{\varepsilon}_p) \right\rangle \right. \\ \left. \left| \mathbf{u} = \mathbf{e}_M \cdot \mathbf{r} + \mathbf{e}_{\text{per}}, \quad \mathbf{e}_{pi} = \langle \boldsymbol{\varepsilon}_p \rangle_i \right. \right\}. \quad (3.1.74)$$

The side constraints from the plastic strains can be included in the minimization problem by considering Lagrange-parameters \mathbf{u}_i , giving the Lagrangian to be

$$L = \left\langle \frac{1}{2} (\boldsymbol{\varepsilon} - \boldsymbol{\varepsilon}_p) : \mathbb{C} : (\boldsymbol{\varepsilon} - \boldsymbol{\varepsilon}_p) \right\rangle + \sum_{i=1}^{N_{\text{sd}}} \mathbf{u}_i : (\mathbf{e}_{pi} - \langle \boldsymbol{\varepsilon}_p \rangle_i). \quad (3.1.75)$$

Stationarity with respect to \mathbf{u}_{per} and \mathbf{e}_{pi} , respectively, returns the balance law over the domain and Lagrange-multipliers per each sub-domain.

$$\nabla \cdot (\mathbb{C} : (\boldsymbol{\varepsilon} - \boldsymbol{\varepsilon}_p)) = \mathbf{0} \quad \text{in } \Omega, \quad (3.1.76)$$

$$\mathbb{C} : (\boldsymbol{\varepsilon} - \boldsymbol{\varepsilon}_p) = \mathbf{u}_i \quad \text{in } \Omega_i. \quad (3.1.77)$$

But $\boldsymbol{\sigma} = \mathbb{C} : (\boldsymbol{\varepsilon} - \boldsymbol{\varepsilon}_p)$, meaning that the balance law from Eq. 3.1.76 is trivially satisfied, whereas Eq. 3.1.77 means $\boldsymbol{\sigma} = \mathbf{u}_i$, implying that the stress is constant in each sub-domain. Applying volume averaging gives the effective stiffness

$$\mathbb{C}_{\text{eff}i} : (\mathbf{e}_i - \mathbf{e}_{pi}) = \mathbf{u}_i, \quad (3.1.78)$$

substituting for \mathbf{u}_i gives

$$\boldsymbol{\varepsilon} - \boldsymbol{\varepsilon}_p = \mathbb{C}^{-1} : \mathbb{C}_{\text{eff}i} : (\mathbf{e}_i - \mathbf{e}_{pi}), \quad (3.1.79)$$

where we introduced the abbreviations

$$\mathbf{e}_i = \langle \boldsymbol{\varepsilon} \rangle_i, \quad \mathbb{C}_{\text{eff}i} = (\langle \mathbb{C}^{-1} \rangle_i)^{-1}. \quad (3.1.80)$$

The resulting effective stiffness is called *Reuss effective stiffness* as a result for the constant stresses (earlier defined in Sec. 2.4.2). Plugging the mean values into Eq. 3.1.74 gives

$$\Psi_{\text{macro}}(\mathbf{e}_M, \mathbf{e}_p) = \inf_{\mathbf{u}_{\text{per}}} \left\{ \sum_{i=1}^{N_{\text{sd}}} \frac{|\Omega_i|}{|\Omega|} \frac{1}{2} (\mathbf{e}_i - \mathbf{e}_{pi}) : \mathbb{C}_{\text{eff}i} : (\mathbf{e}_i - \mathbf{e}_{pi}) \left| \mathbf{u} = \mathbf{e}_M \cdot \mathbf{r} + \mathbf{u}_{\text{per}} \right. \right\}. \quad (3.1.81)$$

Minimization with respect to the mean plastic strains gives the conjugate driving force for the essential internal parameters in each sub-domain

$$\mathbf{q}_i = -\frac{\partial \Psi_{\text{macro}}}{\partial \mathbf{e}_{pi}} = \frac{|\Omega_i|}{|\Omega|} \boldsymbol{\sigma}_i, \quad (3.1.82)$$

where the stress is constant over each sub-domain

$$\boldsymbol{\sigma}_i = \mathbb{C}_{\text{eff}i} : (\mathbf{e}_i - \mathbf{e}_{pi}). \quad (3.1.83)$$

Similarly, the macroscopic dissipation potential can be expressed as

$$\Delta_{\text{macro}}(\dot{\mathbf{e}}_p) = \inf_{\dot{\mathbf{e}}_p} \left\{ \left\langle \sqrt{2/3} \sigma_y \|\dot{\mathbf{e}}_p\| \right\rangle \mid \dot{\mathbf{e}}_{pi} = \langle \dot{\mathbf{e}}_p \rangle_i \right\}. \quad (3.1.84)$$

$\dot{\mathbf{e}}_p$ appears in an algebraic way only, hence, the dissipation potential can be directly interpreted in terms of the mean values corresponding to each sub-domain

$$\Delta_{\text{macro}}(\dot{\mathbf{e}}_p) = \frac{1}{|\Omega|} \sum_{i=1}^{N_{\text{sd}}} |\Omega_i| \Delta_{\text{macro}}^i(\dot{\mathbf{e}}_{pi}), \quad (3.1.85)$$

with

$$\Delta_{\text{macro}}^i(\dot{\mathbf{e}}_{pi}) = \inf_{\dot{\mathbf{e}}_p} \left\{ \left\langle \sqrt{2/3} \sigma_y \|\dot{\mathbf{e}}_p\| \right\rangle_i \mid \dot{\mathbf{e}}_{pi} = \langle \dot{\mathbf{e}}_p \rangle_i \right\}. \quad (3.1.86)$$

In general, $\Delta_{\text{macro}}^i(\dot{\mathbf{e}}_{pi})$ can only be calculated numerically. For this reason, let us assume that $\sigma_y = \sigma_{yi}$ is constant in every sub-domain. Then it follows that

$$\Delta_{\text{macro}}^i(\dot{\mathbf{e}}_{pi}) = \sqrt{2/3} \sigma_{yi} \|\dot{\mathbf{e}}_{pi}\|, \quad (3.1.87)$$

and we get the macroscopic dissipation potential per volume averaging

$$\Delta_{\text{macro}}(\dot{\mathbf{e}}_p) = \sqrt{2/3} \frac{1}{|\Omega|} \sum_{i=1}^{N_{\text{sd}}} |\Omega_i| \sigma_{yi} \|\dot{\mathbf{e}}_{pi}\|. \quad (3.1.88)$$

Making use of Equations 3.1.82 and 3.1.88, we can write the yield conditions for every sub-domain

$$\|\text{dev } \boldsymbol{\sigma}_i\| \leq \sqrt{2/3} \sigma_{yi}. \quad (3.1.89)$$

Remember that each $\boldsymbol{\sigma}_i$ requires the values of all (from each sub-domain) essential internal variables $\mathbf{e}_p = (\mathbf{e}_{pi})$.

3.1.5 Polyhedral sub-domains

Assume the microstructure consists of polyhedral sub-domains bounded by facets F_i . Any microstructure may be approximated in this way with arbitrary accuracy by choosing the facets small enough. Let \mathbf{n}_i be the outward normal vectors to the facets. Then the average strains in every sub-domain can be calculated according to

$$\mathbf{e}_i = \mathbf{e}_M + \frac{1}{|\Omega_i|} \sum_{F_j \subset \partial\Omega_i} \text{sym}(\mathbf{a}_j \otimes \mathbf{n}_j), \quad (3.1.90)$$

where $\text{sym}(\mathbf{T}) = \frac{1}{2}(\mathbf{T} + \mathbf{T}^T)$, and the amplitude vectors \mathbf{a}_i are given by the surface integrals

$$\mathbf{a}_i = \int_{F_i} \mathbf{u}_{\text{per}} dS. \quad (3.1.91)$$

Periodic boundary conditions at the microstructure imply that the amplitude vectors at the opposite facets on the boundary $F_j \subset \partial\Omega$ are dependent. The number of independent amplitude vectors is N_a . Rewriting Eq. 3.1.81 in terms of the amplitude vectors from Eq. 3.1.90, yields the macroscopic energy to be dependent on the amplitude vectors at each facet of the RVE.

$$\Psi_{\text{macro}}(\mathbf{e}_M, \mathbf{e}_p) = \inf_{\mathbf{a}_1, \dots, \mathbf{a}_{N_a}} \left\{ \Psi_{\text{rve}}(\mathbf{e}_M, \mathbf{e}_p, \mathbf{a}_1, \dots, \mathbf{a}_{N_a}) \right\}, \quad (3.1.92)$$

where

$$\Psi_{\text{rve}}(\mathbf{e}_M, \mathbf{e}_p, \mathbf{a}_1, \dots, \mathbf{a}_{N_a}) = \sum_{i=1}^{N_{\text{sd}}} \frac{|\Omega_i|}{|\Omega|} \frac{1}{2} (\mathbf{e}_i - \mathbf{e}_{p_i}) : \mathbb{C}_{\text{eff}i} : (\mathbf{e}_i - \mathbf{e}_{p_i}). \quad (3.1.93)$$

As can be seen, the introduced energy is dependent only on averages of the displacement field \mathbf{u}_{per} over the facets. As a result, the reduced model consists of only averages over the sub-domains for the different quantities. Although $\mathbf{e}_p = (\mathbf{e}_{p_i})$, but this does not require ε or ε_p to be constant on the sub-domains.

Stationarity conditions for the amplitude vectors are given by the minimization

$$\frac{\partial \Psi_{\text{rve}}}{\partial \mathbf{a}_i} = 0, \quad i = 1, \dots, N_a. \quad (3.1.94)$$

The former linear system of equations is under-determined, i.e. has multiple solutions. However, all solutions give the same minimum energy Ψ_{macro} . The macroscopic energy should be quadratic of the form

$$\Psi_{\text{macro}} = \frac{1}{2} \mathbf{e}_M : \mathbb{C}_{\text{eff}} : \mathbf{e}_M - \sum_{i=1}^{N_{\text{sd}}} \mathbf{e}_{p_i} : \mathbb{F}_{\text{eff}i} : \mathbf{e}_M + \sum_{i,j=1}^{N_{\text{sd}}} \frac{1}{2} \mathbf{e}_{p_i} : \mathbb{G}_{\text{eff}ij} : \mathbf{e}_{p_j}, \quad (3.1.95)$$

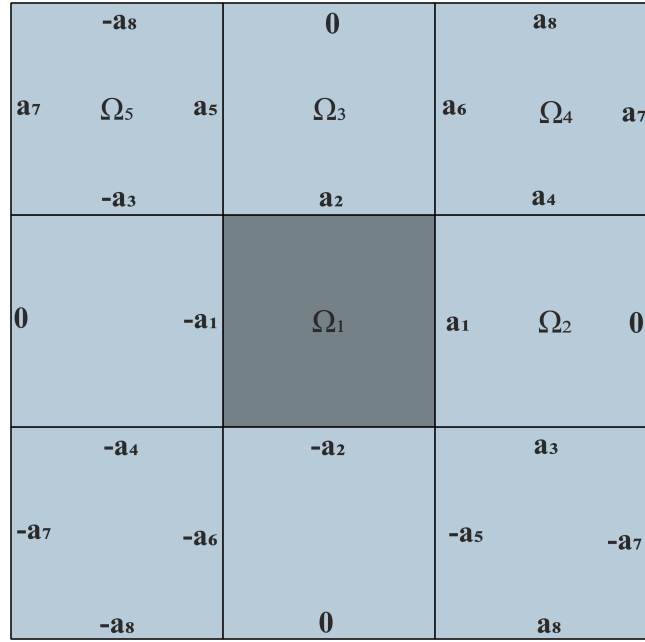


Figure 3.8: Representative volume element with sub-domains and amplitude vectors for symmetric case, with Mat_1 assigned to sub-domain Ω_1 and Mat_2 elsewhere.

where $\mathbb{F}_{\text{eff}i}$ and $\mathbb{G}_{\text{eff}ij}$ are stiffness-like tensors resulting from the minimization. But it is not possible to give a closed form expressions for them. We obtain the thermodynamically driving forces by

$$\mathbf{q}_i = -\frac{\partial \Psi_{\text{macro}}}{\partial \mathbf{e}_{\text{pi}}} = \frac{|\Omega_i|}{|\Omega|} \boldsymbol{\sigma}_i = \mathbb{F}_{\text{eff}i} : \mathbf{e}_M - \sum_{j=1}^{N_{\text{sd}}} \mathbb{G}_{\text{eff}ij} : \mathbf{e}_{\text{pj}}. \quad (3.1.96)$$

Equations 3.1.88 and 3.1.89 are still applicable for the polyhedral sub-domains.

3.1.6 Basic example

In the following we give a basic example for a composite material, consisting of a microstructure provided with 9 polyhedral sub-domains, see Fig. 3.8. Mat_1 is assigned to the center inclusion Ω_1 with a constant elasticity tensor \mathbb{C}_1 and yield stress σ_{y1} , and Mat_2 elsewhere, with a constant elasticity tensor \mathbb{C}_2 and the yield stress σ_{y2} . Considering a symmetric RVE, then only 5 sub-domains possess different average strains. Moreover, periodic boundary conditions require, that only 8 different amplitude vectors have to be considered, see Fig. 3.8.

Let the volumes of each sub-domain be normalized as $|\Omega_i| = 1$, and let $\mathbf{n}_1 = (1, 0)$, $\mathbf{n}_2 = (0, 1)$ be two normal vectors in x - and y - directions respectively. According to Eq. 3.1.90 the average total strains in the shown sub-domains can be computed as

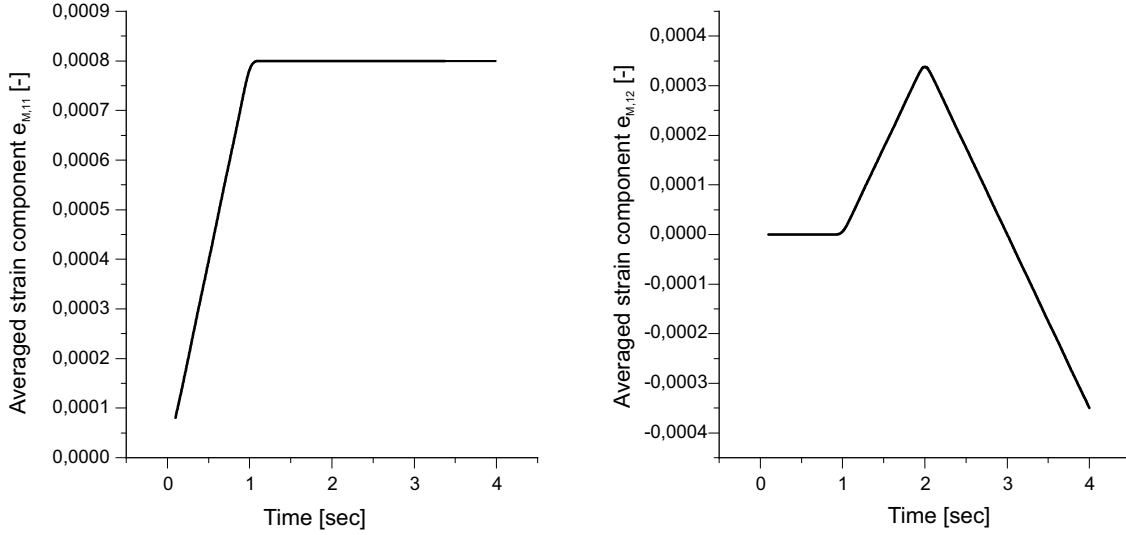


Figure 3.9: Driven essential values of the non-zero components of \mathbf{e}_M , averaged strains in 1– direction (left) and the 1 – 2 shear plane (right).

follows

$$\begin{aligned}
 \mathbf{e}_1 &= \mathbf{e}_M + 2 \operatorname{sym}(\mathbf{a}_1 \otimes \mathbf{n}_1 + \mathbf{a}_2 \otimes \mathbf{n}_2), \\
 \mathbf{e}_2 &= \mathbf{e}_M + \operatorname{sym}(-\mathbf{a}_1 \otimes \mathbf{n}_1 + (\mathbf{a}_4 - \mathbf{a}_3) \otimes \mathbf{n}_2), \\
 \mathbf{e}_3 &= \mathbf{e}_M + \operatorname{sym}((\mathbf{a}_6 - \mathbf{a}_5) \otimes \mathbf{n}_1 - \mathbf{a}_2 \otimes \mathbf{n}_2), \\
 \mathbf{e}_4 &= \mathbf{e}_M + \operatorname{sym}((\mathbf{a}_7 - \mathbf{a}_6) \otimes \mathbf{n}_1 + (\mathbf{a}_8 - \mathbf{a}_4) \otimes \mathbf{n}_2), \\
 \mathbf{e}_5 &= \mathbf{e}_M + \operatorname{sym}((\mathbf{a}_5 - \mathbf{a}_7) \otimes \mathbf{n}_1 + (\mathbf{a}_3 - \mathbf{a}_8) \otimes \mathbf{n}_2),
 \end{aligned} \tag{3.1.97}$$

yielding the macroscopic free energy to be

$$\Psi_{\text{macro}}(\mathbf{e}_M, \mathbf{e}_p) = \inf_{\mathbf{a}_1, \dots, \mathbf{a}_8} \left\{ \Psi_{\text{rve}}(\mathbf{e}_M, \mathbf{e}_p, \mathbf{a}_1, \dots, \mathbf{a}_8) \right\}, \tag{3.1.98}$$

where

$$\begin{aligned}
 \Psi_{\text{rve}}(\mathbf{e}_M, \mathbf{e}_p, \mathbf{a}_1, \dots, \mathbf{a}_8) = \\
 \frac{1}{18} (\mathbf{e}_1 - \mathbf{e}_{p1}) : \mathbb{C}_1 : (\mathbf{e}_1 - \mathbf{e}_{p1}) + \sum_{i=2}^5 \frac{1}{9} (\mathbf{e}_i - \mathbf{e}_{pi}) : \mathbb{C}_2 : (\mathbf{e}_i - \mathbf{e}_{pi}). \tag{3.1.99}
 \end{aligned}$$

Assuming elastoplastic materials with the following material parameters, Mat_1 with $E_1 = 1000 \text{ N/mm}^2$, $\nu_1 = 0.25$, $\sigma_{y1} = 1.5 \text{ N/mm}^2$ in Ω_1 , and Mat_2 with $E_2 = 5000 \text{ N/mm}^2$, $\nu_2 = 0.15$, $\sigma_{y2} = 3.75 \text{ N/mm}^2$ elsewhere. The applied load in terms of the macroscopic strain $\mathbf{e}_M(t)$ is varying in time, with a monotone normal component in 1– direction and an oscillatory shear component in 1 – 2 plane as depicted in Fig. 3.9.

For the numerical implementation, the reduced model RM_1 with the introduced set of equations is implemented in Mathematica. Energy minimization with respect to

the amplitude vectors is calculated first, then the macroscopic stresses in terms of \mathbf{a}_i and the plastic strains from the last time-step are computed applying the second law in thermodynamics (differentiation of the free energy with respect to the averaged strains). Later the updated internal variables, mean plastic strains, are evaluated numerically. Herewith we have solved the material model locally, i.e. on the micro level, macroscopic counterparts are computed per averaging. A very small time step is used $t \approx 0.0041$ sec to ensure the accuracy. On the other hand, a detailed finite element computation *FEM* is provided to allow for an exact solution for comparison. This implementation is performed considering the same boundary conditions and assigning a very fine mesh, namely, 40x40 quadratic elements to each sub-domain resulting in a total number of elements of 14400. We employed quadratic quadrilateral elements with (9-Nodes elements) to attain a higher number of degrees of freedom, performing as an accurate solution. The macroscopic behavior is obtained via Hill-Mandel homogenization scheme, which is a built-in procedure in FEAP software, refer to (Taylor and Govindjee 2022), used for the finite element analysis. All numerical calculations are performed considering a plane strain state.

The reduced model is computed, as well, applying the requirements of Reuss lower bound in which the following condition is considered

$$\mathbf{e}_M = \bigcup_{i=1}^{N_{sd}} \frac{|\Omega_i|}{|\Omega|} \mathbf{e}_i, \quad (3.1.100)$$

A comparison of the reduced model, Reuss lower bound and the finite element computations for the symmetric RVE can be inferred from Fig . 3.10. The macroscopic stress components in time are shown in the top pane and the middle to the left. The overall behavior from FEM is well captured by the reduced model, but the plots in the bottom pane for the macroscopic response in 1– direction and 1 – 2 plane, shows that the elastic stiffness is poorly presented by the reduced model. Moreover, the curves presenting the first component of the plastic strain in the center inclusion captures the behavior properly, however it reflects large deviations in the values. This has yet no great influence on the macroscopic stress history. The curves expressing Reuss model provide a good qualitative behavior but not a quantitative one.

3.1.7 Non-symmetric RVE

In the last example we considered a symmetric distribution of the geometry and material properties for a simplified problem. Nevertheless, the current example presents a more general case, with no point periodicity and additional material Mat_3 to be considered. Then the RVE has 9 different sub-domains imposing 9 different averaged strains as well, which contribute to 18 different amplitude vectors, see Fig. 3.11.

We consider three different isotropic materials within the RVE. Mat_1 in sub-domain Ω_1 , Mat_2 in sub-domain Ω_2 , and Mat_3 elsewhere in the matrix. The material parameters are given as follows: (Mat_1) $E_1 = 1000 \text{ N/mm}^2$, $\nu_1 = 0.25$, $\sigma_{y1} = 1.5 \text{ N/mm}^2$; (Mat_2) $E_2 = 2500 \text{ N/mm}^2$, $\nu_2 = 0.3$, $\sigma_{y2} = 2.0 \text{ N/mm}^2$; and (Mat_3) $E_3 = 5000 \text{ N/mm}^2$, $\nu_3 = 0.15$, $\sigma_{y3} = 3.75 \text{ N/mm}^2$.

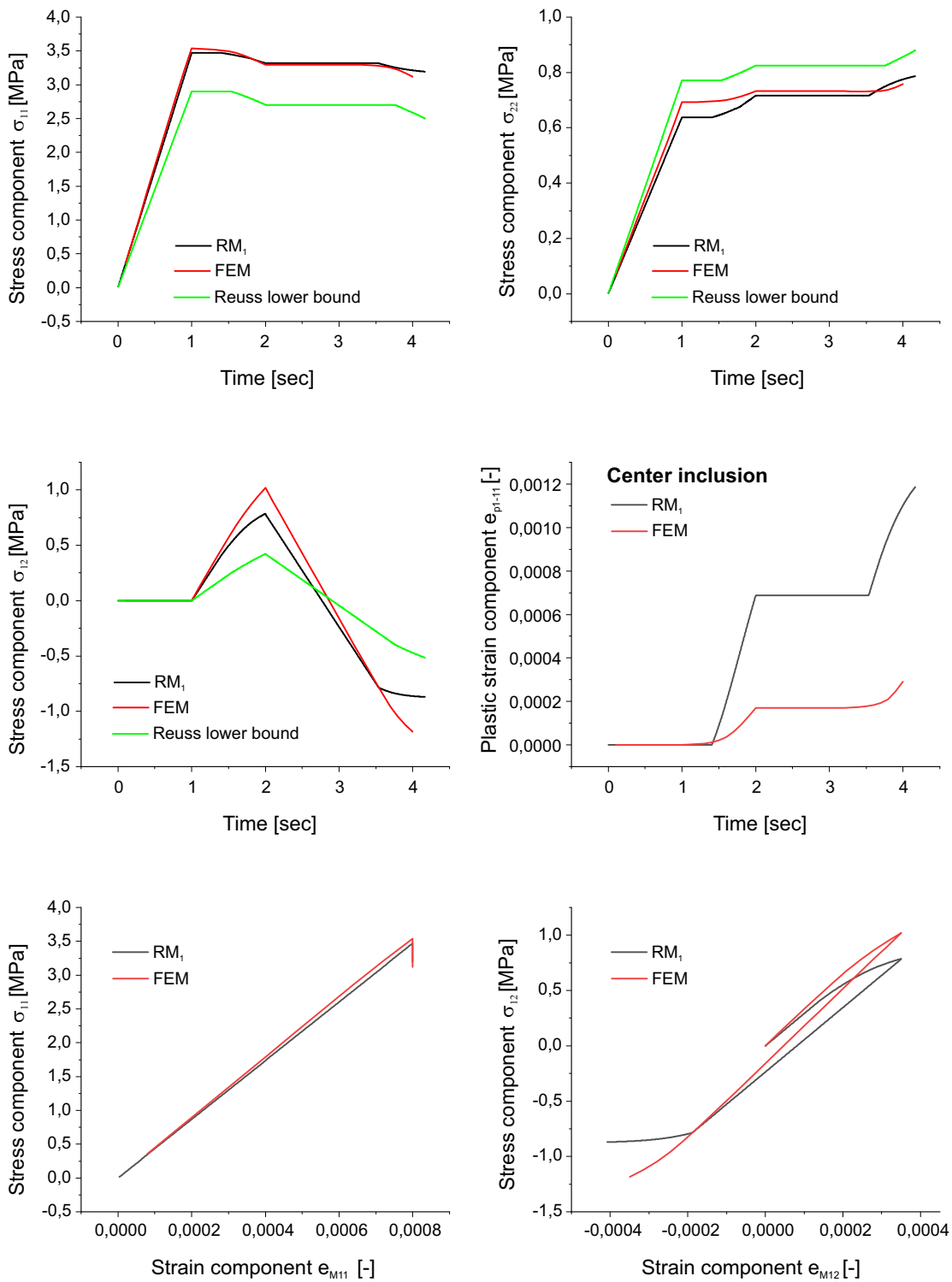


Figure 3.10: Comparison of the effective model, a Reuss model, and a finite element model for a single inclusion RVE: (top row and middle left pane) macroscopic stresses versus time, (middle right pane) 11 component of the average plastic strain, e_{p1} , of the center inclusion versus time, (bottom row) stress-strain response for the normal stress and strain in the 1-direction and the shear stress and strain in the 1-2 plane.

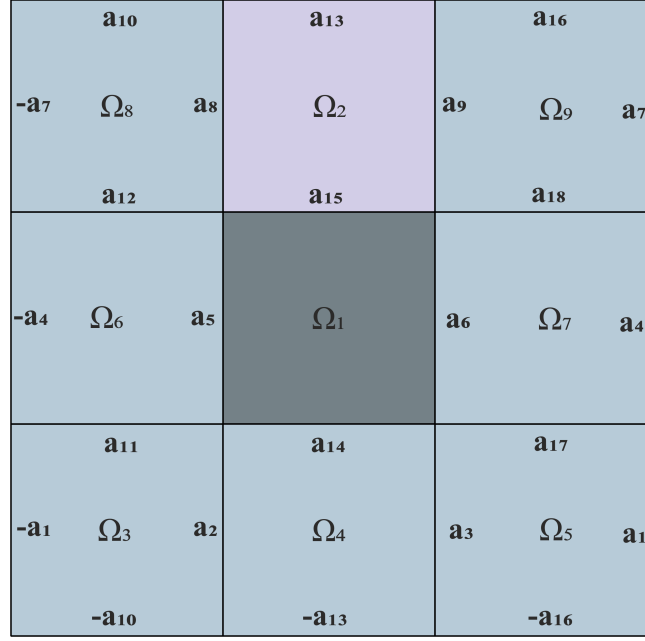


Figure 3.11: Representative volume element with sub-domains and amplitude vectors for periodic boundary conditions but no point periodicity. Mat_1 is assigned to the center inclusion, Mat_2 is assigned to sub-domain Ω_2 and Mat_3 is assigned to the matrix elsewhere.

The average total strains for the non-symmetric RVE are computed in a similar manner to the prior example and are given as

$$\begin{aligned}
\mathbf{e}_1 &= \mathbf{e}_M + \text{sym}((\mathbf{a}_6 - \mathbf{a}_5) \otimes \mathbf{n}_1 + (\mathbf{a}_{15} - \mathbf{a}_{14}) \otimes \mathbf{n}_2), \\
\mathbf{e}_2 &= \mathbf{e}_M + \text{sym}((\mathbf{a}_9 - \mathbf{a}_8) \otimes \mathbf{n}_1 + (\mathbf{a}_{13} - \mathbf{a}_{15}) \otimes \mathbf{n}_2), \\
\mathbf{e}_3 &= \mathbf{e}_M + \text{sym}((\mathbf{a}_2 - \mathbf{a}_1) \otimes \mathbf{n}_1 + (\mathbf{a}_{11} - \mathbf{a}_{10}) \otimes \mathbf{n}_2), \\
\mathbf{e}_4 &= \mathbf{e}_M + \text{sym}((\mathbf{a}_3 - \mathbf{a}_2) \otimes \mathbf{n}_1 + (\mathbf{a}_{14} - \mathbf{a}_{13}) \otimes \mathbf{n}_2), \\
\mathbf{e}_5 &= \mathbf{e}_M + \text{sym}((\mathbf{a}_1 - \mathbf{a}_3) \otimes \mathbf{n}_1 + (\mathbf{a}_{17} - \mathbf{a}_{16}) \otimes \mathbf{n}_2), \\
\mathbf{e}_6 &= \mathbf{e}_M + \text{sym}((\mathbf{a}_5 - \mathbf{a}_4) \otimes \mathbf{n}_1 + (\mathbf{a}_{12} - \mathbf{a}_{11}) \otimes \mathbf{n}_2), \\
\mathbf{e}_7 &= \mathbf{e}_M + \text{sym}((\mathbf{a}_4 - \mathbf{a}_6) \otimes \mathbf{n}_1 + (\mathbf{a}_{18} - \mathbf{a}_{17}) \otimes \mathbf{n}_2), \\
\mathbf{e}_8 &= \mathbf{e}_M + \text{sym}((\mathbf{a}_8 - \mathbf{a}_7) \otimes \mathbf{n}_1 + (\mathbf{a}_{10} - \mathbf{a}_{12}) \otimes \mathbf{n}_2), \\
\mathbf{e}_9 &= \mathbf{e}_M + \text{sym}((\mathbf{a}_7 - \mathbf{a}_9) \otimes \mathbf{n}_1 + (\mathbf{a}_{16} - \mathbf{a}_{18}) \otimes \mathbf{n}_2).
\end{aligned}$$

(3.1.101)

In the following we discuss the numerical results as presented before, see Fig. 3.12. It is observed from the behavior of the macroscopic stresses, that the reduced model is capable properly of representing the full scale model. Even Reuss model seems to be reasonable but fails to give close values. Moreover, the macroscopic response as shown in the last row shows a very good compliance in comparison to the large scale model with much higher number of degrees of freedom. An additional remark can be made to the energy plots versus time (middle right pane) in which the effective free energy from the reduced model is compared to the free energies computed according to Reuss lower bound and Voigt upper bound. The position of the reduced model between the upper and lower bounds provides a good qualitative behavior that complies with Hill's condition given in Eq. 2.4.5.

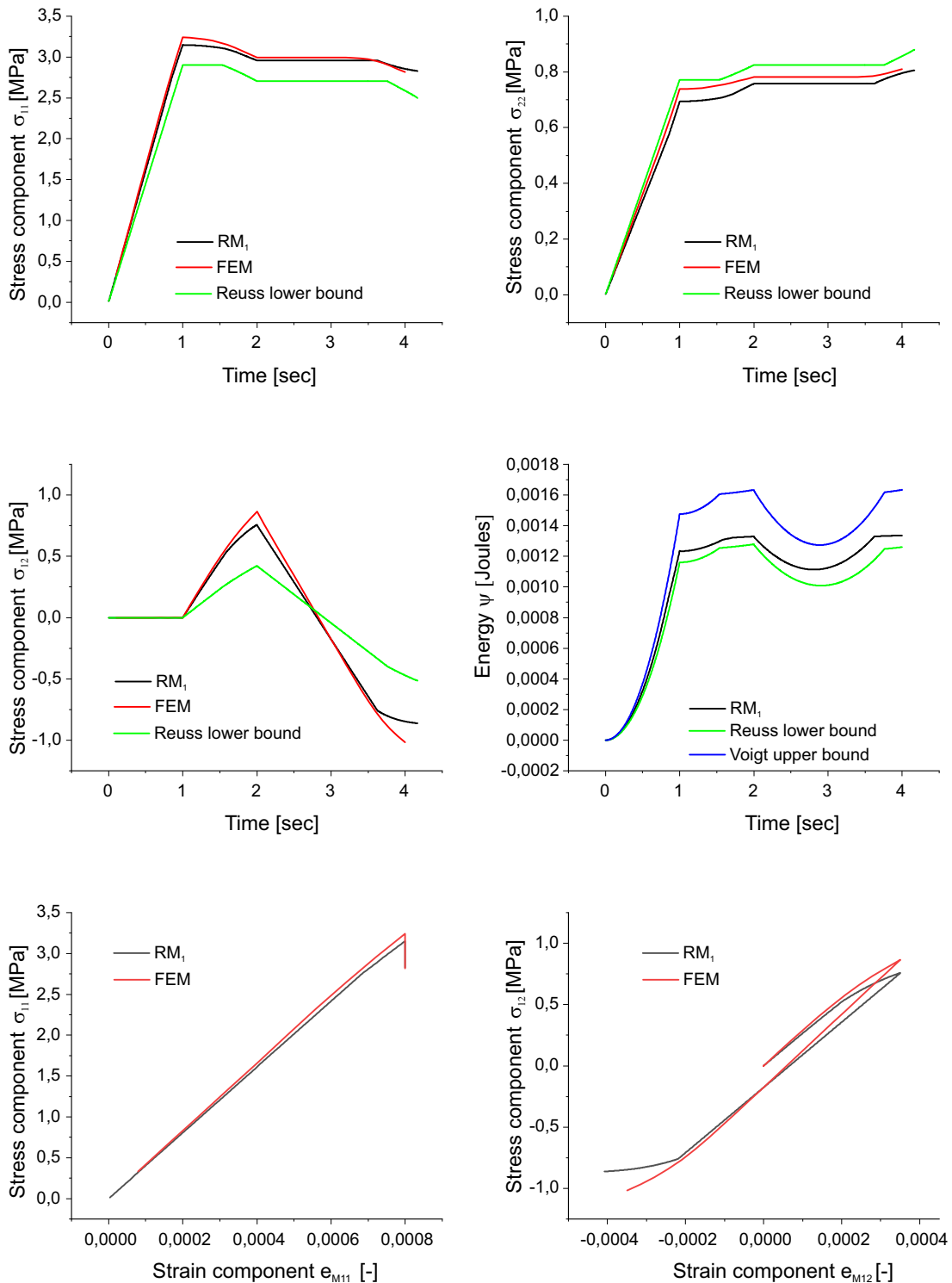


Figure 3.12: Comparison of the effective model, a Reuss model, and a finite element model for a two inclusion RVE: (top row and middle left pane) macroscopic stresses versus time, (middle right pane) RVE energy versus time, (bottom row) stress-strain response for the normal stress and strain in the 1-direction and the shear stress and strain in the 1-2 plane.

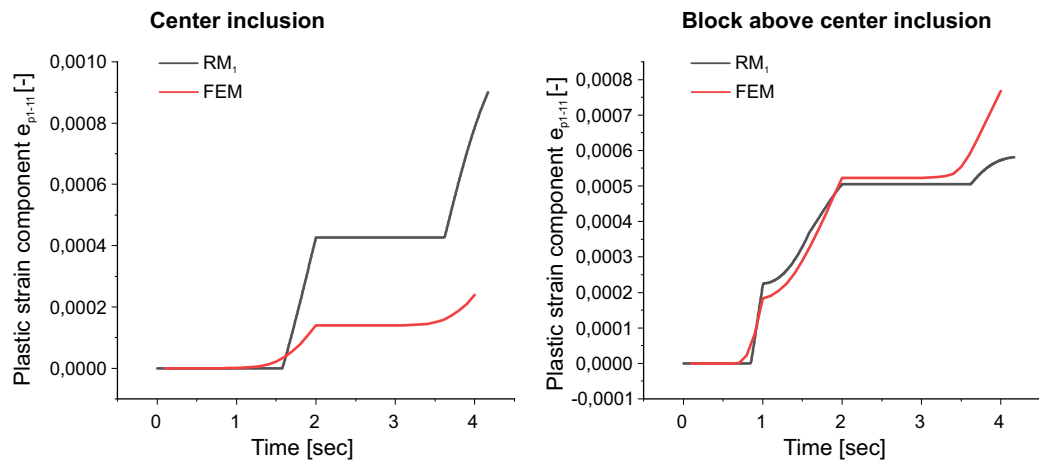


Figure 3.13: Illustration of the plastic strain behavior averaged over Mat_1 at the center inclusion and Mat_2 at sub-domain Ω_2 in comparison to the finite element results.

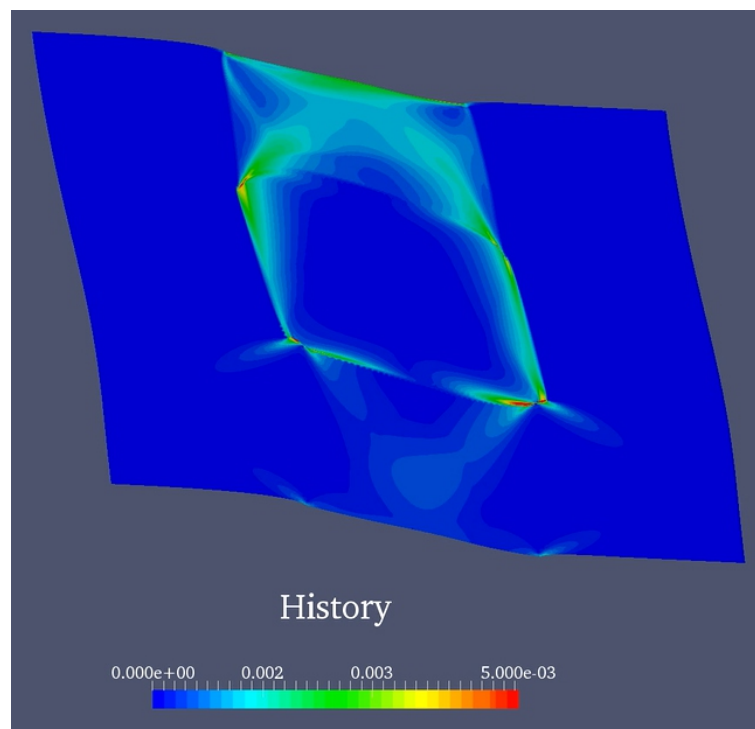


Figure 3.14: Contour plot for the plastic strain distribution from the finite element computation in a deformed view, implementation for the RVE with a square center inclusion.

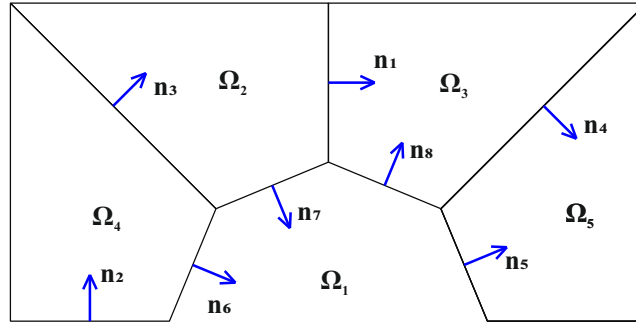


Figure 3.15: Normal vectors to the inclined facets of the representative volume element with an octagon center inclusion.

Plots of the mean plastic strains at the center inclusion and the one above (the 11 components) are shown in Fig. 3.13. Where the plastic strains are averaged per each material. A similar outcome to the symmetric RVE is obtained here also, as we see that the plastic strains from the exact solution (FEM) at the center inclusion are much less in comparison to the results from the reduced model. Nevertheless, the behavior in the block to the top of the center inclusion is quite reasonable. Another view of the plastic strains can be shown in Fig. 3.14, where the contour plot is from the finite element solution shown at the deformed representative volume element. Notice the strain concentration around the corners of the center inclusion. Which might justify, why the reduced model with a very few number of degrees of freedom is incapable of capturing this plastic strain concentration. Generally speaking, how exact the reduced model can capture the behavior of the internal variables is still an open question.

3.1.8 RVE with octagon center inclusion

This example shall examine a new shape for the center inclusion, here an octagon, leading to different volume fractions for the resulting sub-domains (9 sub-domains). Additionally, we need to take into account new orientations. As the facets are now inclined with different angles, therefore we need to compute new normal vectors $\mathbf{n}_3, \mathbf{n}_4, \mathbf{n}_5, \mathbf{n}_6, \mathbf{n}_7, \mathbf{n}_8$ as shown in Fig. 3.15, which have the values

$$\begin{aligned}
 \mathbf{n}_3 &= (\cos(45^\circ), \sin(45^\circ)), & \mathbf{n}_4 &= (\cos(45^\circ), -\sin(45^\circ)), \\
 \mathbf{n}_5 &= (\sin(67.5^\circ), \cos(67.5^\circ)), & \mathbf{n}_6 &= (\sin(67.5^\circ), -\cos(67.5^\circ)), \\
 \mathbf{n}_7 &= (\cos(67.5^\circ), -\sin(67.5^\circ)), & \mathbf{n}_8 &= (\cos(67.5^\circ), \sin(67.5^\circ)).
 \end{aligned}
 \tag{3.1.102}$$

In this example, Mat_1 is assigned to the octagon inclusion, Mat_2 is assigned to sub-domain Ω_2 and Mat_3 elsewhere in the matrix. 20 different amplitude vectors shall

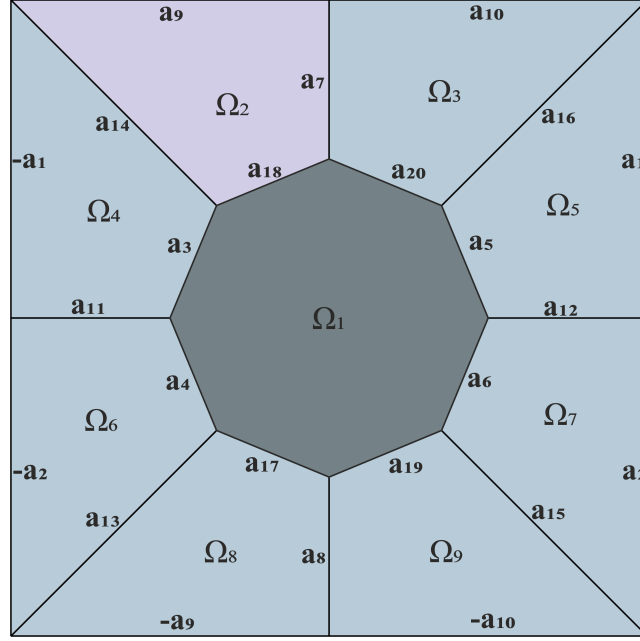


Figure 3.16: Representative volume element with octagon center inclusion and 20 amplitude vectors. Mat_1 is assigned to the center inclusion, Mat_2 is assigned to sub-domain Ω_2 and Mat_3 is assigned elsewhere.

be computed to cover all the different facets under periodic boundary conditions. The average total strains are given as

$$\begin{aligned}
 \mathbf{e}_1 &= \mathbf{e}_M + \text{sym}\left((\mathbf{a}_5 - \mathbf{a}_4) \otimes \mathbf{n}_5 + (\mathbf{a}_6 - \mathbf{a}_3) \otimes \mathbf{n}_6 + (\mathbf{a}_{20} - \mathbf{a}_{17}) \otimes \mathbf{n}_8 + (\mathbf{a}_{19} - \mathbf{a}_{18}) \otimes \mathbf{n}_7\right), \\
 \mathbf{e}_2 &= \mathbf{e}_M + \text{sym}\left(\mathbf{a}_7 \otimes \mathbf{n}_1 - \mathbf{a}_{14} \otimes \mathbf{n}_3 + \mathbf{a}_9 \otimes \mathbf{n}_2 + \mathbf{a}_{18} \otimes \mathbf{n}_7\right), \\
 \mathbf{e}_3 &= \mathbf{e}_M + \text{sym}\left(\mathbf{a}_{16} \otimes \mathbf{n}_4 - \mathbf{a}_7 \otimes \mathbf{n}_1 + \mathbf{a}_{10} \otimes \mathbf{n}_2 - \mathbf{a}_{20} \otimes \mathbf{n}_8\right), \\
 \mathbf{e}_4 &= \mathbf{e}_M + \text{sym}\left(\mathbf{a}_3 \otimes \mathbf{n}_6 - \mathbf{a}_1 \otimes \mathbf{n}_1 + \mathbf{a}_{14} \otimes \mathbf{n}_3 - \mathbf{a}_{11} \otimes \mathbf{n}_2\right), \\
 \mathbf{e}_5 &= \mathbf{e}_M + \text{sym}\left(\mathbf{a}_1 \otimes \mathbf{n}_1 - \mathbf{a}_5 \otimes \mathbf{n}_5 - \mathbf{a}_{16} \otimes \mathbf{n}_4 - \mathbf{a}_{12} \otimes \mathbf{n}_2\right), \\
 \mathbf{e}_6 &= \mathbf{e}_M + \text{sym}\left(\mathbf{a}_4 \otimes \mathbf{n}_5 - \mathbf{a}_2 \otimes \mathbf{n}_1 + \mathbf{a}_{11} \otimes \mathbf{n}_2 + \mathbf{a}_{13} \otimes \mathbf{n}_4\right), \\
 \mathbf{e}_7 &= \mathbf{e}_M + \text{sym}\left(\mathbf{a}_2 \otimes \mathbf{n}_1 - \mathbf{a}_6 \otimes \mathbf{n}_6 - \mathbf{a}_{15} \otimes \mathbf{n}_3 + \mathbf{a}_{12} \otimes \mathbf{n}_2\right). \\
 \mathbf{e}_8 &= \mathbf{e}_M + \text{sym}\left(\mathbf{a}_8 \otimes \mathbf{n}_1 - \mathbf{a}_{13} \otimes \mathbf{n}_4 + \mathbf{a}_{17} \otimes \mathbf{n}_8 - \mathbf{a}_9 \otimes \mathbf{n}_2\right), \\
 \mathbf{e}_9 &= \mathbf{e}_M + \text{sym}\left(\mathbf{a}_{15} \otimes \mathbf{n}_3 - \mathbf{a}_8 \otimes \mathbf{n}_1 - \mathbf{a}_{19} \otimes \mathbf{n}_7 - \mathbf{a}_{10} \otimes \mathbf{n}_2\right).
 \end{aligned}
 \tag{3.1.103}$$

The same isotropic elastoplastic materials, with material parameters from the non-symmetric polyhedral RVE, are implemented in the numerical calculations. For the exact solution obtained from the finite element analysis, a very fine mesh with 40x40 quadrilateral elements is assigned to each sub-domain, whereas the octagon is split into 4 quarters, each with 40x40 quadrilateral elements, resulting in 6400 elements mesh for the center inclusion. A comparison between the reduced model and the exact solution for the RVE with an octagon center can be inferred from Fig. 3.17.

We observe once again that the reduced model is suitable to capture the macroscopic response reasonably in comparison to the FE solution. The macroscopic stress component in 2– direction shows much higher values, even though the behavior is

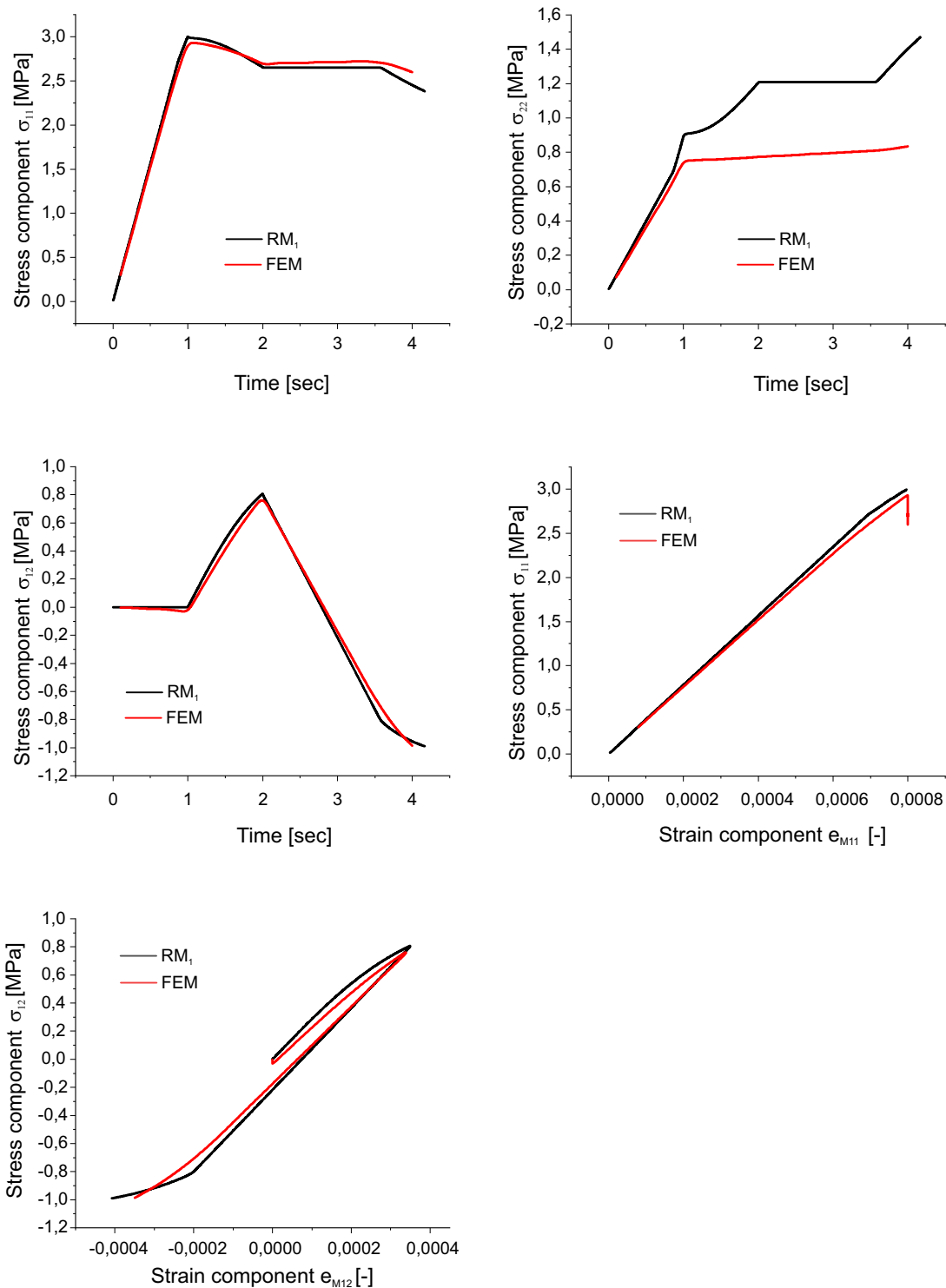


Figure 3.17: Comparison of the effective model and a finite element model for the octagon inclusion RVE. Macroscopic stresses versus time (top row and middle left pane). Stress-strain response for the normal stress and strain in the 1-direction and the shear stress and strain in the 1-2 plane (middle right pane and bottom row).

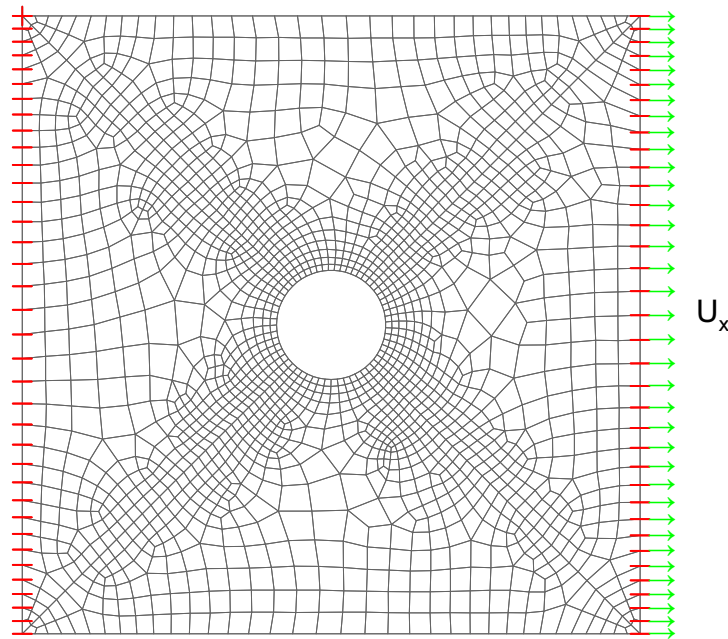


Figure 3.18: A plate with a hole under given displacement at the right hand side.

qualitatively well presented. We aim in the next to integrate the introduced theory of RM_1 into a two-scale homogenization scheme FE^2 as defined in Sec. 2.4.

3.1.9 Two-scale homogenization scheme including the reduced model RM_1

For this implementation, we consider a well known boundary value problem, which is the plate with a hole as shown in Fig. 3.18. The plate has the dimensions 10 mm x 10 mm with a centrally located hole of radius 1.25 mm. The left side of the plate is restrained from moving horizontally and the right side is subjected to a linearly increasing horizontal displacement, U_x , to a magnitude of 0.01 mm. At the macroscopic level the plate is discretized with 1793 hexahedral elements restrained in z -direction, implying a plane-strain state. For an FE^2 implementation, as earlier introduced, we need to provide a finite element discretization at the micro-scale, as well, according to Hill-Mandel procedure, resulting in a very computationally expensive scheme (in its general applications).

The illustrated mesh provides a macrostructure of the concerned problem. Two different microstructures will be pointwise assigned. For the first calculation, the plate with a hole represents a material provided with the RVE with 9 sub-domains and the octagon center inclusion as presented in Sec. 3.1.8, giving reduced two-scale scheme. In the second implementation, a full FE^2 scheme is calculated in which the material of the plate is provided with the same RVE, but discretized into 192 hexahedral elements. A small thickness is considered implying a plane strain state. For both microstructures refer to fig. 3.19. Note that the computation results are independent on the size of the microstructure.

The force-displacement diagram in x -direction computed from the response at the right side of the plate is shown in Fig. 3.20, in which the behavior from the reduced

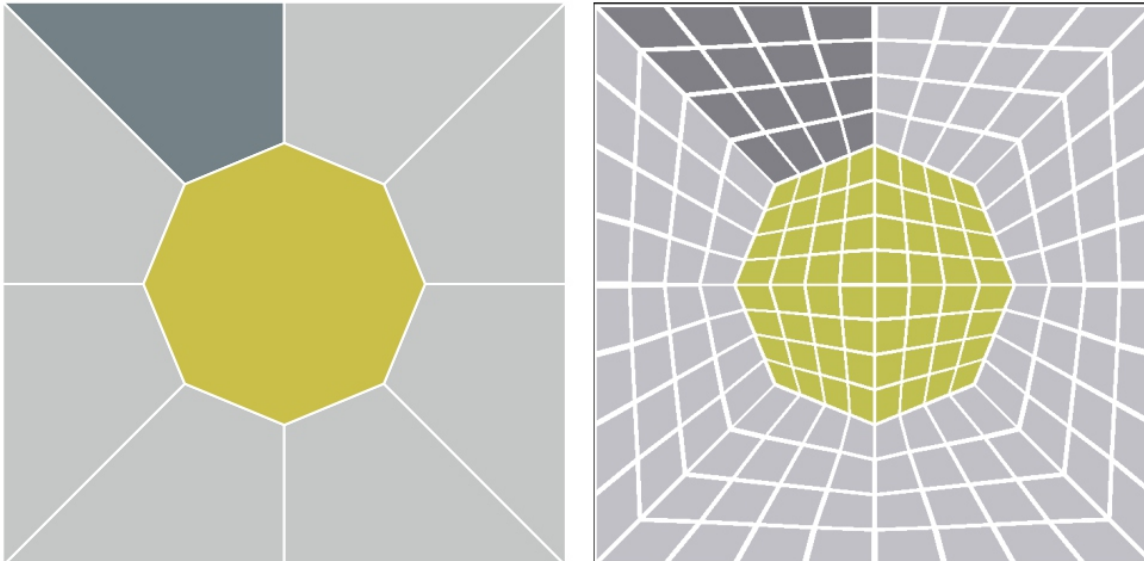


Figure 3.19: RVE at the microstructure, with 9 sub-domains for the reduced model (left) and with 192 finite element mesh for the full model (right).

simulation is well represented in comparison to the much higher degree of freedom FE^2 computations. The compliance can be observed for the elastic phase, as well for the plastic phase when yielding takes place. It can be even enhanced by using higher order elements instead of the linear used ones, but this would once again increase the computation time for the full model remarkably. Similar conclusion could be drawn, when considering Fig. 3.21, where the contour plots for the displacements in x - direction are given, once from the reduced model at microstructure (top) and once from the full-scale model (bottom).

An important advantage worth mentioning is the relative computation times for the two models. The computational time needed to complete the FE^2 was 71700 sec, whereas on the same hardware it was only 8548 sec for the reduced two-scale scheme – a speed up of roughly 8.4 times.

3.1.10 Conclusion - RM_1

The presented reduced model RM_1 is formulated starting from two scalar potentials (the free energy density and the dissipation potential) applying a variational scheme. Making use of the definition of *essential microstructure* given in Sec. 2.5.2, we were able to decrease the number of degrees of freedom vastly. This resulted in a robust model, that is capable of capturing the essential behavior of the full-scale model to a very large extent. The model is applied to structural elements as well to composites, moreover it is preserving the structure of the original system. The examples from the structural elements, the torsion bar and the pressurized sphere, show very good agreement with the full-scale model. On the other hand, the examples from microstructural homogenization shows that the macroscopic stresses and the stress-strain response are very well captured in comparison to a detailed finite element solution. Nevertheless, the averaged plastic strains showed strong concentration in small regions, which did not match the effective solution. One further drawback

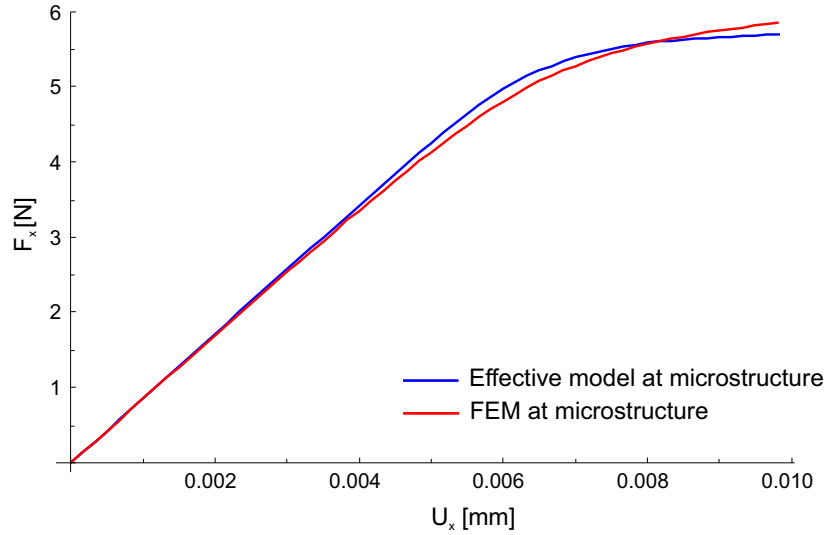


Figure 3.20: Force-Displacement diagram in x -direction for the two-scale homogenization problem: obtained from the effective model (blue) and FE^2 method (red).

of the introduced model is the restriction to be applied only to microstructure with polyhedral sub-domains, in order to be able to define the amplitude vectors normal to each facet. Meaning, microstructure with rounded or elliptical sub-domains can not be presented by this model. Another drawback is the deviation by the effective stiffness, which does not match the exact elastic effective stiffness. One possibility to resolve this problem for applications in microstructural homogenization will be presented in the next section, in the second reduced model RM_2 .

3.2 Second effective model - RM_2

An extended approach for the effective models is considered to overcome the drawbacks arising from the implementation of RM_1 into microstructural homogenization problems. Therefore, we rederive in Sec. 3.2.1 a new reduced model considering higher constraints, then in Sec. 3.2.2 an explanation of the numerical treatment is given. Later on in Secs. 3.2.3, 3.2.4, 3.2.5 and 3.2.6 several numerical problems are presented to clarify the advantages of the second reduced model and its broader applicability. In Sec. 3.2.7 an overall conclusion for RM_2 is given.

3.2.1 Derivation of the model

Higher order moments/variables in the definitions of the essential variables (external and internal) are considered.

$$\frac{1}{2} \int_{\Omega_i} \boldsymbol{\varepsilon} : \mathbb{C} : \boldsymbol{\varepsilon} d\mathbf{V} = \lambda_i \mathbf{q}_i(\mathbf{e}_i), \quad \text{for } \Omega_i \in \Omega. \quad (3.2.1)$$

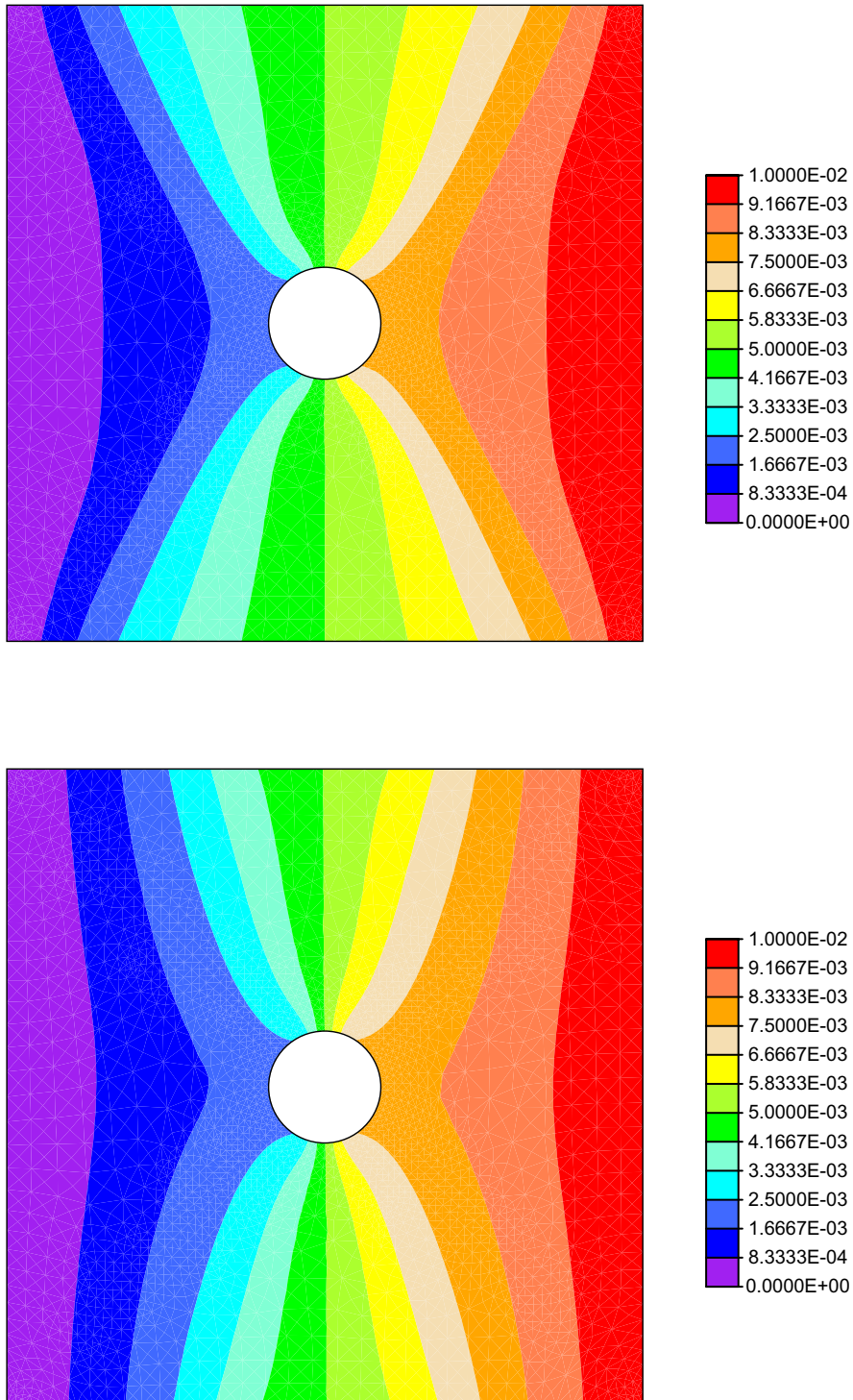


Figure 3.21: Contour plot for the two-scale homogenization problem. Displacements in x -direction at the macrostructure, obtained from the effective model assigned to the microstructure (top) and FE^2 full-scale model (bottom).

$$\frac{1}{2} \int_{\Omega_i} \boldsymbol{\varepsilon}_p : \mathbb{C} : \boldsymbol{\varepsilon}_p d\mathbf{V} = \lambda_i \mathbf{q}_{pi}(\mathbf{e}_{pi}), \quad \text{for } \Omega_i \in \Omega, \quad (3.2.2)$$

Here “:” is the contraction over all components involved, Ω is a suitable parameter space, $\lambda_i \geq 0$ are the volume fractions with $\sum_{i=1}^{N_{sd}} \lambda_i = 1$ and $(\mathbf{q}, \mathbf{q}_p)$ are positive definite quadratic potentials ensuring the next conditions to be fulfilled

$$\boldsymbol{\varepsilon}_M = \mathbf{0} \Rightarrow \boldsymbol{\varepsilon}(\mathbf{x}) = \mathbf{0} \quad \forall \mathbf{x}, \quad \mathbf{e}_{pi} = \mathbf{0} \quad \forall i \Rightarrow \boldsymbol{\varepsilon}_p(\mathbf{x}) = \mathbf{0} \quad \forall \mathbf{x}. \quad (3.2.3)$$

This means that we don't allow strain fluctuations, when the averages are equal to zero. Let us enforce Eq. 3.2.2 by employing a Lagrange multiplier ρ and considering N_{sd} to be the number of sub-domains

$$\begin{aligned} \Psi = \frac{1}{2} \int_{\Omega} (\boldsymbol{\varepsilon} - \boldsymbol{\varepsilon}_p) : \mathbb{C} : (\boldsymbol{\varepsilon} - \boldsymbol{\varepsilon}_p) d\mathbf{V} - \sum_{i=1}^{N_{sd}} \boldsymbol{\sigma}_i : \left(\lambda_i \mathbf{e}_{pi} - \int_{\Omega_i} \boldsymbol{\varepsilon}_p d\mathbf{V} \right) \\ - \sum_{i=1}^{N_{sd}} \rho_i \left(\mathbf{Q}_{pi}(\mathbf{e}_{pi}) - \frac{1}{2} \int_{\Omega_i} \boldsymbol{\varepsilon}_p : \mathbb{C} : \boldsymbol{\varepsilon}_p d\mathbf{V} \right). \end{aligned} \quad (3.2.4)$$

Stationarity with respect to $\boldsymbol{\varepsilon}_p$ returns a uniform stress in each sub-domain as

$$\begin{aligned} \boldsymbol{\sigma}_i &= \mathbb{C} : (\boldsymbol{\varepsilon} - \boldsymbol{\varepsilon}_p) - \rho_i \mathbb{C} : \boldsymbol{\varepsilon}_p = \text{Const.} \quad \text{in } \Omega_i, \\ \boldsymbol{\sigma}_i &= \mathbb{C} : \boldsymbol{\varepsilon} - (1 + \rho_i) \mathbb{C} : \boldsymbol{\varepsilon}_p. \end{aligned} \quad (3.2.5)$$

Averaging over Ω_i gives

$$\mathbb{C}_{Ri} : (\mathbf{e}_i - \mathbf{e}_{pi}) - \rho_i \mathbb{C}_{Ri} : \mathbf{e}_{pi} = \boldsymbol{\sigma}_i. \quad (3.2.6)$$

Recall, the constant stresses in each sub-domain, imply Reuss stiffness \mathbb{C}_{Ri} . Substitute Eq. 3.2.5) into Eq. 3.2.6 and solve for $\boldsymbol{\varepsilon}_p$, we get

$$\boldsymbol{\varepsilon}_p = \frac{1}{1 + \rho_i} (\boldsymbol{\varepsilon} - \mathbb{C}^{-1} : \mathbb{C}_{Ri} : \mathbf{e}_i) + \mathbb{C}^{-1} : \mathbb{C}_{Ri} : \mathbf{e}_{pi}. \quad (3.2.7)$$

The elastic strains can be computed as

$$\boldsymbol{\varepsilon} - \boldsymbol{\varepsilon}_p = \frac{\rho_i}{1 + \rho_i} \boldsymbol{\varepsilon} + \frac{1}{1 + \rho_i} \mathbb{C}^{-1} : \mathbb{C}_{Ri} : \mathbf{e}_i - \mathbb{C}^{-1} : \mathbb{C}_{Ri} : \mathbf{e}_{pi} \quad \text{in } \Omega_i. \quad (3.2.8)$$

Plugging into the free energy gives

$$\begin{aligned}
2\Psi &= \int_{\Omega_i} (\boldsymbol{\varepsilon} - \boldsymbol{\varepsilon}_p) : \mathbb{C} : (\boldsymbol{\varepsilon} - \boldsymbol{\varepsilon}_p) d\mathbf{V}, \\
&= \left(\frac{\rho_i}{1 + \rho_i} \right)^2 \int_{\Omega_i} \boldsymbol{\varepsilon} : \mathbb{C} : \boldsymbol{\varepsilon} d\mathbf{V} + 2\lambda_i \frac{\rho_i}{(1 + \rho_i)^2} \mathbf{e}_i : \mathbb{C}_{Ri} : \mathbf{e}_i \\
&\quad - 2\lambda_i \frac{\rho_i}{1 + \rho_i} \mathbf{e}_i : \mathbb{C}_{Ri} : \mathbf{e}_{pi} + \lambda_i \frac{1}{(1 + \rho_i)^2} \mathbf{e}_i : \mathbb{C}_{Ri} : \mathbf{e}_i \\
&\quad\quad\quad - 2\lambda_i \frac{1}{1 + \rho_i} \mathbf{e}_i : \mathbb{C}_{Ri} : \mathbf{e}_{pi} + \lambda_i \mathbf{e}_{pi} : \mathbb{C}_{Ri} : \mathbf{e}_{pi}, \quad (3.2.9) \\
&= \left(\frac{\rho_i}{1 + \rho_i} \right)^2 \int_{\Omega_i} \boldsymbol{\varepsilon} : \mathbb{C} : \boldsymbol{\varepsilon} d\mathbf{V} + \lambda_i \frac{1 + 2\rho_i}{(1 + \rho_i)^2} \mathbf{e}_i : \mathbb{C}_{Ri} : \mathbf{e}_i \\
&\quad\quad\quad - 2\lambda_i \mathbf{e}_i : \mathbb{C}_{Ri} : \mathbf{e}_{pi} + \lambda_i \mathbf{e}_{pi} : \mathbb{C}_{Ri} : \mathbf{e}_{pi}, \\
&= \left(\frac{\rho_i}{1 + \rho_i} \right)^2 \left[\int_{\Omega_i} \boldsymbol{\varepsilon} : \mathbb{C} : \boldsymbol{\varepsilon} d\mathbf{V} - \lambda_i \mathbf{e}_i : \mathbb{C}_{Ri} : \mathbf{e}_i \right] \\
&\quad\quad\quad + \lambda_i (\mathbf{e}_i - \mathbf{e}_{pi}) : \mathbb{C}_{Ri} : (\mathbf{e}_i - \mathbf{e}_{pi}).
\end{aligned}$$

Finally the effective free energy in terms of the first constraint can be written as

$$\begin{aligned}
\Psi_{\text{macro}} &= \frac{1}{2} \sum_{i=1}^{N_{\text{sd}}} \lambda_i (\mathbf{e}_i - \mathbf{e}_{pi}) : \mathbb{C}_{Ri} : (\mathbf{e}_i - \mathbf{e}_{pi}) \\
&\quad\quad\quad + \sum_{i=1}^{N_{\text{sd}}} \left(\frac{\rho_i}{1 + \rho_i} \right)^2 \lambda_i \left[\mathbf{q}_i(\mathbf{e}_i) - \frac{1}{2} \mathbf{e}_i : \mathbb{C}_{Ri} : \mathbf{e}_i \right]. \quad (3.2.10)
\end{aligned}$$

In a similar manner and making use of Eq. 3.2.7 we get

$$\begin{aligned}
\int_{\Omega_i} \boldsymbol{\varepsilon}_p : \mathbb{C} : \boldsymbol{\varepsilon}_p d\mathbf{V} &= \left(\frac{1}{1 + \rho_i} \right)^2 \int_{\Omega_i} \boldsymbol{\varepsilon} : \mathbb{C} : \boldsymbol{\varepsilon} d\mathbf{V} - 2\lambda_i \frac{1}{(1 + \rho_i)^2} \mathbf{e}_i : \mathbb{C}_{Ri} : \mathbf{e}_i \\
&\quad + 2\lambda_i \frac{1}{1 + \rho_i} \mathbf{e}_i : \mathbb{C}_{Ri} : \mathbf{e}_{pi} + \lambda_i \frac{1}{(1 + \rho_i)^2} \mathbf{e}_i : \mathbb{C}_{Ri} : \mathbf{e}_i \\
&\quad\quad\quad - 2\lambda_i \frac{1}{1 + \rho_i} \mathbf{e}_i : \mathbb{C}_{Ri} : \mathbf{e}_{pi} + \lambda_i \mathbf{e}_{pi} : \mathbb{C}_{Ri} : \mathbf{e}_{pi}, \\
&= \left(\frac{1}{1 + \rho_i} \right)^2 \left[\int_{\Omega_i} \boldsymbol{\varepsilon} : \mathbb{C} : \boldsymbol{\varepsilon} d\mathbf{V} - \lambda_i \mathbf{e}_i : \mathbb{C}_{Ri} : \mathbf{e}_i \right] \\
&\quad\quad\quad + \lambda_i \mathbf{e}_{pi} : \mathbb{C}_{Ri} : \mathbf{e}_{pi}. \quad (3.2.11)
\end{aligned}$$

Rearranging, the second constraint in Eq. 3.2.2 can be formulated

$$\begin{aligned}
\left(\frac{1}{1 + \rho_i} \right)^2 \left[\int_{\Omega_i} \boldsymbol{\varepsilon} : \mathbb{C} : \boldsymbol{\varepsilon} d\mathbf{V} - \lambda_i \mathbf{e}_i : \mathbb{C}_{Ri} : \mathbf{e}_i \right] &= \\
2\lambda_i \mathbf{q}_{pi}(\mathbf{e}_{pi}) - \lambda_i \mathbf{e}_{pi} : \mathbb{C}_{Ri} : \mathbf{e}_{pi}. \quad (3.2.12)
\end{aligned}$$

To evaluate the used Lagrange-multipliers ρ_i , we introduce the abbreviations

$$\Psi_{0i}(\mathbf{a}_i) = \frac{1}{2} \mathbf{a}_i : \mathbb{C}_{Ri} : \mathbf{a}_i, \quad \Psi_0 = \sum_{i=1}^{N_{\text{sd}}} \lambda_i \Psi_{0i}. \quad (3.2.13)$$

Giving

$$\rho_i = \left[\frac{\mathbf{q}_i(\mathbf{e}_i) - \Psi_{0i}(\mathbf{e}_i)}{\mathbf{q}_{pi}(\mathbf{e}_{pi}) - \Psi_{0i}(\mathbf{e}_{pi})} \right]^{\frac{1}{2}} - 1, \quad (3.2.14)$$

and

$$\frac{\rho_i}{1 + \rho_i} = 1 - \left[\frac{\mathbf{q}_{pi}(\mathbf{e}_{pi}) - \Psi_{0i}(\mathbf{e}_{pi})}{\mathbf{q}_i(\mathbf{e}_i) - \Psi_{0i}(\mathbf{e}_i)} \right]^{\frac{1}{2}}. \quad (3.2.15)$$

Plugging Eqs. 3.2.14 and 3.2.15 into Eq. 3.2.10 we get the macroscopic energy to be

$$\begin{aligned} \Psi_{\text{macro}} &= \Psi_0(\mathbf{e}_i - \mathbf{e}_{pi}) + \sum_{i=1}^{N_{sd}} \lambda_i \left(\mathbf{q}_i(\mathbf{e}_i) - \Psi_{0i}(\mathbf{e}_i) \right) \quad (3.2.16) \\ &\quad \left[1 - 2 \left(\frac{\mathbf{q}_{pi}(\mathbf{e}_{pi}) - \Psi_{0i}(\mathbf{e}_{pi})}{\mathbf{q}_i(\mathbf{e}_i) - \Psi_{0i}(\mathbf{e}_i)} \right)^{\frac{1}{2}} + \frac{\mathbf{q}_{pi}(\mathbf{e}_{pi}) - \Psi_{0i}(\mathbf{e}_{pi})}{\mathbf{q}_i(\mathbf{e}_i) - \Psi_{0i}(\mathbf{e}_i)} \right], \\ &= \Psi_0(\mathbf{e}_i - \mathbf{e}_{pi}) + \sum_{i=1}^{N_{sd}} \lambda_i [\mathbf{q}_i(\mathbf{e}_i) + \mathbf{q}_{pi}(\mathbf{e}_{pi}) - \Psi_{0i}(\mathbf{e}_i) - \Psi_{0i}(\mathbf{e}_{pi})] \\ &\quad - 2 \sum_{i=1}^{N_{sd}} \lambda_i \left[\left(\mathbf{q}_i(\mathbf{e}_i) - \Psi_{0i}(\mathbf{e}_i) \right)^{\frac{1}{2}} \left(\mathbf{q}_{pi}(\mathbf{e}_{pi}) - \Psi_{0i}(\mathbf{e}_{pi}) \right)^{\frac{1}{2}} \right]. \end{aligned}$$

Let us redefine the quadratic potentials (in the last energy equation) in terms of the averages by the following

$$\mathbf{q}_{pi} = \Psi_{0i}(\mathbf{e}_{pi}) = \frac{1}{2} \mathbf{e}_{pi} : \mathbb{C}_{Ri} : \mathbf{e}_{pi}, \quad (3.2.17)$$

$$\mathbf{q}_i = \Psi_{0i}(\mathbf{e}_i) = \frac{1}{2} \mathbf{e}_i : \mathbb{A}_i : \mathbf{e}_i. \quad (3.2.18)$$

To define the tensor \mathbb{A}_i , we can compute the macroscopic stresses by differentiating the macroscopic energy with respect to the averaged strains

$$\begin{aligned} \boldsymbol{\sigma}_M &= \mathbb{A}_i : \mathbf{e}_i - \mathbb{C}_{Ri} : \mathbf{e}_{pi} = \mathbb{A}_{eff} : \left(\mathbf{e}_M - \sum_{i=1}^{N_{sd}} \lambda_i \mathbb{A}_i^{-1} : \mathbb{C}_{Ri} : \mathbf{e}_{pi} \right), \\ &= \mathbb{A}_{eff} : (\mathbf{e}_M - \mathbf{e}_{pM}). \end{aligned} \quad (3.2.19)$$

Here \mathbb{A}_{eff} is the effective stiffness, and \mathbf{e}_{pM} is the averaged plastic strain computed according to the next relations

$$\mathbb{A}_{eff} = \left(\sum_{i=1}^{N_{sd}} \lambda_i \mathbb{A}_i^{-1} \right)^{-1}, \quad \mathbf{e}_{pM} = \sum_{i=1}^{N_{sd}} \lambda_i \mathbb{A}_i^{-1} : \mathbb{C}_{Ri} : \mathbf{e}_{pi}. \quad (3.2.20)$$

Notice that the macroscopic stress reduces in the elastic case to

$$\boldsymbol{\sigma}_M = \mathbb{A}_i : \mathbf{e}_i = \mathbb{A}_{eff} : \mathbf{e}_M. \quad (3.2.21)$$

Now, let \mathbb{B} be the strain-concentration tensor, given by the solution of the elastic boundary value problem defined as

$$\boldsymbol{\varepsilon}(\mathbf{x}) = \mathbb{B}(\mathbf{x}) : \mathbf{e}_M, \quad (3.2.22)$$

then we obtain the macroscopic stresses

$$\boldsymbol{\sigma}_M = \langle \mathbb{C}(\mathbf{x}) : \boldsymbol{\varepsilon}(\mathbf{x}) \rangle = \langle \mathbb{C}(\mathbf{x}) : \mathbb{B}(\mathbf{x}) \rangle : \mathbf{e}_M = \mathbb{A}_i : \langle \mathbb{B} \rangle_i : \mathbf{e}_M, \quad (3.2.23)$$

with

$$\mathbf{e}_i = \langle \mathbb{B} \rangle_i : \mathbf{e}_M, \quad \mathbb{A}_{eff} = \langle \mathbb{C} : \mathbb{B} \rangle, \quad \mathbb{A}_i = \mathbb{A}_{eff} : \langle \mathbb{B} \rangle_i^{-1},$$

and the brackets $\langle \rangle$ are used for averaging. The effective stiffness appearing in Eq. 3.2.23(2) returns the exact elastic stiffness through the influence of the strain concentration tensor \mathbb{B} . The derivation of its components as per Eq. 3.2.22 will be discussed later on in the numerical preparation section. The importance of the concentration tensor is that it shifts the burden from finding \mathbb{C} , now approximated by Reuss-stiffness, into finding the concentration tensor \mathbb{B} resulting from the solution of an elastic problem. This appeared in the literature for example in the works of (Zohdi and Wriggers 2001) and (Parnell 2016). Let us plug \mathbb{A} tensor into the macroscopic energy

$$\begin{aligned} \Psi_{\text{macro}} &= \frac{1}{2} \sum_{i=1}^{N_{\text{sd}}} \lambda_i \mathbf{e}_i : \mathbb{A}_i : \mathbf{e}_i + \frac{1}{2} \sum_{i=1}^{N_{\text{sd}}} \lambda_i (\mathbf{e}_i - \mathbf{e}_{pi}) : \mathbb{C}_{Ri} : (\mathbf{e}_i - \mathbf{e}_{pi}) \\ &\quad - \frac{1}{2} \sum_{i=1}^{N_{\text{sd}}} \lambda_i \mathbf{e}_i : \mathbb{C}_{Ri} : \mathbf{e}_i, \end{aligned} \quad (3.2.24)$$

giving the stresses per each sub-domain to be

$$\begin{aligned} \boldsymbol{\sigma}_i &= (\mathbb{A}_i - \mathbb{C}_{Ri}) : \mathbf{e}_i + \mathbb{C}_{Ri} : (\mathbf{e}_i - \mathbf{e}_{pi}), \\ \boldsymbol{\sigma}_i &= \mathbb{A}_i : \mathbf{e}_i - \mathbb{C}_{Ri} : \mathbf{e}_{pi}. \end{aligned} \quad (3.2.25)$$

Multiplying both sides from the left hand side with \mathbb{A}_i^{-1} , we get

$$\mathbb{A}_i^{-1} : \boldsymbol{\sigma}_i = \mathbf{e}_i - \mathbb{A}_i^{-1} : \mathbb{C}_{Ri} : \mathbf{e}_{pi}. \quad (3.2.26)$$

Averaging gives,

$$\begin{aligned} \mathbb{A}_{\text{eff}}^{-1} : \boldsymbol{\sigma} &= \mathbf{e}_M - \sum_{i=1}^{N_{\text{sd}}} \lambda_i \mathbb{A}_i^{-1} : \mathbb{C}_{Ri} : \mathbf{e}_{pi}, \\ \Leftrightarrow \boldsymbol{\sigma} &= \mathbb{A}_{\text{eff}} : \mathbf{e}_M - \mathbb{A}_{\text{eff}} : \sum_{i=1}^{N_{\text{sd}}} \lambda_i \mathbb{A}_i^{-1} : \mathbb{C}_{Ri} : \mathbf{e}_{pi}. \end{aligned} \quad (3.2.27)$$

Substituting the value of σ in Eq. 3.2.26 and evaluating for \mathbf{e}_i gives

$$\begin{aligned} \mathbf{e}_i = \mathbb{A}_i^{-1} : \mathbb{C}_{Ri} : \mathbf{e}_{pi} + \mathbb{A}_i^{-1} : \mathbb{A}_{\text{eff}} : \mathbf{e}_M \\ - \mathbb{A}_i^{-1} : \mathbb{A}_{\text{eff}} : \sum_{j=1}^{N_{\text{sd}}} \lambda_j \mathbb{A}_j^{-1} : \mathbb{C}_{Rj} : \mathbf{e}_{pj}. \end{aligned} \quad (3.2.28)$$

We can now evaluate the quadratic terms obtained in Eq. 3.2.24

$$\begin{aligned} \sum_{i=1}^{N_{\text{sd}}} \lambda_i \mathbf{e}_i : \mathbb{A}_i : \mathbf{e}_i = \sum_{i=1}^{N_{\text{sd}}} \lambda_i \mathbf{e}_{pi} : \mathbb{C}_{Ri} : \mathbb{A}_i^{-1} : \mathbb{C}_{Ri} : \mathbf{e}_{pi} \\ + 2 \sum_{i=1}^{N_{\text{sd}}} \lambda_i \mathbf{e}_{pi} : \mathbb{C}_{Ri} : \mathbb{A}_i^{-1} : \mathbb{C}_{Ri} : \mathbf{e}_M \\ - 2 \sum_{i=1}^{N_{\text{sd}}} \lambda_i \mathbf{e}_{pi} : \mathbb{C}_{Ri} : \mathbb{A}_i^{-1} : \mathbb{A}_{\text{eff}} : \sum_{j=1}^{N_{\text{sd}}} \lambda_j \mathbb{A}_j^{-1} : \mathbb{C}_{Rj} : \mathbf{e}_{pj} \\ + \mathbf{e}_M : \mathbb{A}_{\text{eff}} : \mathbf{e}_M - 2 \mathbf{e}_M : \mathbb{A}_{\text{eff}} : \sum_{j=1}^{N_{\text{sd}}} \lambda_j \mathbb{A}_j^{-1} : \mathbb{C}_{Rj} : \mathbf{e}_{pj} \\ + \left(\sum_{j=1}^{N_{\text{sd}}} \lambda_j \mathbb{A}_j^{-1} : \mathbb{C}_{Rj} : \mathbf{e}_{pj} \right) : \mathbb{A}_{\text{eff}} : \sum_{k=1}^{N_{\text{sd}}} \lambda_k \mathbb{A}_k^{-1} : \mathbb{C}_{Rk} : \mathbf{e}_{pk}, \end{aligned} \quad (3.2.29)$$

$$\begin{aligned} \sum_{i=1}^{N_{\text{sd}}} \lambda_i \mathbf{e}_i : \mathbb{C}_{Ri} : \mathbf{e}_{pi} = \sum_{i=1}^{N_{\text{sd}}} \lambda_i \mathbf{e}_{pi} : \mathbb{C}_{Ri} : \mathbb{A}_i^{-1} : \mathbb{C}_{Ri} : \mathbf{e}_{pi} \\ + \sum_{i=1}^{N_{\text{sd}}} \lambda_i \mathbf{e}_{pi} : \mathbb{C}_{Ri} : \mathbb{A}_i^{-1} : \mathbb{A}_{\text{eff}} : \mathbf{e}_M \\ - \sum_{i=1}^{N_{\text{sd}}} \lambda_i \mathbf{e}_{pi} : \mathbb{C}_{Ri} : \mathbb{A}_i^{-1} : \mathbb{A}_{\text{eff}} : \sum_{j=1}^{N_{\text{sd}}} \lambda_j \mathbb{A}_j^{-1} : \mathbb{C}_{Rj} : \mathbf{e}_{pj}. \end{aligned} \quad (3.2.30)$$

The thermodynamically driving force can be computed as follows

$$\begin{aligned} \sigma_i = \mathbf{q}_i = - \frac{1}{\lambda_i} \frac{\partial \Psi}{\partial \mathbf{e}_{pi}}, \\ = \mathbb{C}_{Ri} : \mathbb{A}_i^{-1} : \mathbb{A}_{\text{eff}} : (\mathbf{e}_M - \mathbf{e}_{pM}) - \mathbb{C}_{Ri} : (\mathbb{C}_{Ri}^{-1} - \mathbb{A}_i^{-1}) : \mathbb{C}_{Ri} : \mathbf{e}_{pi}. \end{aligned} \quad (3.2.31)$$

We substitute and rearrange to get the final set of equations that will be used in the numerical computations.

$$\begin{aligned} \Psi_{\text{macro}} = & \frac{1}{2} (\mathbf{e}_M - \mathbf{e}_{pM}) : \mathbb{A}_{\text{eff}} : (\mathbf{e}_M - \mathbf{e}_{pM}) \\ & + \frac{1}{2} \sum_{i=1}^{N_{\text{sd}}} \lambda_i \mathbf{e}_{pi} : (\mathbb{C}_{Ri} - \mathbb{C}_{Ri} : \mathbb{A}_i^{-1} : \mathbb{C}_{Ri}) : \mathbf{e}_{pi}, \end{aligned} \quad (3.2.32)$$

$$\boldsymbol{\sigma}_i = \mathbb{C}_{Ri} : \mathbb{A}_i^{-1} : \mathbb{A}_{\text{eff}} : (\mathbf{e}_M - \mathbf{e}_{pM}) - \mathbb{C}_{Ri} : (\mathbb{C}_{Ri}^{-1} - \mathbb{A}_i^{-1}) : \mathbb{C}_{Ri} : \mathbf{e}_{pi}, \quad (3.2.33)$$

$$\mathbf{e}_i = \langle \mathbb{B} \rangle_i : \mathbf{e}_M, \quad (3.2.34)$$

$$\mathbb{A}_{\text{eff}} = \langle \mathbb{C} : \mathbb{B} \rangle, \quad \mathbb{A}_i = \mathbb{A}_{\text{eff}} : \langle \mathbb{B} \rangle_i^{-1}. \quad (3.2.35)$$

3.2.2 Numerical preparation

In order to show the enhancement achieved by the second reduced model RM_2 in comparison to RM_1 , we consider for the numerical examples the same material parameters as before, i.e. (Mat_1) $E_1 = 1000 \text{ N/mm}^2$, $\nu_1 = 0.25$, $\sigma_{y1} = 1.5 \text{ N/mm}^2$; (Mat_2) $E_2 = 2500 \text{ N/mm}^2$, $\nu_2 = 0.3$, $\sigma_{y2} = 2.0 \text{ N/mm}^2$; and (Mat_3) $E_3 = 5000 \text{ N/mm}^2$, $\nu_3 = 0.15$, $\sigma_{y3} = 3.75 \text{ N/mm}^2$. We compute the composites with the square and octagon inclusions as in Sections 3.1.7 and 3.1.8 and then consider additional examples, which are only possible to compute with the second reduced model. Therefore, we consider the same cyclic loading path as shown in Fig. 3.9.

For the finite element results, representing the exact solution, we employ Hill-Mandel homogenization scheme, as given earlier. Very fine meshes per each sub-domain are employed in order to capture the inhomogeneities of the microstructure. Therefore, the polyhedral RVE is provided with (40x40) quadratic quadrilateral elements (9-nodes elements) per each sub-domain, whereas the RVE with the octagon center inclusion has 6400 elements (quadratic quadrilaterals) at the center and (40x40) quadratic elements for the other inclusions. Beside the exact finite element solution, we need for the implementation of the second reduced model RM_2 , the components of the strain concentration tensor \mathbb{B}_i for each sub-domain. This allows to write the averaged strains per each sub-domain \mathbf{e}_i , which can be achieved by running three elastic finite element calculations (only one time-step each). It is the case due to the plane strain state leaving only three nontrivial components for the strain tensor to be identified. Let us write Eq. 3.2.22 in index notations

$$\begin{aligned} \mathbf{e}_{11} = 1\mathbf{e}_1 \otimes \mathbf{e}_1, & \implies \boldsymbol{\varepsilon}_{ij}(\mathbf{x}) = \mathbb{B}_{ij11}(\mathbf{x})1, \\ \mathbf{e}_{22} = 1\mathbf{e}_2 \otimes \mathbf{e}_2, & \implies \boldsymbol{\varepsilon}_{ij}(\mathbf{x}) = \mathbb{B}_{ij22}(\mathbf{x})1, \\ \mathbf{e}_{12} = 1\mathbf{e}_1 \otimes \mathbf{e}_2, & \implies \boldsymbol{\varepsilon}_{ij}(\mathbf{x}) = \mathbb{B}_{ij12}(\mathbf{x})1. \end{aligned} \quad (3.2.36)$$

Then the components of \mathbb{B}_i are obtained from the three arising strains per each sub-domain (notice the dependence on the position \mathbf{x}). Meaning that each strain

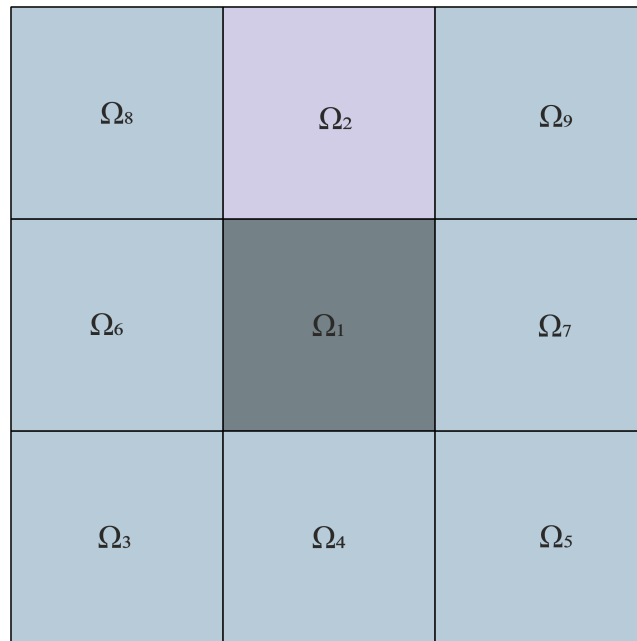


Figure 3.22: Representative volume element with 9 sub-domains under periodic boundary conditions. Mat_1 is assigned to the center inclusion, Mat_2 is assigned to sub-domain Ω_2 and Mat_3 is assigned to the matrix elsewhere.

contributes to a column in \mathbb{B}_i at the corresponding position. No more amplitude vectors shall be computed here as required in RM_1 removing the restriction by the implementation to the polyhedral sub-domains.

3.2.3 RVE with square center inclusion

This example consists of 9 different sub-domains with uniform distribution, i.e. the same volume fractions $|\Omega_i|/|\Omega| = 1/9$. Three isotropic elastoplastic materials are assigned to the domains as shown in Fig. 3.22.

The averaged response is compared to the response from the first reduced model and a macroscopic response from the finite element analysis associated with a much higher number of degrees of freedom, refer to Fig. 3.23.

It is obvious that the second reduced model shows a very good agreement with the finite element solution. Not only in the elastic phase, which is now exactly matching, but even the plastic phase after yielding is properly represented by the reduced model RM_2 . At the same time, a comparison of the plastic strains averaged over Mat_1 and Mat_2 in sub-domains Ω_1 and Ω_2 respectively, as given in Fig. 3.24, shows that the reduced model is not capturing the exact behavior of the plastic strains at the correct position. It can be interpreted that the averaged plastic strains are combined at the neighboring sub-domains, which implies a different mean value in comparison to the exact solution from the finite element computations. Therefore, as long as the macroscopic response is not influenced, we might say that plastic yielding is well represented but its exact distribution is not.

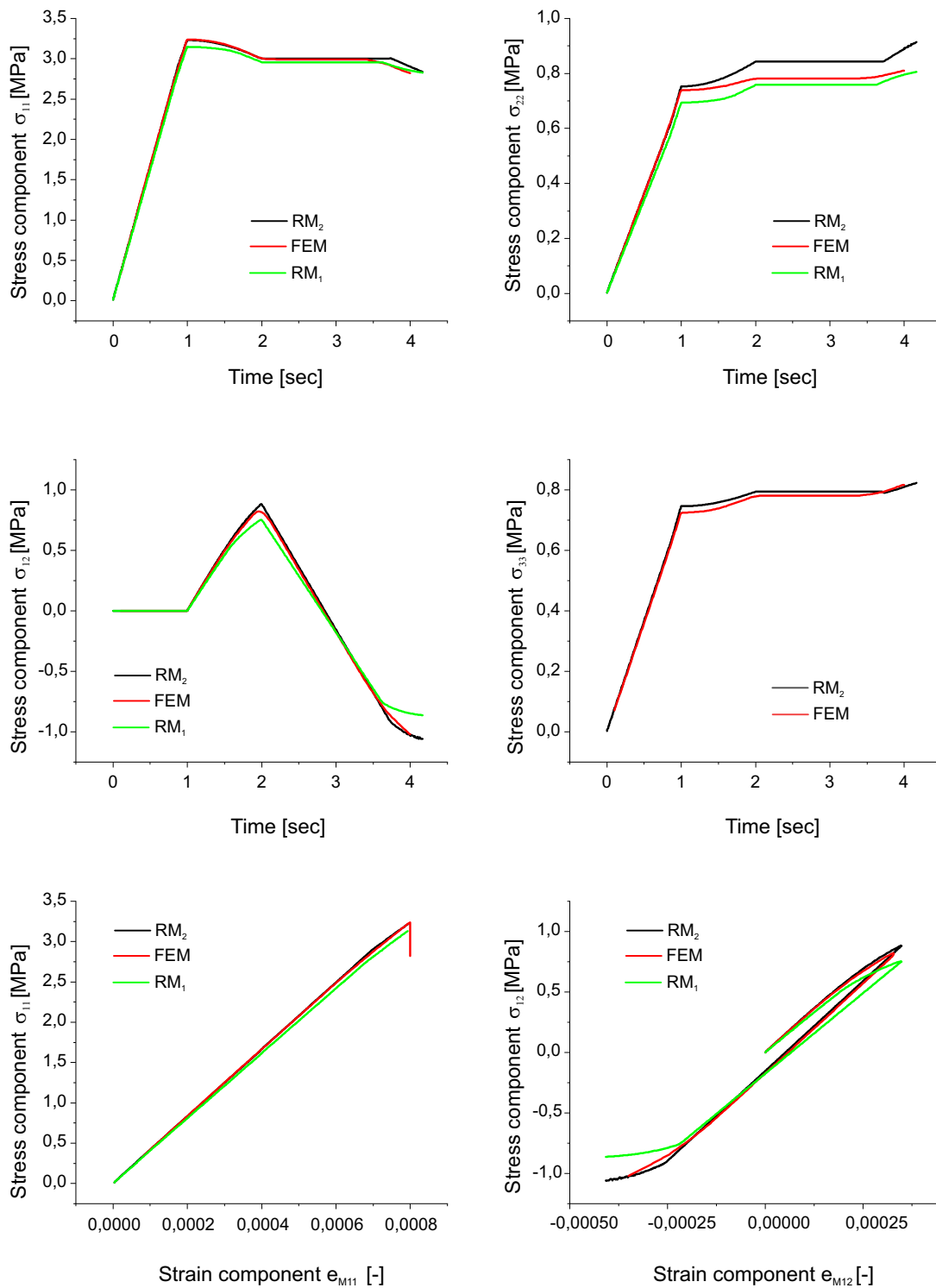


Figure 3.23: Comparison of the effective models RM_1 , RM_2 and a finite element model for the square inclusion RVE. Macroscopic stresses versus time (top row and middle pane). Stress-strain response for the normal stress and strain in the 1-direction and the shear stress and strain in the 1-2 plane (bottom row).

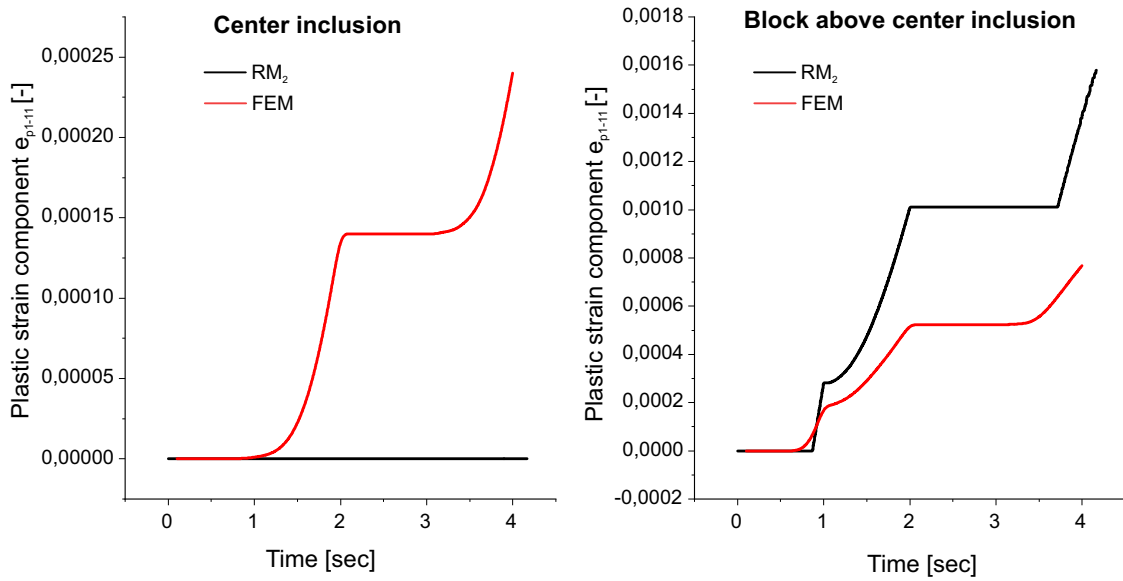


Figure 3.24: Illustration of the plastic strain from RM_2 , averaged over Mat_1 at the center inclusion and Mat_2 at sub-domain Ω_2 , in comparison to the finite element results.

3.2.4 RVE with octagon center inclusion

Here we have a bigger center inclusion with a volume fraction of $|\Omega_1|/|\Omega| = 0.1768$ and the other volume fractions have the value $\lambda_i = 0.1029$ for $i = 2, \dots, 9$. Material assignment to the different sub-domains can be inferred from Fig. 3.25. We can make the same positive conclusion after comparing the macroscopic stress behavior to the one from the first reduced model and the finite element computations. See Fig. 3.26. A very good compliance is achieved by the second reduced model even in terms of the second component of the macroscopic stress, in the first row to the right, which shows a large deviation to the exact solution for the results from the first reduced model.

On the other hand, the comparison of the mean plastic strains at sub-domains Ω_1 and Ω_2 would emphasize the last conclusion (the combined values at the neighboring sub-domains). See Fig. 3.27. As the bigger size of the center inclusion (the octagon) allowed to show some values of the initiated plastic strain, and is not only vanishing as was the case for the square center inclusion. In contrary to the center inclusion, the results from sub-domain Ω_2 show higher values for the averaged plastic strains. These are influenced by the arising plastic strains distributed over the surrounding inclusions associated with Mat_3 .

A drawback beyond the first reduced model RM_1 was the capability of prescribing microstructure with curved edges. However, the second reduced model RM_2 with the higher order restraints added to the energy potential, allowed to overcome this problem. Therefore, we investigate in the next examples microstructure with elliptical inclusions.

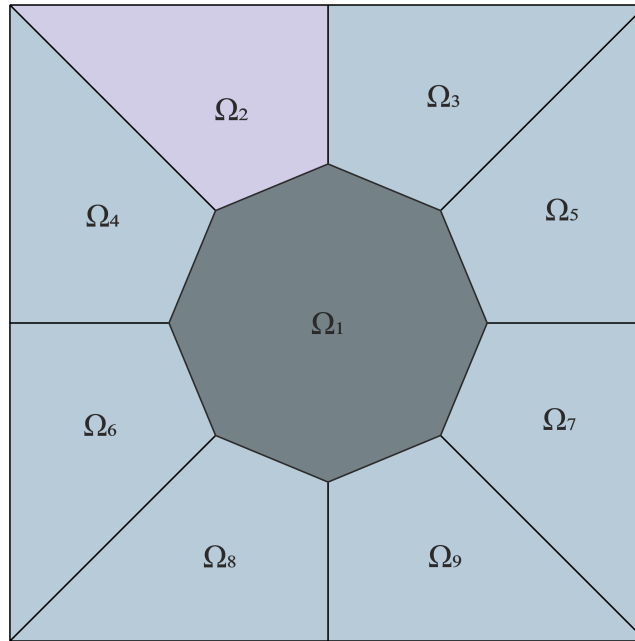


Figure 3.25: Representative volume element with an octagon center inclusion. Mat_1 is assigned to the octagon, Mat_2 is assigned to sub-domain Ω_2 and Mat_3 is assigned to the matrix elsewhere.

3.2.5 RVE with ellipse center inclusion

Now we consider a more general case, where the RVE is split into 9 non-uniform sub-domains. Consisting of an elliptical center inclusion and different volumes for the other inclusions within the matrix. The volume fractions for the different inclusions are given as follows $\lambda_1 = 0.1619$, $\lambda_{2,4,5,9} = 0.1222$ and $\lambda_{3,6,7,8} = 0.0874$. See Fig. 3.28 for an illustration of the sub-divisions and the material allocations.

The finite element solution is obtained by assigning 9600 quadratic quadrilateral elements (9-nodes elements) to the ellipse and 40×40 elements to each other sub-domain. Employing a finite element problem with 179198 degrees of freedom to provide the exact solution. This is then compared to the reduced scale problem (only 9 sub-domains) computed according to RM_2 .

The resulting macroscopic stresses and the macroscopic response are shown in Fig. 3.29. The solution from the reduced model matches the exact solution to a very large extent. We notice that all the tangents and the peaks are properly captured in all the curves, whether in the elastic or the plastic zones.

Even the mean plastic strains averaged over materials Mat_1 and Mat_2 are well represented, see Fig. 3.30. From the curves to the left, we notice that yielding in the center inclusion is shown from the finite element solution earlier than the one from the reduced model RM_2 . At the same time the values from the reduced model, in the neighboring sub-domain Ω_2 , are higher than the ones from the exact solution. Meaning that a sum of the mean values from both sub-domains would imply the exact mean value for the plastic strain. Nevertheless, the reduced scale model with much less number of degrees of freedom is not able to express the exact distribution.

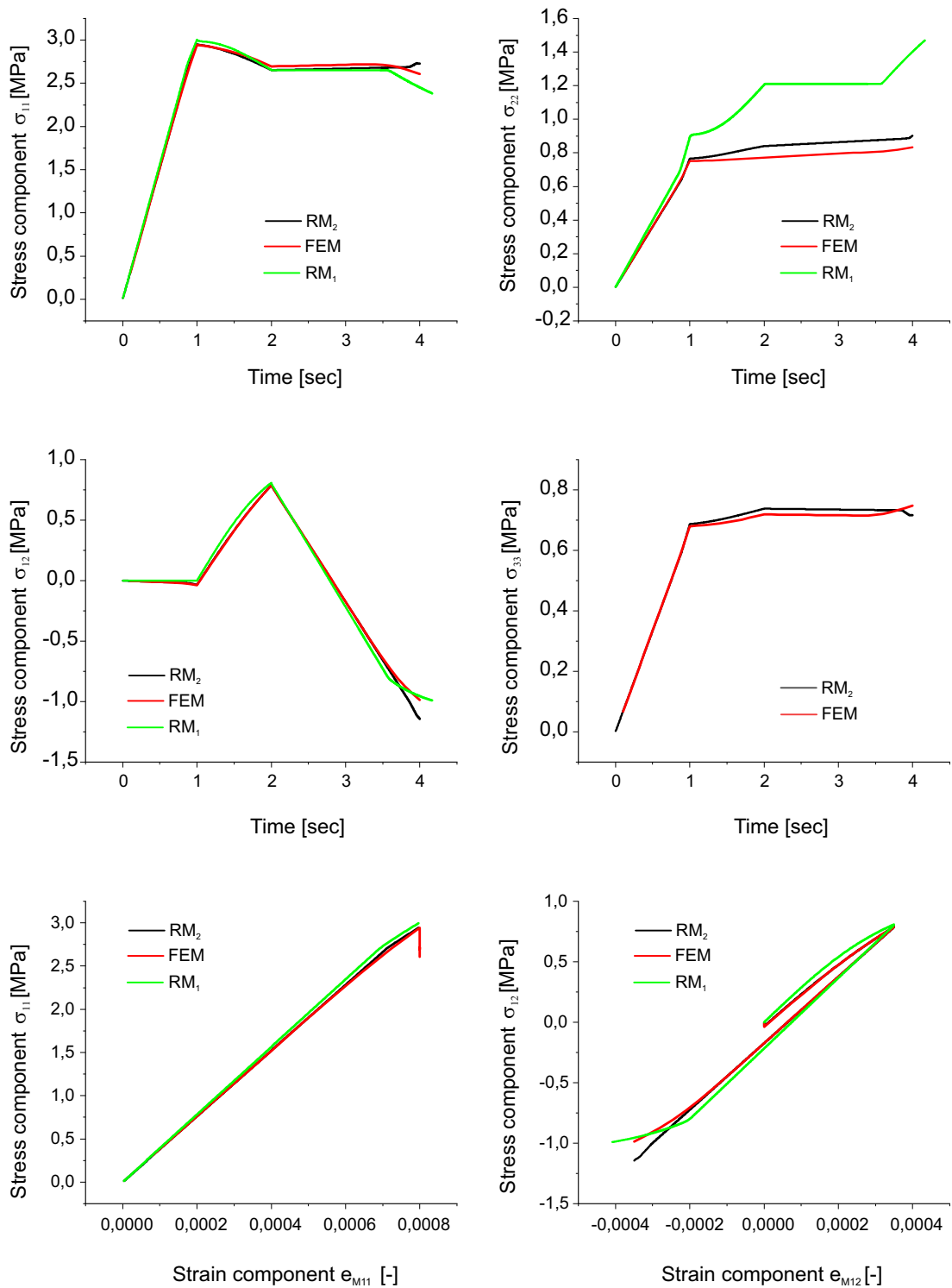


Figure 3.26: Comparison of the effective models RM_1 , RM_2 and a finite element model for the RVE with an octagon center inclusion. Macroscopic stresses versus time (top row and middle pane). Stress-strain response for the normal stress and strain in the 1-direction and the shear stress and strain in the 1-2 plane (bottom row).

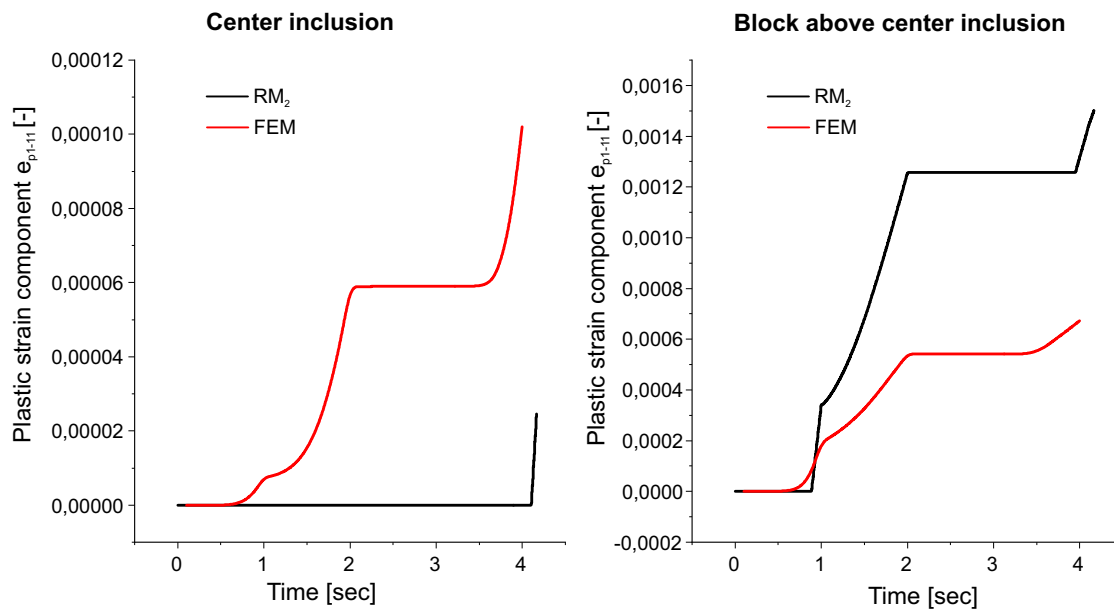


Figure 3.27: Illustration of the plastic strain from RM_2 , averaged over Mat_1 at the octagon inclusion and over Mat_2 at sub-domain Ω_2 , in comparison to the finite element results.

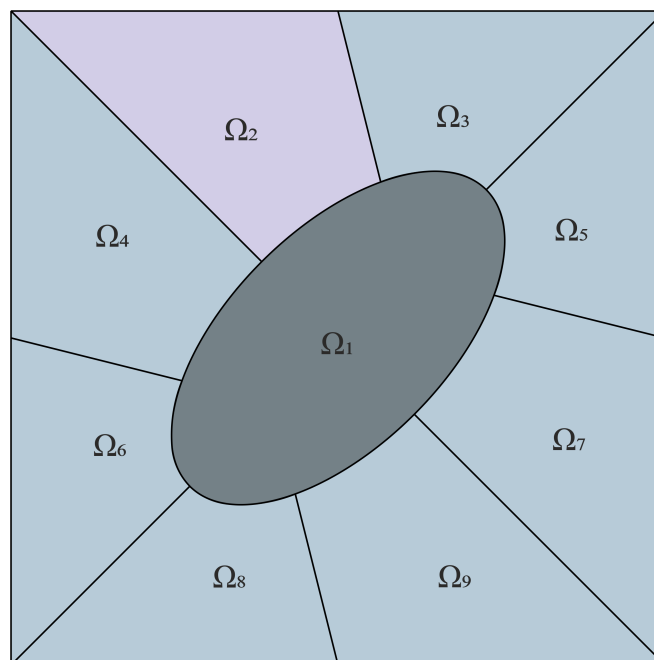


Figure 3.28: Representative volume element with an elliptical center inclusion. Mat_1 is assigned to the ellipse, Mat_2 is assigned to sub-domain Ω_2 and Mat_3 is assigned to the matrix elsewhere.

3.2.6 RVE with random inclusions

The last example is extended in a way that more elliptical inclusions are inserted. See Fig. 3.31. We consider 13 sub-domains, with Mat_1 assigned to the octagon center inclusion and Mat_2 assigned to the ellipses ($\Omega_2, \dots, \Omega_7$) and Mat_3 assigned to the rest of the matrix ($\Omega_8, \dots, \Omega_{13}$). Notice that the reduced scale solution requires for each ellipse the corresponding components of the strain concentration tensor ($\mathbb{B}_2, \dots, \mathbb{B}_7$), despite the same material assignment. The reduced model is computed in this example with the following volume fractions $\lambda_1 = 0.0509$, $\lambda_{2,\dots,8} = 0.0307$, $\lambda_{8,9,11,12} = 0.1386$ and $\lambda_{10,13} = 0.1051$.

For the reference solution derived from the finite element analysis we split the octagon into 1600 elements, each ellipse into 800 elements, sub-domains $\Omega_{10,13}$ into 3200 elements and sub-domains $\Omega_{8,9,11,12}$ into 5600 elements producing a total number of 35200 quadratic quadrilateral elements (9-nodes elements), which shall return a very accurate solution. Three isotropic elastoplastic materials are assigned, as mentioned before, and Hill-Mandel homogenization scheme is applied. The macroscopic stresses are averaged over the whole domain Ω and the mean plastic strains are averaged per each material, i.e. over sub-domain Ω_1 for Mat_1 and over sub-domains $\Omega_2, \dots, \Omega_7$ for Mat_2 and over the remaining sub-domains for Mat_3 .

A comparison between the macroscopic stresses from the reduced model RM_2 and their counterparts from the finite element implementation shows a very good agreement, see Fig. 3.33.

On the other hand, the comparison between the mean plastic strains averaged over the different materials with the mean values from the finite element solution, as seen in Fig. 3.32, shows a weakly presented behavior. Once again the mean plastic strain at the center inclusion is vanishing and the values in the neighboring sub-domains associated with Mat_2 are higher than the mean values from the exact solution. Assisting our understanding in terms of the gathered values for the mean plastic strains.

3.2.7 Conclusion - RM_2

In this section we extended the first reduced model RM_1 defined in Sec. 3.1. Employing higher order moments, we are able to deliver the exact effective stiffness in the elastic phase due to the contribution of the strain concentration tensors. Another considerable enhancement in comparison to the first reduced model is the applicability to microstructure with curved edges.

By means of several numerical examples, we proved that the reduced model is capable of describing the macroscopic behavior of the different RVEs successfully in terms of the macroscopic stress-strain behavior. Nevertheless, the drawback of the first reduced model in representing the essential internal variables is still persisting.

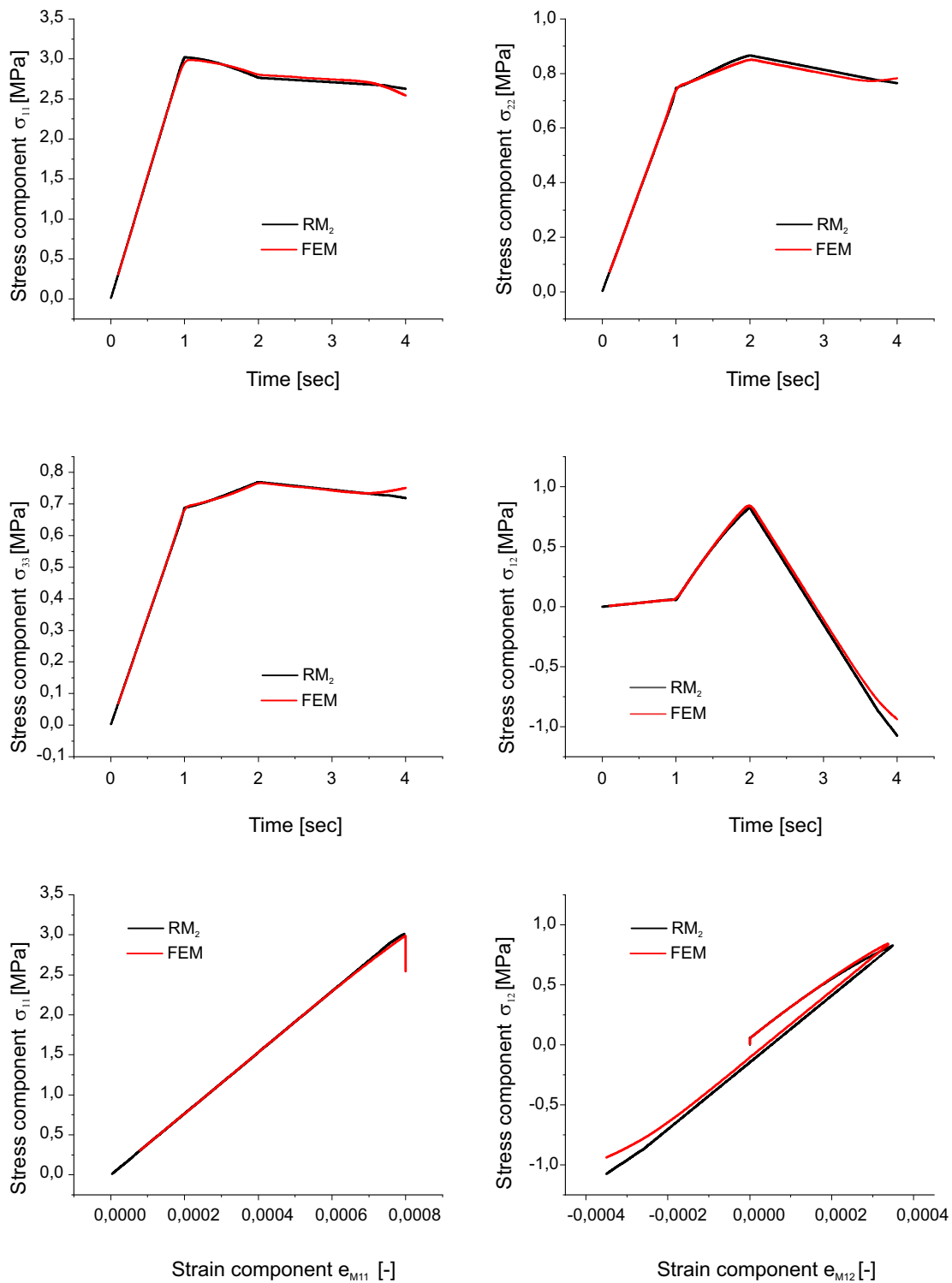


Figure 3.29: Comparison of the effective model RM_2 and a finite element model for the RVE with an elliptical center inclusion. Macroscopic stresses versus time (top row and middle pane). Stress-strain response for the normal stress and strain in the 1-direction and the shear stress and strain in the 1-2 plane (bottom row).

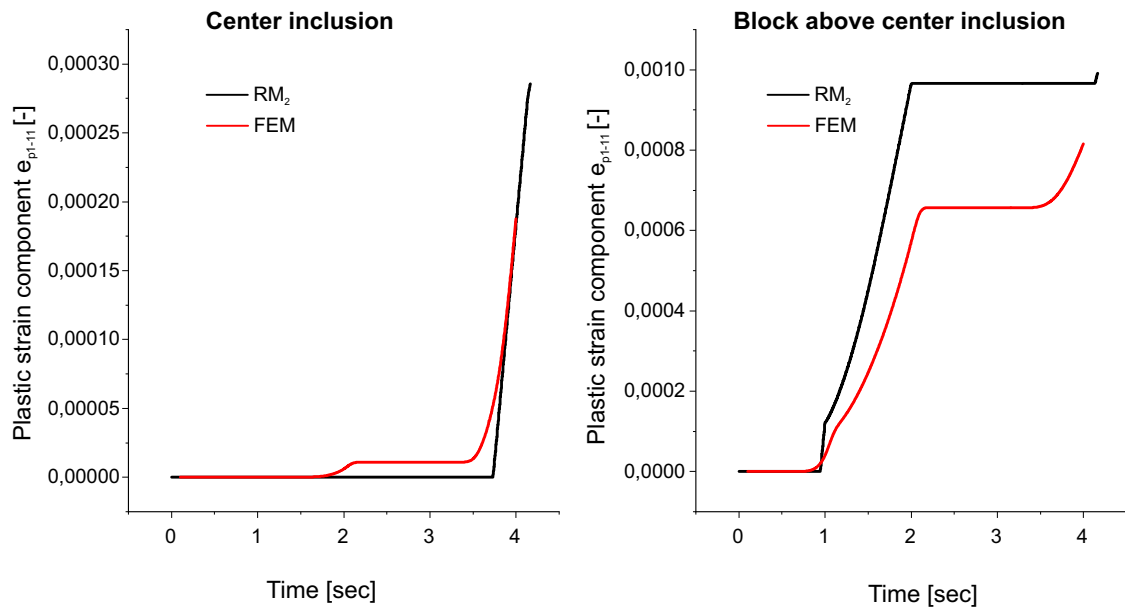


Figure 3.30: Illustration of the plastic strain from RM_2 , averaged over Mat_1 at the elliptical inclusion and over Mat_2 at sub-domain Ω_2 , in comparison to the finite element results.

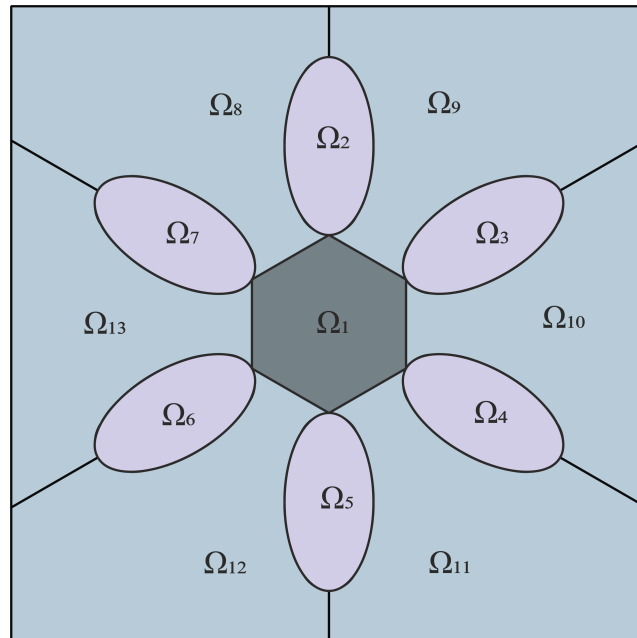


Figure 3.31: Representative volume element with random shaped inclusions. Mat_1 is assigned to the octagon in the center, Mat_2 is assigned to ellipses and Mat_3 is assigned to the matrix elsewhere.

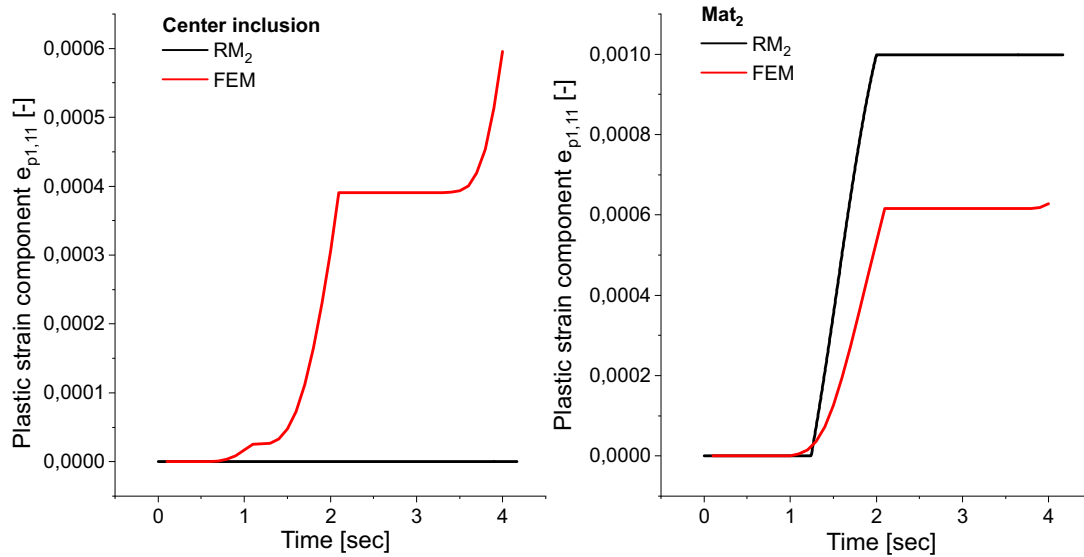


Figure 3.32: Illustration of the plastic strain from RM₂, averaged over Mat₁ at the octagon inclusion and over Mat₂ at the elliptical inclusions, in comparison to the finite element results.

As the mean values of the plastic strains are rather gathered around some edges, therefore they are not present at the exact position, i.e. sub-domain. However, this disadvantage does not seem to have an influence on the overall macroscopic response.

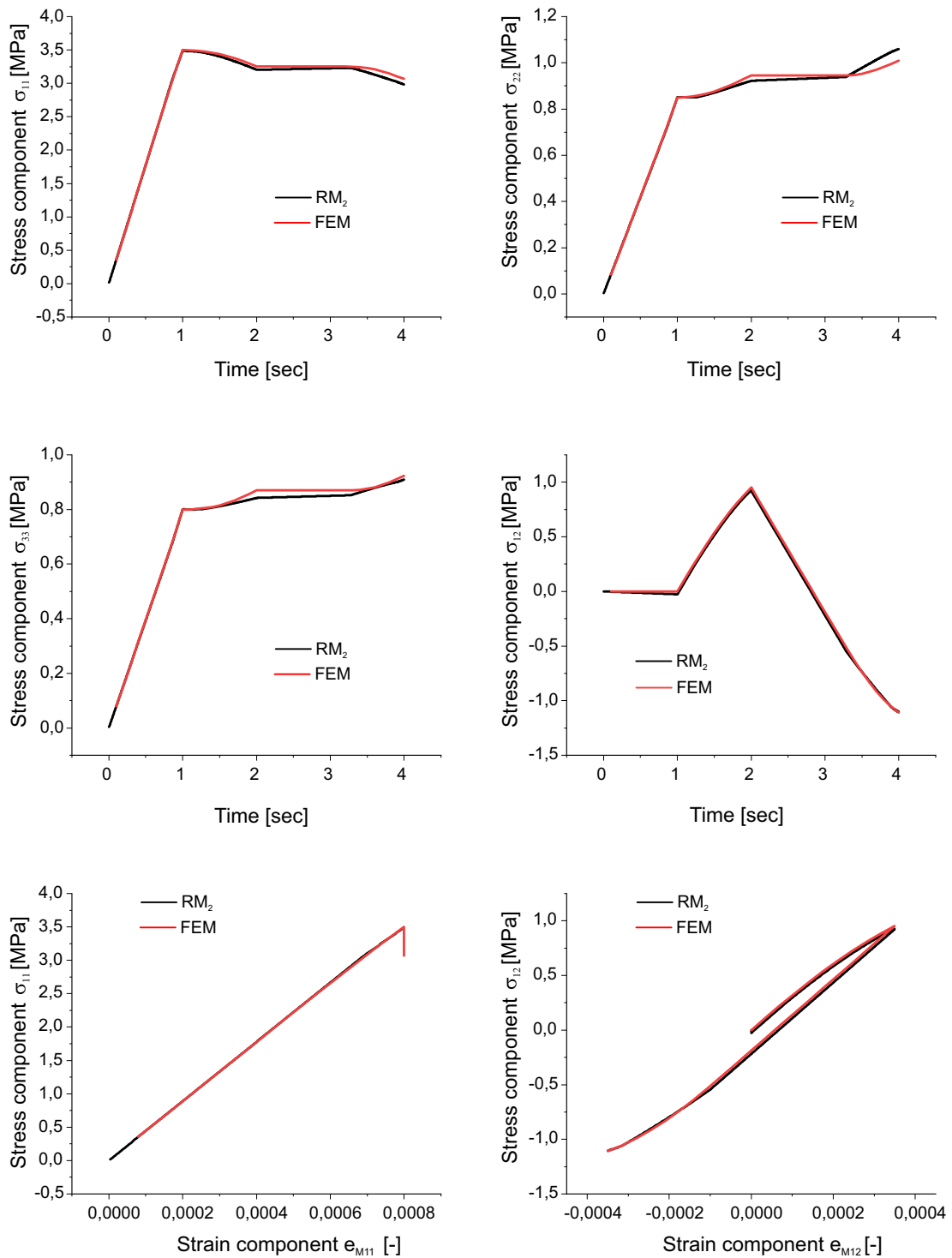


Figure 3.33: Comparison of the effective model RM_2 and a finite element model for the RVE with random inclusions. Macroscopic stresses versus time (top row and middle pane). Stress-strain response for the 1-direction and 1-2 plane (bottom row).

4 Pressure dependent plasticity

This chapter is devoted to granular materials (silt, clay, sand, . . .) possessing pressure-dependent plastic behavior, which has been explained so far by the classical models in soil mechanics via linearized plasticity based on pressure-dependent flow rules. Despite the applicability of these models to engineering purposes, they can not explain the complex structures observed in experiments, see (Wolf, König, and Triantafyllidis 2003), where shear band patterns in different granular materials under the application of various boundary conditions have been detected.

In fact, shear bands can be understood as jumps in the strain field (deformation gradient) under increasing stresses in which the variational problem under time discretization is nonconvex, meaning that the variational problem might not have a minimizer and a microstructure is observed. Such problems have been treated in the literature by the relaxation methods, see (Conti and Dolzmann 2018) and (Conti and Dolzmann 2015) as examples for applications on phase transformation and plasticity problems, or other applications as in (Bartels 2004) and (Bartels 2005).

In terms of the variational approach, these shear band patterns are understood as laminate microstructure and determined through mathematical compatibility conditions, which require in the nonlinear theory that two adjacent elastic strains \mathbf{A} and \mathbf{B} be rank-one connected in the sense that $\mathbf{A} - \mathbf{B} = \mathbf{a} \otimes \mathbf{n}$. The vector \mathbf{n} provides geometric information since it represents the orientation of planes that can connect the two states \mathbf{A} and \mathbf{B} . Minimizing the original energy with respect to such compatible microstructures results in the relaxed energy. Definitions and notions of relaxation can be inferred from Sec. 2.6.2.

In the following, we want to introduce analytical and numerical relaxation results for the proposed type of problem. Therefore, we start with a review of the classical models in soil mechanics in Sec. 4.1, then in Sec. 4.2 we give the variational formulations needed for the relaxation method. Later in Sec. 4.3 a one-dimensional model with analytical relaxation results will be introduced and next an extension to a three-dimensional case with numerical results is given in Secs. 4.4 and 4.5. An evolution of the microstructure with numerical applications is investigated in Sec. 4.7. Finally, this chapter is concluded in Sec. 4.8.

4.1 Classical models in pressure-dependent plasticity

The main class of materials comprising pressure-dependent plastic behavior are soils and granular media. They consist of heterogeneous mixture of fluids (air and water) and particles (silt, clay, sand and gravel) with no to a very little cementation.

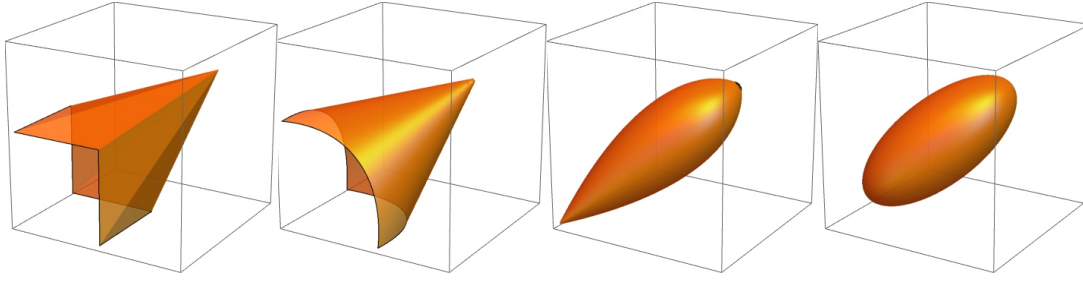


Figure 4.1: Mohr-Coulomb, Drucker-Prager, Cam-Clay, and modified Cam-Clay yield-surfaces.

The shear strength of soil materials is given by friction and interlocking of the particles in which densely packed grains tend to spread apart from each other under shear strains. This expansion of the soil matrix under shearing is called dilatancy, see (Schofield 2005). Dilative soils become looser, whereas contractive soils become denser. A critical state line separates the dilatant and contractive states for soils.

The importance of the critical state soil mechanics is that soil and other granular materials, if continuously being sheared and distorted, will ultimately reach a state in which the soil behaves as a frictional fluid with a constant volume and a constant ratio of shear stress to mean normal stress, regardless of the initial state of the material, see (Yu, Zhuang, and Mo 2019). Many elastoplastic models based on the critical state theory were successfully developed prescribing mechanical problems for soils. Important examples are Mohr-Coulomb failure criterion and its smooth form, Drucker-Prager, in addition to the original and modified Cam-Clay models. The critical yield surface of the different mentioned models can be inferred from Fig. 4.1

A key point of elastoplastic materials is that, unlike elastic materials, they maintain permanent change of their configuration upon unloading, if sufficiently large shear strains occur in the material. On the other hand, they may support arbitrary hydrostatic pressures. This behavior is usually modeled in linearized settings via a convex set $\mathbb{K} \subset \mathbb{R}_{\text{sym}}^{n \times n}$, which prescribes the set of admissible stresses in the material leading to elastic deformations. Contrarily, for stresses acting on $\partial\mathbb{K}$, the permanent plastic deformations occur. These deformations are defined via a flow rule that determines the evolution of the plastic part of the total elastoplastic deformation field. Now the set \mathbb{K} is an infinite cylinder with

$$\mathbb{K} = \bigcup_{\pi \in \mathbb{R}} \pi \mathbf{I} \oplus \mathbf{K} = \bigcup_{\pi \in \mathbb{R}} \{\pi \mathbf{I} + \mathbf{e}, \mathbf{e} \in \mathbf{K}\}, \quad (4.1.1)$$

where \mathbf{I} denotes the identity matrix, and \mathbf{K} is a compact subset in $\mathbb{R}_{\text{D}}^{n \times n}$ defined as

$$\mathbb{R}_{\text{D}}^{n \times n} = \{\mathbf{E} \in \mathbb{R}^{n \times n} : \mathbf{E} = \mathbf{E}^T, \text{tr}(\mathbf{E}) = 0\}, \quad (4.1.2)$$

which is the set of all symmetric and trace free matrices.

Thus the basic problem in the theory of linear elastoplasticity can be formulated as follows. Given a material body described in its reference configuration by a domain

$\Omega \subset \mathbb{R}^n$, find a deformation $\mathbf{y} : \Omega \rightarrow \mathbb{R}^n$ and a decomposition of the symmetrized displacement gradient $\boldsymbol{\varepsilon}$ defined by

$$\mathbf{y}(\mathbf{x}) = \mathbf{x} + \mathbf{u}(\mathbf{x}), \quad \boldsymbol{\varepsilon}(\mathbf{x}) = \frac{1}{2}(\nabla \mathbf{u}(\mathbf{x}) + \nabla \mathbf{u}(\mathbf{x})^T), \quad (4.1.3)$$

into an elastic and a plastic part, $\boldsymbol{\varepsilon} = \boldsymbol{\varepsilon}_e + \boldsymbol{\varepsilon}_p$, $\boldsymbol{\varepsilon}_p \in \mathbb{R}_D^{n \times n}$, such that the following system of equations holds:

- constitutive equation $\boldsymbol{\sigma} = \mathbb{C} : \boldsymbol{\varepsilon}_e$,
- balance of momentum $\mathbf{u}_{tt} - \operatorname{div} \boldsymbol{\sigma} = \mathbf{f}$,
or the equilibrium condition $-\operatorname{div} \boldsymbol{\sigma} = \mathbf{f}$,
- stress constraint $\boldsymbol{\sigma} \in \mathbb{K}$,
- associated flow rule $(\boldsymbol{\xi} - \boldsymbol{\sigma}) : \dot{\boldsymbol{\varepsilon}}_p \leq 0$ for every $\boldsymbol{\xi} \in \mathbb{K}$.

Please notice that the last assumption is not realistic for materials in which frictional effects play a dominant role as in clay, sands and other granular materials. Here pressure-dependency needs to be considered, leading to a flow rule that can not be prescribed by an infinite cylinder, like in the classical Mises plasticity models, but rather with cones in the space of principle stresses, like the Drucker-Prager and Mohr-Coulomb models. To be specific, let $\pi = -1/3 \operatorname{tr} \boldsymbol{\sigma}$ denote the pressure, then the convex elastic domain is given as

$$\mathbb{K} = \bigcup_{\pi=\pi_{\min}}^{\pi_{\max}} \pi \mathbf{I} \oplus K_\pi = \bigcup_{\pi=\pi_{\min}}^{\pi_{\max}} \{\pi \mathbf{I} + \mathbf{E}, \mathbf{E} \in K_\pi\}, \quad (4.1.4)$$

where K_π is a compact subset in $\mathbb{R}_D^{n \times n}$ and $-\infty \leq \pi_{\min} < \pi_{\max} \leq \infty$. In order to comply with experimental observations, plastic deformation should still be volume preserving. For this purpose, the former flow rule is then replaced by the non-associated flow rule and the full system of equations in its quasistatic form is given by

- constitutive equation $\boldsymbol{\sigma} = \mathbb{C} : \boldsymbol{\varepsilon}_e$,
- the equilibrium condition $-\operatorname{div} \boldsymbol{\sigma} = \mathbf{f}$,
- stress constraint $\boldsymbol{\sigma} \in \mathbb{K}$,
- non-associated flow rule $(\boldsymbol{\xi} - \boldsymbol{\sigma}) : \dot{\boldsymbol{\varepsilon}}_p \leq 0$ for every $\boldsymbol{\xi} \in \mathbb{K}_\pi$.

It is important to point out that $\dot{\boldsymbol{\varepsilon}}_p$ is now normal to the boundary of $\mathbb{K}_\pi \subset \mathbb{R}_D^{n \times n}$ but not normal to $\mathbb{K} \subset \mathbb{R}_{\text{sym}}^{n \times n}$, see Fig. 4.2. This is an observation, that lies in the heart of soil mechanics problems investigated by means of the variational formulation.

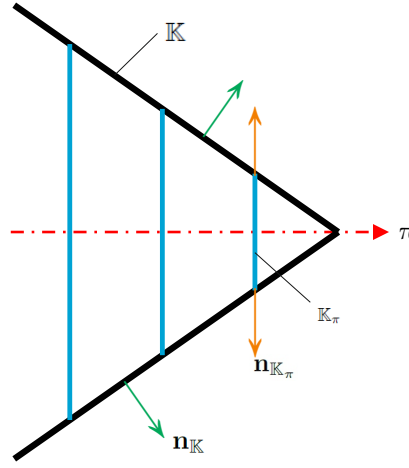


Figure 4.2: Illustration of the sets \mathbb{K} and \mathbb{K}_π , normal vector on \mathbb{K} in green color, leading to an associated flow-rule, normal vector on \mathbb{K}_π in orange color, leading to a non-associated flow-rule.

4.2 Variational settings

In this section we want to provide all the necessary equations required for the variational implementation, some examples from the literature can be found in (Hackl and Fischer 2008), (Miehe, Schotte, and Lambrecht 2002) and (Hackl 1997). Let us consider a physical system expressed in terms of (a set of) external; controllable; state variables, here given by the total strain tensor $\boldsymbol{\varepsilon}$ and internal state variables $\mathbf{z} = \{\boldsymbol{\varepsilon}_p, p\}$, where $\boldsymbol{\varepsilon}_p$ is the plastic strain tensor and $p \geq 0$ is a hardening variable. Starting with the same scheme as in Sec. 3, we assume that the system behavior can be prescribed with only two scalar potentials: the free energy $\Psi(\boldsymbol{\varepsilon}, \mathbf{z})$ and the dissipation potential $\Delta(\boldsymbol{\varepsilon}, \mathbf{z}, \dot{\mathbf{z}})$. Then minimizing Lagrange function, as in Eq. 2.3.21, returns by stationarity condition

$$\dot{\mathbf{z}} = \arg \inf_{\dot{\mathbf{z}}} \left\{ \dot{\Psi} + \Delta \right\}, \quad (4.2.1)$$

which can be expressed in terms of the Biot equation

$$\mathbf{0} \in \frac{\partial \Psi}{\partial \mathbf{z}} + \frac{\partial \Delta}{\partial \dot{\mathbf{z}}}. \quad (4.2.2)$$

Let the free energy be given as

$$\Psi = \frac{K}{2} \text{tr} \boldsymbol{\varepsilon}^2 + \mu \|\text{dev} \boldsymbol{\varepsilon} - \boldsymbol{\varepsilon}_p\|^2 + \rho(\text{tr} \boldsymbol{\varepsilon}) p + \frac{\beta}{2} \|\boldsymbol{\varepsilon}_p\|^2, \quad (4.2.3)$$

where K is the bulk-modulus, μ is the shear-modulus, β is the hardening-modulus and $\rho(\text{tr} \boldsymbol{\varepsilon})$ is a concave function governing the pressure-dependency. This function is defined within an interval $[\text{tr} \boldsymbol{\varepsilon}_{\min}, \text{tr} \boldsymbol{\varepsilon}_{\max}]$ and is zero outside of it and can be shown for a typical model, for example, capped Drucker-Prager as in Fig. 4.3.

According to the second law in thermodynamics, the stress tensor can be derived as

$$\boldsymbol{\sigma} = \frac{\partial \Psi}{\partial \boldsymbol{\varepsilon}} = (K \text{tr} \boldsymbol{\varepsilon} + \rho'(\text{tr} \boldsymbol{\varepsilon}) p) \mathbf{I} + 2\mu (\text{dev} \boldsymbol{\varepsilon} - \boldsymbol{\varepsilon}_p). \quad (4.2.4)$$

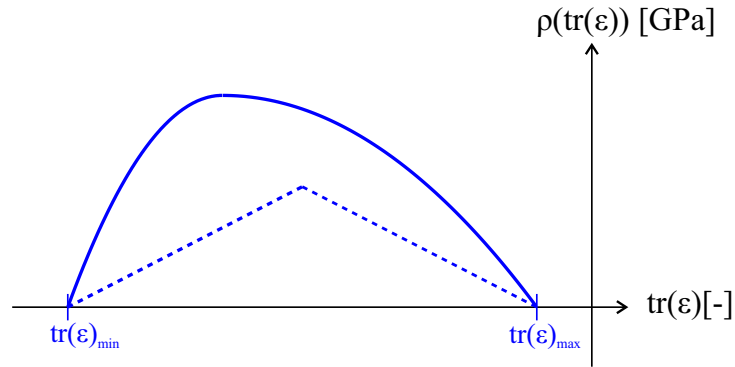


Figure 4.3: Typical functions ρ in the definition of a pressure-dependent yield surface covered by our theory; one function is continuously differentiable (solid line), one is piece-wise affine (dashed line).

In the last equation, the volumetric part (the pressure) is given by $\pi = -K \text{tr} \boldsymbol{\varepsilon} - \rho'(\text{tr} \boldsymbol{\varepsilon}) p$. Here, the second term may be interpreted as a consolidation pressure due to an inelastic volume change governed by the hardening variable p . Nevertheless, a more consistent variational approach would be achieved, if in the energy equation an explicit internal variable θ_p prescribing the inelastic volume change is included, as in the following energy equation

$$\Psi_{\text{consol}} = \frac{K}{2} (\text{tr} \boldsymbol{\varepsilon} - \theta_p)^2 + \mu \|\text{dev} \boldsymbol{\varepsilon} - \boldsymbol{\varepsilon}_p\|^2 + \rho(\theta_p) p + \frac{\beta}{2} \|\boldsymbol{\varepsilon}_p\|^2. \quad (4.2.5)$$

However, we keep for the mean time everything simple and use the energy equation from Eq. 4.2.3. The dissipation potential is assumed to be

$$\Delta(\dot{\boldsymbol{\varepsilon}}_p, \dot{p}) = \begin{cases} 0 & \text{for } \|\dot{\boldsymbol{\varepsilon}}_p\| \leq \dot{p}, \\ \infty & \text{otherwise.} \end{cases} \quad (4.2.6)$$

Substitution into Eq. 4.2.2 gives

$$\text{dev} \boldsymbol{\sigma} - \beta \boldsymbol{\varepsilon}_p \in \rho(\text{tr} \boldsymbol{\varepsilon}) \text{sign} \dot{\boldsymbol{\varepsilon}}_p, \quad (4.2.7)$$

or expressed equivalently in terms of the yield function as

$$\Phi := \|\text{dev} \boldsymbol{\sigma} - \beta \boldsymbol{\varepsilon}_p\| - \rho(\text{tr} \boldsymbol{\varepsilon}) \leq 0, \quad (4.2.8)$$

and the internal variables can be given by the flow rules

$$\dot{p} = \|\dot{\boldsymbol{\varepsilon}}_p\|, \quad \dot{\boldsymbol{\varepsilon}}_p = \kappa (\text{dev} \boldsymbol{\sigma} - \beta \boldsymbol{\varepsilon}_p), \quad (4.2.9)$$

where $\kappa \geq 0$ is a consistency parameter satisfying the Kuhn-Tucker conditions

$$\kappa \geq 0, \quad \Phi \leq 0, \quad \kappa \Phi = 0. \quad (4.2.10)$$

We have now everything set to switch into a time-incremental approach as done in the works of (Carstensen, Hackl, and Mielke 2002) and (Ortiz and Repetto 1999). This approach allows us to investigate the evolution of the material microstructure. Let us consider a time increment $\Delta t = [t_n, t_{n+1}]$, then for given external forces and boundary conditions at time t_{n+1} , we can find the values $\boldsymbol{\varepsilon}_{n+1}$ and \mathbf{z}_{n+1} starting from the values of the internal variables \mathbf{z}_n at time step t_n .

The dissipation distance gives the time-incremental version of the dissipation potential as

$$\begin{aligned} & D(\boldsymbol{\varepsilon}_{p,0}, p_0, \boldsymbol{\varepsilon}_{p,1}, p_1) \\ &= \inf_{\boldsymbol{\varepsilon}_p, p} \left\{ \int_{t_0}^{t_1} \Delta(\dot{\boldsymbol{\varepsilon}}_p(t), \dot{p}(t)) dt \mid \boldsymbol{\varepsilon}_p(0) = \boldsymbol{\varepsilon}_{p,0}, p(0) = p_0, \boldsymbol{\varepsilon}_p(1) = \boldsymbol{\varepsilon}_{p,1}, p(1) = p_1 \right\}, \\ &= \begin{cases} 0 & \text{for } \|\boldsymbol{\varepsilon}_{p,1} - \boldsymbol{\varepsilon}_{p,0}\| \leq p_1 - p_0, \\ \infty & \text{otherwise.} \end{cases} \end{aligned} \quad (4.2.11)$$

And the minimization problem in Eq. 4.2.1 gives now the updated internal variables as

$$\{\boldsymbol{\varepsilon}_{p,n+1}, p_{n+1}\} = \arg \inf_{\boldsymbol{\varepsilon}_p, p} \left\{ \Psi(\boldsymbol{\varepsilon}, \boldsymbol{\varepsilon}_p, p) + D(\boldsymbol{\varepsilon}_{p,n}, p_n, \boldsymbol{\varepsilon}_p, p) \right\}. \quad (4.2.12)$$

Minimization with respect to p gives immediately

$$p - p_n = \|\boldsymbol{\varepsilon}_p - \boldsymbol{\varepsilon}_{p,n}\|. \quad (4.2.13)$$

Substituting Eq. 4.2.13 into Eq. 4.2.12 and minimizing with respect to $\boldsymbol{\varepsilon}_p$ gives

$$2\mu(\text{dev}\boldsymbol{\varepsilon} - \boldsymbol{\varepsilon}_p) - \beta\boldsymbol{\varepsilon}_p \in \rho(\text{tr}\boldsymbol{\varepsilon})\text{sign}(\boldsymbol{\varepsilon}_p - \boldsymbol{\varepsilon}_{p,n}). \quad (4.2.14)$$

Solving for $\boldsymbol{\varepsilon}_p$ in Eq. (4.2.14) yields

$$\boldsymbol{\varepsilon}_p = \boldsymbol{\varepsilon}_{p,n} + \frac{1}{2\mu + \beta} [2\mu\|\text{dev}\boldsymbol{\varepsilon} - \boldsymbol{\varepsilon}_{p,n}\| - \rho(\text{tr}\boldsymbol{\varepsilon})]_+ \text{sign}(\text{dev}\boldsymbol{\varepsilon} - \boldsymbol{\varepsilon}_{p,n}), \quad (4.2.15)$$

with $[x]_+ = \max\{0, x\}$. Now we are able to write the formerly defined condensed energy in Sec. 2.5.1.

$$\Psi_{\text{cond}}(\boldsymbol{\varepsilon}, \boldsymbol{\varepsilon}_{p,n}, p_n) = \inf_{\boldsymbol{\varepsilon}_p, p} \left\{ \Psi(\boldsymbol{\varepsilon}, \boldsymbol{\varepsilon}_p, p) + D(\boldsymbol{\varepsilon}_{p,n}, p_n, \boldsymbol{\varepsilon}_p, p) \right\}, \quad (4.2.16)$$

which yields

$$\begin{aligned} \Psi_{\text{cond}}(\boldsymbol{\varepsilon}, \boldsymbol{\varepsilon}_{p,n}, p_n) &= \frac{K}{2} \text{tr}\boldsymbol{\varepsilon}^2 + \mu \|\text{dev}\boldsymbol{\varepsilon} - \boldsymbol{\varepsilon}_{p,n}\|^2 + \rho(\text{tr}\boldsymbol{\varepsilon})p_n + \frac{\beta}{2} \|\boldsymbol{\varepsilon}_{p,n}\|^2 \\ &\quad - \frac{1}{2} \frac{1}{2\mu + \beta} [2\mu\|\text{dev}\boldsymbol{\varepsilon} - \boldsymbol{\varepsilon}_{p,n}\| - \rho(\text{tr}\boldsymbol{\varepsilon})]_+^2. \end{aligned} \quad (4.2.17)$$

The condensed energy can be considered as formally elastic depending on the parameters $\varepsilon_{p,n}, p_n$ at the previous time-step. It gives information about the initiation of the microstructure but not its evolution. Herewith, the inelastic problem can be replaced by a sequence of elastic problems. Moreover, the internal variables can be updated using equations 4.2.13 and 4.2.15.

4.3 A one-dimensional model problem

Starting with the former derivation, it can be observed that the resulting condensed energy is nonconvex due to the concavity of the function $\rho(\text{tr}\varepsilon)$. Then, we need to compute a quasiconvex envelope to prescribe the effective behavior of the system. However, a quasiconvex envelope can be calculated analytically only in rare special cases. Therefore, we restrict ourselves to a one-dimensional problem in which the quasiconvex envelope and the convex one do coincide. To achieve this description, we apply a specific deformation state considering a slender bar with fibers of material under uniform tension or compression and shear. We assume the fibers to be stiff enough, so that no bending deformations would appear. Then the only remaining non-vanishing strain components in Cartesian coordinates are

$$u_x = u(x), \quad u_y = v(x) + y u'(x), \quad u_z = z u'(x), \quad (4.3.1)$$

$$\varepsilon_{xx} = \varepsilon_{yy} = \varepsilon_{zz} = u', \quad \varepsilon_{yx} = \varepsilon_{xy} = \frac{1}{2} v', \quad (4.3.2)$$

where we neglected terms of the form yu'' and zu'' , which are small due to the slenderness of the bar. For the plastic strains, we assume that the only remaining components are the ones corresponding to shearing in the plane $x - y$, i.e. $\varepsilon_p := \varepsilon_{pyx} = \varepsilon_{pxy}$. Then the free energy can be rewritten in terms of the above non-vanishing strain components as

$$\Psi = \frac{K}{2} \varepsilon_{xx}^2 + \mu \left((\varepsilon_{yx} - \varepsilon_{pyx})^2 + (\varepsilon_{xy} - \varepsilon_{pxy})^2 \right) + \rho(\varepsilon_{xx}) p + \beta \varepsilon_{pxy}^2. \quad (4.3.3)$$

Plug Eq. 4.3.1 into Eq. 4.3.3

$$\Psi = \frac{K}{2} (u')^2 + 2\mu \left(\frac{1}{2} v' - \varepsilon_p \right)^2 + \rho(u') p + \beta \varepsilon_p^2. \quad (4.3.4)$$

Analog to the previous implementation, minimizing with respect to ε_p and p gives the condensed energy, now for the one-dimensional model problem

$$\begin{aligned} \Psi_{\text{cond}}(u', v', \varepsilon_{p,n}, p_n) &= \frac{K}{2} (u')^2 + 2\mu \left(\frac{1}{2} v' - \varepsilon_{p,n} \right)^2 + \rho(u') p_n \\ &\quad - \frac{1}{2} \frac{1}{2\mu + \beta} \left[2\mu \left| \frac{1}{2} v' - \varepsilon_{p,n} \right| - \rho(u') \right]_+^2. \end{aligned} \quad (4.3.5)$$

In the next derivations, we will consider for simplicity that $p_n = 0$, which allows to ease the mathematical treatment. Confirming once again that the model can deliver information about the initiation of the microstructure only (the updated internal variables do not enter the condensed energy). Nevertheless, a model investigating the evolution of the microstructure will be presented in Sec. 4.7.

It is convenient for the mathematical treatment to seek a dimensionless formulation. For this purpose, we define modified variables and quantities with the following transformation relations

$$y_1 = \sqrt{\frac{K}{2\mu}} u', \quad y_2 = \frac{1}{2} v', \quad r(y_1) = \frac{1}{2\mu} \rho(u'), \quad b = \frac{\beta}{2\mu}, \quad (4.3.6)$$

employing the condensed energy to take the form

$$\begin{aligned} & \Psi_{\text{cond}}(y_1, y_2, \varepsilon_{p,n}, p_n) \\ &= 2\mu \left[\frac{1}{2} y_1^2 + \frac{1}{2} (y_2 - \varepsilon_{p,n})^2 - \frac{1}{2} \frac{1}{b+1} \left[|y_2 - \varepsilon_{p,n}| - r(y_1) \right]_+^2 \right]. \end{aligned} \quad (4.3.7)$$

Finally we may drop the multiplicative constant 2μ and write $z_n = \varepsilon_{p,n}$. Since Ψ_{cond} is the free energy density in the variational functional that needs to be minimized in the first time step, it is crucial to understand the convexity properties of Ψ_{cond} in order to employ the direct method in the calculus of variations. It turns out that the concavity of r leads to a lack of convexity of Ψ_{cond} and the approach via relaxation (Dacorogna 2007) requires one to characterize the quasiconvex envelope of Ψ_{cond} , which, in the scalar case, reduces to the convex envelope. This task is accomplished in the next paragraph.

For any function $f : \mathbb{R}^2 \rightarrow \mathbb{R}$ we denote the convex envelope of f by f_c and, if f is differentiable at $y \in \mathbb{R}^2$, the linear Taylor polynomial of f about the point y by $T_y f$. Fix $b > 0$ and $y_{\min}, y_{\max} \in \mathbb{R}$ with $y_{\min} < y_{\max}$. Define the set of admissible dissipation functions by

$$\mathcal{R} := \{r \in C(\mathbb{R}, [0, \infty)) \mid \text{supp}(r) = [y_{\min}, y_{\max}], r|_{[y_{\min}, y_{\max}]} \text{ concave}\}. \quad (4.3.8)$$

Fix $y_{\text{mid}} := (y_{\min} + y_{\max})/2$ and define the piece-wise affine function $r_0 \in \mathcal{R}$ by

$$r_0(y_1) = \sqrt{b} \cdot \left(\frac{y_{\max} - y_{\min}}{2} - |y_1 - y_{\text{mid}}| \right) \cdot \chi_{[y_{\min}, y_{\max}]}(y_1), \quad (4.3.9)$$

Note that the slope of r_0 is only related to the hardening parameter b and, depending on the relative size of $r_{\max} = \max r$ and b , the two curves may have intersections or not. Our theory covers the case of small values of b for which the two curves do not intersect. For $r \in \mathcal{R}$, the condensed energy is given by

$$f_{z_n}^{(r)}(y) = \frac{1}{2} (y_1^2 + (y_2 - z_n)^2) - \frac{(|y_2 - z_n| - r(y_1))_+^2}{2(b+1)}. \quad (4.3.10)$$

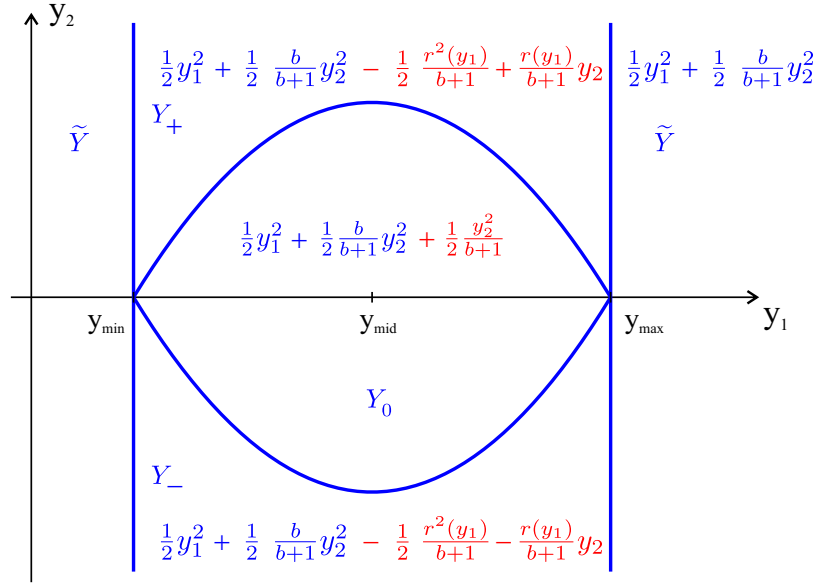


Figure 4.4: Definition of the condensed energy for the model problem. The set Y_0 in Eq. 4.3.11 is enclosed by the blue curves ($\pm r$), the sets Y_{\pm} correspond to the sets above and below Y_0 , respectively, and the set \tilde{Y} is the complement of these three sets in \mathbb{R}^2 .

Since the energy depends only on $y_2 - z_n$, it is sufficient to calculate the convex envelope $f_c^{(r)}$ of $f^{(r)} := f_0^{(r)}$ with $z_n = 0$; the convex envelope of $f_{z_n}^{(r)}(y_1, y_2)$ is given by $f_c^{(r)}(y_1, y_2 - z_n)$. If the dissipation function is uniquely defined from the context, we simply write f instead of $f^{(r)}$. Define the disjoint sets

$$\begin{aligned} \tilde{Y} &= \{y \in \mathbb{R}^2 : y_1 \leq y_{\min} \text{ or } y_1 \geq y_{\max}\}, \\ Y_0 &= \{y \in \mathbb{R}^2 : y_1 \in (y_{\min}, y_{\max}), |y_2| < r(y_1)\}, \\ Y_{\pm} &= \{y \in \mathbb{R}^2 : y_1 \in (y_{\min}, y_{\max}), \pm y_2 \geq r(y_1)\}, \end{aligned} \quad (4.3.11)$$

whose union is \mathbb{R}^2 , see Fig. 4.4. These sets describe the regions in which the condensed energy $f^{(r)}$ is given by different algebraic expressions, depending on the sign of $|y_2| - r(y_1)$.

A natural approach to calculate the convex envelope of a continuous function $f : \mathbb{R}^d \rightarrow \mathbb{R}$ is to find pairwise distinct points $y^{(1)}, \dots, y^{(q)} \in \mathbb{R}^d$ with $q \leq d + 1$ that satisfy the subgradient condition

$$\exists v \in \bigcap_{i=1}^q \partial f(y^{(i)}) : \forall i, j \in \{1, \dots, q\} : f(y^{(i)}) - \langle v, y^{(i)} \rangle = f(y^{(j)}) - \langle v, y^{(j)} \rangle, \quad (4.3.12)$$

and to define, for all $y \in \text{Conv}(\{y^{(1)}, \dots, y^{(q)}\})$, the convex hull of the points $y^{(1)}, \dots, y^{(q)}$, a candidate for the convex envelope of f by

$$y = \sum_{i=1}^q \lambda_i y^{(i)}, \quad f_c(y) = \sum_{i=1}^q \lambda_i f(y^{(i)}), \quad \lambda_i \in (0, 1], \quad \sum_{i=1}^q \lambda_i = 1. \quad (4.3.13)$$

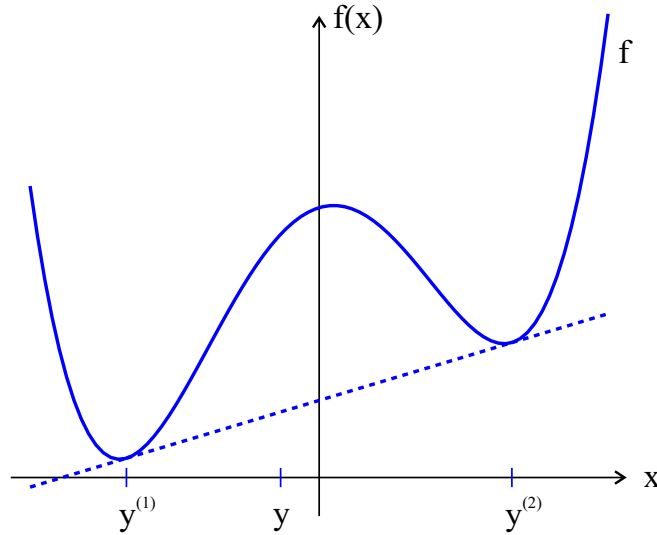


Figure 4.5: Characterization of the convex envelope (thick, dashed) of a nonconvex function f (thick). The value $f_c(y)$ is calculated from two points $y^{(1)}$ and $y^{(2)}$ on the graph of f and the derivatives of f_c at the three points $y^{(1)}$, $y^{(2)}$ and y coincide. The convex hull coincides on $[y^{(1)}, y^{(2)}]$ with the tangent to f at both the points $y^{(i)}$.

It is useful to note that the representation in 4.3.13 is related to the tangent plane of f if one of the points $y^{(i)}$ in case that f is differentiable at $y^{(i)}$. In fact, if for some direction $w \in \mathbb{R}^d$ and some $y \in \mathbb{R}^d$ the directional derivative $D_w f(y)$ exists, then $v \in \partial f(y)$ implies $\langle v, w \rangle = D_w f(y)$. If f is even differentiable in y , then $\{\partial f(y)\} = \{\nabla f(y)\}$. This leads to the observation that, if $y^{(1)}, \dots, y^{(q)} \in \mathbb{R}^d$ is a solution of Eq. 4.3.12 and if f is differentiable in some $y^{(i)}$, then for all $y \in \text{Conv}(\{y^{(1)}, \dots, y^{(q)}\})$ the function f_c is given by

$$f_c(y) = (T_{y^{(i)}} f)(y) = f(y^{(i)}) + \langle \nabla f(y^{(i)}), y - y^{(i)} \rangle. \quad (4.3.14)$$

The calculation of the subgradient involves an evaluation of the values of f on the whole space, and the solution of Eq. 4.3.12 is in general challenging, further necessary calculations can be found in (Behr, Dolzmann, Hackl, and Jezdan 2023).

Theorem 1. Recall the definition of \tilde{Y} in 4.3.11 and define the disjoint sets

$$Y_1 = \{y \in \mathbb{R}^2, |y_2| < r_0(y_1)\}, \quad (4.3.15)$$

$$Y_2 = \{y \in (y_{\min}, y_{\max}) \times \mathbb{R}, r_0(y_1) \leq |y_2| < \frac{b+1}{\sqrt{b}} \frac{y_{\max} - y_{\min}}{2} - \frac{r_0(y_1)}{b}\},$$

$$Y_3 = \{y \in (y_{\min}, y_{\max}) \times \mathbb{R}, \frac{b+1}{\sqrt{b}} \frac{y_{\max} - y_{\min}}{2} - \frac{r_0(y_1)}{b} \leq |y_2| \leq \frac{b+1}{\sqrt{b}} \frac{y_{\max} - y_{\min}}{2}\},$$

$$Y_4 = \{y \in (y_{\min}, y_{\max}) \times \mathbb{R}, \frac{b+1}{\sqrt{b}} \frac{y_{\max} - y_{\min}}{2} < |y_2|\},$$

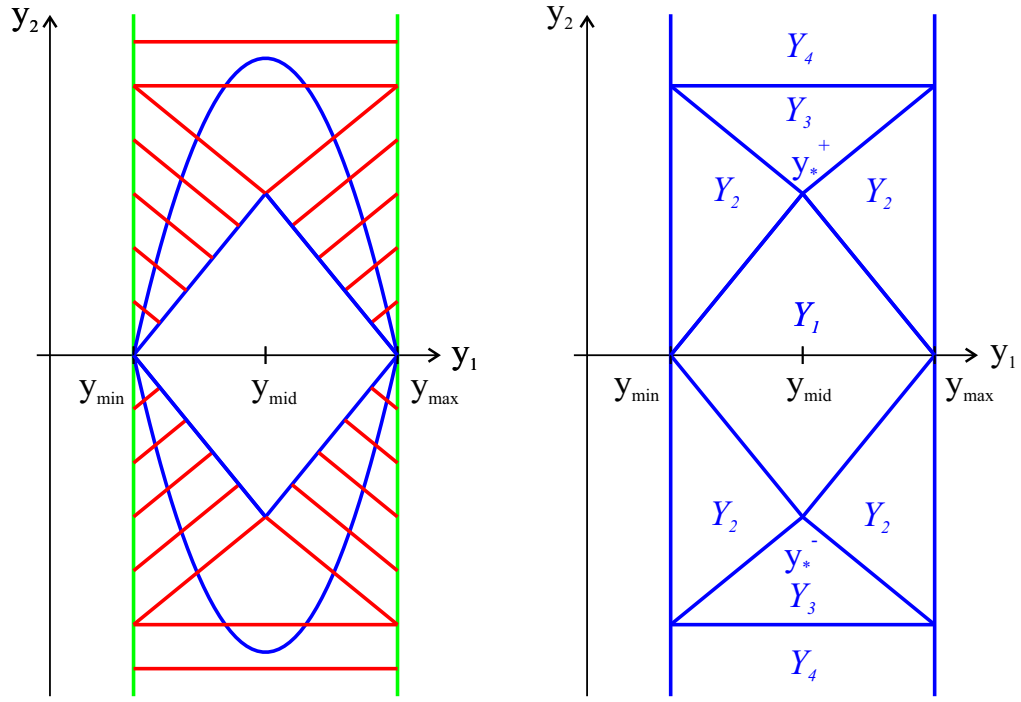


Figure 4.6: Construction of the relaxed energy. The sides of the rhombus Y_1 have slope $\pm\sqrt{b}$ and correspond to the dashed dissipation function in Figure 4.3.

as shown in the right panel in Figure 4.6. Then the convex envelope f_c of f is given by

$$f_c(y) = \begin{cases} \frac{1}{2}y_1^2 + \frac{1}{2}\frac{b}{b+1}y_2^2 & \text{on } \tilde{Y}, \\ \frac{1}{2}y_1^2 + \frac{1}{2}y_2^2 & \text{on } Y_1, \\ \frac{1}{2}y_1^2 + \frac{1}{2}y_2^2 - \frac{(|y_2| - r_0(y_1))^2}{2(b+1)} & \text{on } Y_2, \\ \frac{1}{2}y_1^2 + \frac{1}{2}y_2^2 - \frac{(|y_2| - r_0(y_1))^2}{2(b+1)} & \text{on } Y_3, \\ -\frac{1}{2}\frac{b}{b+1} \left(|y_2| - \frac{b+1}{\sqrt{b}} \frac{y_{\max} - y_{\min}}{2} + \frac{r_0(y_1)}{b} \right)^2 & \text{on } Y_3, \\ \frac{1}{2}y_1^2 + \frac{1}{2}\frac{b}{b+1}y_2^2 + \frac{1}{2}(y_1 - y_{\min}) \cdot (y_{\max} - y_1) & \text{on } Y_4. \end{cases} \quad (4.3.16)$$

For a detailed mathematical proof refer to (Behr, Dolzmann, Hackl, and Jezdan 2023). It is based on the verification of the geometry for the calculation of f_c in the left panel in Fig. 4.6, which formalizes the intuitive picture for the convex hull of a function in Fig. 4.5. In fact, $f_c = f$ on Y_1 and for $y \in Y_2$ the convex hull $f_c(y)$ is obtained as an average of two function values where the red line segments intersect the green and the blue line, respectively. Finally, for $y \in Y_3$ the value of $f_c(y)$ is an average of three points, namely of the function values in the three corners of the triangle Y_3 . The convex hull coincides with the tangent plane to f at y_*^+ as indicated in Eq. (4.3.14).

For the construction of the convex envelope of the condensed energy $f^{(r)}$ we first derive pairs and triples of points $y^{(1)}, \dots, y^{(q)} \in \mathbb{R}^2$ ($q = 2, 3$), in which $f^{(r)}$ is differentiable in the variable y_2 and in which $\partial_2 f^{(r)}$ is equal. Then we derive a candidate for the direction $v \in \mathbb{R}^d$ satisfying the equation in Eq. (4.3.12). However, at this point we do not know whether this v is indeed a subgradient of f in all the points $y^{(1)}, \dots, y^{(q)}$. For those pairs and triples for which we expect this to be true, we do not show explicitly that the first part in Eq. (4.3.12) is satisfied, rather we apply the construction described in Eqs. (4.3.13) and (4.3.14) and prove in Theorem 1 that this construction leads to the convex envelope. It is a remarkable result of the subsequent analysis that the explicit formulas for the relaxed energy show a very different behavior with respect to the dependence on the dissipation function r . In fact, for small values of b relative to r , i.e., for

$$\sqrt{b} \cdot \frac{y_{\max} - y_{\min}}{2} \leq r \left(\frac{y_{\min} + y_{\max}}{2} \right), \quad (4.3.17)$$

which is the case of relevance in soil mechanics, the relaxed energy is in fact independent of r .

4.4 Extension to three-dimensional model problem

The convex envelope in the one-dimensional case for the function $f(y_1, y_2, \varepsilon_{p,n}, p_n)$ given in Theorem 1 may be generalized in a natural way to three dimensions by employing a substitution inspired by the transformation of variables defined in Eq. 4.3.6. In this sense, we define a formally relaxed energy as

$$\Psi_{\text{rel}}(\varepsilon, \varepsilon_{p,n}, p_n) = f \left(\sqrt{\frac{K}{2\mu}} \text{tr} \varepsilon, \|\text{dev} \varepsilon\|, \varepsilon_{p,n}, p_n \right). \quad (4.4.1)$$

Observe that, when applying the same substitution to the one-dimensional condensed energy given in Eq. 4.3.7, we recover the original three-dimensional condensed energy given in Eq. 4.2.17. We give now the physical formulation of r_0 from Eq. 4.3.9.

$$\rho_0(\text{tr} \varepsilon) = \sqrt{\beta K} \left(\frac{\text{tr} \varepsilon_{\max} - \text{tr} \varepsilon_{\min}}{2} - \left| \text{tr}(\varepsilon) - \frac{\text{tr} \varepsilon_{\max} + \text{tr} \varepsilon_{\min}}{2} \right| \right) \quad (4.4.2)$$

The relaxed energies as per Eq. 4.3.16 and their derivatives with respect to the strain tensor, i.e. the corresponding relaxed stress tensors are presented on the domains $Y_i, i = 1, \dots, 4$ by the following expressions.

Domain Y_1 :

$$\Psi_{1,\text{rel}} = \frac{K}{2} (\text{tr} \varepsilon)^2 + \mu \|\text{dev} \varepsilon\|^2, \quad \sigma_{1,\text{rel}} = K(\text{tr} \varepsilon) \mathbf{I} + 2\mu \text{dev} \varepsilon. \quad (4.4.3)$$

Domain Y_2 :

$$\Psi_{2,\text{rel}} = \frac{K}{2}(\text{tr}\boldsymbol{\varepsilon})^2 + \mu \|\text{dev}\boldsymbol{\varepsilon}\|^2 - \frac{4\mu^2}{2(2\mu + \beta)} \left(\|\text{dev}\boldsymbol{\varepsilon}\| - \frac{1}{2\mu}\rho_0(\text{tr}\boldsymbol{\varepsilon}) \right)^2, \quad (4.4.4)$$

$$\begin{aligned} \sigma_{2,\text{rel}} = K(\text{tr}\boldsymbol{\varepsilon})\mathbf{I} + 2\mu \text{dev}\boldsymbol{\varepsilon} - \frac{4\mu^2}{2\mu + \beta} \left(\|\text{dev}\boldsymbol{\varepsilon}\| - \frac{1}{2\mu}\rho_0(\text{tr}\boldsymbol{\varepsilon}) \right) \frac{\text{dev}\boldsymbol{\varepsilon}}{\|\text{dev}\boldsymbol{\varepsilon}\|} \\ - \frac{2\mu\sqrt{\beta K}}{2\mu + \beta} \left(\|\text{dev}\boldsymbol{\varepsilon}\| - \frac{1}{2\mu}\rho_0(\text{tr}\boldsymbol{\varepsilon}) \right) \mathbf{I}. \end{aligned} \quad (4.4.5)$$

Domain Y_3 :

$$\begin{aligned} \Psi_{3,\text{rel}} = \frac{K}{2}(\text{tr}\boldsymbol{\varepsilon})^2 + \mu \|\text{dev}\boldsymbol{\varepsilon}\|^2 - \frac{4\mu^2}{2(2\mu + \beta)} \left(\|\text{dev}\boldsymbol{\varepsilon}\| - \frac{1}{2\mu}\rho_0(\text{tr}\boldsymbol{\varepsilon}) \right)^2 \\ - \frac{2\mu\beta}{2(2\mu + \beta)} \left(\|\text{dev}\boldsymbol{\varepsilon}\| + \frac{1}{\beta}\rho_0(\text{tr}\boldsymbol{\varepsilon}) - \frac{2\mu + \beta}{2\mu} \sqrt{\frac{K}{\beta}} \frac{\text{tr}\boldsymbol{\varepsilon}_{\max} - \text{tr}\boldsymbol{\varepsilon}_{\min}}{2} \right)^2, \end{aligned} \quad (4.4.6)$$

$$\begin{aligned} \sigma_{3,\text{rel}} = K(\text{tr}\boldsymbol{\varepsilon})\mathbf{I} + 2\mu \text{dev}\boldsymbol{\varepsilon} - \frac{4\mu^2}{2\mu + \beta} \left(\|\text{dev}\boldsymbol{\varepsilon}\| - \frac{1}{2\mu}\rho_0(\text{tr}\boldsymbol{\varepsilon}) \right) \frac{\text{dev}\boldsymbol{\varepsilon}}{\|\text{dev}\boldsymbol{\varepsilon}\|} \\ - \frac{2\mu\sqrt{\beta K}}{2\mu + \beta} \left(\|\text{dev}\boldsymbol{\varepsilon}\| - \frac{1}{2\mu}\rho_0(\text{tr}\boldsymbol{\varepsilon}) \right) \mathbf{I} \\ - \frac{2\mu\sqrt{\beta K}}{2\mu + \beta} \left(\|\text{dev}\boldsymbol{\varepsilon}\| + \frac{1}{\beta}\rho_0(\text{tr}\boldsymbol{\varepsilon}) - \frac{2\mu + \beta}{2\mu} \sqrt{\frac{K}{\beta}} \frac{\text{tr}\boldsymbol{\varepsilon}_{\max} - \text{tr}\boldsymbol{\varepsilon}_{\min}}{2} \right) \mathbf{I} \\ - \frac{2\mu\beta}{2\mu + \beta} \left(\|\text{dev}\boldsymbol{\varepsilon}\| + \frac{1}{\beta}\rho_0(\text{tr}\boldsymbol{\varepsilon}) - \frac{2\mu + \beta}{2\mu} \sqrt{\frac{K}{\beta}} \frac{\text{tr}\boldsymbol{\varepsilon}_{\max} - \text{tr}\boldsymbol{\varepsilon}_{\min}}{2} \right) \frac{\text{dev}\boldsymbol{\varepsilon}}{\|\text{dev}\boldsymbol{\varepsilon}\|}. \end{aligned} \quad (4.4.7)$$

Domain Y_4 :

$$\Psi_{4,\text{rel}} = \frac{K}{2}(\text{tr}\boldsymbol{\varepsilon})^2 + \frac{2\mu\beta}{2(2\mu + \beta)} \|\text{dev}\boldsymbol{\varepsilon}\|^2 + \frac{K}{2} \left(\text{tr}\boldsymbol{\varepsilon} - \text{tr}\boldsymbol{\varepsilon}_{\min} \right) \left(\text{tr}\boldsymbol{\varepsilon}_{\max} - \text{tr}\boldsymbol{\varepsilon} \right), \quad (4.4.8)$$

$$\sigma_{4,\text{rel}} = K(\text{tr}\boldsymbol{\varepsilon})\mathbf{I} + \frac{2\mu\beta}{2\mu + \beta} \text{dev}\boldsymbol{\varepsilon} + K \left(\frac{\text{tr}\boldsymbol{\varepsilon}_{\max} + \text{tr}\boldsymbol{\varepsilon}_{\min}}{2} - \text{tr}\boldsymbol{\varepsilon} \right) \mathbf{I}. \quad (4.4.9)$$

4.5 Numerical results 1D

We make use of the dimensionless formulation introduced in Eq. 4.3.6. The function $r(y_1)$ is selected to fit the yield surface of a modified Drucker-Prager model employ-

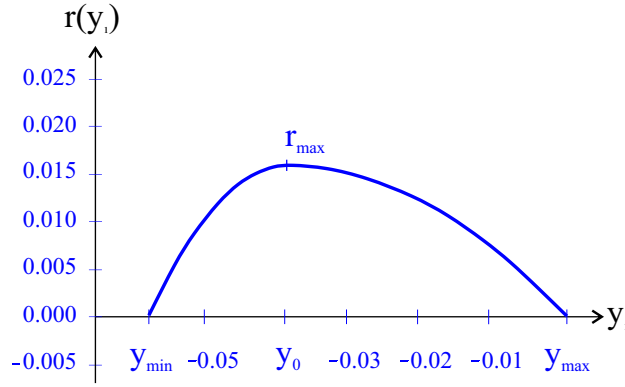


Figure 4.7: Elastic region given by the function $r(y_1)$.

ing piece-wise quadratic function given by

$$r(y_1) = r_{\max} \begin{cases} 1 - \frac{(y_1 - y_0)^2}{(y_0 - y_{\min})^2} & , \text{ for } y_{\min} \leq y_1 \leq y_0, \\ 1 - \frac{(y_1 - y_0)^2}{(y_{\max} - y_0)^2} & , \text{ for } y_0 \leq y_1 \leq y_{\max}, \\ 0 & , \text{ otherwise,} \end{cases} \quad (4.5.1)$$

where $y_{\min} = -0.058$, $y_{\max} = 0.00107$, $y_0 = -0.0385$ and $r_{\max} = 0.016$, see Fig. 4.7. We choose a hardening parameter $b = 0.095$ to insure that we are within the regime of small values of b treated in Sec. 4.3.

The first numerical test is for a one-dimensional specimen (beam) of length $L = 1$, represented by a domain $\Omega = (0, 1)$. We employ a space discretization using $n = 80$ standard linear finite elements. The specimen is fixed at the left-hand side, $(u, v)(0) = (0, 0)$, and subjected to given displacements $(u, v)(L) = (u_{\text{ext}}, v_{\text{ext}})$ in x - and y -direction, respectively, at the right-hand side.

The affine solution is given by $x \mapsto (u(x), v(x)) = x(u_{\text{ext}}, v_{\text{ext}})$ with constant derivative $(u_{\text{ext}}, v_{\text{ext}})$. We fix u_{ext} throughout our calculations and vary v_{ext} exploring four different regions in the phase diagram from Fig. 4.6, which correspond to the four panels in Figs. 4.8 and 4.9: $(u_{\text{ext}}, v_{\text{ext}})$ in (a) Y_1 , (b) $Y_2 \cap \{y_2 \leq r(y_1)\}$, (c) $Y_2 \setminus \{y_2 \leq r(y_1)\}$ and (d) Y_3 , respectively.

The total energies are then functions of the vectors of nodal displacements $\mathbf{u} = \{u_1, \dots, u_{n+1}\}$, $\mathbf{v} = \{v_1, \dots, v_{n+1}\}$ with $u_1 = v_1 = 0$ and $u_{n+1} = u_{\text{ext}}$, $v_{n+1} = v_{\text{ext}}$, given as

$$W_{\text{cond,rel}}(\mathbf{u}, \mathbf{v}) = \sum_{j=1}^n \psi_{\text{cond,rel}}\left(\frac{u_{j+1} - u_j}{L/n}, \frac{v_{j+1} - v_j}{L/n}\right) \frac{L}{n}, \quad (4.5.2)$$

for the condensed and the relaxed energy, respectively. The minimization is performed using the *Mathematica* function *FindMinimum*, which employs a gradient-based local search. Note, that for the relaxed energy, the minimum is obtained for the affine displacements $u_i = \frac{i-1}{n}u_{\text{ext}}$, $v_i = \frac{i-1}{n}v_{\text{ext}}$.

We add a random perturbation of amplitude α to the exact solution given above as an initial guess for the minimization procedure. Hence, let $\text{rand}(i)$ be a random function possessing a uniform distribution within the interval $[-1, 1]$. Then the initial guess is for $i = 2, \dots, n$ given by

$$u_i^{\text{ini}} = \frac{i-1}{n}u_{\text{ext}} + \alpha \frac{L}{n} \text{rand}(i), \quad (4.5.3)$$

$$v_i^{\text{ini}} = \frac{i-1}{n}v_{\text{ext}} + \alpha \frac{L}{n} \text{rand}(n+i). \quad (4.5.4)$$

Two tests are performed, once with the a perturbation of amplitude $\alpha = 0.01$ and a second test with $\alpha = 0.1$. Results are depicted in Figs. 4.8 and 4.9. The numerical simulations reflect the predictions based on the phase diagram in Fig. 4.6. We expect the calculations employing the condensed energy to return microstructure consisting of up to three distinct points in y_1 - y_2 -space. These microstructures will approximate the actual minimum more or less successfully depending on the quality of the initial guess. This behavior is precisely reflected by the points in red color corresponding to the condensed energy in Figs. 4.8 and 4.9. The calculations employing the relaxed energy, on the other hand, are expected to return the actual minimum up to round-off errors, which is precisely what is found. Due to the fact that the graph of the relaxed energy contains affine (flat) areas, the variational problem with the relaxed energy does have a unique affine minimizer, the displacement gradients are not expected to take only values in the local minima of the nonconvex free energy leading to the formation of microstructure, and can in fact take any value on the affine parts of the energy. The only restriction is the global restriction, that the total energy of the displacement is equal to the minimum. This behavior is reflected once again by the points in green color corresponding to the relaxed energy in Figs. 4.8 and 4.9. In the following, we comment on the outcome from Figs. 4.8 and 4.9 in detail.

In case (a) with $v_{\text{ext}} \in [0, 0.0036]$, both the relaxed and the condensed energy are convex with $f = f_c$ and the corresponding minimizers are affine with gradient $(u_{\text{ext}}, v_{\text{ext}})$. For larger values of $v_{\text{ext}} \in [0.0036, 0.014]$ the function f is locally convex but different from its relaxation f_c which is obtained by a mixture of two states and which is affine on lines parallel to the boundary of the region Y_3 , see the red lines in the left panel in Fig. 4.6. Thus the calculation with the condensed energy is expected to discover the microstructure supported on two points while the calculation with f_c can use all the gradients on the affine part. In fact, the second panel in Figs. 4.8 and 4.9 shows exactly this behavior. The case (c) corresponds to $v_{\text{ext}} \in [0.014, 0.063]$ and shows the same behavior of case (b), the only difference being that f is not locally convex at the point $(u_{\text{ext}}, v_{\text{ext}})$. Finally, for $v_{\text{ext}} \in [0.0163, 0.15]$ the condensed energy f is not locally convex and the relaxed energy f_c is affine on the triangle Y_3 . Therefore the range of the gradient of the numerical solution for the calculation with the condensed energy is expected to be located in the three corners of the triangle while the gradient of the solution with the relaxed energy can explore the full triangle. The last panel in Figs. 4.8 and 4.9 confirms this prediction.

Notice, that considering a larger value for the amplitude of perturbation α results in more scattered values as the initial guess is further a way from the exact minimum. This difference is obviously noticed in the last panel from Fig. 4.9, where the points of the approximate minimizer from the relaxed energy are spread even outside the

relaxation region Y_3 . Despite this higher perturbation, the gradient of the solution from the relaxed energy for the cases (a), (b) and (c) (as shown in the panels 1-3 in Fig. 4.9) is still able to return the exact minimum.

The procedure employing the condensed energy does not recover the exact minimum, but produces values which are between 10% and 20% higher. However, the values are lower than the energy of the condensed energy evaluated at the affine solution. The approximate minimizer attempts to mimic the construction of the relaxed energy by concentrating points at the corresponding positions within the y_1 - y_2 -plane. The procedure employing the relaxed energy returns the exact minimum with working precision in all cases.

In the following, we present a third test for the one-dimensional problem (the beam) assigning convex perturbation in time. Meaning that we increase the displacement at the right hand side in m steps to its final value (here $m = 50$ steps). In each step, we take for the minimization the initial guess from the previous one. These values are randomized (with α) and adapted to avoid any unrealistic high gradient in the rightmost element as follows:

$$u_i^{\text{ini},k} = \frac{k}{k-1} u_i^{k-1} \left(1 + \alpha \frac{L}{n} \text{rand}(i) \right), \quad v_i^{\text{ini},k} = \frac{k}{k-1} v_i^{k-1} \left(1 + \alpha \frac{L}{n} \text{rand}(n+i) \right), \\ i = 2, \dots, n, \quad (4.5.5)$$

where k denotes the number of the specific step and n gives the mesh size.

Results are depicted in Fig. 4.10. The procedure employing the relaxed energy again recovers the exact minimum within working precision, but the minimizers comprise a smaller number of points now. The procedure employing the condensed energy still does not recover the exact minimum.

In order to decide how close can the implemented minimizing procedure attain the exact minimum, the relative error from the relaxed and condensed energy with respect to the exact energy is investigated. The calculations are performed for a randomly perturbed initial guess with $\alpha = 0.1$ and considering $m = 0$ and $m = 50$ time-steps. The results can be inferred from Fig. 4.11. We notice from the green curves (representing the relative error of the relaxed energies), that the applied relaxation covers the exact minimum with a considerably small error in the different relaxation regions and under different initial values. On the other hand, the condensed energy fails to find the exact solution, when the minimization is starting with an initial guess that is too far away from the exact solution, as can be seen in the last two graphs from the right panel in Fig. 4.11.

4.6 Numerical results 2D

The generalization to a three-dimensional model derived formerly in Sec. 4.4 is tested through two-dimensional boundary value problems (in plane strain settings). First, the results from the square plate with a circular hole are provided, then the calculation results from the double notch and the cracked plate are shown.

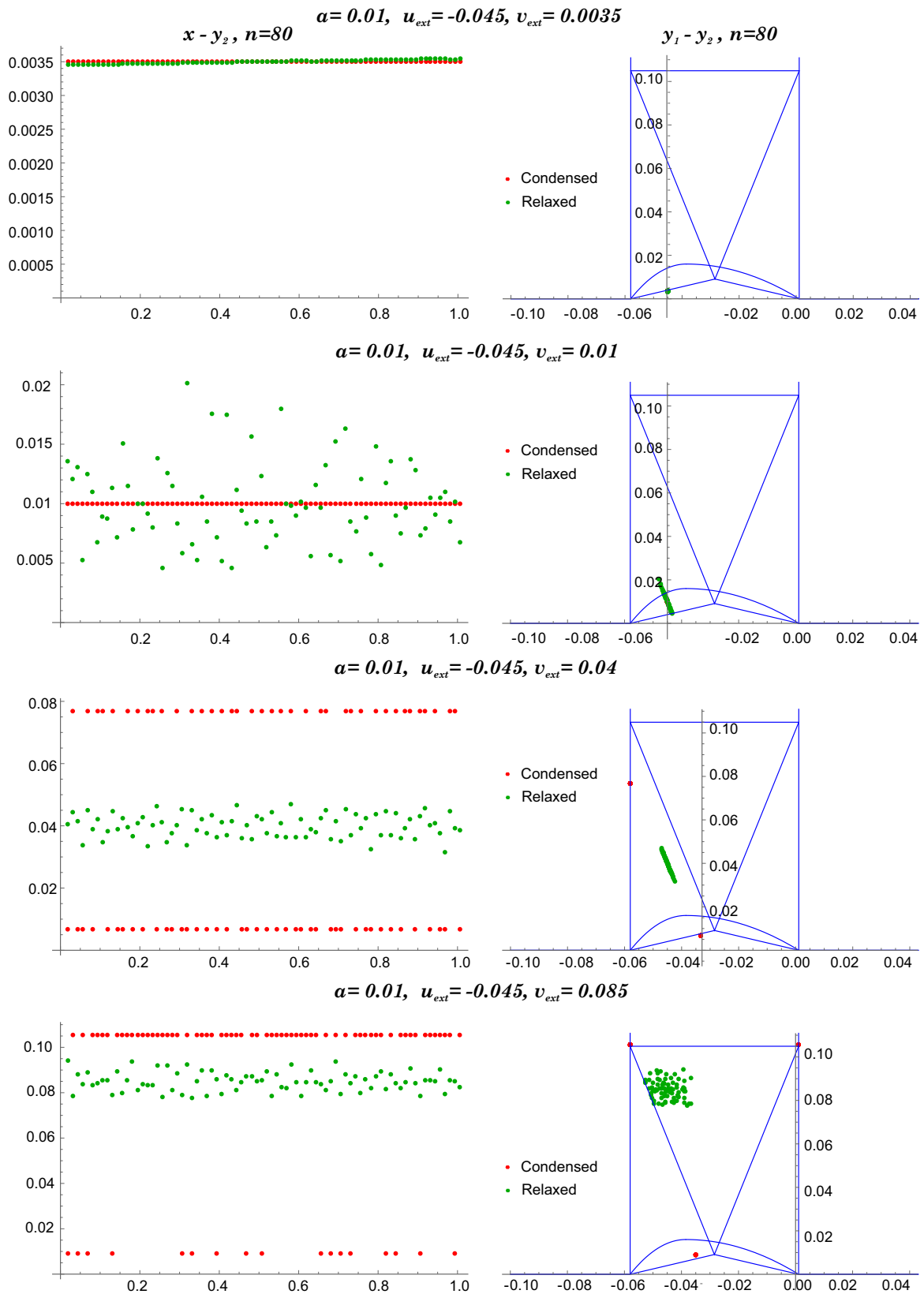


Figure 4.8: Minimization with exact initial guess plus random perturbation ($\alpha = 0.01$) for increasing boundary values u_{ext}, v_{ext} . Left column: $y_2 = v'(x)$ versus position x of the beam, right column: points of the approximate minimizers (y_1, y_2) within relaxation domains as depicted in Fig. 4.6. Comparison from the condensed and relaxed energies for a mesh with 80 elements.

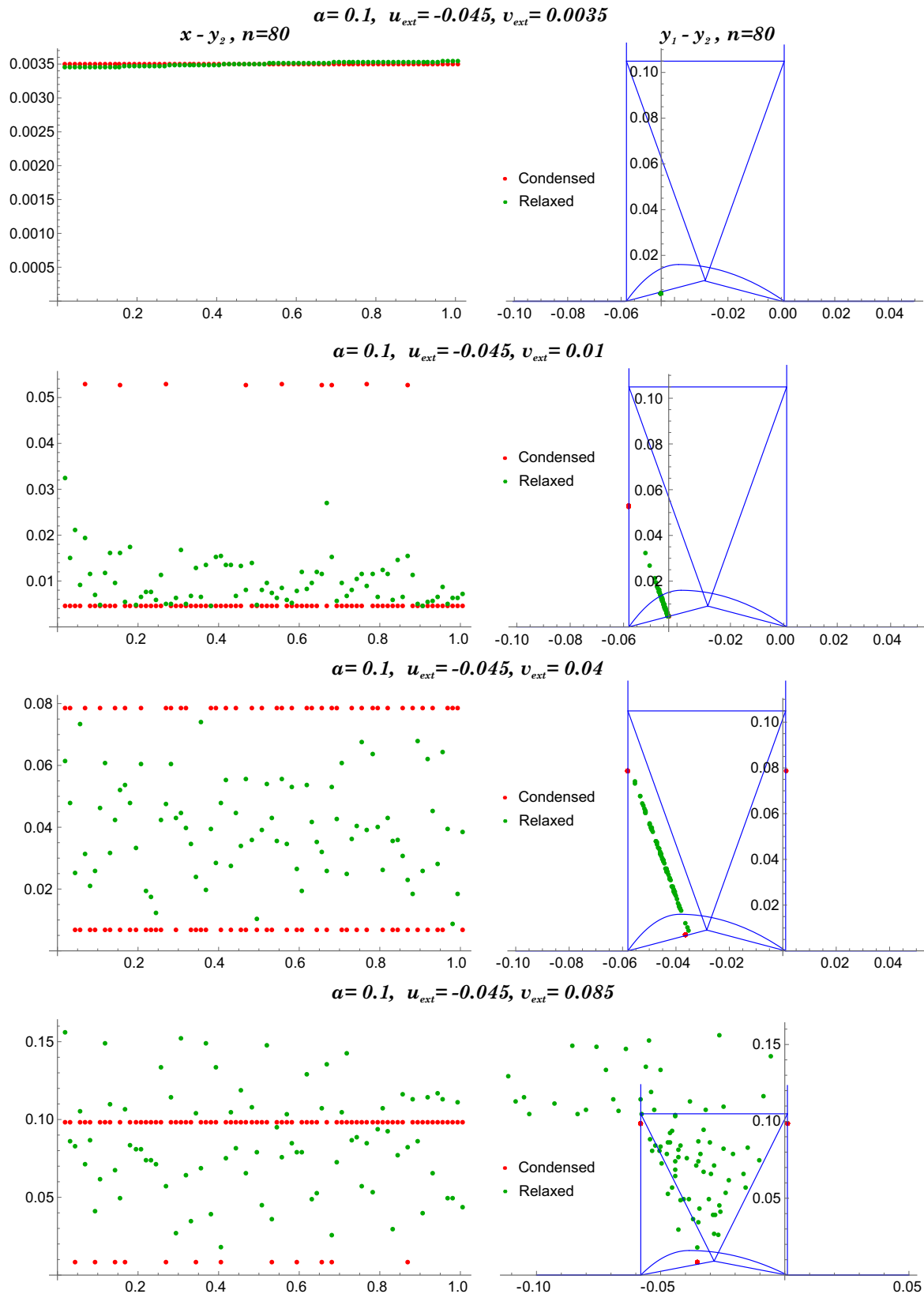


Figure 4.9: Minimization with exact initial guess plus random perturbation ($\alpha = 0.1$) for increasing boundary values u_{ext}, v_{ext} . Left column: $y_2 = v'(x)$ versus position x of the beam, right column: points of the approximate minimizers (y_1, y_2) within relaxation domains as depicted in Fig. 4.6. Comparison from the condensed and relaxed energies for a mesh with 80 elements.

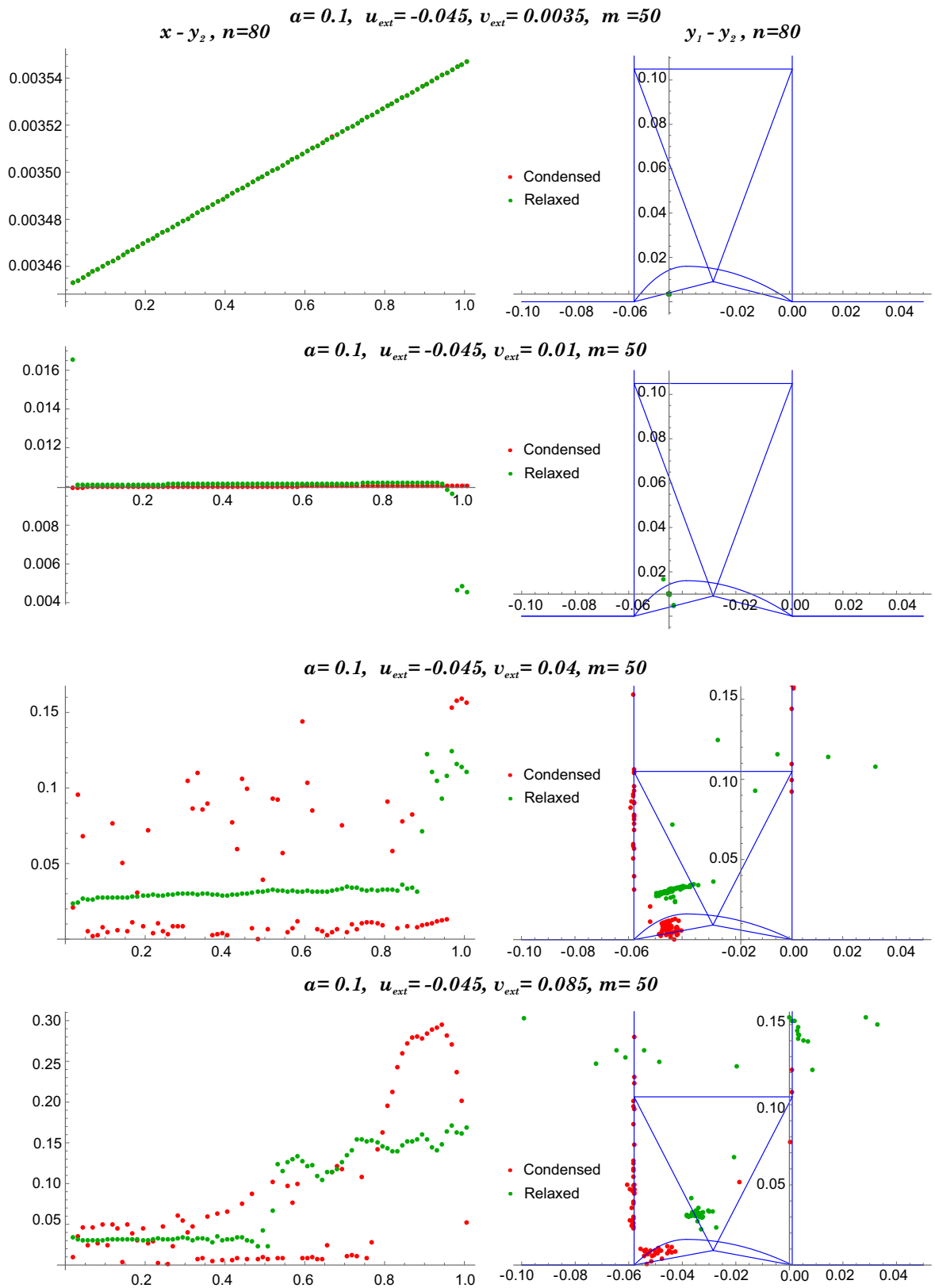


Figure 4.10: Minimization with perturbed initial guess plus time-increment for increasing boundary values u_{ext}, v_{ext} . Left column: $y_2 = v'(x)$ versus position x of the beam, right column: points of the approximate minimizers (y_1, y_2) within relaxation domains as depicted in Fig. 4.6. Comparison from the condensed and relaxed energies for a mesh with 80 elements.

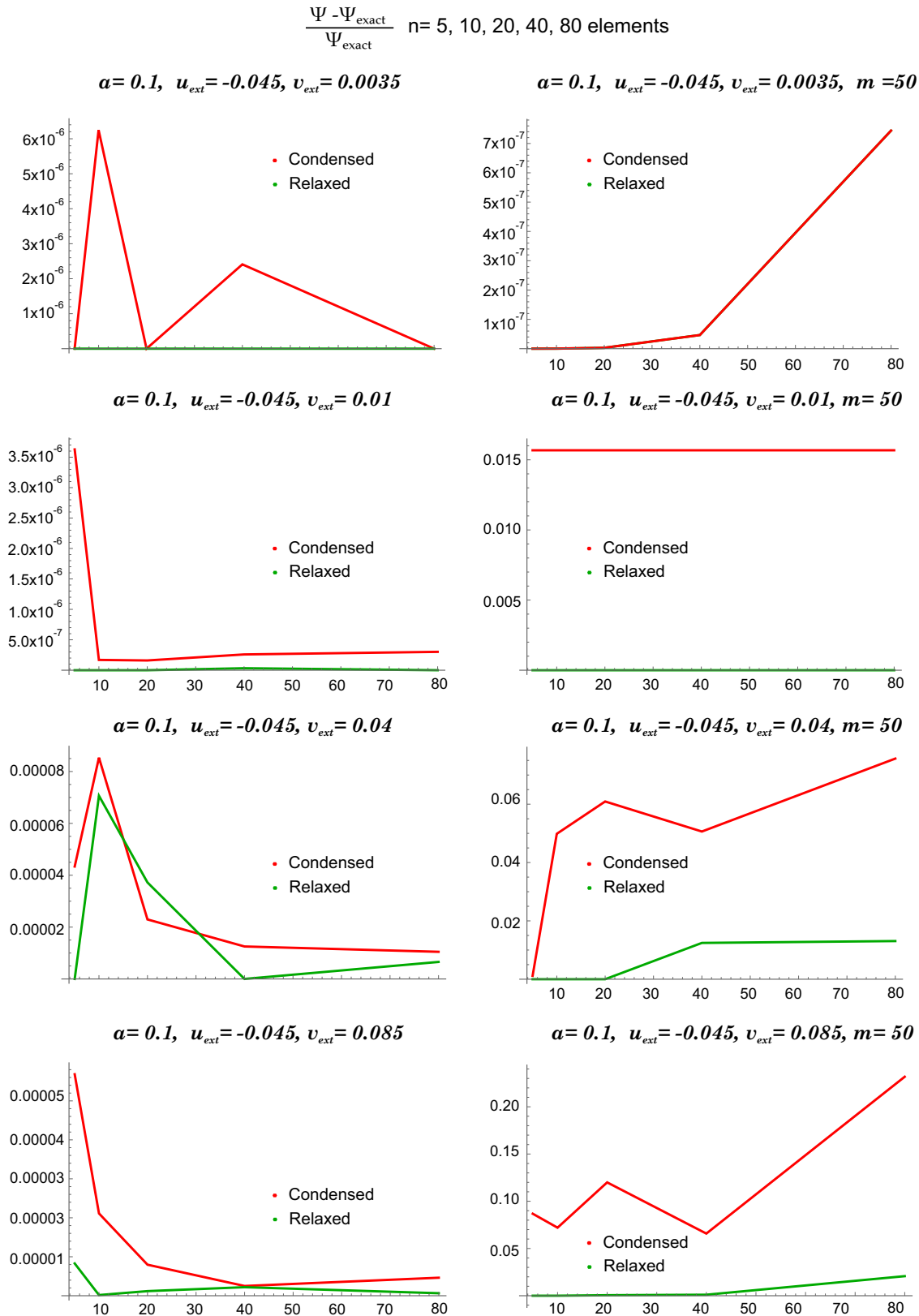


Figure 4.11: Comparison of the relaxed and condensed energy with the energy comprising the exact solution for the beam with 80 elements mesh, applying random perturbation and increasing boundary values for $u_{\text{ext}}, v_{\text{ext}}$. Right panel with time-discretization, left panel without.

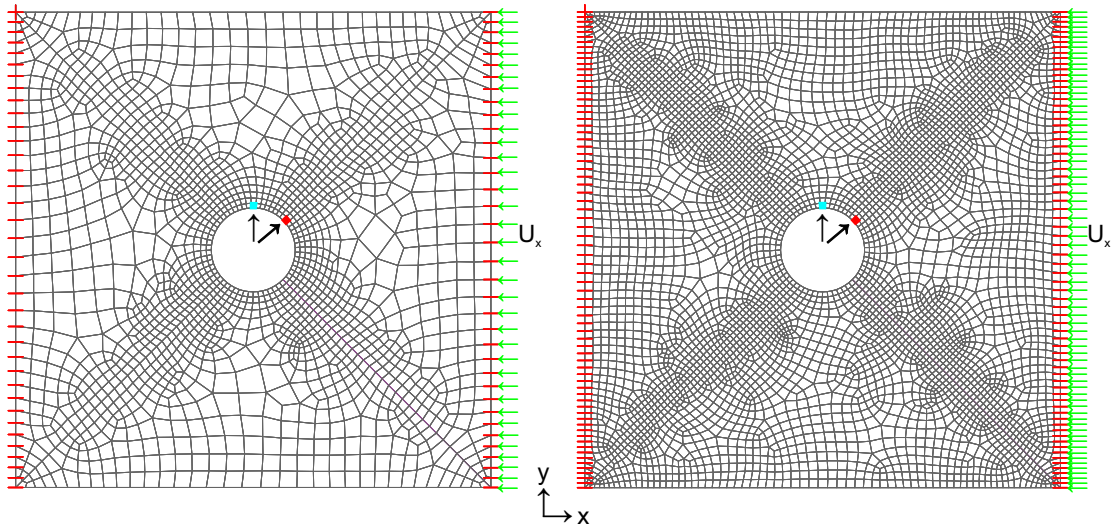


Figure 4.12: A plate with a circular hole subject to a given displacement in x -direction on the right-hand side. The figure to the left shows the coarse mesh with 1793 elements and that to the right the fine mesh with 4917 elements. The elements employed for the stress plots are marked in red and cyan.

4.6.1 A plate with a hole

A square plate with the dimensions 10 mm x 10 mm and a centrally located hole of radius 1.25 mm is investigated. The left-hand side of the plate is fixed and it is subject to displacements in x -direction along the right-hand side. The applied displacements are linearly increasing in time. Unlike the studied plate in Sec. 3.1.9, we consider now loading in compression in order to study the critical case for granular materials under pressure. Two unstructured meshes are computed, a coarse one with 1793 elements and a finer mesh with 4917 elements. The meshes are shown in Fig. 4.12.

Finite element computations are performed using the finite element analysis program FEAP, (Taylor and Govindjee 2022). Standard hexahedral (8-Nodes) elements are used, they are restricted in the 3^{rd} direction employing plane strain conditions. Stresses are calculated as analytical derivatives of the energies with respect to the strains. Tangent operators are calculated as second derivatives of the energies with respect to the strains, numerically via perturbation. Equilibrium states are obtained by standard Newton-Raphson procedure.

For the computations, we use the same material parameters as in the one-dimensional case taken from a modified Mohr-Coulomb material model, see (Shen, Shi, and Barton 2018), with bulk modulus $K = 3.9$ GPa, shear modulus $\mu = 2.8$ GPa, internal friction angle $\phi = 32^\circ$, cohesion $c = 25$ MPa, Poisson's ratio $\nu = 0.25$, and tensile strength $\sigma_t = 5$ MPa. Under load increment, the elements in the neighborhood of the hole start to plastify first. Therefore, we compare the results for the model employing the relaxed energy at the marked elements adjacent to the hole for both meshes. The values are taken from a specific integration point at these elements. We

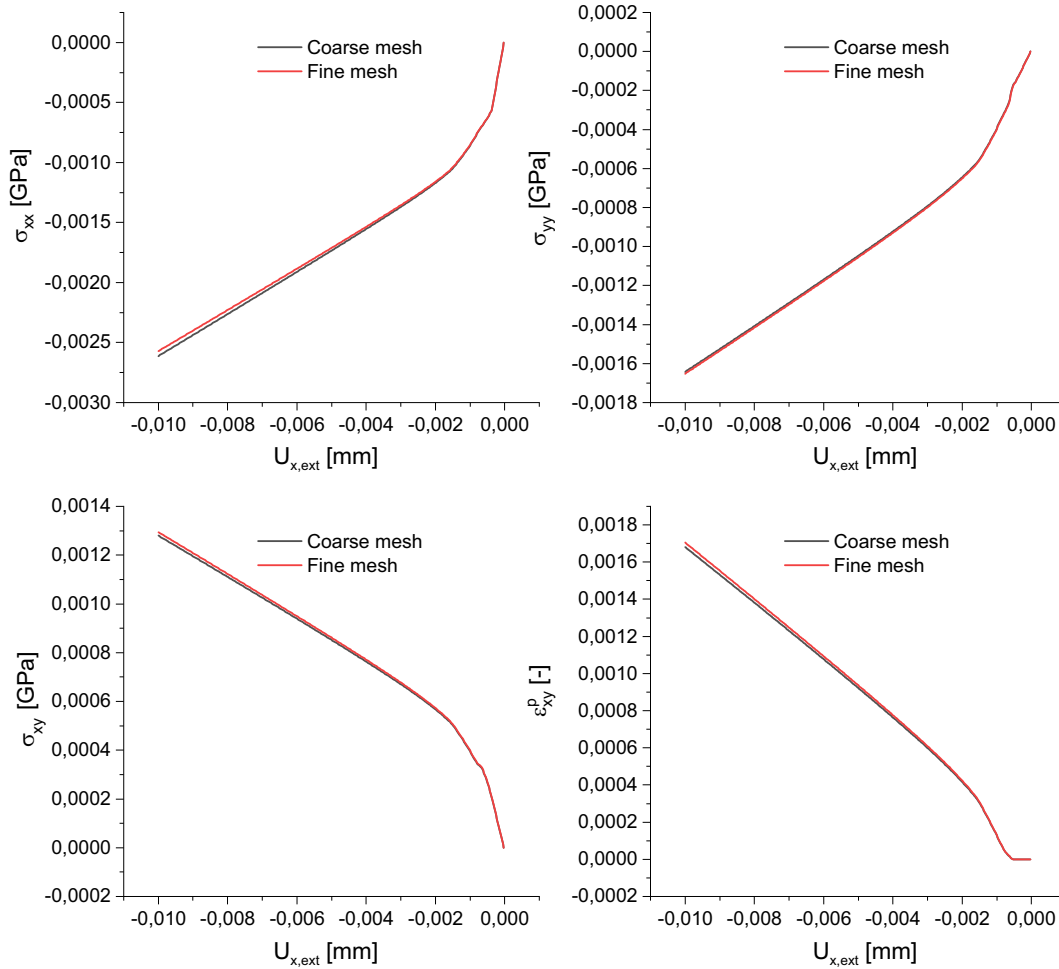


Figure 4.13: Square plate with circular hole: from top left to bottom right: stresses σ_{xx} , at the marked elements in cyan, and σ_{yy} , σ_{xy} and plastic strain ε_{xy}^p , at the marked elements in red, as a function of the external boundary displacement $u_{x,ext}$.

would like to mention, that a comparison to the condensed energy is not possible, as the lack of convexity causes severe numerical instabilities. Therefore, only the behavior of the relaxed model can be inferred from the results below.

The final external displacement is reached employing 100 load steps. The corresponding strains switch from domain Y_1 into domain Y_2 , inducing an initiation of microstructure. In Fig. 4.13, we show the stresses and plastic strains (calculated as the difference of total and elastic strains) at the elements marked in Fig. 4.12 against the external displacements. The point marked in cyan color in Fig. 4.12 correspond to the Gauss-integration point closest to the vertical axis of symmetry. The point marked in red color in Fig. 4.12 correspond to the Gauss-integration point closest to the diagonal. A global comparison for a force-displacement diagram at the free edge to the right of the plate can be seen in Fig. 4.14.

The distribution of the stresses σ_{yy} and σ_{xy} at the same instant are given in Fig. 4.15. It can be seen, that for both meshes the results agree very well for local and global quantities. Microstructure is initiating at the same positions and load step despite the different spatial discretization. Contours of the plastic strains are shown in Fig. 4.16

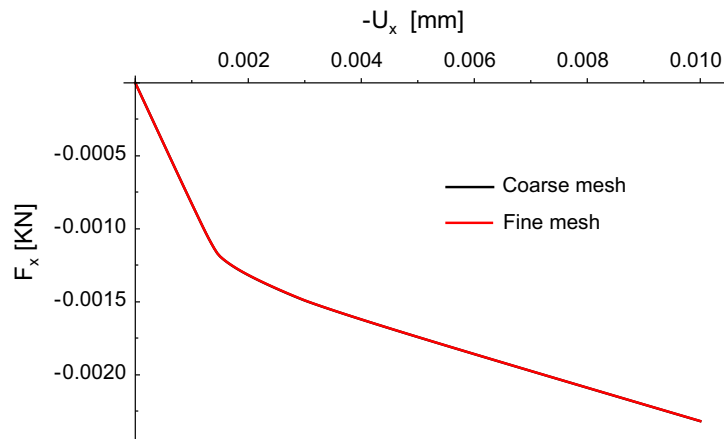


Figure 4.14: Square plate with circular hole: force-displacement diagram at the free end to the right of the plate.

for a state shortly after microstructure initiation at $u_{\text{ext}} = 0.0014$ mm. This demonstrates, that the relaxed model is mesh independent and capable of capturing the material behavior in different zones of relaxation.

4.6.2 Double notch

The next boundary value problem is a double-notched specimen fixed at the bottom, and exposed vertically to time-dependent displacement in y -direction at the top edge. The specimen has the dimensions 18 mm x 50 mm and a thickness of 3 mm. We fix the movement in z -direction, implying a plane strain state for all computations. The upper edge is loaded linearly into a total magnitude of $u_y = -0.04$ mm. Two spatial discretizations using tri-linear hexahedral elements are considered, giving a coarse mesh with 1147 elements, and a finer mesh with 2898 elements, as can be seen in Fig. 4.17. The Finite element computations are performed using FEAP software.

We employ in our computations the same material parameters from the modified Mohr-Coloumb material model implemented in the plate with a hole boundary value problem. Under loading the zones around the notches start to plastify first, and then the microstructure initiation proceeds to spread along the center line connecting the notches. The global quantities from the free edge to the top of the specimen can be seen in Fig. 4.18. In addition to a local comparison of the stresses against the external displacement at the marked elements (in red) at a specific integration point as shown in Fig. 4.19.

We observe a very good compliance from the coarse and fine meshes, on both the global and the local level, implying mesh-independent behavior under relaxation. Further investigations of the contour plots of the coarse and fine meshes can be inferred from Figs. 4.20 and 4.21. We see in Fig. 4.20 the distribution of the stresses in xx and yy directions at the end of loading time, whereas Fig. 4.21 shows the distribution of the shear stresses for the total loading magnitude, in addition to the

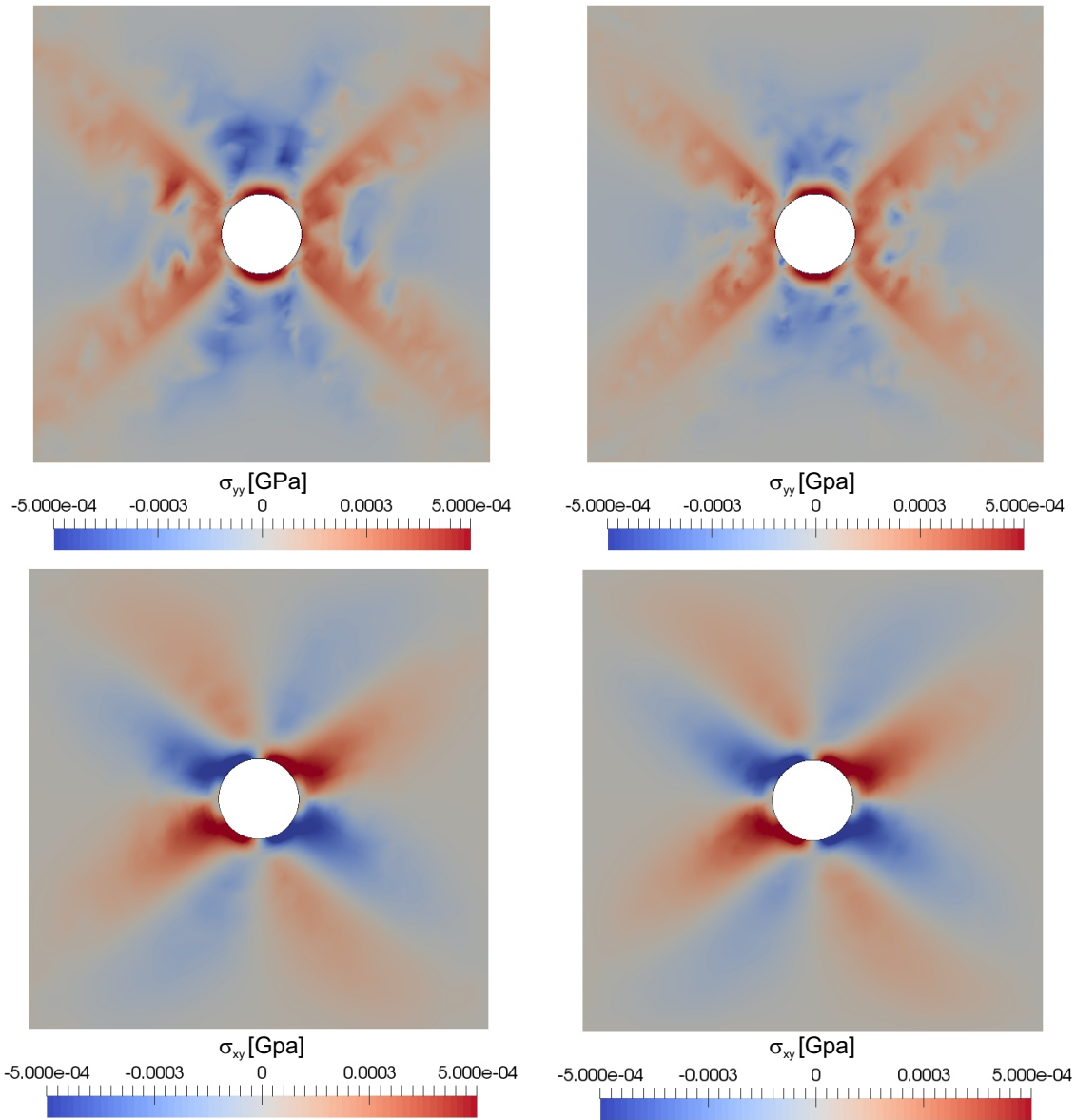


Figure 4.15: Contours from the plate with a hole. Distribution of the stresses σ_{yy} and σ_{xy} . Coarse mesh (left) and fine mesh (right).

contour plots of the plastic strains around a loading value $u_{y,\text{ext}} = 0.01$ mm, taken shortly after the initiation of the microstructure. We come up with the same conclusion, that the relaxed model is capable of capturing the initiation of microstructure to a very good extent. Notice the same global distribution and stress concentration zones. Besides, the evolution of the plastic strains is taking place at the same time and same positions despite the different meshes.

4.6.3 Crack problem

A more sophisticated boundary value problem, namely the cracked plate, will be considered next. The plate has the dimensions 50 mm x 50 mm and a thickness of 5 mm, with a prior opening crack in the plate. The lower side of the plate is fixed and

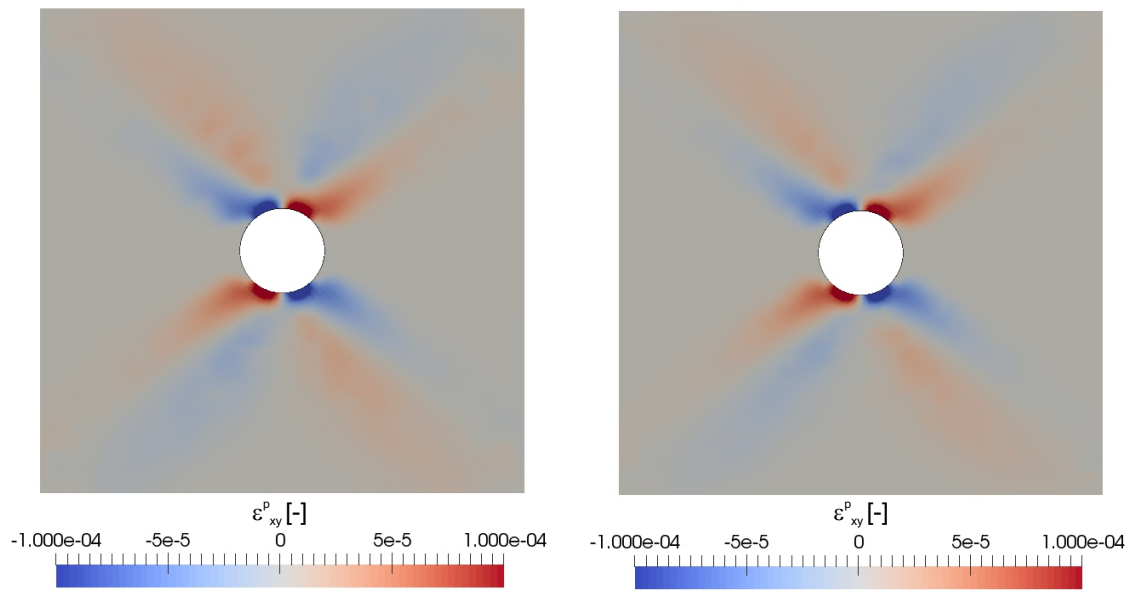


Figure 4.16: Contours from the plate with a hole. Distribution of the plastic strain ε_{xy}^p shortly after microstructure initiation. Coarse mesh (left) and fine mesh (right).

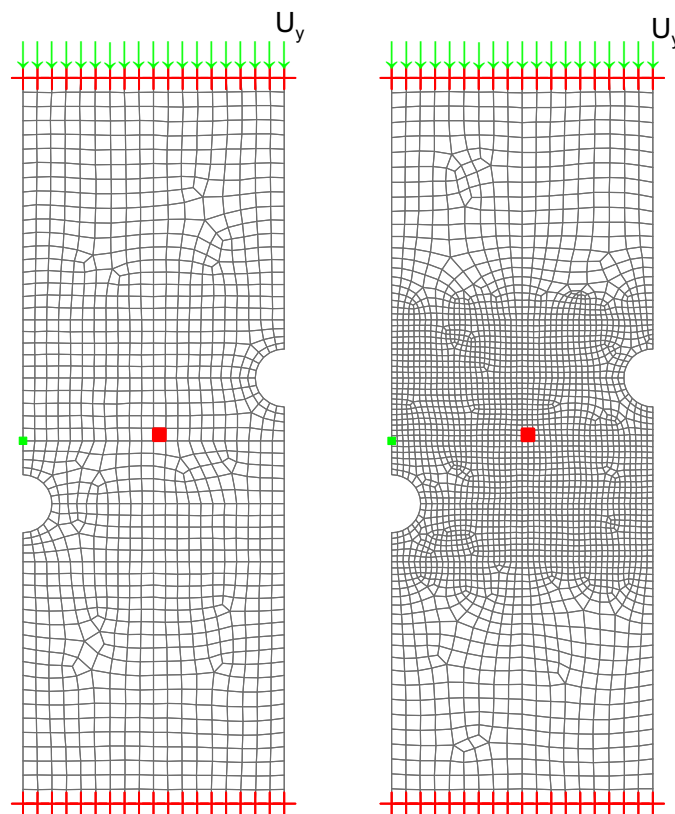


Figure 4.17: A Specimen notched to the left and right sides, subject to a given displacement in y -direction on the top free edge. The figure to the left shows the coarse mesh with 1147 elements and that to the right the fine mesh with 2898 elements. The elements employed for the stress plots are in the center marked in red. The nodes marked in green on the left edge are used for the displacement comparison.

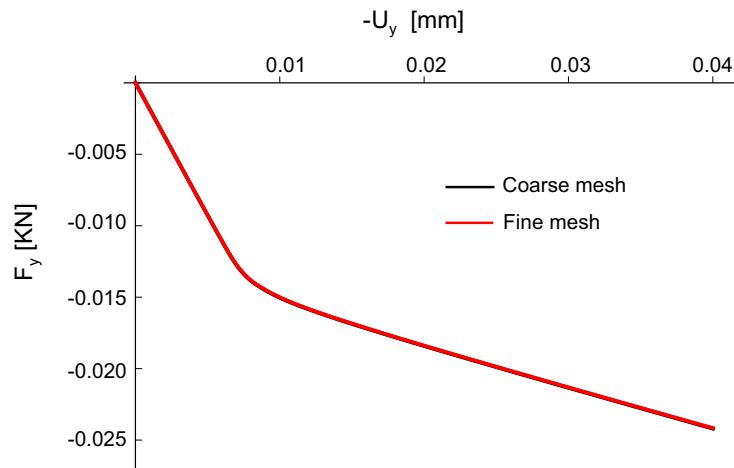


Figure 4.18: Double notch: force-displacement diagram at the free edge to the top of the specimen.

the upper side is compressed by means of a given displacement linearly increasing in time, to a total magnitude of $u_y = -0.05$ mm. Three different meshes are investigated, a coarse mesh with 720 elements, a fine mesh with 2000 elements and a finer mesh with 5600 elements, see Fig. 4.22. Tri-linear hexahedral elements are assigned for the finite element computations, with a fixed thickness, z - direction, implying a plane strain state for all computations.

The global response in terms of the force-displacement diagram in y - direction from the upper free edge of the plate is shown in Fig. 4.23. The curves are matching despite the different mesh sizes.

An additional comparison is provided at the marked elements to the top of the crack tip, as given in Fig. 4.24. Shown are the shear stress components and the evolving plastic strains from the different meshes. We observe very good results, even though the shear stresses from the very fine mesh is a little bit deviated, but this is due to the effect of refinement for the local comparison and not a mesh-dependent evidence. As the plastic strains are complying very well. An additional evidence for the mesh-independency can be observed even from the global distribution of the shear stresses given in Fig. 4.25 for the three meshes. The same distribution and concentration domains are obtained in the different contour plots.

In the presented effective model and the subsequent examples, only an initiation of the microstructure was captured. Therefore, the goal of the next section is to investigate a detailed time-incremental evolution of the microstructure.

4.7 Evolution of the microstructure

The aforementioned inelastic material, with a non-quasiconvex free energy seen in Eq. 4.2.17, tends to reduce its energy under energy minimization and attains an energy minimum. However, this does not happen through homogeneous deformation

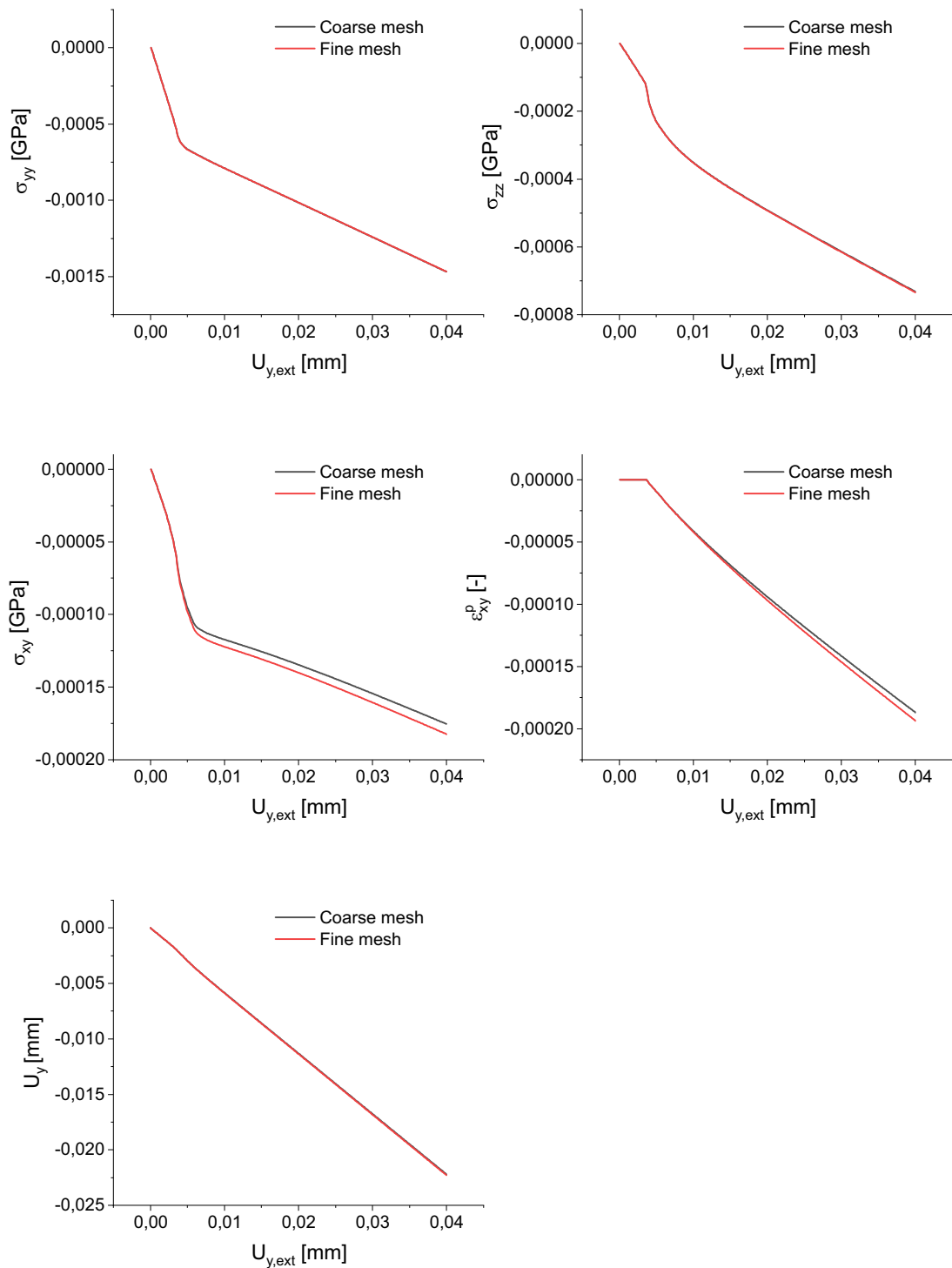


Figure 4.19: Double notch: from top left to bottom left: stresses σ_{yy} , σ_{zz} , σ_{xy} and plastic strain ϵ_{xy}^p , at the marked elements in red, and the displacement u_y , at the marked node in green, as a function of the external boundary displacement $u_{y,ext}$.

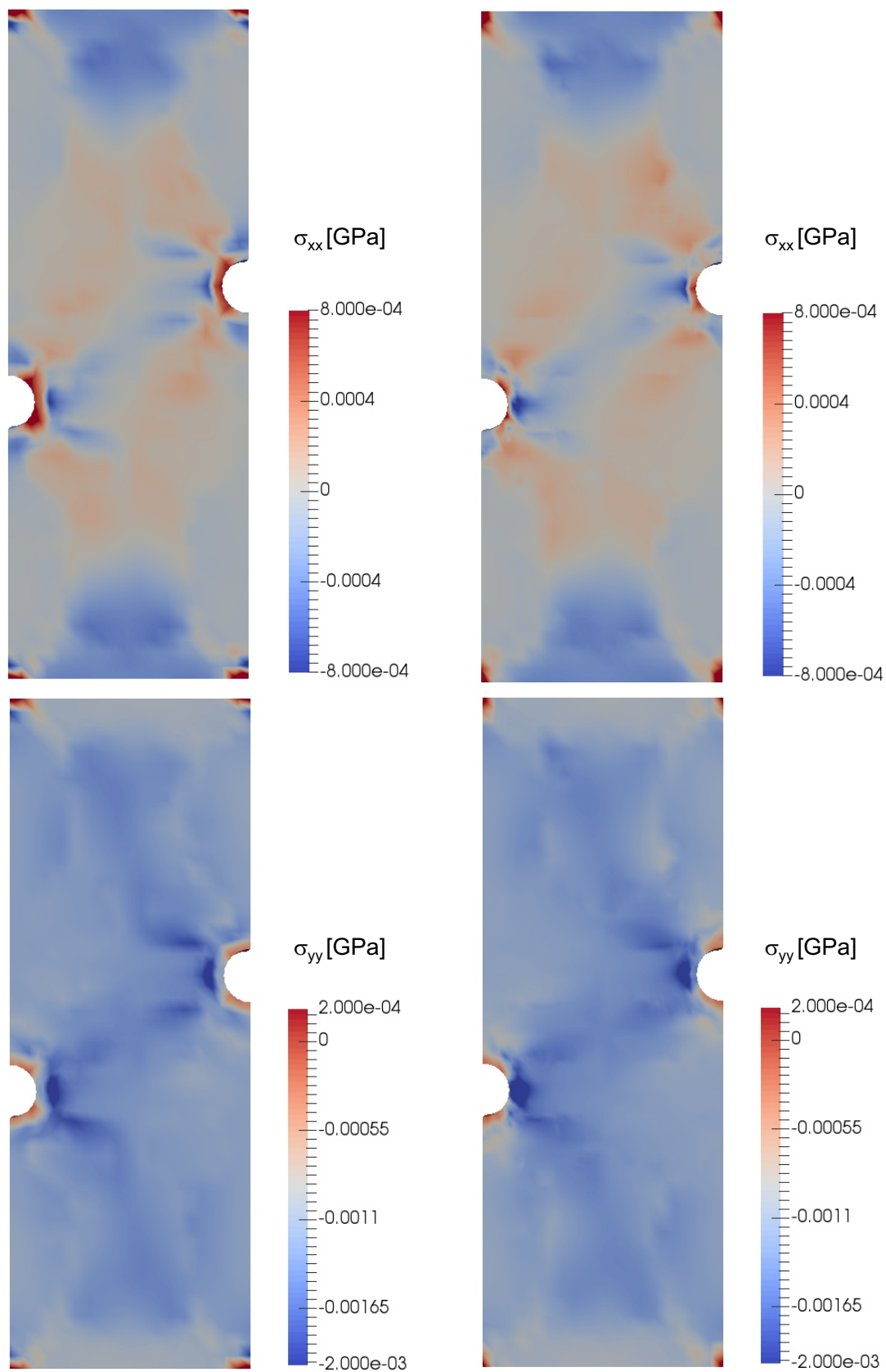


Figure 4.20: Contours from the double notch problem. Distribution of the stresses σ_{xx} and σ_{yy} . Coarse mesh (left) and fine mesh (right).

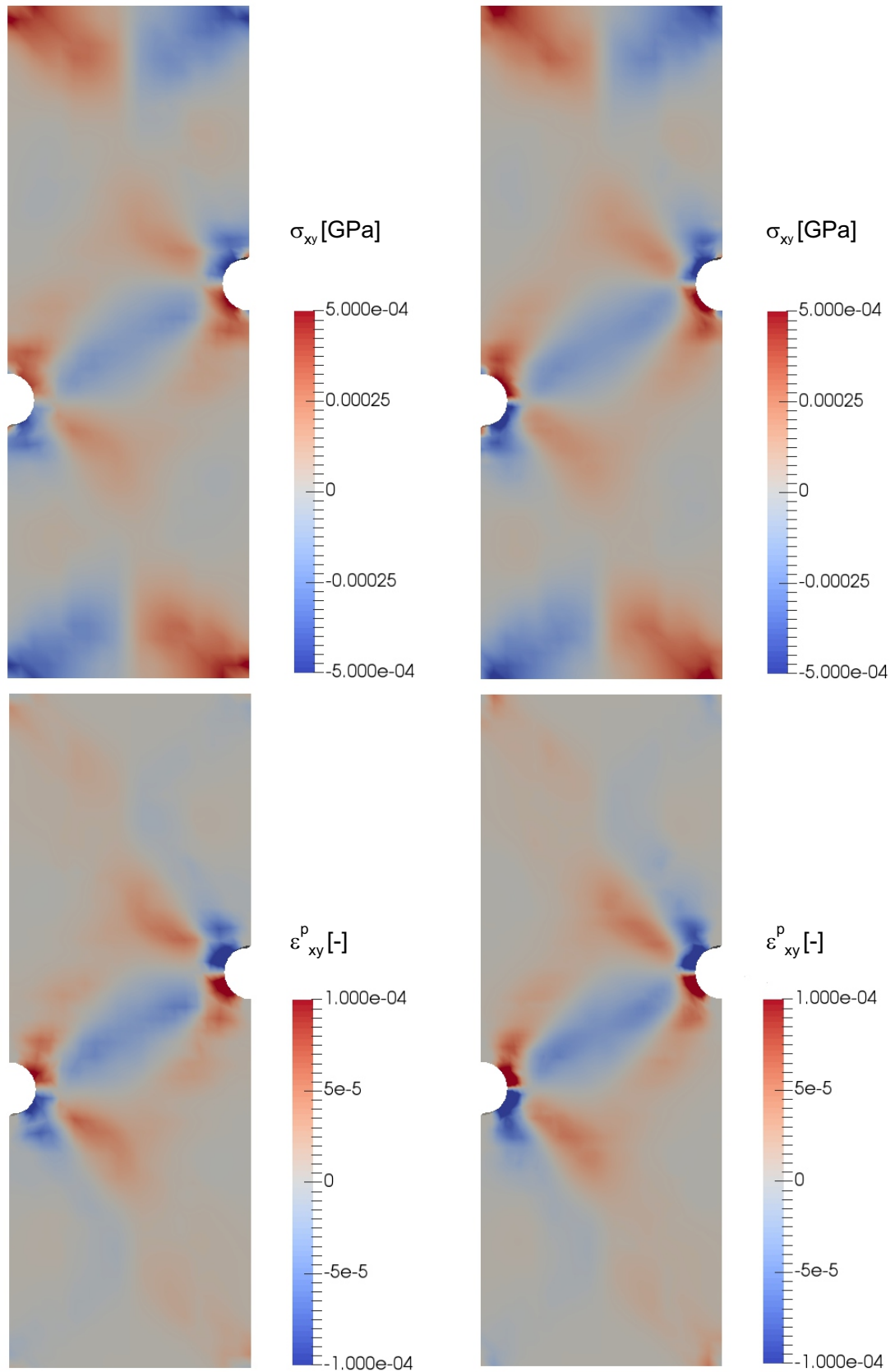


Figure 4.21: Contours from the double notch problem. Distribution of the shear stresses σ_{xy} at the end of loading time and the plastic strain ε_{xy}^p shortly after microstructure initiation. Coarse mesh (left) and fine mesh (right).

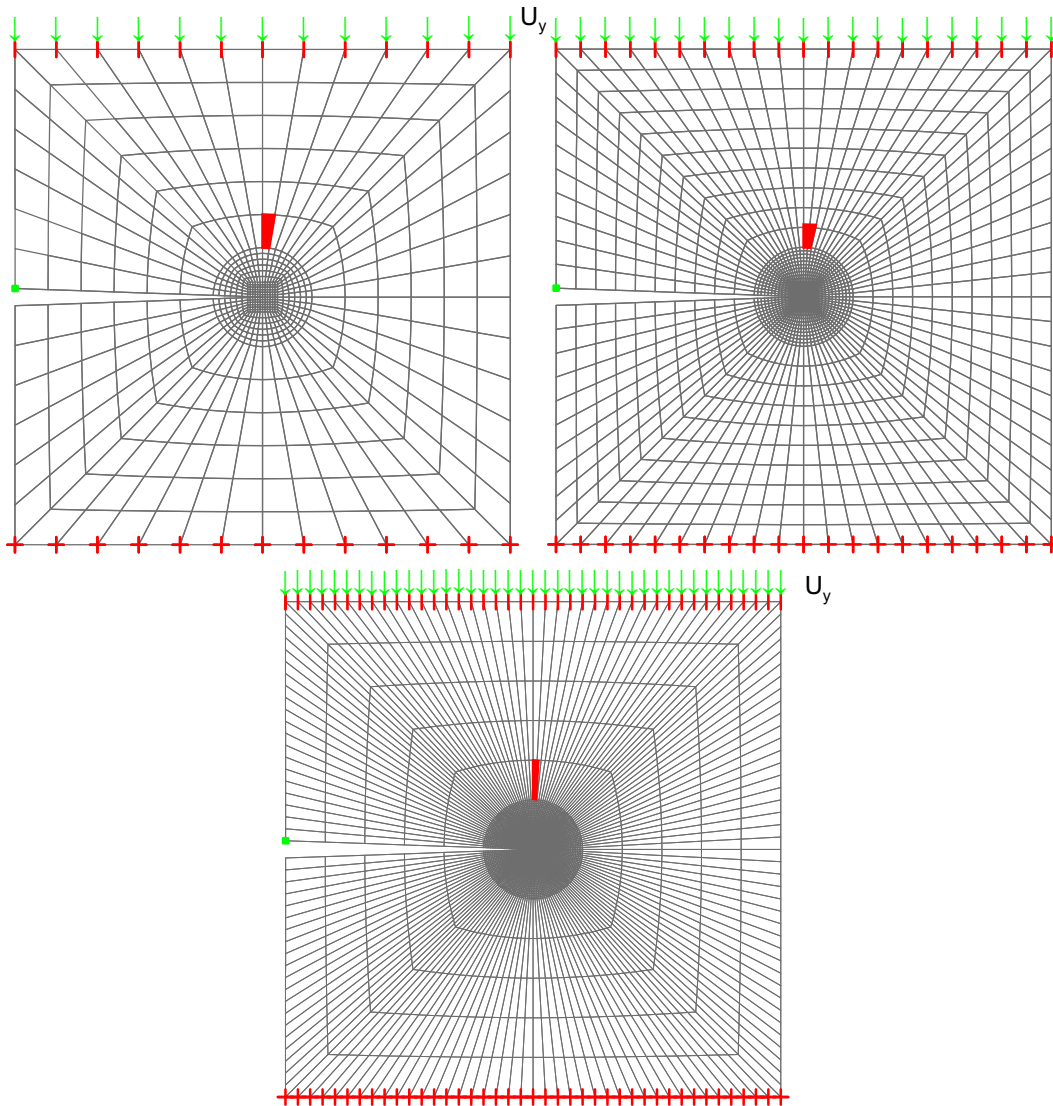


Figure 4.22: Crack problem: a coarse mesh with 720 elements to the left, a fine mesh with 2000 elements to the right and a finer mesh with 5600 elements to the bottom. The elements marked in red are employed for the of the stress comparison and the green nodes to the left are for the displacement comparison.

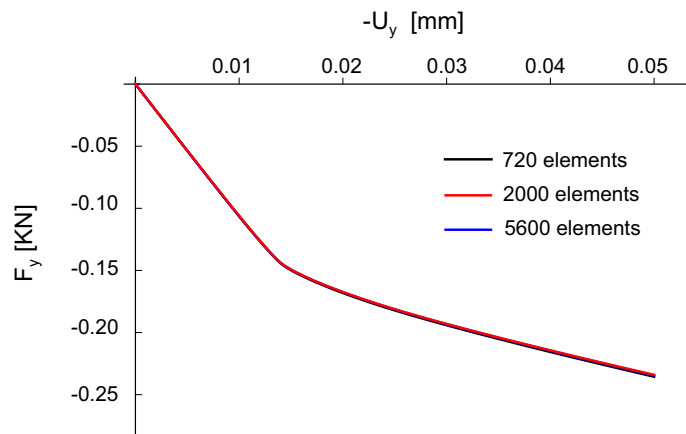


Figure 4.23: Crack problem: force-displacement diagram at the free edge to the top of the plate.

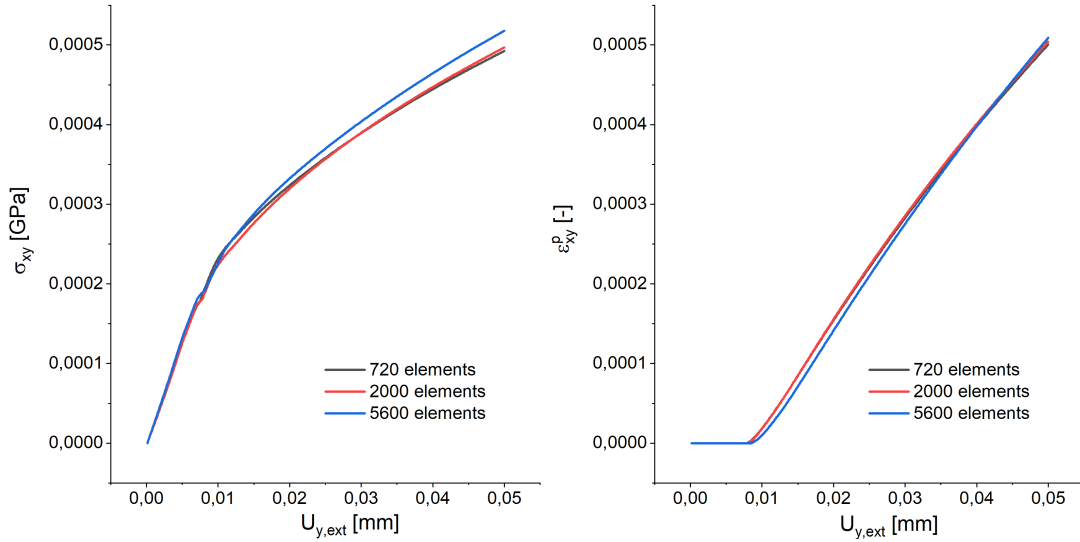


Figure 4.24: Crack problem: shear stresses in xy plane to the left and plastic strains ϵ_{xy}^p to the right.

state, but it rather breaks up into finer-scale microstructure. Therefore, we need a statistical description for these small-scale structures, by identifying probability measures, here the volume fractions. These volume fractions contribute to effective quantities by applying volume averaging for the small-scale structures at the micro-scale into the macro-scale. This scheme is called relaxation (refer to Sec. 2.5.3). An approximation of the convex envelope for the free energy is computed, due to the fact that the computation of a quasi-convex envelope is in general too complicated.

The material under investigation shows an elastic behavior, as long as the loading pairs $[\text{tr}\epsilon, \text{dev}\epsilon]$ are within domain Y_1 , see the right panel of Fig. 4.6. Nevertheless, as the material leaves the elastic region, the findings from the relaxation approach presented in Sec. 4.3 have shown different relaxed regions depending on the sides of the interval $[\xi_{\min}, \xi_{\max}]$ on which the function $\rho(\text{tr}\epsilon)$ is defined, meaning that for each relaxed zone a mixed state is encountered. Therefore, the statistical measure prescribing the evolving microstructure shall distinguish between the different domains. Domain Y_1 accounts for an elastic or one-phase region, domains Y_2 mixes elastic and plastic behavior in a two-phase region with different contributions, whether from the side of ξ_{\min} or ξ_{\max} . On the other hand, domain Y_3 prescribes a three-phase region for the elastic and plastic contributions from both sides. Lastly, domain Y_4 is a two-phase region with only plastic evolution and no elastic behavior is observed more. Hence, we consider three volume fractions $\lambda_0, \lambda_1, \lambda_2$, enforcing $\lambda_i \geq 0$ and $\sum_{i=0}^2 \lambda_i = 1$ for $i = 0, 1, 2$.

The introduced volume fractions correspond to a new set of internal variables $e_{p,1}, e_{p,2}, p_1, p_2$ (plastic strain histories and hardening parameters). Now we can formulate the

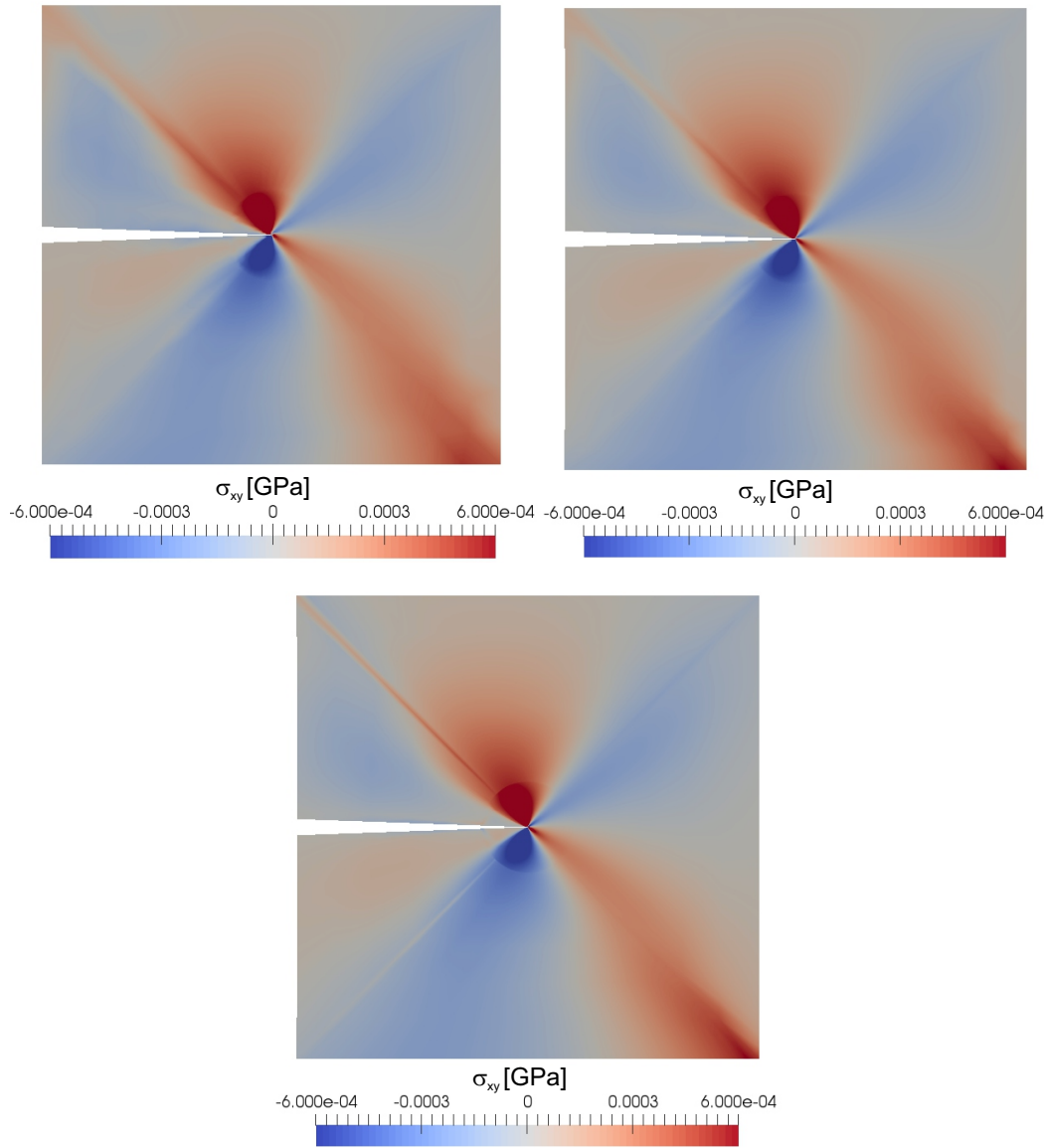


Figure 4.25: Crack problem: contours of the shear stresses in xy plane, coarse mesh top left, fine mesh top right and a finer mesh lower lane.

relaxed energy in terms of these newly defined internal variables

$$\begin{aligned}
 \Psi_{\text{eff}} &= \Psi_{\text{vol}} + \Psi_{\text{dev}}, \\
 &= \frac{K}{2} \frac{(\text{tr}\boldsymbol{\varepsilon} - \lambda_1 \xi_{\text{min}} - \lambda_2 \xi_{\text{max}})^2}{1 - \lambda_1 - \lambda_2} + \mu \|\text{dev}\boldsymbol{\varepsilon} - \lambda_1 \mathbf{e}_{p,1} - \lambda_2 \mathbf{e}_{p,2}\|^2 \\
 &\quad + \frac{\beta}{2} (\lambda_1 p_1^2 + \lambda_2 p_2^2).
 \end{aligned} \tag{4.7.1}$$

In order to model a time-continuous evolution of the microstructure, we need to capture the dissipation required to change from one state in time to the next. Thus, we define the effective dissipation potential as

$$\Delta_{\text{eff}} = \frac{1}{2\gamma} (\dot{\lambda}_1^2 + \dot{\lambda}_2^2) + \begin{cases} 0 & \text{for } \|\dot{\mathbf{e}}_{p,i}\| \leq \dot{p}_i, \dot{\lambda}_i \geq 0, \\ \infty & \text{otherwise,} \end{cases} \quad i = 1, 2. \tag{4.7.2}$$

where $\gamma > 0$ is a viscous parameter applying time regularization. Consider a finite time increment $\Delta t = t_{n+1} - t_n$, we can write the dissipation distance as follows

$$\begin{aligned}
& D(\lambda_{i,0}, \lambda_{i,1}, p_{i,0}, p_{i,1}, \mathbf{e}_{p,i,0}, \mathbf{e}_{p,i,1}) \\
&= \inf_{\lambda_i} \left\{ \int_{t_0}^{t_1} \Delta_{\text{eff}}(\dot{\lambda}_i(t), \dot{\mathbf{e}}_{p,i}(t), \dot{p}_i(t)) dt \mid p_i(0) = p_{i,0}, p_i(1) = p_{i,1}, \right. \\
&\quad \left. \lambda_i(0) = \lambda_{i,0}, \lambda_i(1) = \lambda_{i,1}, \mathbf{e}_{p,i}(0) = \mathbf{e}_{p,i,0}, \mathbf{e}_{p,i}(1) = \mathbf{e}_{p,i,1} \right\}, \\
&= \frac{1}{2\gamma} \left(\left(\frac{\lambda_{1,1} - \lambda_{1,0}}{\Delta t} \right)^2 + \left(\frac{\lambda_{2,1} - \lambda_{2,0}}{\Delta t} \right)^2 \right) \\
&\quad + \begin{cases} 0 & \text{for } \|\mathbf{e}_{p,i,1} - \mathbf{e}_{p,i,0}\| \leq p_{i,1} - p_{i,0}, \\ \infty & \text{otherwise.} \end{cases} \quad (4.7.3)
\end{aligned}$$

Then the minimization problem to solve is given by

$$\{\lambda_{1,n+1}, \lambda_{2,n+1}\} = \arg \inf_{\lambda_1, \lambda_2} \left\{ \dot{\Psi}_{\text{eff}}(\boldsymbol{\varepsilon}_{n+1}, \mathbf{e}_{p,i,n}, p_{i,n}, \lambda_{i,n}) + D(\mathbf{e}_{p,i,n}, p_{i,n}, \lambda_{i,n}) \right\}. \quad (4.7.4)$$

Returning the time-incremental evolution equations for the set of internal variables

$$\mathbf{e}_{p,i,n+1} = \mathbf{e}_{p,i,n} + \frac{1}{2\mu + \beta} \left(2\mu \|\text{dev} \boldsymbol{\varepsilon}_{n+1}\| - \beta p_{i,n} \right)_+ \text{sign dev} \boldsymbol{\varepsilon}_{n+1}, \quad (4.7.5)$$

$$p_{i,n+1} = p_{i,n} + \|\mathbf{e}_{p,i,n+1} - \mathbf{e}_{p,i,n}\|, \quad (4.7.6)$$

$$\lambda_{i,n+1} = \lambda_{i,n} + \gamma \Delta t (q_i)_+, \quad (4.7.7)$$

here Δt is the time-increment and q_i is the thermodynamically driving force prescribing the evolution of the microstructure, which can be computed according to the second law in thermodynamics as follows

$$\begin{aligned}
q_i &= -\frac{\partial \Psi_{\text{eff}}}{\partial \lambda_i}(\text{tr} \boldsymbol{\varepsilon}_{n+1}, \text{dev} \boldsymbol{\varepsilon}_{n+1}, \mathbf{e}_{p,i,n}, p_{i,n}, \lambda_{i,n}), \quad i = 1, 2, \\
&= \frac{K \xi_{\text{max,min}}(\text{tr} \boldsymbol{\varepsilon} - \lambda_1 \xi_{\text{min}} - \lambda_2 \xi_{\text{max}})}{1 - \lambda_1 - \lambda_2} - \frac{K(\text{tr} \boldsymbol{\varepsilon} - \lambda_1 \xi_{\text{min}} - \lambda_2 \xi_{\text{max}})^2}{2(1 - \lambda_1 - \lambda_2)^2} \\
&\quad - \frac{\beta}{2} p_i^2 + 2\mu(\text{dev} \boldsymbol{\varepsilon} - \lambda_1 \mathbf{e}_{p,1} - \lambda_2 \mathbf{e}_{p,2}) : \mathbf{e}_{p,i}.
\end{aligned} \quad (4.7.8)$$

4.7.1 Initiation

A critical point in computing the evolution of microstructure is to check its initiation, i.e. to check whether it is getting energetically favorable to form a microstructure or not. Considering a similar procedure as in (Kochmann and Hackl 2011), we

maximize the driving force subject to the constraint $p_i = \|\mathbf{e}_{p,i}\|$, then substitute in Eq. 4.7.8 to get

$$q_{i,ini}(\text{dev}\boldsymbol{\varepsilon}, \text{tr}\boldsymbol{\varepsilon}, \mathbf{e}_{p,i}, p_i, \lambda_i) = \lim_{\lambda_i \rightarrow 0} q_i(\text{dev}\boldsymbol{\varepsilon}, \text{tr}\boldsymbol{\varepsilon}, \mathbf{e}_{p,i}, p_i, \lambda_i), \quad (4.7.9)$$

giving

$$q_{1,ini}(\lambda_1 = 0) = \frac{K\xi_{\min}(\text{tr}\boldsymbol{\varepsilon} - \lambda_2\xi_{\max})}{1 - \lambda_2} - \frac{K(\text{tr}\boldsymbol{\varepsilon} - \lambda_2\xi_{\max})^2}{2(1 - \lambda_2)^2} - \frac{\beta}{2}\|\mathbf{e}_{p,1}\|^2 + 2\mu(\text{dev}\boldsymbol{\varepsilon} - \lambda_2\mathbf{e}_{p,2}) : \mathbf{e}_{p,1}, \quad (4.7.10)$$

$$q_{2,ini}(\lambda_2 = 0) = \frac{K\xi_{\max}(\text{tr}\boldsymbol{\varepsilon} - \lambda_1\xi_{\min})}{1 - \lambda_1} - \frac{K(\text{tr}\boldsymbol{\varepsilon} - \lambda_1\xi_{\min})^2}{2(1 - \lambda_1)^2} - \frac{\beta}{2}\|\mathbf{e}_{p,2}\|^2 + 2\mu(\text{dev}\boldsymbol{\varepsilon} - \lambda_1\mathbf{e}_{p,1}) : \mathbf{e}_{p,2}. \quad (4.7.11)$$

The initial plastic strains and hardening variables maximizing the driving forces result from the equations

$$\frac{\partial q_{1,ini}(\lambda_1 = 0)}{\partial \mathbf{e}_{p,1}} = -\beta \mathbf{e}_{p,1} + 2\mu(\text{dev}\boldsymbol{\varepsilon} - \lambda_2\mathbf{e}_{p,2}) = 0, \quad (4.7.12)$$

$$\frac{\partial q_{2,ini}(\lambda_2 = 0)}{\partial \mathbf{e}_{p,2}} = -\beta \mathbf{e}_{p,2} + 2\mu(\text{dev}\boldsymbol{\varepsilon} - \lambda_1\mathbf{e}_{p,1}) = 0, \quad (4.7.13)$$

giving

$$\mathbf{e}_{p,1,ini} = \frac{2\mu}{\beta}(\text{dev}\boldsymbol{\varepsilon} - \lambda_2\mathbf{e}_{p,2}), \quad p_{1,ini} = \|\mathbf{e}_{p,1,ini}\|, \quad (4.7.14)$$

$$\mathbf{e}_{p,2,ini} = \frac{2\mu}{\beta}(\text{dev}\boldsymbol{\varepsilon} - \lambda_1\mathbf{e}_{p,1}), \quad p_{2,ini} = \|\mathbf{e}_{p,2,ini}\|. \quad (4.7.15)$$

We plug these initial values into the driving forces to get two test conditions, which decide whether the evolution of a specific phase is getting preferable or not. So $test_1$ leads to initiation of λ_1 and $test_2$ leads to initiation of λ_2 . These test conditions are computed as follows

$$q_{1,max} = \frac{K\xi_{\min}(\text{tr}\boldsymbol{\varepsilon} - \lambda_2\xi_{\max})}{1 - \lambda_2} - \frac{K(\text{tr}\boldsymbol{\varepsilon} - \lambda_2\xi_{\max})^2}{2(1 - \lambda_2)^2} - \frac{2\mu^2}{\beta}\|\text{dev}\boldsymbol{\varepsilon} - \lambda_2\mathbf{e}_{p,2}\|^2 + \frac{4\mu^2}{\beta}\|\text{dev}\boldsymbol{\varepsilon} - \lambda_2\mathbf{e}_{p,2}\|^2 = 0, \quad (4.7.16)$$

simplifying gives the relation for $test_1$ implying an evolution of λ_1

$$q_{1,max} = -\frac{K(\text{tr}\boldsymbol{\varepsilon} + (-1 + \lambda_2)\xi_{\min} - \lambda_2\xi_{\max})^2}{2(-1 + \lambda_2)^2} + \frac{2\mu^2}{\beta}\|\text{dev}\boldsymbol{\varepsilon} - \lambda_2\mathbf{e}_{p,2}\|^2 = 0. \quad (4.7.17)$$

analogously, $test_2$ giving the evolution of λ_2 reads as

$$q_{2,max} = -\frac{K(\text{tr}\boldsymbol{\varepsilon} + (-1 + \lambda_1)\xi_{\max} - \lambda_1\xi_{\min})^2}{2(-1 + \lambda_1)^2} + \frac{2\mu^2}{\beta}\|\text{dev}\boldsymbol{\varepsilon} - \lambda_1\mathbf{e}_{p,1}\|^2 = 0. \quad (4.7.18)$$

We have now everything set to show the numerical implementation for the preceding theory.

4.7.2 Numerical treatment

We have derived time-incremental equations suitable for the numerical implementation. The given relaxation scheme returns a well-posed problem under minimization. In order to solve the resulting coupled problem, we apply a staggered scheme, meaning, for each time-step t_{n+1} we have from the boundary conditions and the loading state $\text{tr}\boldsymbol{\varepsilon}_{n+1}$, $\text{dev}\boldsymbol{\varepsilon}_{n+1}$ in addition to the internal variables from the previous time-step $p_{1,n}$, $p_{2,n}$, $\mathbf{e}_{p,1,n}$, $\mathbf{e}_{p,2,n}$, $\lambda_{1,n}$, $\lambda_{2,n}$. The initiation conditions given by $test_1$ in Eq. 4.7.17 and $test_2$ in Eq. 4.7.18 are calculated and three cases are investigated, a) only $test_1$ is satisfied, b) only $test_2$ is satisfied or c) $test_1$ and $test_2$ are satisfied together.

Fulfillment of $test_1$ implies an evolution of the plastic phase-1 with λ_1 , therefore $p_{1,ini,n+1}$, $\mathbf{e}_{p,1,ini,n+1}$ and $q_{1,n+1}$ from Eq. 4.7.8 are computed with $p_{2,n}$, $\mathbf{e}_{p,2,n}$, $\lambda_{2,n}$ to remain fixed. The internal variables corresponding to phase-1 $\mathbf{e}_{p,1,n+1}$, $p_{1,n+1}$, $\lambda_{1,n+1}$ are then updated according to Eqs. 4.7.5, 4.7.6, 4.7.7 respectively.

However, if $test_2$ is fulfilled, then the same steps are done for phase-2 with the internal variables $\mathbf{e}_{p,2,n+1}$, $p_{2,n+1}$, $\lambda_{2,n+1}$ to be updated and the internal variables corresponding to phase-1 are fixed. On the other hand, loading pairs contributing to coupled evolution, i.e. causing a fulfillment of $test_1$ and $test_2$ together, then an evolution of the microstructure is present in the three-phase region. Therefore, the internal variables from both plastic phases shall be updated, but in a staggered way as well. The updated values are then passed to the next time-step. Please notice that as long as the time-step and loading-increment are kept small enough, the order of solving the previous equations should not influence the final results.

Several numerical calculations will be given to emphasize the introduced relaxation scheme. We provide first two examples computed locally, i.e at the material point.

Later on applications using the finite element method for well known boundary value problems are given. The same applied material parameters, as in Sec. 4.6, are used. The material parameters are bulk-modulus $K = 3.9$ GPa, the shear-modulus $\mu = 2.8$ GPa and Poisson's ratio $\nu = 0.25$. The hardening parameter is selected as $\beta = 0.53$ GPa. Nevertheless, the concave function $\rho(\text{tr}\epsilon)$ is beyond our interest, as it is necessary only for the condensed energy, which is proven to cause numerical instability due to the lack of convexity. However, the values for the interval on which the pressure-dependent function is defined are important. Hence, we give the values $\xi_{\min} = -0.0695$ and $\xi_{\max} = 0.00128$. The viscosity term has the value $\gamma = 100 \frac{1}{\text{GPa}\cdot\text{s}}$.

4.7.3 Material subject to uniaxial compression and simple shear

We consider the material is exposed to hydrostatic pressure and simple shear increasing linearly in time with the following values for the strain tensor

$$\epsilon = \begin{pmatrix} -0.0003 \text{ t} & 0.0006 \text{ t} & 0 \\ 0.0006 \text{ t} & -0.0003 \text{ t} & 0 \\ 0 & 0 & -0.0003 \text{ t} \end{pmatrix}, \quad (4.7.19)$$

where a time-increment of $\Delta t = 0.00625$ sec is applied. Under loading the material leaves the elastic region Y_1 to enter the region Y_2 to the side of ξ_{\min} employing a transition from the elastic phase-0 to the plastic phase-2. This leads to an initiation of λ_2 with the corresponding internal variables in phase-2, namely, p_2 and $e_{p,2}$. With further loading, the material enters the three-phase region Y_3 , see the right panel in Fig. 4.6, allowing the initiation of λ_1 with its corresponding internal variables p_1 , $e_{p,1}$ as well.

The resulting stresses and internal variables under uniaxial-pressure can be inferred from Fig. 4.26. Notice the peak around a total time of 32 sec ($\epsilon_{xy} = 0.017$) in the response curve for the shear plane (graph to the top right panel), which refer to the transition from a two-phase into a three-phase region. We can observe that at this transition point, as the microstructure in phase-1 evolves, the driving force q_2 is getting negative, causing no further updates to the internal variables corresponding to phase-2. Therefore, they remain constant for the rest of the loading time.

4.7.4 Material under shearing and constant pressure

In the following test, we subject the material under consideration to constant uniaxial-pressure with shearing in plane $x - y$ increasing in time, according to the next strain tensor

$$\epsilon = \begin{pmatrix} -0.015 & 0.0015 \text{ t} & 0 \\ 0.0015 \text{ t} & -0.015 & 0 \\ 0 & 0 & -0.015 \end{pmatrix}, \quad (4.7.20)$$

The applied time-step is $\Delta t = 0.0025$ sec. The given strains produce loading pairs $[\text{tr}\epsilon, \text{dev}\epsilon]$ that cause a horizontal movement along $\text{tr}\epsilon$ axis at the very beginning,

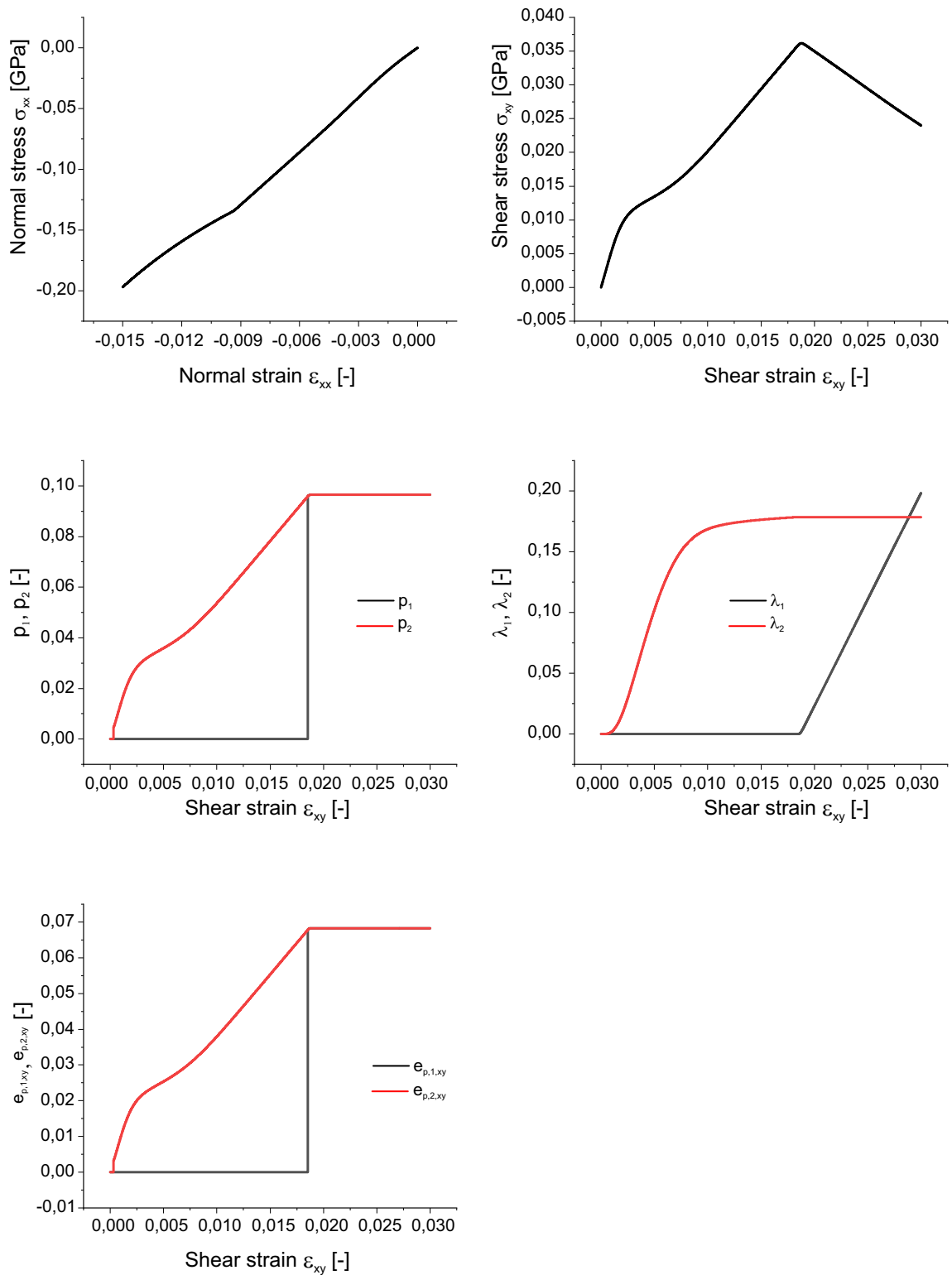


Figure 4.26: Output from the test of uniaxial compression. From top left to bottom left: the response in the normal directions to the left and the response in shear plane $x - y$ to the right, the evolving plastic parameters in addition to the volume fractions from both directions, the plastic strain histories in $x - y$ shear plane.

and then a gradual vertical increment (deviatoric effect) takes place. Meaning, under loading, the material leaves the elastic zone Y_1 , then moves further vertically to enter the two-phase region Y_2 , and then even further to achieve the three-phase region Y_3 . Outputs from this test are shown in Fig.4.27.

At the beginning, an evolution of λ_1 with its internal variables takes place, as long as the loading pairs are in the two-phase region to the side of ξ_{\max} . Later on, loading proceeds and the material enters the mixed zone, initializing λ_2 and causing the internal variables from phase-2 to evolve as well. We can observe the curve of λ_1 , with a changing tangent and two peaks that reflect the mentioned region transition, the first one is for a transition from Y_1 to Y_2 and the second peak shows the change between Y_2 and Y_3 . The different relaxation regions can be inferred from Fig. 4.6.

4.7.5 Finite element comparison for the plate with a hole

We have presented so far only local results for the relaxation scheme introduced above. Now we want to extend our investigations to a global comparison computed via the finite element method. For this purpose, we studied for the sake of comparison, the same boundary value problem as in Sec. 4.6.1, a rectangular plate with a centered hole. The right side of the plate is subject to a horizontal displacement increasing linearly in time, to a total magnitude of $u_x = -0.035$ mm. To ensure the stability of the staggered scheme mentioned before, we apply the given displacement in very small increments $|\Delta u_x| = 0.0000875$ mm. The same coarse and fine meshes are tested, as shown in Fig. 4.12. Tri-linear hexahedral elements with a fixed thickness are used implying a plane strain state. The implementations are performed using the finite element program FEAP. The elements employed for stress comparison and comparison of the internal variables are the ones marked in red.

A global comparison of the force-displacement curves from the coarse and fine meshes at the right free edge of the plate can be seen in Fig. 4.28. Notice the matching behavior under relaxation within the elastic phase and after evolution, meaning that the minimization problem solved is able to return one global minimum despite the different mesh-size.

In addition to the global results, we want to compare the evolving internal variables locally. These results are captured at the elements beside the hole marked in red, see Fig. 4.12. The comparison of the stresses and the internal variables as a result of the evolving microstructure are plotted against the external applied displacements, results can be inferred from Fig. 4.29.

The results from the plate with a hole reflects one transition under the given displacement from the elastic zone into a two-phase region Y_2 to the side of ξ_{\min} . In the top pane we see the normal stress component σ_{yy} and the shear stress component σ_{xy} at a specific integration point from the marked elements. A very good compliance from the coarse and fine meshes in the different regions can be observed. The following curves in the mid and lower rows represent the arising internal variables, which are initiating at the same time and providing the same behavior despite the different mesh-size.

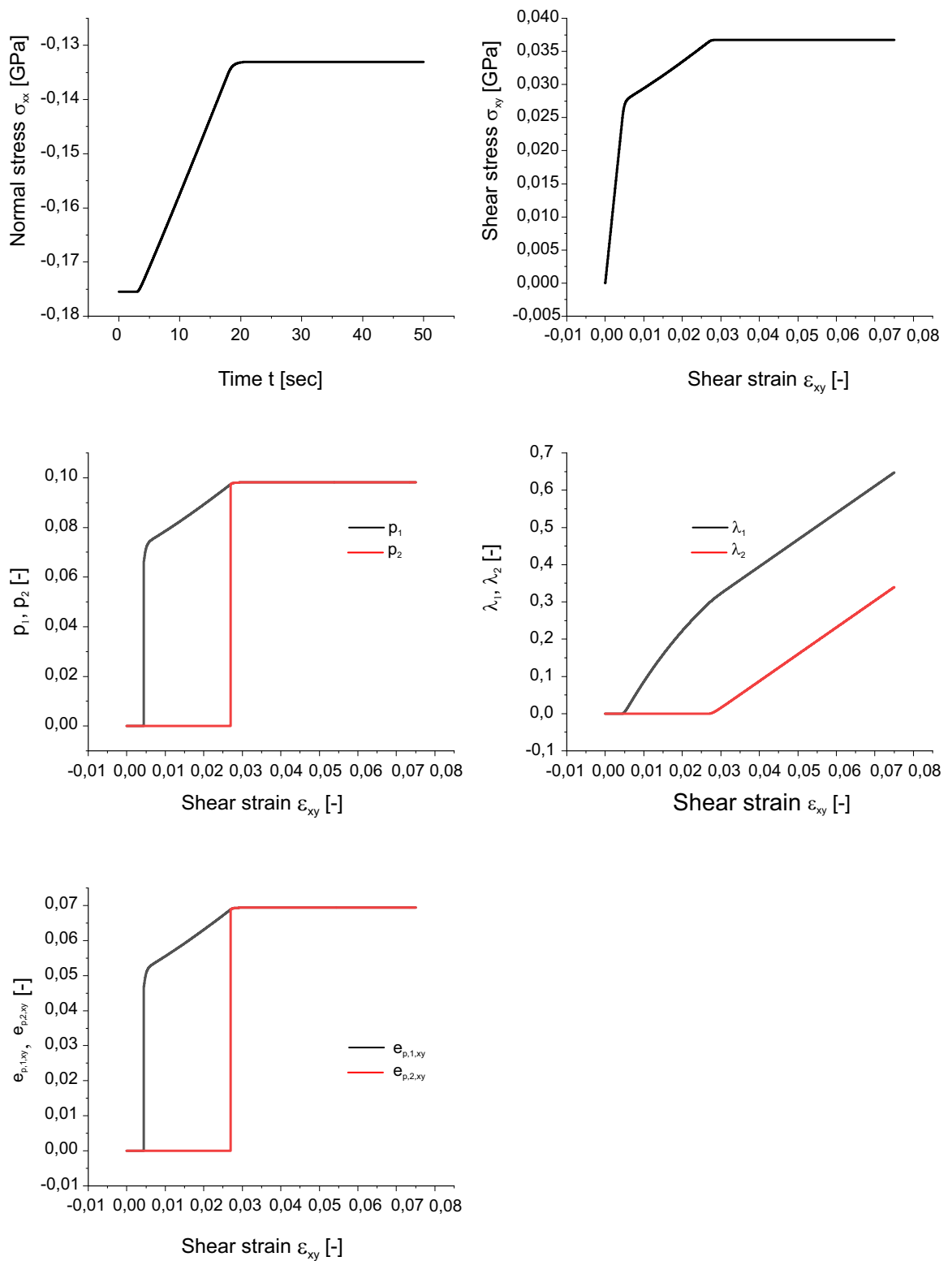


Figure 4.27: Output from the simple-shear test. From top left to bottom left: the response in the normal directions to the left and the response in shear plane $x - y$ to the right, the evolving plastic parameters in addition to the volume fractions from both directions, the plastic strain histories in $x - y$ shear plane.

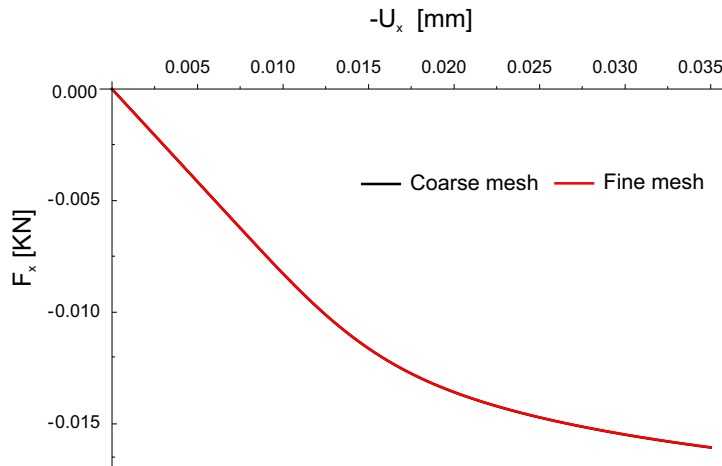


Figure 4.28: A plate with a hole (evolution), force-displacement diagram in x -direction at the right free side.

An additional evidence for the well-posedness of the variational problem under consideration can be obtained from figures 4.30 and 4.31. They show the stress distribution and contour plots of the internal variables from the coarse mesh (to the left) and the fine mesh (to the right). Notice the same evolution positions and distribution. A very good agreement from both meshes is observed, which reflects a mesh-independent behavior for the relaxed evolution model.

4.7.6 Finite element comparison for the double notch

We study the double notched specimen shown in Fig. 4.17. The bottom edge of the specimen is fixed and the upper edge is subject to a vertical displacement increasing linearly in time, to a total magnitude of $u_y = -0.085$ mm, with a very small loading increment of $|\Delta u_y| = 0.0002125$ mm.

We apply the finite element computations for the two shown meshes. As a result, we get the global force-displacement diagram in y -direction at the upper free edge, to be inferred from Fig. 4.32. Yielding at the upper side of the specimen takes more time in comparison to the results from the relaxed model in Fig. 4.18, but here as well, the matching global compliance implies a mesh-independent behavior.

Moreover, we observe in Fig. 4.33 the resulting displacements in x - and y -directions at the marked nodes in green (in Fig. 4.17) beside the local values of the stresses σ_{yy} and σ_{zz} at the marked elements in red for the same integration point. Whether from the shown displacements to the left of the specimen or from the stresses at the center, we observe very good compliance despite the different spatial discretizations.

A further comparison can be inferred from Fig. 4.34, in which the internal variables are given. Notice that the plots reflect evolution in the two-phase domain with an initiation of all internal variables from phase-2. Although the plastic parameter and plastic strain seem to evolve first, but this can be understood in the negative values

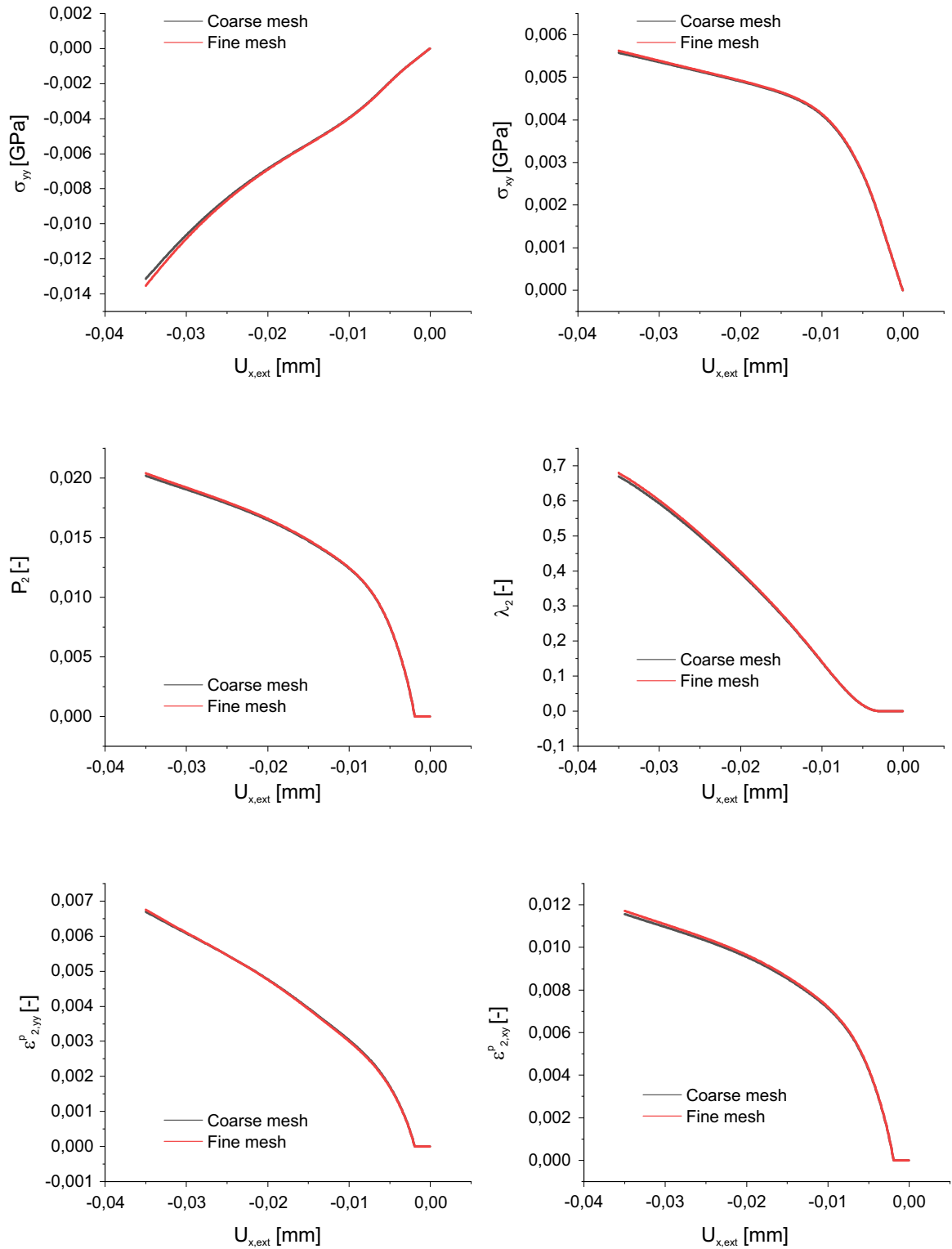


Figure 4.29: Output from the plate with a hole (evolution). Top row: the response of the normal component yy to the left and the response in shear plane $x - y$ to the right, mid pane: the plastic parameter p_2 to the left and the volume fraction λ_2 to the right, bottom row: the plastic strains in phase-2, the normal component yy to the left and the shear component xy to the right.

of the driving force of λ_2 , as shown in Eq. 4.7.7. Therefore, λ_2 remains zero for some time before it starts to evolve as q_2 turns positive. The comparison is from the marked elements in red at the center of the specimen.

The distribution of the stresses σ_{xx}, σ_{xy} over the double-notched specimen is shown in Fig. 4.35. We observe a very good matching behavior, in addition to some small deviations for the stress concentrations around the notches. But concentrations around the notches are expected and this behavior can be enhanced by seeking further mesh refinement.

The contour plots from the internal variables are given in Fig. 4.36. They show the same distribution and evolution positions for the internal variables. Emphasizing once again the well-posedness of the minimization problem under relaxation.

4.7.7 Finite element comparison for the crack problem

The next example under consideration is the cracked plate, shown in Fig. 4.22. We consider in our computations here only two meshes, the coarse mesh with 720 elements and the fine mesh with 2000 elements. The upper side of the plate is exposed to a vertical displacement increasing linearly in time, to a total magnitude of $u_y = -0.075$ mm, with a very small loading increment of $|\Delta u_y| = 0.0001875$ mm. All requirements for the plane strain state are fulfilled here as well.

An evolution of the microstructure starts at the zone surrounding the crack tip, where the loading values lead to a contribution to phase-2 with an initiation of the corresponding internal variables $\lambda_2, p_2, \mathbf{e}_{p,2}$. The resulting displacements at the nodes marked in green from the coarse and fine meshes in addition to the response in the normal direction yy and in shear plane xy are shown in Fig. 4.37. Stress plots are captured from an integration point at the elements beside the crack tip, marked in red in Fig. 4.22.

A view of the internal variables is given in Fig. 4.38, compared as well at the marked elements beside the crack tip. A very good compliance between the different meshes is observed. Although λ_2 does not evolve directly after the evolution but rather later on, when the thermodynamically driving force gets positive, i.e. as $\mathbf{e}_{p,2}$ becomes more negative.

A contour plot comparison gives an insight into the global behavior of the cracked plate. The comparison of the stress distribution and the contours of the internal variables can be inferred from Fig. 4.39. We observe a very good agreement in the global behavior, which leads to the same conclusion that our introduced model is mesh-independent.

The cracked plate is a very complicated boundary value problem characterized with high stress concentrations at the crack tip, yet assigning higher refinement around the crack tip, returned well-posed stable results from the performed computations of the relaxed model.

4.8 Conclusion - pressure-dependent plasticity

We established a variational model for pressure-dependent plasticity common in models of soil mechanics. Our approach employed a novel aspect by using a characteristic function as dissipation potential. That way, it was possible to establish a dissipation distance as well as a condensed energy connected to a time-incremental setting in a consistent manner. This allowed us to investigate the initiation of microstructure via relaxation theory by calculating the quasiconvex envelope of the condensed energy. For a one-dimensional model problem, for which the quasiconvex envelope coincides with the convex envelope, we succeeded in arriving at a closed-form expression. Interestingly, the quasiconvex envelope turned out to be largely independent of the yield surface of the original model for small values of the hardening parameter b . The proof of this surprising fact illustrates that even the microstructure can be chosen independently of the yield surface. Numerical simulations confirmed the predictions of the analytical results and illustrated the qualitatively different behavior of the variational models using the condensed and the relaxed energy, respectively. In particular, the simulations employing the condensed energy succeeded in finding the necessary oscillations. It was possible to extend the one-dimensional formulation to higher dimensions in an empirical manner. Numerical simulations for a paradigmatic model problem provided strong evidence for the superior predictive power of the relaxed model.

A time-incremental evolution model has been introduced, which is based on the approximation of a convex envelope characterizing the evolving microstructure. The relaxation techniques are inspired by the findings from the first investigations on pressure-dependent plasticity, where the relaxation zones are encountering mixed states. Therefore, these relaxation parameters turn out to be the internal variables of the relaxed problem. By means of different numerical results we clarified the introduced model and its applicability delivering a very good compliance in the local and global behavior. This has been proved in terms of the mesh-independent results from different numerical simulations.

Some future additions to the proposed models can be mentioned, for example an enhancement from the variational point of view can be obtained by considering an additional internal variable to prescribe the plastic volumetric change. Besides, a better relaxed envelope, applying a relaxation via lamination, can be calculated to get a more physical relaxed envelope closer to the quasiconvex one.

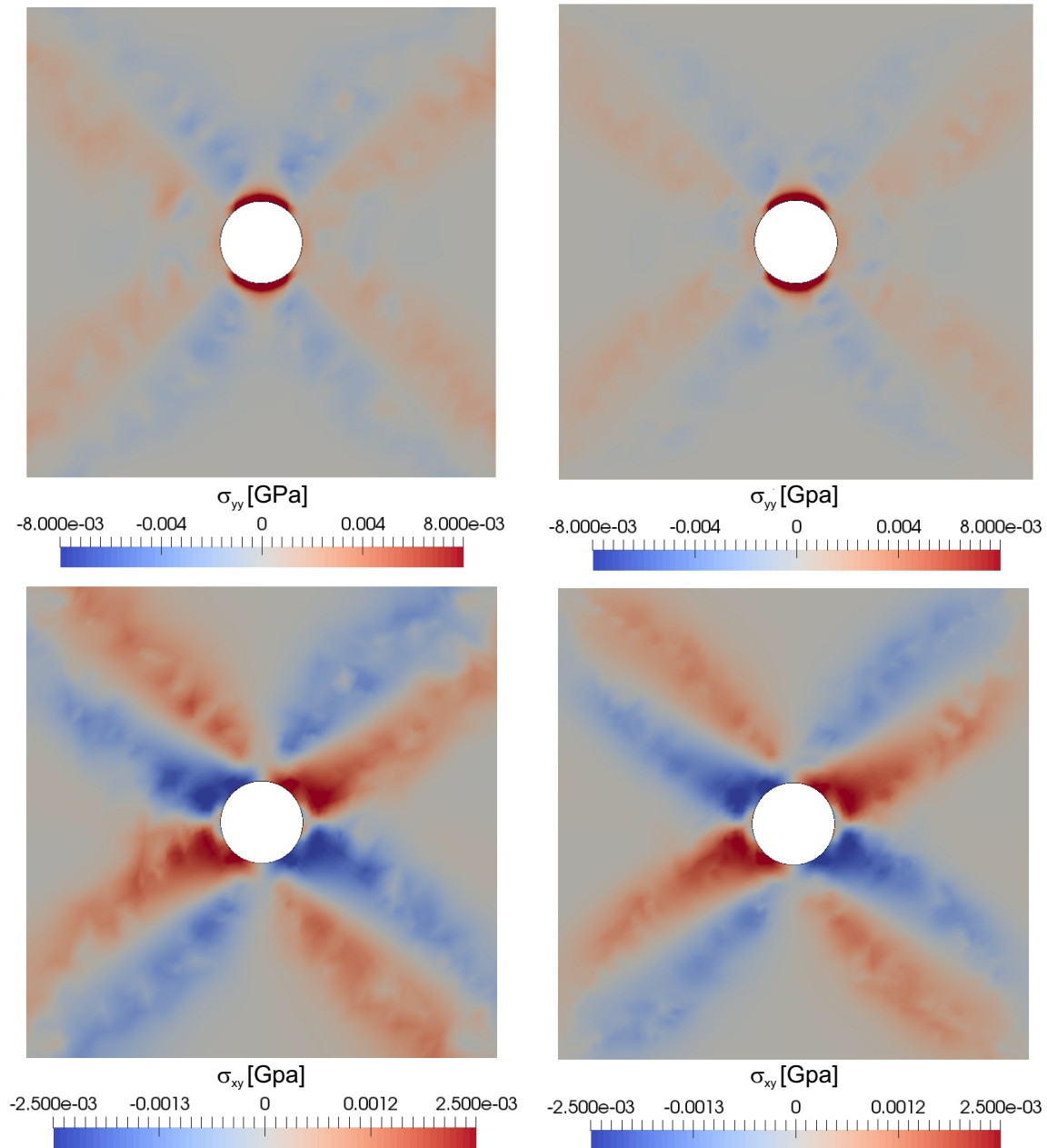


Figure 4.30: Contour plot from the plate with a hole (evolution). Distribution of the normal stresses σ_{yy} and shear stresses in plane $x-y$. Coarse mesh (left) and fine mesh (right).

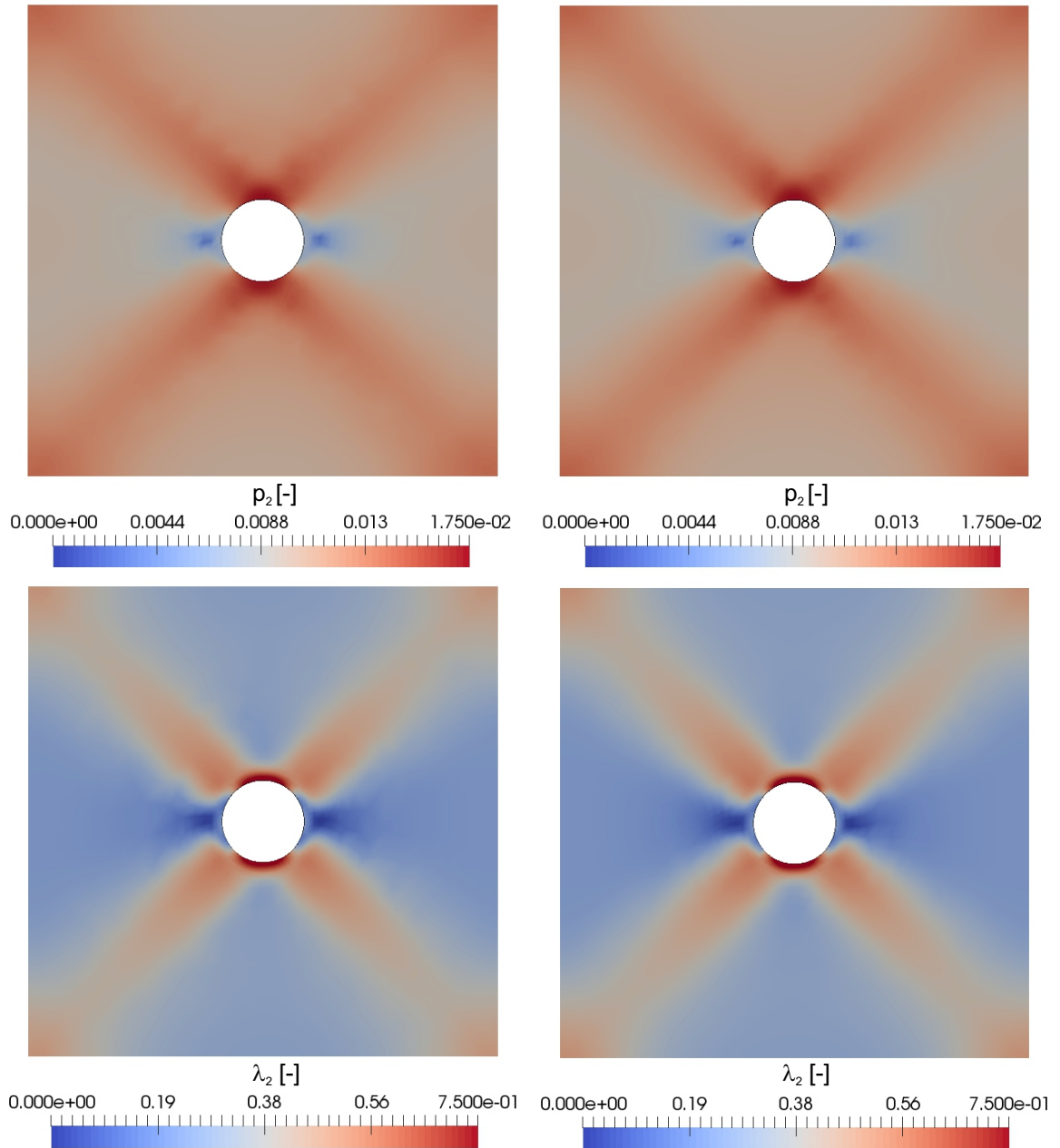


Figure 4.31: Contour plot from the plate with a hole (evolution). Distribution of the internal variables, plastic parameter p_2 and the volume fraction λ_2 . Coarse mesh (left) and fine mesh (right)

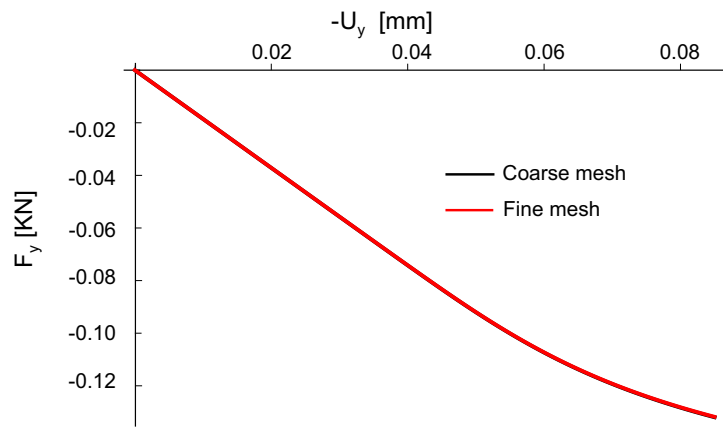


Figure 4.32: Double notch (evolution): force-displacement diagram at the free edge to the top of the specimen.

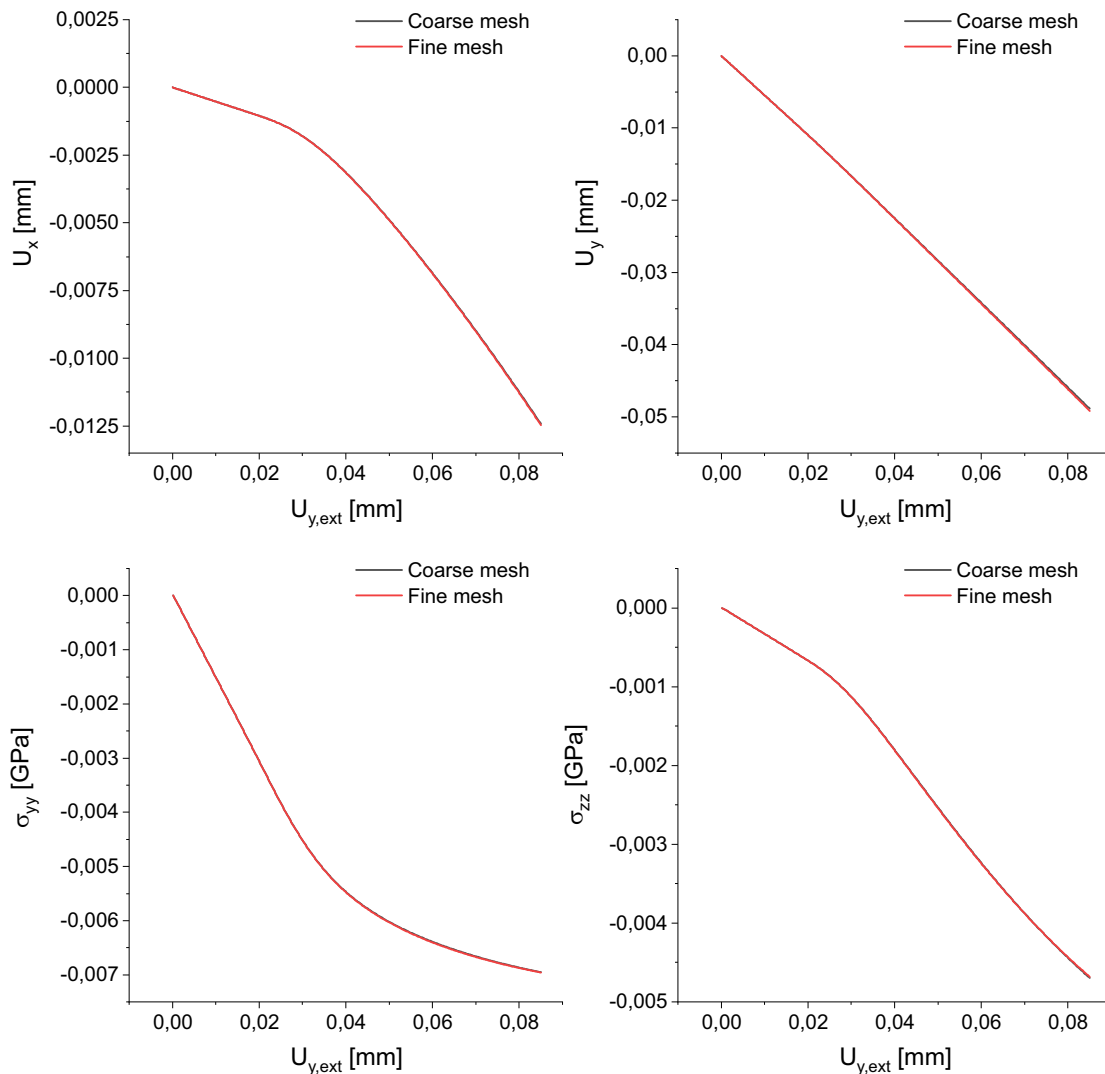


Figure 4.33: Double notch (evolution): from top left to bottom right: displacements in x - and y -directions, stresses σ_{yy} and σ_{zz} , as a function of the external boundary displacement $u_{y,ext}$. Stress comparison at the marked elements in red, and displacement comparison at the marked nodes in green.

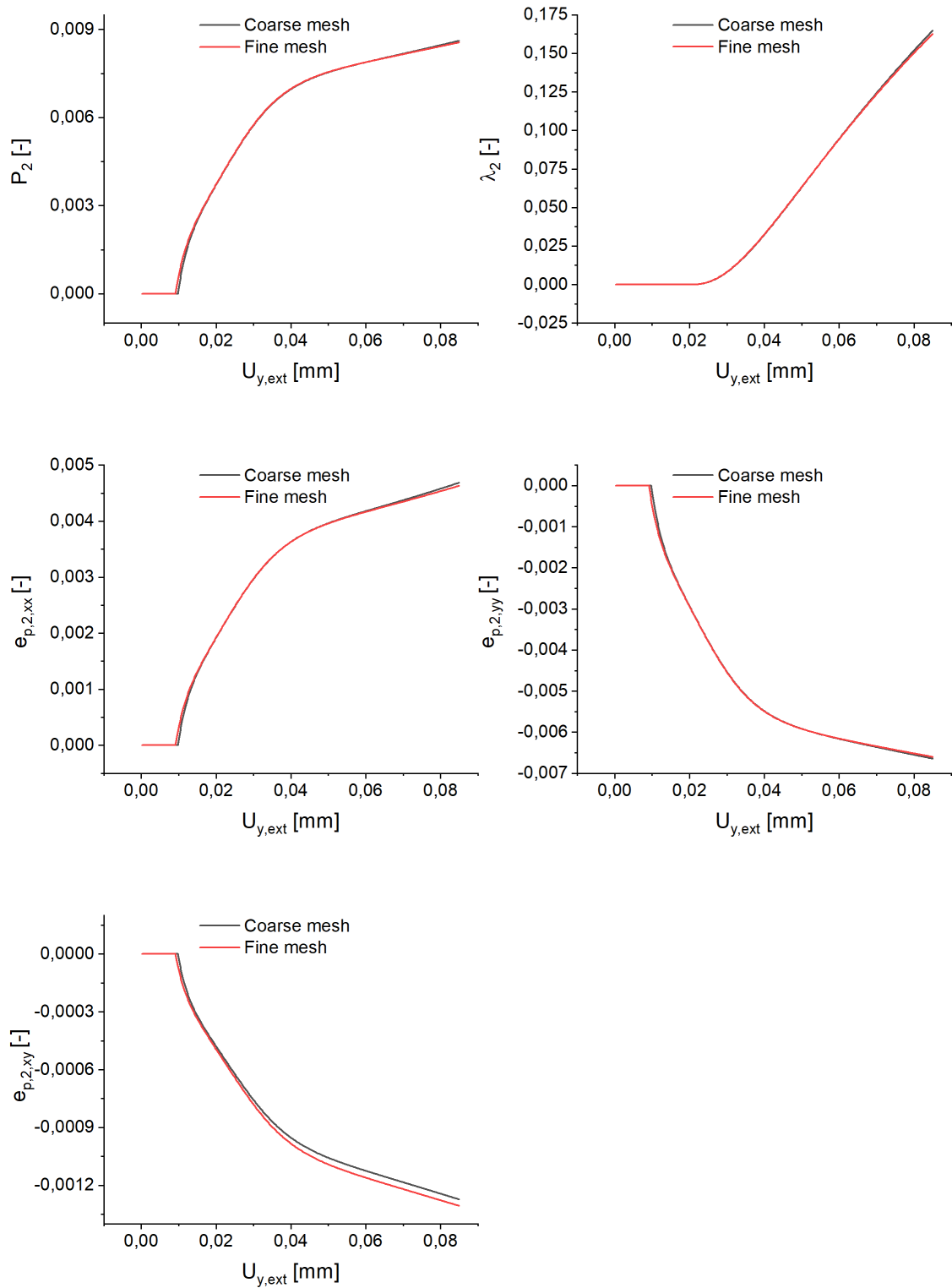


Figure 4.34: Double notch (evolution): from top left to bottom left: plastic parameter p_2 , volume fraction λ_2 , and plastic strain components $e_{p,2,xx}$, $e_{p,2,yy}$, $e_{p,2,xy}$, as a function of the external boundary displacement $u_{y,ext}$. Comparison at the marked elements in red.

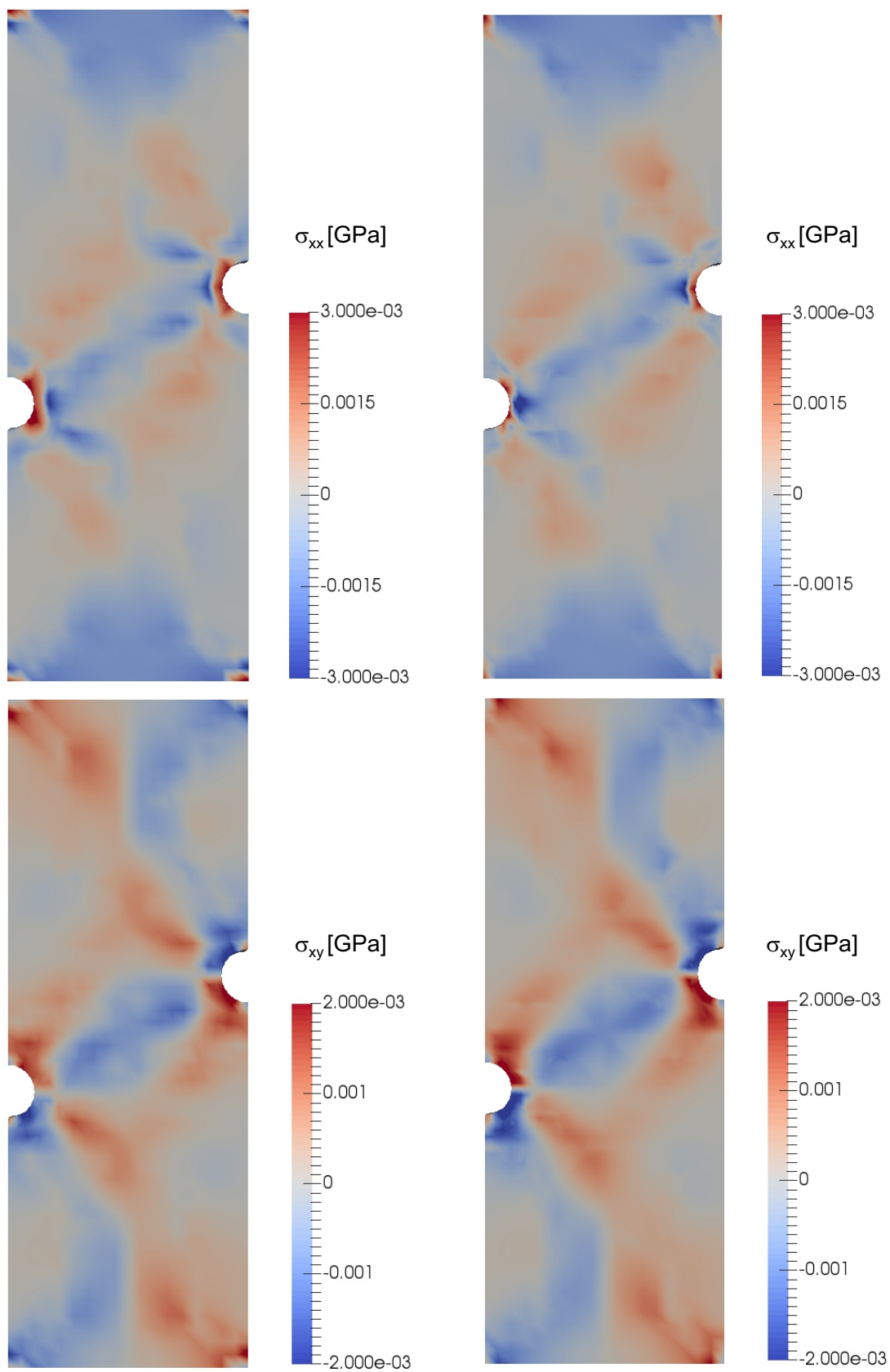


Figure 4.35: Contours from the double notch problem (evolution). Distribution of the stresses σ_{xx} and σ_{xy} . Coarse mesh (left) and fine mesh (right).

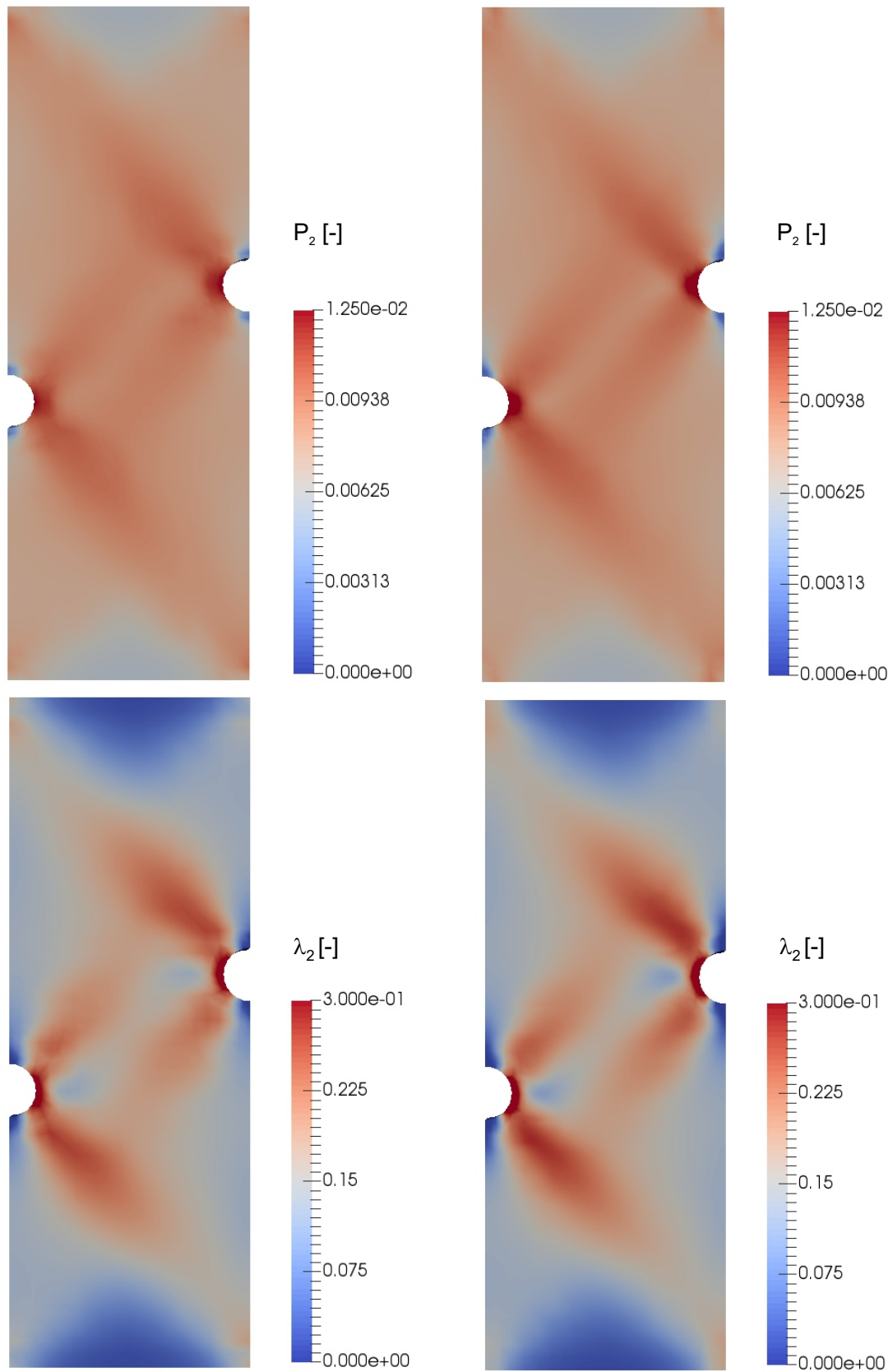


Figure 4.36: Contours from the double notch problem (evolution). Distribution of the plastic variable p_2 and the volume fraction λ_2 at the end of loading time. Coarse mesh (left) and fine mesh (right).

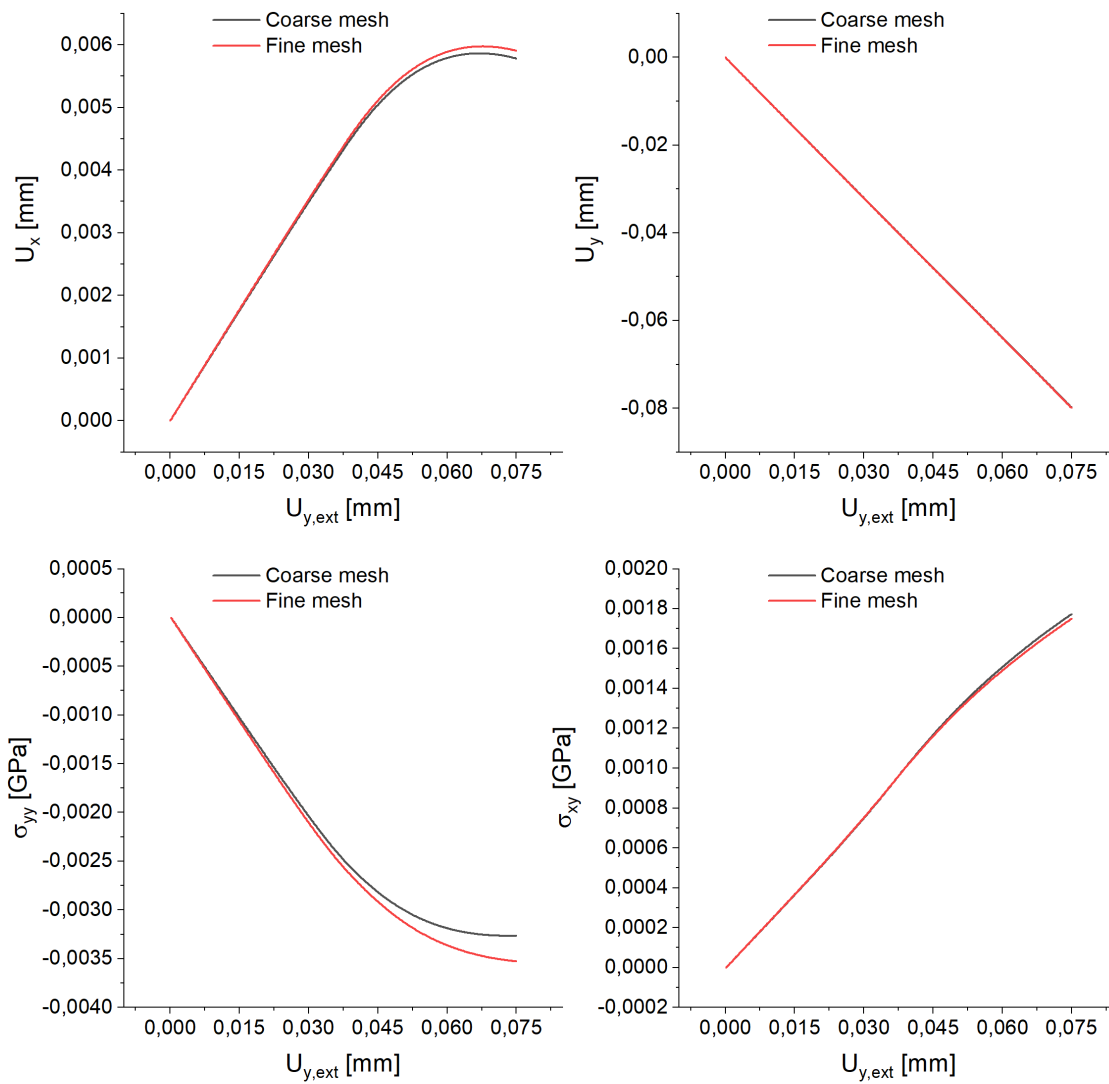


Figure 4.37: Crack problem (evolution): from top left to bottom right: displacements in x - and y -directions, stresses σ_{yy} and σ_{xy} , σ_{xy} , as a function of the external boundary displacement $u_{y,ext}$.

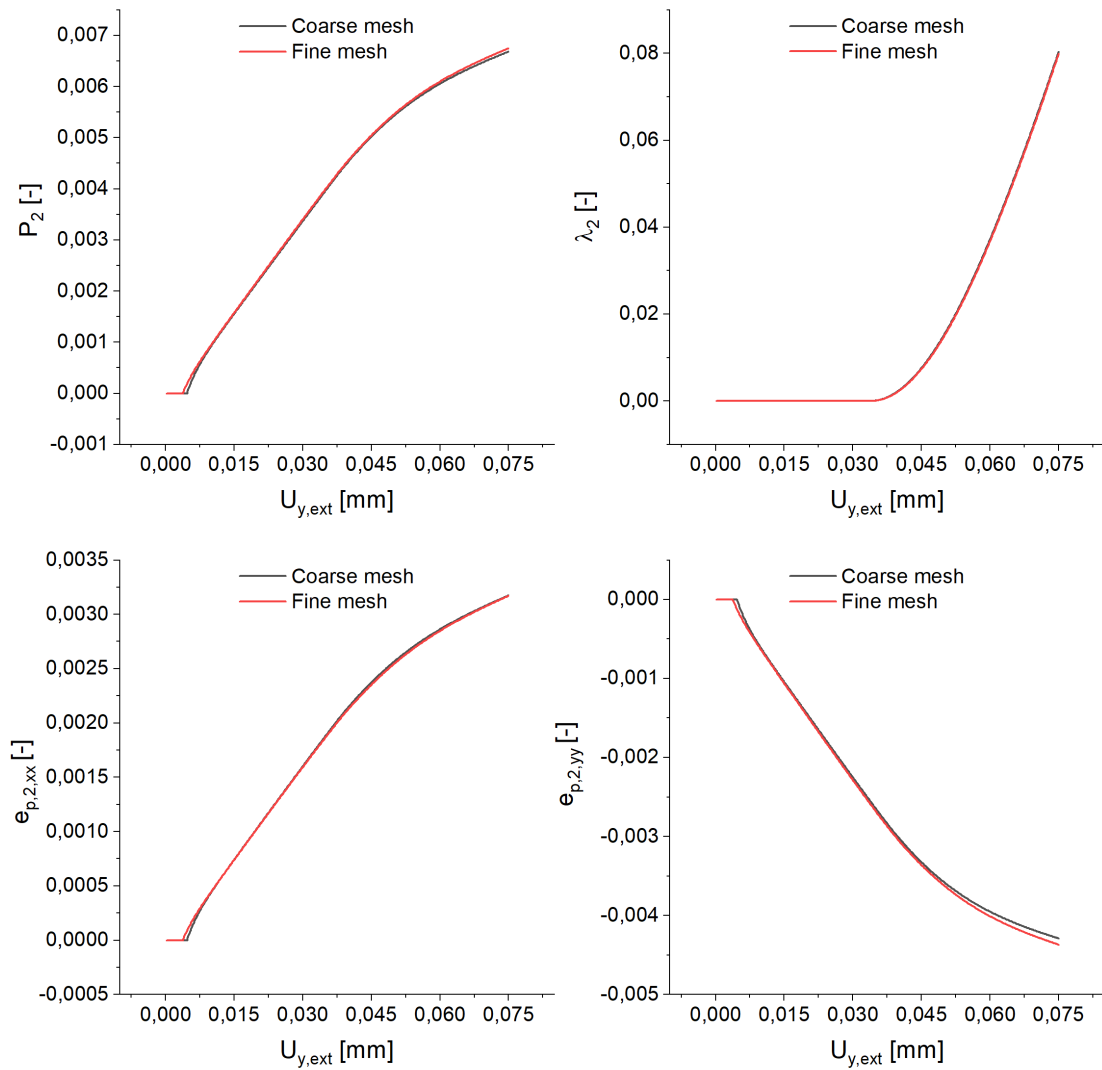


Figure 4.38: Crack problem (evolution): from top left to bottom right: plastic parameter p_2 , the volume fraction λ_2 , and plastic strain components $e_{p,2,xx}$, $e_{p,2,yy}$, as a function of the external boundary displacement $u_{y,ext}$.

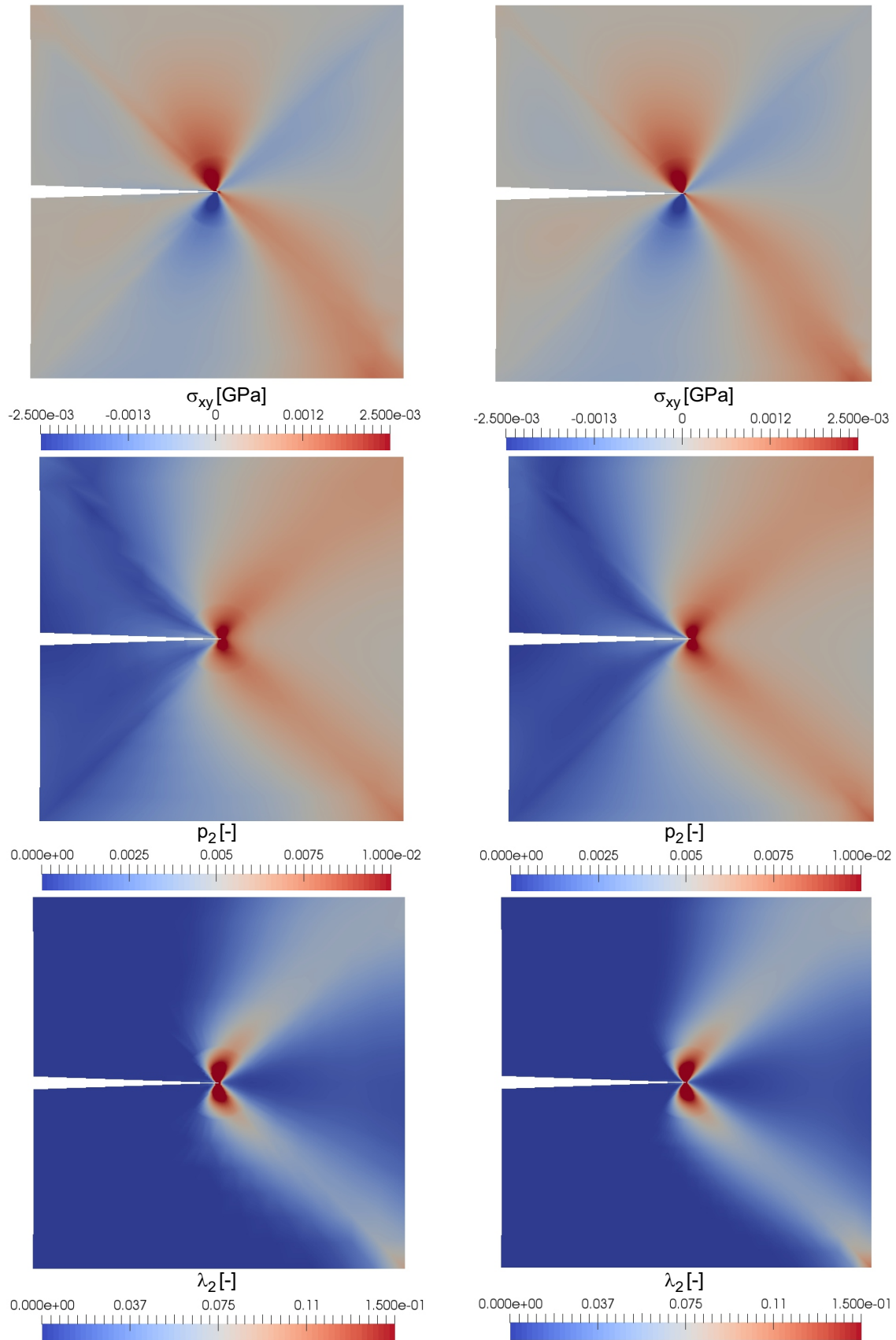


Figure 4.39: Contours from the crack problem (evolution). Distribution of the stresses σ_{xy} , the plastic parameter p_2 and the volume fraction λ_2 . Coarse mesh (left) and fine mesh (right).

5 Outlook

Applications of the variational method in the literature are manifold. We provided so far different approaches in order to attract the attention to this field of research. Nevertheless, further investigations are still open. For example, applying the reduced models to materials with non-linear constitutive laws like for example damage models, or a straight-forward extension to viscous materials with rate-dependent contribution in the characteristic dissipation function. A further application field would be to consider uncertainty analysis by applying random distributions for the case of homogenization with periodic microstructure.

The first findings from the presented inelastic materials characterized with pressure-dependency can broaden the fields of investigation to cover different materials with similar behavior like elastomer foams, or even design new solid materials (bio-materials or others), which has parameter-dependency driving the inelastic behavior.

Bibliography

- Aubry, S., M. Fago, and M. Ortiz (2003). A constrained sequential-lamination algorithm for the simulation of sub-grid microstructure in martensitic materials. *Computer Methods in Applied Mechanics and Engineering* 192(26-27), 2823–2843.
- Bakhvalov, N. S. and G. Panasenko (2012). *Homogenisation: averaging processes in periodic media: mathematical problems in the mechanics of composite materials*, Volume 36. Springer Science & Business Media.
- Ball, J. M. and R. D. James (1987). Fine phase mixtures as minimizers of energy. *Archive for Rational Mechanics and Analysis* 100, 13–52.
- Ball, J. M. and R. D. James (1992). Proposed experimental tests of a theory of fine microstructure and the two-well problem. *Philosophical Transactions of the Royal Society of London. Series A: Physical and Engineering Sciences* 338(1650), 389–450.
- Balzani, D., J. Schröder, and D. Brands (2010). Fe₂-simulation of microheterogeneous steels based on statistically similar rves. In *IUTAM Symposium on Variational Concepts with Applications to the Mechanics of Materials: Proceedings of the IUTAM Symposium on Variational Concepts with Applications to the Mechanics of Materials, Bochum, Germany, September 22-26, 2008*, pp. 15–28. Springer.
- Bartels, S. (2004). Linear convergence in the approximation of rank-one convex envelopes. *ESAIM: Mathematical Modelling and Numerical Analysis* 38(5), 811–820.
- Bartels, S. (2005). Reliable and efficient approximation of polyconvex envelopes. *SIAM Journal on Numerical Analysis* 43(1), 363–385.
- Bartels, S., C. Carstensen, K. Hackl, and U. Hoppe (2004). Effective relaxation for microstructure simulations: algorithms and applications. *Computer Methods in Applied Mechanics and Engineering* 193(48-51), 5143–5175.
- Bedford, A. and Bedford (1985). *Hamilton's principle in continuum mechanics*, Volume 139. Springer.
- Behr, F., G. Dolzmann, K. Hackl, and G. Jezdan (2023). Analytical and numerical relaxation results for models in soil mechanics. *Continuum Mechanics and Thermodynamics*, 1–23.
- Biot, M. A. (1962). Mechanics of deformation and acoustic propagation in porous media. *Journal of applied physics* 33(4), 1482–1498.
- Carstensen, C., S. Conti, and A. Orlando (2008). Mixed analytical–numerical relaxation in finite single-slip crystal plasticity. *Continuum Mechanics and Thermodynamics* 20, 275–301.
- Carstensen, C., K. Hackl, and A. Mielke (2002). Non-convex potentials and microstructures in finite-strain plasticity. *Proceedings of the royal society of London. Series A: mathematical, physical and engineering sciences* 458(2018), 299–317.
- Chipot, M. and D. Kinderlehrer (1988). Equilibrium configurations of crystals.

- Archive for Rational Mechanics and Analysis* 103, 237–277.
- Chou, P. C. and N. J. Pagano (1992). *Elasticity: tensor, dyadic, and engineering approaches*. Courier Corporation.
- Coleman, B. D. and M. E. Gurtin (1967). Thermodynamics with internal state variables. *The journal of chemical physics* 47(2), 597–613.
- Conti, S. and G. Dolzmann (2015). On the theory of relaxation in nonlinear elasticity with constraints on the determinant. *Archive for Rational Mechanics and Analysis* 217, 413–437.
- Conti, S. and G. Dolzmann (2018). An adaptive relaxation algorithm for multi-scale problems and application to nematic elastomers. *Journal of the Mechanics and Physics of Solids* 113, 126–143.
- Conti, S., G. Dolzmann, and C. Klust (2009). Relaxation of a class of variational models in crystal plasticity. *Proceedings of the Royal Society A: Mathematical, Physical and Engineering Sciences* 465(2106), 1735–1742.
- Conti, S. and M. Ortiz (2005). Dislocation microstructures and the effective behavior of single crystals. *Archive for Rational Mechanics and Analysis* 176, 103–147.
- Dacorogna, B. (2007). *Direct methods in the calculus of variations*, Volume 78. Springer Science & Business Media.
- de Souza Neto, E. A., D. Peric, and D. R. Owen (2011). *Computational methods for plasticity: theory and applications*. John Wiley & Sons.
- Dimitrijevic, B. J. and K. Hackl (2008). A method for gradient enhancement of continuum damage models. *Technische Mechanik-European Journal of Engineering Mechanics* 28(1), 43–52.
- Frankenreiter, I., D. Rosato, and C. Miehe (2010). A hybrid micromacromodel for the description of evolving anisotropy in finite polycrystal plasticity. *PAMM* 10(1), 291–292.
- Govindjee, S., K. Hackl, and R. Heinen (2007). An upper bound to the free energy of mixing by twin-compatible lamination for n-variant martensitic phase transformations. *Continuum Mechanics and Thermodynamics* 18, 443–453.
- Günther, C., P. Junker, and K. Hackl (2015). A variational viscosity-limit approach to the evolution of microstructures in finite crystal plasticity. *Proceedings of the Royal Society A: Mathematical, Physical and Engineering Sciences* 471(2180), 20150110.
- Gürses, E. and C. Miehe (2011). On evolving deformation microstructures in non-convex partially damaged solids. *Journal of the Mechanics and Physics of Solids* 59(6), 1268–1290.
- Gurtin, M. E., E. Fried, and L. Anand (2010). *The mechanics and thermodynamics of continua*. Cambridge University Press.
- Hackl, K. (1997). Generalized standard media and variational principles in classical and finite strain elastoplasticity. *Journal of the Mechanics and Physics of Solids* 45(5), 667–688.
- Hackl, K. and F. D. Fischer (2008). On the relation between the principle of maximum dissipation and inelastic evolution given by dissipation potentials. *Proceedings of the Royal Society A: Mathematical, Physical and Engineering Sciences* 464(2089), 117–132.
- Hackl, K., F. D. Fischer, and J. Svoboda (2011). A study on the principle of maximum dissipation for coupled and non-coupled non-isothermal processes in materials. *Proceedings of the Royal Society A: Mathematical, Physical and Engineering Sciences* 467(2128), 1186–1196.

- Hackl, K. and D. M. Kochmann (2008). Relaxed potentials and evolution equations for inelastic microstructures. In *IUTAM Symposium on Theoretical, Computational and Modelling Aspects of Inelastic Media: Proceedings of the IUTAM Symposium held at Cape Town, South Africa, January 14–18, 2008*, pp. 27–39. Springer.
- Hamilton, W. R. (1834). Xv. on a general method in dynamics; by which the study of the motions of all free systems of attracting or repelling points is reduced to the search and differentiation of one central relation, or characteristic function. *Philosophical transactions of the Royal Society of London* (124), 247–308.
- Hamilton, W. R. (1835). Vii. second essay on a general method in dynamics. *Philosophical Transactions of the Royal Society of London* (125), 95–144.
- Hashin, Z. (1983). Analysis of composite materials—a survey.
- Hashin, Z. and S. Shtrikman (1963). A variational approach to the theory of the elastic behaviour of multiphase materials. *Journal of the Mechanics and Physics of Solids* 11(2), 127–140.
- Hill, R. (1952). The elastic behaviour of a crystalline aggregate. *Proceedings of the Physical Society. Section A* 65(5), 349.
- Hill, R. (1963). Elastic properties of reinforced solids: some theoretical principles. *Journal of the Mechanics and Physics of Solids* 11(5), 357–372.
- Hill, R. (1965). A self-consistent mechanics of composite materials. *Journal of the Mechanics and Physics of Solids* 13(4), 213–222.
- Holzapfel, G. A. (2002). Nonlinear solid mechanics: a continuum approach for engineering science.
- Hoormazdi, G. (2021). Modeling of soil-tool abrasive wear processes in mechanized tunneling.
- Junker, P. and K. Hackl (2011). Finite element simulations of poly-crystalline shape memory alloys based on a micromechanical model. *Computational Mechanics* 47, 505–517.
- Junker, P. and K. Hackl (2014). A thermo-mechanically coupled field model for shape memory alloys. *Continuum Mechanics and Thermodynamics* 26, 859–877.
- Junker, P. and K. Hackl (2016). A discontinuous phase field approach to variational growth-based topology optimization. *Structural and Multidisciplinary Optimization* 54, 81–94.
- Junker, P., J. Makowski, and K. Hackl (2014). The principle of the minimum of the dissipation potential for non-isothermal processes. *Continuum Mechanics and Thermodynamics* 26, 259–268.
- Junker, P., S. Schwarz, D. R. Jantos, and K. Hackl (2019). A fast and robust numerical treatment of a gradient-enhanced model for brittle damage. *International Journal for Multiscale Computational Engineering* 17(2).
- Kochmann, D. M. and K. Hackl (2011). The evolution of laminates in finite crystal plasticity: a variational approach. *Continuum Mechanics and Thermodynamics* 23, 63–85.
- Kouznetsova, V., W. Brekelmans, and F. Baaijens (2001). An approach to micro-macro modeling of heterogeneous materials. *Computational mechanics* 27(1), 37–48.
- Mandel, J. (1973). Equations constitutives et directeurs dans les milieux plastiques et viscoplastiques. *International Journal of Solids and Structures* 9(6), 725–740.
- Miehe, C., M. Lambrecht, and E. Gürses (2004). Analysis of material instabilities

- in inelastic solids by incremental energy minimization and relaxation methods: evolving deformation microstructures in finite plasticity. *Journal of the Mechanics and Physics of Solids* 52(12), 2725–2769.
- Miehe, C., J. Schotte, and M. Lambrecht (2002). Homogenization of inelastic solid materials at finite strains based on incremental minimization principles. application to the texture analysis of polycrystals. *Journal of the Mechanics and Physics of Solids* 50(10), 2123–2167.
- Mielke, A. (2002). *Finite elastoplasticity Lie groups and geodesics on $SL(d)$* . Springer.
- Mielke, A. (2004). Deriving new evolution equations for microstructures via relaxation of variational incremental problems. *Computer Methods in Applied Mechanics and Engineering* 193(48-51), 5095–5127.
- Morrey, C. B. (1966). Multiple integrals in the calculus of variations. *Grundlehren der mathematischen Wissenschaften*.
- Noll, W., B. D. Coleman, and W. Noll (1974). The thermodynamics of elastic materials with heat conduction and viscosity. *The Foundations of Mechanics and Thermodynamics: Selected Papers*, 145–156.
- Onsager, L. (1931). Reciprocal relations in irreversible processes. i. *Physical review* 37(4), 405.
- Ortiz, M. and E. Repetto (1999). Nonconvex energy minimization and dislocation structures in ductile single crystals. *Journal of the Mechanics and Physics of Solids* 47(2), 397–462.
- Ortiz, M. and L. Stainier (1999). The variational formulation of viscoplastic constitutive updates. *Computer methods in applied mechanics and engineering* 171(3-4), 419–444.
- Parnell, W. J. (2016). The eshelby, hill, moment and concentration tensors for ellipsoidal inhomogeneities in the newtonian potential problem and linear elastostatics. *Journal of Elasticity* 125(2), 231–294.
- Reuß, A. (1929). Berechnung der fließgrenze von mischkristallen auf grund der plastizitätsbedingung für einkristalle. *ZAMM-Journal of Applied Mathematics and Mechanics/Zeitschrift für Angewandte Mathematik und Mechanik* 9(1), 49–58.
- Rockafellar, R. T. (1997). *Convex analysis*, Volume 11. Princeton university press.
- Schofield, A. N. (2005). *Disturbed soil properties and geotechnical design*. Thomas Telford.
- Schröder, J. and K. Hackl (2013). *Plasticity and beyond: microstructures, crystal-plasticity and phase transitions*, Volume 550. Springer.
- Schwarz, S. (2019). *Efficient approaches for regularized damage models: variational modeling and numerical treatment*. Ph. D. thesis, Ruhr-Universität Bochum.
- Shen, B., J. Shi, and N. Barton (2018). An approximate nonlinear modified mohr-coulomb shear strength criterion with critical state for intact rocks. *Journal of Rock Mechanics and Geotechnical Engineering* 10(4), 645–652.
- Silhavy, M. (1997). *The Mechanics and Thermodynamics of Continuous Media*. Springer Science & Business Media.
- Suquet, P. (1997). *Effective properties of nonlinear composites*. Springer.
- Taylor, R. and S. Govindjee (2022). *Feap-a finite element analysis program, programmer manual: v8. 6*. University of California: Berkeley, CA, USA.
- Truesdell, C., W. Noll, C. Truesdell, and W. Noll (2004). *The non-linear field theories of mechanics*. Springer.

- Voigt, W. (1889). Ueber die beziehung zwischen den beiden elasticitätsconstanten isotroper körper. *Annalen der physik* 274(12), 573–587.
- Voigt, W. (1910). *Lehrbuch der kristallphysik:(mit ausschluss der kristalloptik)*, Volume 34. BG Teubner.
- Waimann, J. (2018). *Variationelle Modellierung irreversibler Effekte in polykristallinen Formgedachtnislegierungen*. Ph. D. thesis, Dissertation, Bochum, Ruhr-Universität Bochum, 2018.
- Waimann, J., P. Junker, and K. Hackl (2016). A coupled dissipation functional for modeling the functional fatigue in polycrystalline shape memory alloys. *European Journal of Mechanics-A/Solids* 55, 110–121.
- Willis, J. R. (1981). Variational and related methods for the overall properties of composites. *Advances in applied mechanics* 21, 1–78.
- Wolf, H., D. König, and T. Triantafyllidis (2003). Experimental investigation of shear band patterns in granular material. *Journal of Structural Geology* 25(8), 1229–1240.
- Wolfgang Demtroder, W. D. (2017). *Mechanics and thermodynamics*.
- Yu, H.-S., P.-Z. Zhuang, and P.-Q. Mo (2019). A unified critical state model for geomaterials with an application to tunnelling. *Journal of Rock Mechanics and Geotechnical Engineering* 11(3), 464–480.
- Zienkiewicz, O. C. and R. L. Taylor (2005). *The finite element method for solid and structural mechanics*. Elsevier.
- Zohdi, T. I. and P. Wriggers (2001). Computational micro-macro material testing. *Archives of Computational Methods in Engineering* 8, 131–228.

Reference to pre-publications

In accordance with §7(1), parts of this dissertation have been published in international scientific journals and conference proceedings in consultation with the supervisor, Prof. Dr. rer. nat. Klaus Hackl. Where appropriate, references in this thesis note the following pre-publications:

- Jezdan, G., Govindjee, S., and Hackl, K. (2023). A variational approach to effective models for inelastic systems. *International Journal of Solids and Structures*, 112567. DOI: 10.1016/j.ijsolstr.2023.112567.
- Behr, F., Dolzmann, G., Hackl, K., and Jezdan, G. (2023). Analytical and numerical relaxation results for models in soil mechanics. *Continuum Mechanics and Thermodynamics*, 1-23. DOI: 10.1007/s00161-023-01225-9
- Jezdan, G., Behr, F., Dolzmann, G., and Hackl, K. (2023). A study of energies in pressure dependent plasticity - mathematical model and mechanical analogies. *PAMM*, DOI: 10.1002/pamm.202200160.
- Jezdan, G., Govindjee, S., and Hackl, K. (2021). Variational based effective models for inelastic materials. *PAMM*, DOI: 10.1002/pamm.202100053 .

Curriculum Vitae

Personal data

Name	Ghina Nabil Jezdan
Date of Birth	January 02, 1986
Place of Birth	Damascus, Syria
Nationality	German, Syrian
Marital Status	Married, 2 kids

Employment

10.2017 - present	Research associate, Institute of Mechanics of Materials, Department of Civil and Environmental Engineering, Ruhr-University Bochum, Germany
01.2014 - 08.2014	Shelter Expert, United Nations for Human Settlements (UN-Habitat), Damascus, Syria
10.2012 - 12.2013	Structural team leader, EBLA Office for Engineering and Consultation, Damascus, Syria
11.2008 - 05. 2012	Structural Engineer, Halcrow Group Ltd. (Later: <i>CH₂MHill</i>) Damascus, Syria

University Education

10.2017 - present	Doctoral student, Institute of Mechanics of Materials, Department of Civil and Environmental Engineering, Ruhr-University Bochum, Germany
10.2015 - 09.2017	Master of Science, Computational Engineering, Ruhr-University Bochum, Germany
06.2016 - 09.2017	Scholarship from DAAD Rise-Programm
10.2003 - 08.2008	Bachelor of Science, Civil Engineering, Specialization: Structural Engineering, Damascus University, Syria

School Education

10.2002 - 06.2003	Baccalaureate, Damascus, Syria
-------------------	--------------------------------

Voluntary Work

08.2017 - present	Support and Organization for Acolytes groups, Liebfrauen Catholic Church, Bochum-Linden, Germany
-------------------	--

**Mitteilungen aus dem Institut für Mechanik
RUHR-UNIVERSITÄT BOCHUM
Nr. 192**

ISBN 978-3-935892-70-4